TISSUE REMODELING IN HEALTH AND DISEASE CAUSED BY BACTERIA, PARASITES, FUNGI, AND VIRUSES

EDITED BY: Sigrun Lange and Marcel I. Ramirez
PUBLISHED IN: Frontiers in Cellular and Infection Microbiology

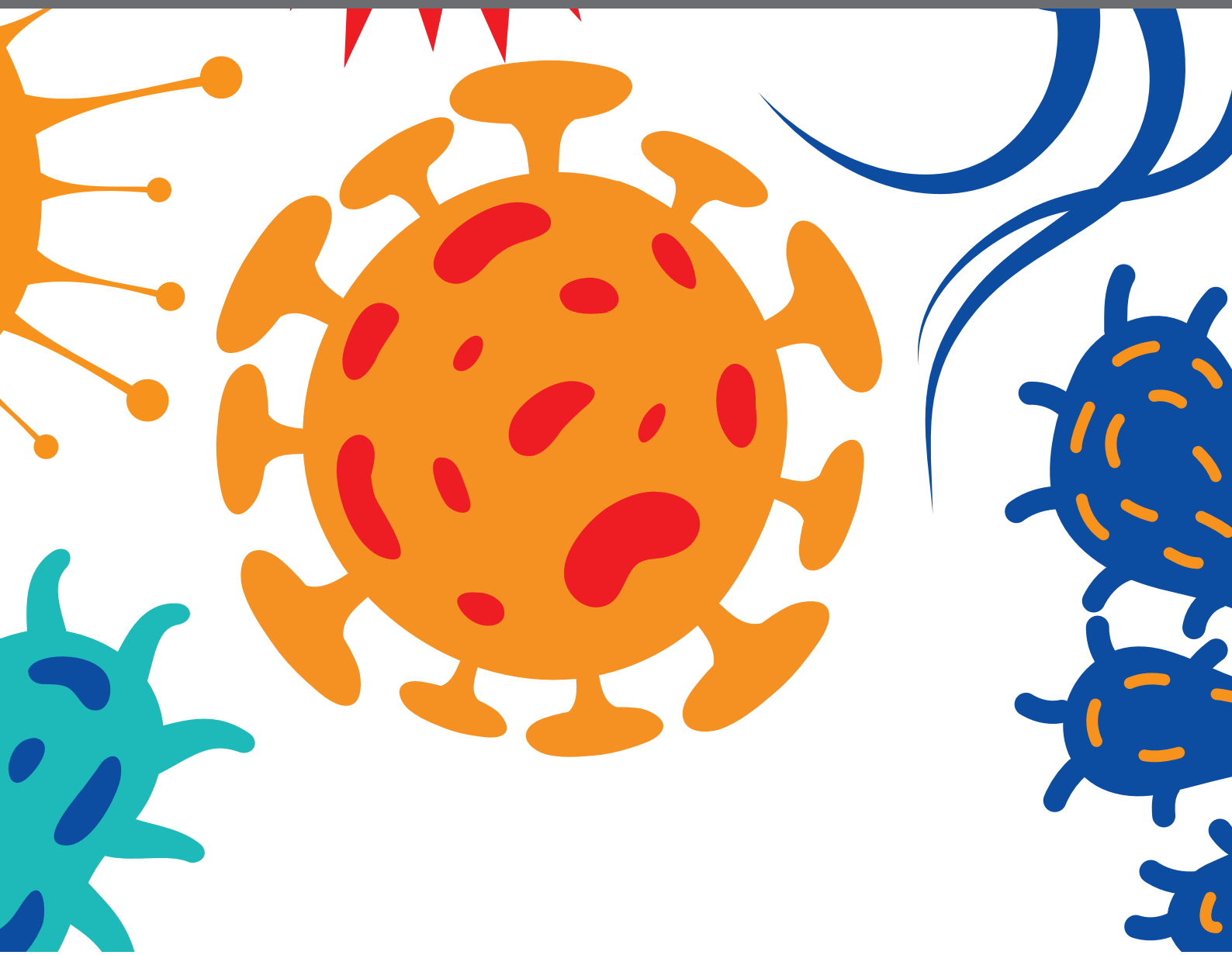

frontiers Research Topics

Frontiers eBook Copyright Statement

The copyright in the text of individual articles in this eBook is the property of their respective authors or their respective institutions or funders. The copyright in graphics and images within each article may be subject to copyright of other parties. In both cases this is subject to a license granted to Frontiers.

The compilation of articles constituting this eBook is the property of Frontiers.

Each article within this eBook, and the eBook itself, are published under the most recent version of the Creative Commons CC-BY licence. The version current at the date of publication of this eBook is CC-BY 4.0. If the CC-BY licence is updated, the licence granted by Frontiers is automatically updated to the new version.

When exercising any right under the CC-BY licence, Frontiers must be attributed as the original publisher of the article or eBook, as applicable.

Authors have the responsibility of ensuring that any graphics or other materials which are the property of others may be included in the CC-BY licence, but this should be checked before relying on the CC-BY licence to reproduce those materials. Any copyright notices relating to those materials must be complied with.

Copyright and source acknowledgement notices may not be removed and must be displayed in any copy, derivative work or partial copy which includes the elements in question.

All copyright, and all rights therein, are protected by national and international copyright laws. The above represents a summary only. For further information please read Frontiers' Conditions for Website Use and Copyright Statement, and the applicable CC-BY licence.

ISSN 1664-8714
ISBN 978-2-88966-580-8
DOI 10.3389/978-2-88966-580-8

About Frontiers

Frontiers is more than just an open-access publisher of scholarly articles: it is a pioneering approach to the world of academia, radically improving the way scholarly research is managed. The grand vision of Frontiers is a world where all people have an equal opportunity to seek, share and generate knowledge. Frontiers provides immediate and permanent online open access to all its publications, but this alone is not enough to realize our grand goals.

Frontiers Journal Series

The Frontiers Journal Series is a multi-tier and interdisciplinary set of open-access, online journals, promising a paradigm shift from the current review, selection and dissemination processes in academic publishing. All Frontiers journals are driven by researchers for researchers; therefore, they constitute a service to the scholarly community. At the same time, the Frontiers Journal Series operates on a revolutionary invention, the tiered publishing system, initially addressing specific communities of scholars, and gradually climbing up to broader public understanding, thus serving the interests of the lay society, too.

Dedication to Quality

Each Frontiers article is a landmark of the highest quality, thanks to genuinely collaborative interactions between authors and review editors, who include some of the world's best academicians. Research must be certified by peers before entering a stream of knowledge that may eventually reach the public - and shape society; therefore, Frontiers only applies the most rigorous and unbiased reviews.
Frontiers revolutionizes research publishing by freely delivering the most outstanding research, evaluated with no bias from both the academic and social point of view. By applying the most advanced information technologies, Frontiers is catapulting scholarly publishing into a new generation.

What are Frontiers Research Topics?

Frontiers Research Topics are very popular trademarks of the Frontiers Journals Series: they are collections of at least ten articles, all centered on a particular subject. With their unique mix of varied contributions from Original Research to Review Articles, Frontiers Research Topics unify the most influential researchers, the latest key findings and historical advances in a hot research area! Find out more on how to host your own Frontiers Research Topic or contribute to one as an author by contacting the Frontiers Editorial Office: frontiersin.org/about/contact

TISSUE REMODELING IN HEALTH AND DISEASE CAUSED BY BACTERIA, PARASITES, FUNGI, AND VIRUSES

Topic Editors:
Sigrun Lange, University of Westminster, United Kingdom
Marcel I. Ramirez, Oswaldo Cruz Foundation (Fiocruz), Brazil

Citation: Lange, S., Ramirez, M. I., eds. (2021). Tissue Remodeling in Health and Disease Caused by Bacteria, Parasites, Fungi, and Viruses. Lausanne: Frontiers Media SA. doi: 10.3389/978-2-88966-580-8

Table of Contents

04 ***Editorial: Tissue Remodeling in Health and Disease Caused by Bacteria, Parasites, Fungi, and Viruses***
Sigrun Lange and Marcel I. Ramirez

06 ***Serum Lipidomics Analysis of Classical Swine Fever Virus Infection in Piglets and Emerging Role of Free Fatty Acids in Virus Replication* in vitro**
Shengming Ma, Qian Mao, Wenxian Chen, Mengpo Zhao, Keke Wu, Dan Song, Xin Li, Erpeng Zhu, Shuangqi Fan, Lin Yi, Hongxing Ding, Mingqiu Zhao and Jinding Chen

21 ***Mechanisms of Oral Bacterial Virulence Factors in Pancreatic Cancer***
Zhong Sun, ChengLong Xiong, Seoh Wei Teh, Jonathan Chee Woei Lim, Suresh Kumar and Karuppiah Thilakavathy

28 ***Association of* Plasmodium berghei *With the Apical Domain of Hepatocytes is Necessary for the Parasite's Liver Stage Development***
Lakshmi Balasubramanian, Vanessa Zuzarte-Luís, Tabish Syed, Debakshi Mullick, Saptarathi Deb, Harish Ranga-Prasad, Jana Meissner, Ana Almeida, Tobias Furstenhaupt, Kaleem Siddiqi, Miguel Prudêncio, Cecilia M. P. Rodrigues, Maria Mota and Varadharajan Sundaramurthy

40 ***Kupffer Cells: Important Participant of Hepatic Alveolar Echinococcosis***
Yumei Liu, Fengming Tian, Jiaoyu Shan, Jian Gao, Bin Li, Jie Lv, Xuan Zhou, Xuanlin Cai, Hao Wen and Xiumin Ma

49 ***Defective Granuloma Formation in Elderly Infected Patients***
Aurélie Daumas, Benjamin Coiffard, Céline Chartier, Amira Ben amara, Julie Alingrin, Patrick Villani and Jean-Louis Mege

60 ***Mesoporous Hydroxyapatite/Chitosan Loaded With Recombinant-Human Amelogenin Could Enhance Antibacterial Effect and Promote Periodontal Regeneration***
Yue Liao, Huxiao Li, Rong Shu, Huiwen Chen, Liping Zhao, Zhongchen Song and Wei Zhou

74 ***Serum Proteomics Reveals Alterations in Protease Activity, Axon Guidance, and Visual Phototransduction Pathways in Infants With* In Utero *Exposure to Zika Virus Without Congenital Zika Syndrome***
Janaina Macedo-da-Silva, Lívia Rosa-Fernandes, Raquel Hora Barbosa, Claudia B. Angeli, Fabiana Rabe Carvalho, Renata Artimos de Oliveira Vianna, Paulo C. Carvalho, Martin R. Larsen, Claudete Araújo Cardoso and Giuseppe Palmisano

frontiers in Cellular and Infection Microbiology

EDITORIAL
published: 02 February 2021
doi: 10.3389/fcimb.2021.642311

Editorial: Tissue Remodeling in Health and Disease Caused by Bacteria, Parasites, Fungi, and Viruses

Sigrun Lange[1*] *and Marcel I. Ramirez*[2,3]

[1] Tissue Architecture and Regeneration Research Group, School of Life Sciences, University of Westminster, London, United Kingdom, [2] Instituto Oswaldo Cruz, Rio de Janeiro, Brazil, [3] Departamento de Bioquímica e Biologia Molecular, Universidade Federal do Paraná, Curitiba, Brazil

Keywords: tissue remodeling, host manipulation, parasites, bacteria, fungi, viruses, zoonosis, host-pathogen interaction

Editorial on the Research Topic

Tissue Remodeling in Health and Disease Caused by Bacteria, Parasites, Fungi, and Viruses

INTRODUCTION

Tissues undergo constant remodeling to maintain architecture during growth, in normal physiology and in response to disease. Interactions of the host with both commensals and pathogens, which include bacteria, viruses, fungi, and parasites, may affect not only immune responses due to recognition of pathogen associated molecular patterns (PAMPS), but also tissue remodeling including for example through the generation of neo-epitopes and damage-associated molecular patterns (DAMPS). Roles for the microbiome, viriome, fungi, as well as pathogenic bacteria and parasites, in both homeostasis and in host-pathogen interactions, is a topic of considerable interest regarding effects relating to chronic disease, cancer, dysbiosis, the gut-brain axis, host metabolism, drug metabolism, and zoonotic disease.

AIMS AND OBJECTIVES

This Research Topic sought to collect state-of-the-art primary research studies and review articles from international experts and diverse groups in the field to further current understanding of the contributions of both commensals and pathogens in tissue remodeling in physiological and pathophysiological processes of the host.

FINDINGS

Ma et al. used serum lipidomics analysis of classical swine fever virus infection in piglets to investigate the emerging role of free fatty acids in virus replication. This shows impact of lipids metabolism in CSFV infection using *in vivo* and *in vitro* approaches, identifying 167 differentially

OPEN ACCESS

Edited and reviewed by:
Jeroen P. J. Saeij, University of California, Davis, United States

***Correspondence:**
Sigrun Lange
S.Lange@westminster.ac.uk

Specialty section:
This article was submitted to Parasite and Host, a section of the journal Frontiers in Cellular and Infection Microbiology

Received: *15 December 2020*
Accepted: *11 January 2021*
Published: *02 February 2021*

Citation:
Lange S and Ramirez MI (2021) Editorial: Tissue Remodeling in Health and Disease Caused by Bacteria, Parasites, Fungi, and Viruses. Front. Cell. Infect. Microbiol. 11:642311. doi: 10.3389/fcimb.2021.642311

expressed lipid metabolites in piglets infected with CSFV, also relating to metabolites effects on mitochondrial and IFN signaling pathways. These findings provide new understanding of specific lipid metabolites in virus replication.

Balasubramanian et al. identified that the association of *Plasmodium berghei* with the apical domain of hepatocytes is necessary for the parasite's liver stage development. *Plasmodium* amplification in infected hepatocytes requires large-scale interactions with, and manipulations of, host cell functions. Using 3-D imaging and advanced image analysis of Plasmodium-infected liver tissues, the authors showed how the parasite is actively involved in modulating the architecture of the bile canicular liver tissue by associating with the apical domain of hepatocytes.

Sun et al. discuss differences in bacterial flora in pancreatic cancer versus normal pancreatic tissue and highlight putative roles for oral bacteria associated with pancreatic cancer and their virulence factors linked with cancer. This emphasizes novel preventive and therapeutic strategies based on bacterial and virulence factors in pancreatic cancer.

Liu et al. investigated the roles for Kupffer Cells as important participant of hepatic alveolar echinococcosis (AE), which is caused by *Echinococcus multilocularis* and is characterized by a large multilocular cyst with a jelly-like substance. This causes hepatomegaly and recurrent jaundice in patients. The authors showed that KC have immune-protective effect of anti-echinococcosis and promote liver fiber repair, indicating novel potential therapeutic value for patients with hepatic AE.

Daumas et al. assessed defective granuloma formation in elderly patients with sepsis by monitoring granuloma formation over the time course of infection with TB or *Coxiella burnetii*, compared with non-infected controls. The authors showed that impairment of granuloma formation was associated with reduced production of tumor necrosis factor without overproduction of interleukin-10, while furthermore genes specifically modulated in granulomatous cells were down-modulated in patients with defective granuloma formation.

Liao et al. investigate regenerative approaches in periodontitis, which is one of the most prevalent oral diseases, caused by bacterial infection and leads to destruction of alveolar bone. The authors generated scaffolds from mesoporous hydroxyapatite/chitosan, loaded with recombinant-human amelogenin, which exhibited antibacterial effects against both *Fusobacterium nucleatum* and *Porphyromonas gingivalis*, also promoting the formation of bone and cementum-like tissue.

Macedo-da-Silva et al. used serum proteomics approaches to investigate putative disease predictive biomarkers in infants with in utero exposure to Zika virus, but who were born without congenital Zika syndrome. Zika is one of the major zoonotic viruses and causes a range of, including severe, developmental neurological problems. The authors identified alterations in protease activity, axon guidance, and visual phototransduction proteome pathways in these infants, highlighting early biomarkers that are predictive for future late complications.

CONCLUSION

The collection of articles presented here in this Research Topic is a small representation of research into host-pathogen/commensal interactions, highlighting the complexity of the interplay with the host in both health and disease. The co-evolution of pathogens and hosts must be considered, both in shaping the immune system throughout evolution, gut-brain axis communication, metabolism, chronic disease, and cancers, as well as in relation to zoonotic and emerging diseases.

AUTHOR CONTRIBUTIONS

SL: Writing original manuscript. MR: Manuscript writing—Review and editing. All authors contributed to the article and approved the submitted version.

Conflict of Interest: The authors declare that the research was conducted in the absence of any commercial or financial relationships that could be construed as a potential conflict of interest.

Copyright © 2021 Lange and Ramirez. This is an open-access article distributed under the terms of the Creative Commons Attribution License (CC BY). The use, distribution or reproduction in other forums is permitted, provided the original author(s) and the copyright owner(s) are credited and that the original publication in this journal is cited, in accordance with accepted academic practice. No use, distribution or reproduction is permitted which does not comply with these terms.

frontiers in Cellular and Infection Microbiology

ORIGINAL RESEARCH
published: 03 December 2019
doi: 10.3389/fcimb.2019.00410

Serum Lipidomics Analysis of Classical Swine Fever Virus Infection in Piglets and Emerging Role of Free Fatty Acids in Virus Replication *in vitro*

Shengming Ma, Qian Mao, Wenxian Chen, Mengpo Zhao, Keke Wu, Dan Song, Xin Li, Erpeng Zhu, Shuangqi Fan, Lin Yi, Hongxing Ding, Mingqiu Zhao and Jinding Chen**

College of Veterinary Medicine, South China Agricultural University, Guangzhou, China

OPEN ACCESS

Edited by:
Marcel I. Ramirez, Oswaldo Cruz Foundation (Fiocruz), Brazil

Reviewed by:
Julià Blanco, IrsiCaixa, Spain
Peter Halfmann, University of Wisconsin-Madison, United States

***Correspondence:**
Mingqiu Zhao
zmingqiu@scau.edu.cn
Jinding Chen
jdchen@scau.edu.cn

Specialty section:
This article was submitted to Virus and Host, a section of the journal Frontiers in Cellular and Infection Microbiology

Received: *10 August 2019*
Accepted: *18 November 2019*
Published: *03 December 2019*

Citation:
Ma S, Mao Q, Chen W, Zhao M, Wu K, Song D, Li X, Zhu E, Fan S, Yi L, Ding H, Zhao M and Chen J (2019) Serum Lipidomics Analysis of Classical Swine Fever Virus Infection in Piglets and Emerging Role of Free Fatty Acids in Virus Replication in vitro. Front. Cell. Infect. Microbiol. 9:410. doi: 10.3389/fcimb.2019.00410

Lipids metabolism plays a significant role in cellular responses to virus pathogens. However, the impact of lipids metabolism in CSFV infection is not yet confirmed. In the present study, for the fist time, we performed serum lipidomics analysis of piglets infected with CSFV based on ultra-high performance liquid chromatography coupled with quadrupole time-of-flight mass spectrometry (UHPLC-QTOF-MS), and identified 167 differentially expressed lipid metabolites. Interestingly, free fatty acids (FFAs) accumulated significantly in these metabolites, accompanied by an increase in sphingolipids and a decrease in glycerolipids and glycerophospholipids, suggesting that CSFV infection markedly changed the serum lipid metabolism of piglets. FFAs are the principal constituents of many complex lipids and are essential substrates for energy metabolism. Based on this, we focused on whether FFAs play a prominent role in CSFV infection. We found that CSFV infection induced FFAs accumulation *in vivo* and *in vitro*, which is due to increased fatty acid biosynthesis. Meanwhile, we discovered that alteration of cellular FFAs accumulation by a mixture of FFAs or inhibitors of fatty acid biosynthesis affects progeny virus production *in vitro*. Furthermore, in the absence of glucose or glutamine, CSFV still has replication capacity, which is significantly reduced with the addition of fatty acid beta oxidation inhibitors, suggesting that the process of FFAs enter the mitochondria for beta oxidation to produce ATP is necessary for virus replication. Finally, we demonstrated CSFV induced FFAs accumulation results in impaired type I IFN signaling-mediated antiviral responses by down-regulating RIG-I-like receptors (RLRs) signaling molecules, which may represent a mechanism of CSFV replication. Taken together, these findings provide the first data on lipid metabolites during CSFV infection and reveal a new view that CSFV infection requires FFAs to enhance viral replication.

Keywords: CSFV, lipidomics, free fatty acids, virus replication, IFN signaling

INTRODUCTION

Classical swine fever virus (CSFV) is a member of the Pestivirus genus within the *Flaviviridae* family that is the causative agent of classical swine fever (CSF) in pigs and its genome consists of a single-stranded positive-sense genomic RNA of about 12.5 kb (Becher et al., 2003). CSF has a serious destructive effect on the immune and hematopoietic system, causing a series of clinical symptoms such as high fever, multiple hemorrhage, leukopenia, neurological dysfunction, abortion, and high mortality, which seriously endangers the healthy development of pig industry worldwide (Kleiboeker, 2002; Lohse et al., 2012). At present, CSF is largely controlled through mass vaccination because of limited treatment options (König et al., 1995; Moormann et al., 2000). Despite extensive efforts to control the spread of CSF disease through mass vaccination strategies, there is evidence that the emergence of CSFV with moderate or attenuated virulence leads to persistent recessive virulence and immunosuppression in pigs, which brings greater difficulties and challenges to the control and eradication of CSF (Edwards et al., 2000; Moennig, 2000; Stegeman et al., 2000). To develop new vaccines or specific drugs for effectively controlling infection, it is necessary to further understand the relationship between host and CSFV. Although numerous studies related to the mechanism of CSFV replication have been performed, the pathogenesis of CSFV is still poorly understood.

Lipids play an important role in regulating various life processes, not only as an important component of cells and internal organelle membranes, but also in regulating cell homeostasis in energy conversion, material transport, information recognition and signal transmission, cell development and differentiation, and cell apoptosis (Christie, 1978; Hadley, 1991). As an intracellular parasitic microorganism, viruses need lipid biogenesis participation in various steps of infection, such as viral replication, assembly, and energy supply (Bramhall and Wisnieski, 1981; Lorizate and Krausslich, 2011). Viruses hold specific classes of lipids and enrich them in the envelope structure to enhance their infectivity (Mercer and Helenius, 2008; Strating, 2012). In addition, viruses also alter lipid metabolism and provide favorable conditions for their replication (Nagy et al., 2016; Strating and Van Kuppeveld, 2017). More and more elementary studies show that abnormal lipid metabolism may be an important factor in the occurrence and development of many viral infectious diseases (Seo and Cresswell, 2013; Melanie, 2014). In recent years, the changes of lipid composition, lipid distribution, and lipid content in cell membranes and cells, and abnormal lipid metabolism have also attracted more and more attention and research as potential pathogenesis of various viral infectious diseases. Lipidomics is a comprehensive and systematic analysis and identification of lipids in cells and molecules interacting with them, which can be used as an effective tool for the discovery and subsequent identification of molecules associated with various diseases (Wenk and Markus, 2005; Sethi and Brietzke, 2017; Scott et al., 2018). It is helpful to explore the potential pathogenic mechanism of viruses by studying the lipidomics of viruses infected host cells. However, compared to genomics and proteomics, lipidomic studies of viruses, and their producer cells are limited.

Cellular lipids are abundant and diverse. Free fatty acids (FFAs) are the major constituents of many complex lipids and are essential substrates for energy metabolism (Yoshida et al., 1986; Hayyan et al., 2012). Fatty acids metabolism mainly includes *de novo* synthesis of fatty acids, oxidation of fatty acids, desaturation of fatty acids and elongation to produce fatty acids with different degrees of saturation and different carbon chain lengths (Watkins, 2013). Normally, cells mainly acquire fatty acids from dietary sources. However, in pathological cases, fatty acids in virus-infected or cancer cells are derived from fatty acid biosynthesis (Menendez and Lupu, 2007). A number of studies have reported that fatty acids have a prominent role on the replication of various viruses, including West Nile virus (WNV), rotaviruses (RV), hepatitis C virus (HCV), human immunodefciency virus type-1 (HIV-1), dengue virus (DENV), and respiratory syncytial virus (RSV) (Superti et al., 1995; Kapadia and Chisari, 2005; Hilmarsson et al., 2007; Heaton and Randall, 2010; Luchessi, 2010; Martin-Acebes et al., 2014). Chemicals inhibition of fatty acid synthesis by C75, TOFA, or triacsin C decreases the replication ability of these viruses (Yang et al., 2008; Miguel et al., 2011; Gaunt et al., 2013; Tang et al., 2014; Ohol et al., 2015; Kulkarni et al., 2017).

Our previous work has confirmed that CSFV rebuild cellular metabolic programs *in vitro*, thus aiding viral replication (Hongchao et al., 2017; Wenjie et al., 2017). However, systematic changes in lipid metabolites in CSFV-infected cells remain unknown. In the current study, and for the first time, we performed a serum lipidomics analysis of piglets infected with CSFV based on ultra-high performance liquid chromatography coupled with quadrupole time-of-flight mass spectrometry (UHPLC-QTOF-MS), as well as the differential lipids were identified. In particular, among these differential lipids, FFAs were significantly increased during CSFV infection. Moreover, we explored the effect of the FFAs on CSFV replication and type I IFN (interferon) signaling pathway by adding a mixture of FFAs (oleic: palmitoleic=2:1) or disturbing the fatty acid biosynthase pathway with C75 and TOFA in CSFV-infected PK-15 and 3D4/2 cells. These studies provide the first data regarding the lipid metabolites during CSFV infection, which may represent potential anti-viral drug targets. Meanwhile, the current results demonstrated the important role of FFAs in CSFV replication, which may represent a mechanism of CSFV replication and CSFV induced immunomodulation.

RESULTS

Establishment of a Platform for Serum Lipidomics Analysis in Piglets Infected With CSFV

To investigate the effect of CSFV infection on lipid metabolism *in vivo*, experiments were carried out using piglets infected with Shimen, a representational virulent strain of CSFV. A total of ten 2-month-old piglets were randomly divided into two groups, one challenged with 10^5 $TCID_{50}$ of CSFV (Group S) and one

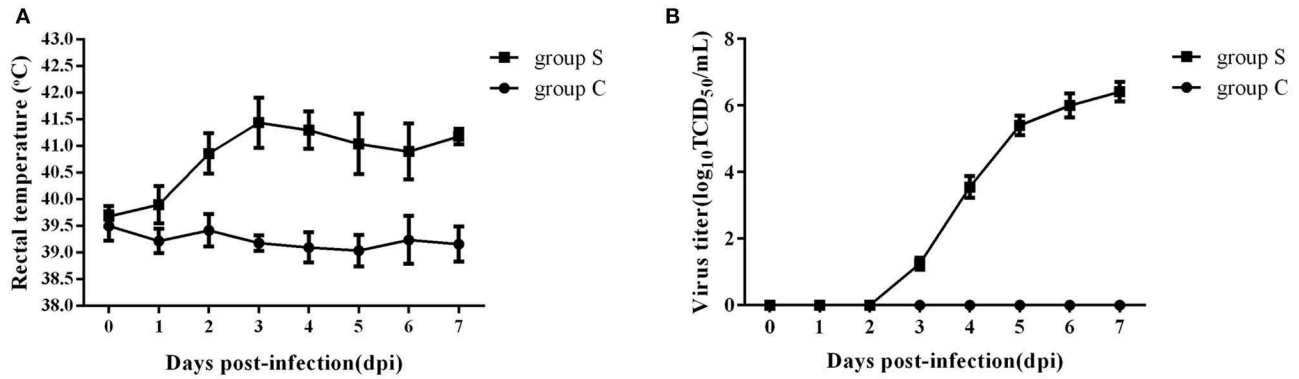

FIGURE 1 | Changes of rectal temperature and blood viral load of piglets infected with CSFV. **(A)** Daily rectal temperature from 0 to 7 days after CSFV infection in piglets. **(B)** Daily blood viral load from 0 to 7 days after CSFV infection in piglets.

inoculated with an equal volume of normal PK-15 cell-culture supernatant served as negative controls (Group C) ($n = 5$ each), and the rectal temperature and the blood viral load were daily detected after infection. As shown in **Figure 1**, group S piglets has a high fever from 39.4°C to 42.1°C (**Figure 1A**), and the blood viral load was first detected at 3 days post infection (dpi) and reached to a peak at 6 dpi (**Figure 1B**), while group C piglets had a stable rectal temperature and no virus was observed. During the whole infection period, the onset of clinical symptoms and autopsy lesions of group S piglets was consistent with the typical CSFV cases, while no significant changes in group C piglets. Thus, the typical disease form of CSF has been successfully established by shimen infection.

We next performed lipidomics analysis using UHPLC-QTOF-MS with lipids isolated from serum of group S and group C piglets at 6 dpi. The accurate m/z of precursors and product ions were matched against LipidBlast database and in-house standard library including retention time, accurate precursors, and product ions. The chromatographic retention of the same group samples will not change, and the signal of each substance is slightly different. As shown in **Figure 2**, we select a single representative from group S and group C samples and draw the typical base peak ion (BPI) chromatograms under the positive (ESI+) or negative ion mode (ESI-) to show the distribution of metabolite signals in the chromatogram. The threshold of matching similarity is >80% (**Figure 2**). These results suggest that the platform of UHPLC-QTOF-MS is reliable and can be utilized in the subsequent study.

CSFV Infection Alters Serum Lipid Metabolism of Piglets

To truly reflect the lipidomics differences between group S and group C piglets, SIMCA (Version 14.1) software was performed to make the principal component analysis (PCA). Under the positive or negative ion mode, the PCA score chart showed that there was a significant trend of separation between group S and group C (**Figures 3A,B**). In order to eliminate the influence of background noise and thus highlight the differences between groups, the PLS-DA supervised multidimensional statistical analysis method was used to analyze the samples of group S and group C. In positive ion mode, a PLS-DA model with three effective principal components was established, $R_2X = 0.832$, $R_2Y = 0.995$, $Q_2 = 0.964$ (**Figure 3E**). Similarly, in the negative ion mode, a PLS-DA model with two effective principal components was established, $R_2X = 0.74$, $R_2Y = 0.994$, $Q_2 = 0.79$ (**Figure 3F**). The main parameters for judging the quality of the model are R_2Y (model cumulative interpretation rate) and Q_2 (model cumulative prediction rate). When R_2Y is >0.5, it indicates that the current model is suitable for explaining the difference between the two groups; when the value of Q_2 is >0.5, the current model is suitable for prediction. The replacement test showed that the current model is very reliable (**Figures 3C,D**). The PLS-DA score chart showed that there was significant spectral separation between group S and group C (**Figures 3E,F**). In order to further distinguish between the two groups of different substances, the OPLS-DA model was established in the positive or negative ion mode, respectively. In positive ion mode, the OPLS-DA model with one principal component and three orthogonal components is automatically established. The main quality parameters of the model are $R_2X = 0.885$, $R_2Y = 0.999$, $Q_2 = 0.963$ (**Figure 3G**); in negative ion mode, one is automatically established. The main component and the OPLS-DA model of one orthogonal component, the main quality parameters of the model are $R_2X = 0.74$, $R_2Y = 0.994$, $Q_2 = 0.982$ (**Figure 3H**). The OPLS-DA score chart indicated that the current model can distinguish very effectively between the two groups of samples in group C and group S (**Figures 3G,H**). All those data indicate that CSFV infection markedly changed the serum lipid metabolism of piglets.

Identification of Serum Differential Lipids in Piglets Infected With CSFV

According to the criteria set for the variable importance in the projection (*VIP*) > 1 obtained from the PLS-DA model and *P*-value < 0.05 in the Student's *t*-test, totals of 167 differential lipids were identified between group S and group C. Among these differential lipids, 65 lipids were observed to be increased

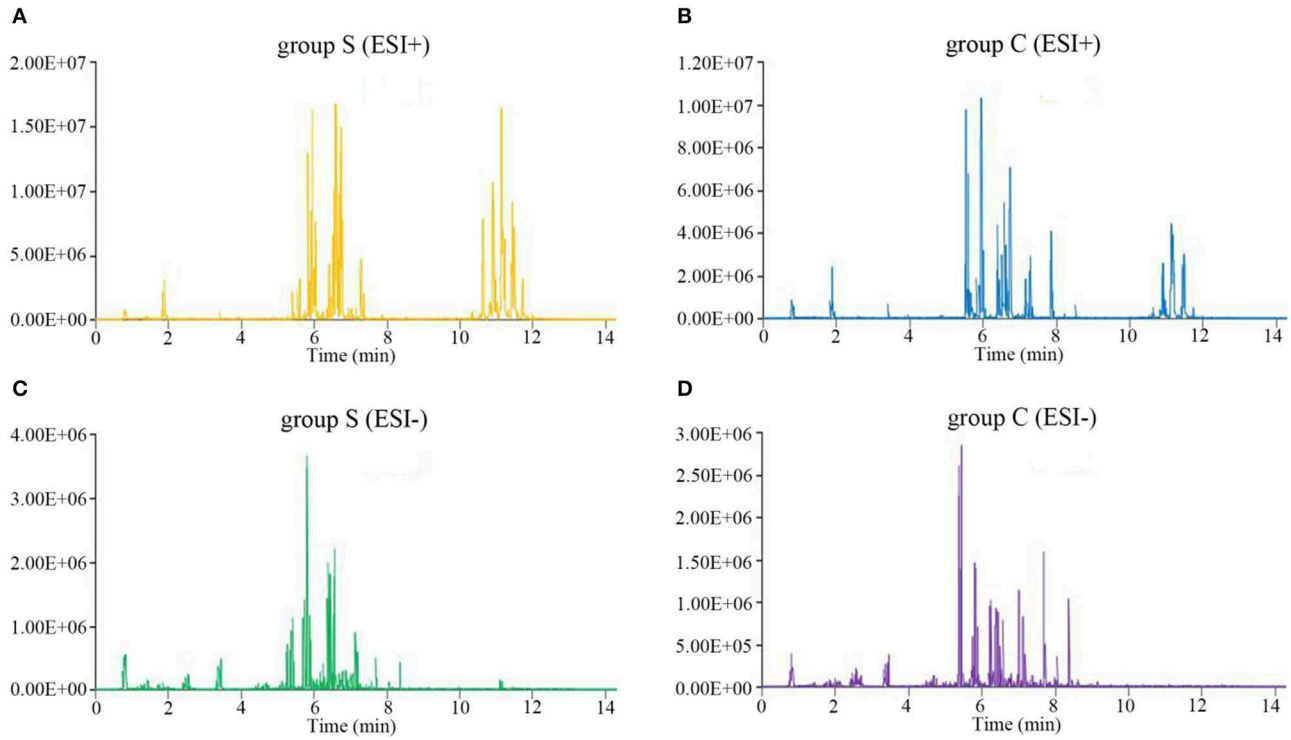

FIGURE 2 | The typical base peak ion (BPI) chromatograms under the positive (ESI+) or negative ion mode (ESI-). **(A)** CSFV-infected piglets (ESI+). **(B)** DMEM-infected piglets (ESI+). **(C)** CSFV-infected piglets (ESI−). **(D)** DMEM-infected piglets (ESI−).

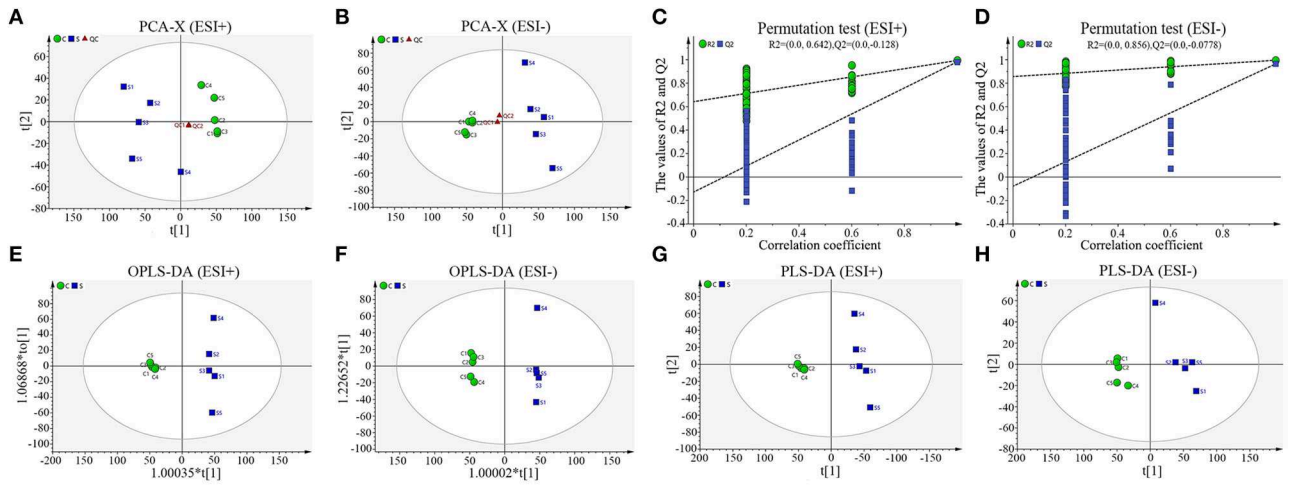

FIGURE 3 | Sample score diagrams of group S and group C and OPLS-DA model replacement test diagrams under the positive (ESI+) or negative ion mode (ESI−). **(A)** The PCA score chart of group S and group C samples under ESI+. **(B)** The PCA score chart of group S and group C samples under ESI−. **(C)** The replacement test of group S and group C samples under ESI+. **(D)** The replacement test of group S and group C samples under ESI-. **(E)** The PLS-DA score chart of group S and group C samples under ESI+. **(F)** The PLS-DA score chart of group S and group C samples under ESI-. **(G)** The OPLS-DA score chart of group S and group C samples under ESI+. **(H)** The OPLS-DA chart plot of group S and group C samples under ESI-.

during CSFV infection, along with the simultaneous down-regulation of 102 lipids, respectively, in **Tables S1**, **S2**. The increased differential lipids mainly belonged to free fatty acids (FFAs), and sphingolipids including sphingomyelin (SM), ceramide non-hydroxyfatty acid-sphingosine (Cer-NS), and hexosylceramide non-hydroxyfatty acid-sphingosine (HexCer-NS). The decreased differential lipids mainly belonged to glycerolipids including cholesteryl ester (CE)

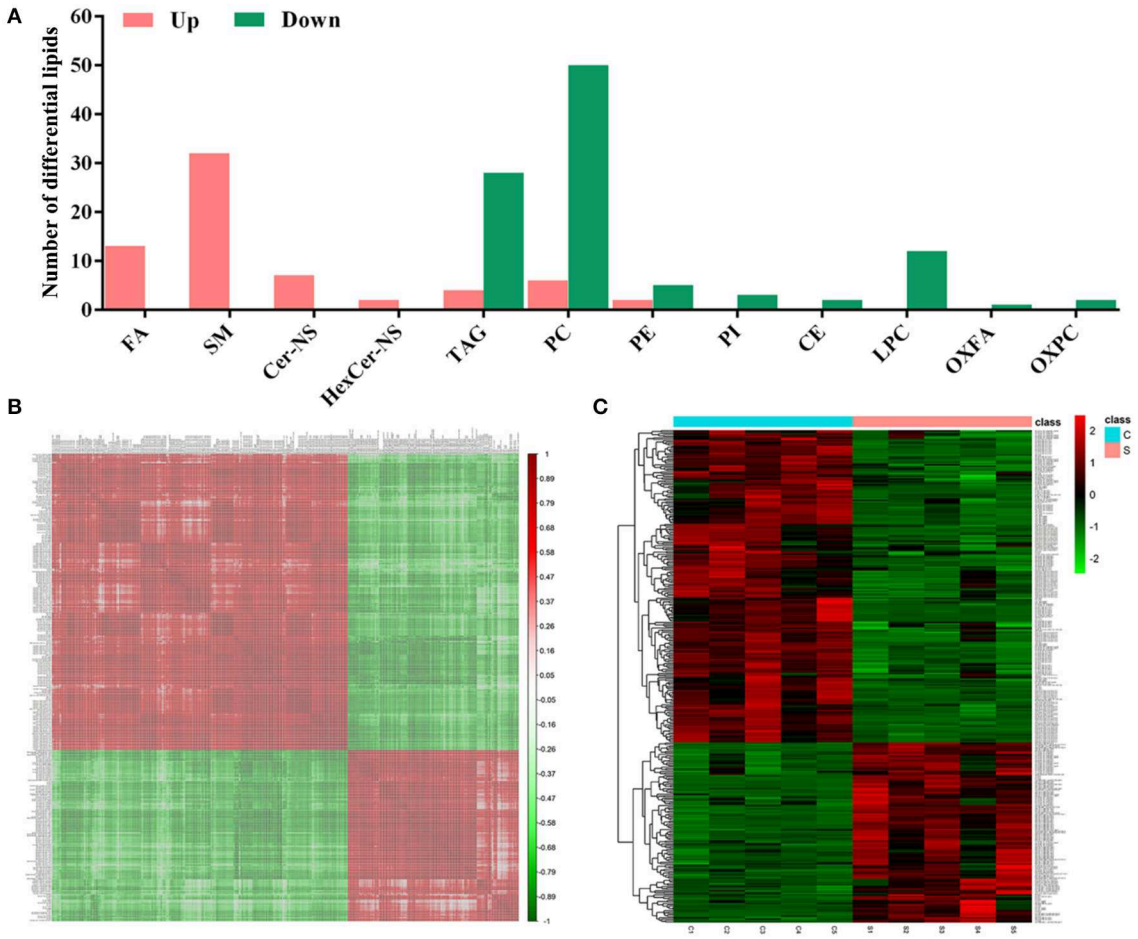

FIGURE 4 | Differential metabolites between group S and group C. **(A)** Statistical analysis of differential metabolites between group S and group C. **(B)** Relevance matrix diagram of differential metabolites between group S and Group C. **(C)** Heat map of differential metabolites in Group S and Group C.

and triacylglycerol (TAG), and glycerophospholipids including lysophophatidylcholine (LPC), phosphatidylcholine (PC), phosphatidylethanolamine (PE), phosphatidylinositol (PI), oxidized fatty acid (OXFA), and oxidized phosphatidylcholine (OXPC) (**Figure 4A**). Further, we performed a correlation matrix analysis of the differential compounds ($p < 0.05$) using R (version 3.4.1) software. To characterize the (concentration) correlation between the different metabolites, we performed a correlation (Pearson Correlation) analysis of the quantitative information for these substances, as showed in **Figure 4B**. Both rows and columns in the figure represent differential metabolites. The correlation coefficient metric is shown on the right side of the figure. The color shades of the squares in the figure are related to the correlation between the different metabolites. The differential lipids correlation matrix analyzed showed that there was no significant correlation between group S and group C (**Figure 4B**). In addition, we performed heat map analysis of differential compounds ($p < 0.05$) using R (version 3.4.1) software. The heat map analysis of the difference material is shown in **Figure 4C**. Each row represents a differential metabolite, each column represents a sample (number), the upper tree structure represents the similarity clustering relationship between samples, and the left tree structure represents the similarity between different metabolites class relationship. Heatmap analysis showed that all the differential lipids within group S or group C can be clustered together, but not between groups (**Figure 4C**). These results suggest that CSFV infection leads to abnormal expression of different lipids, which further indicate that CSFV infection causes lipid metabolism disorder.

CSFV-Induced FFAs Accumulation Is Mainly Due to the Increase of Fatty Acid Synthesis

FFAs are the main components in the synthesis of different lipids and play an important role in the regulation of lipid metabolism (Yoshida et al., 1986; Hayyan et al., 2012). To characterize the difference FFAs between group S and group C, we used R (version 3.4.1) software to make box plot of differential compounds ($p < 0.05$). As shown in **Figure 5A**, all differential

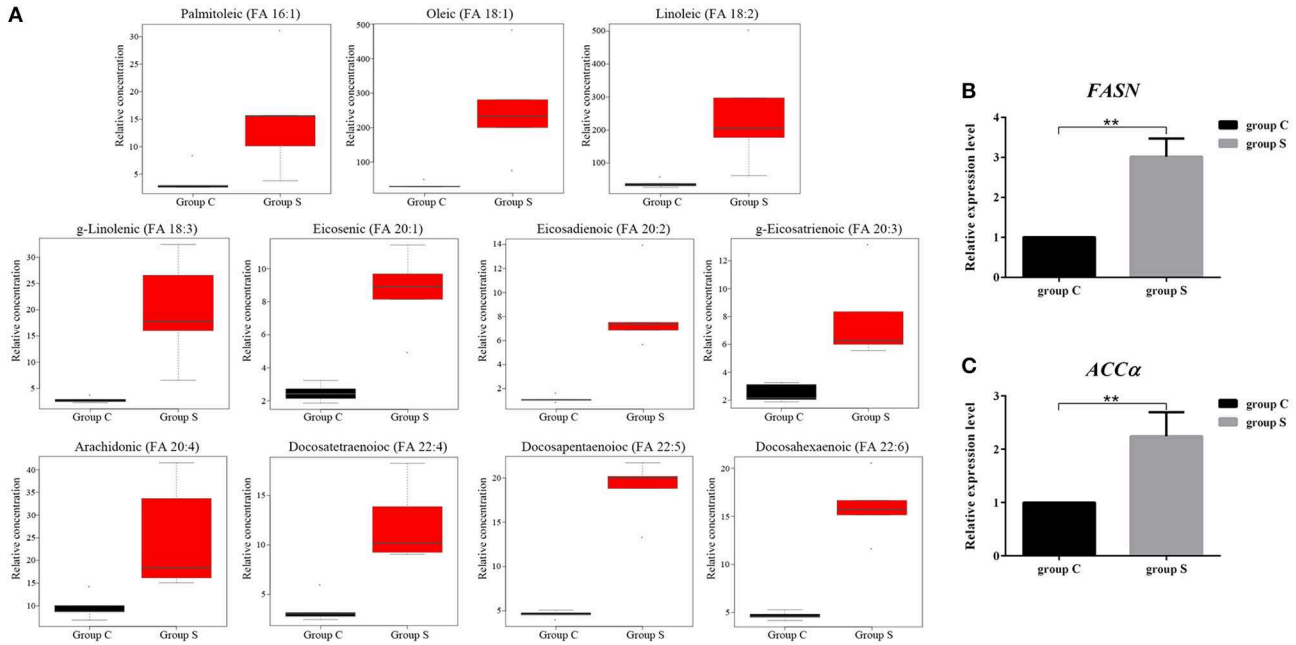

FIGURE 5 | CSFV-induced FFAs accumulation is mainly due to the increase of fatty acid synthesis in serum of piglets. **(A)** Box diagram of the differentially expressed FFAs ($p < 0.05$) in Group S and Group C using R (version 3.4.1) software. **(B,C)** The transcription levels of FASN **(B)** and ACCα **(C)** in serum of Group S and Group C piglets were deteced by qRT-PCR as described in Materials and Methods. $^{**}P < 0.01$. *P*-values were calculated using an One-way ANOVA test.

FFAs including palmitoleic (FA 16:1), oleic (FA 18:1), linoleic (FA 18:2), g-linolenic (FA 18:3), eicosenic (FA 20:1), eicosadienoic (FA 20:2), g-eicosatrienoic (FA 20:3), arachidonic (FA 20:4), docosatetraenoioc (FA 22:4), docosapentaenoioc (FA 22:5), and docosahexaenoic (FA 22:6) were significant increased during CSFV infection. In addition to the degradation of glycerides, phospholipids, sphingolipids, and steroids by lipase, another important source of intracellular FFAs is the increase in fatty acid synthesis. Previous studies have shown that FFAs in virus-infected cells or cancer cells are mainly derived from fatty acid biosynthesis (Menendez and Lupu, 2007). To determine whether CSFV-induced FFAs accumulation is due to the increase of fatty acid biosynthesis, we used quantitative real time PCR (qRT-PCR) to evaluate the mRNA expression levels of the key enzymes in fatty acid biosynthesis in serum of group S and group C piglets at 6 dpi, including fatty acid synthase (FASN) and acetyl CoA carboxylase alpha (ACCα). Results showed that the transcription levels of FASN and ACCα were significantly increased in group S piglets as compared to group C piglets (**Figures 5B,C**), indicating that CSFV infection increased fatty acid biosynthesis, which may leads to the accumulation of FFAs.

CSFV-Induced FFAs Accumulation and Increased Fatty Acid Synthesis *in vitro*

To further investigate the roles of cellular FFAs in CSFV infection, we chose PK-15 and 3D4/2 cell lines as cell models of CSFV infection *in vitro*, and examined the levels of FFAs in cell supernatants at different hours post infection (hpi) with CSFV using FFAs ELISA Kit (Zcibio, ZC-39969). As shown in **Figures 6A,E**, the levels of FFAs in the supernatant of cells infected with CSFV increased significantly at 24 and 48 hpi. Further, we detected the expression levels of FASN and ACCα in cells using qRT-PCR. Results showed that the mRNA levels of FASN and ACCα observed an increased tendency from 24 to 48 hpi (**Figures 6B,C,E,F**), suggesting that cellular up-regulated fatty acid biosynthesis was responsible for FFAs accumulation following CSFV infection. More importantly, we used ultraviolet (UV)-inactivated CSFV to evaluate whether FFAs can be up-regulated following treatment. Results showed that no significant changes in the relative levels of FFAs, FASN and ACCα were observed during UV-CSFV infection (**Figures 6A–C,E–G**), indicating that FFAs is required for effective viral replication. Meanwhile, CSFV protein NS5B was detected by qRT-PCR to evaluate the progression of viral infection, result shown that the transcription level of NS5B gene was detected only in CSFV-infected PK-15 and 3D4/2 cells, and increased gradually with the prolongation of infection time, while the expression of NS5B gene was not detected in mock and UV-infected cells (**Figures 6D,H**).

FFAs Are Required for CSFV Replication *in vitro*

To further determine the effect of FFAs on CSFV replication, fatty acid biosynthesis inhibitor C75 (20 μM) and TOFA (30 μM) were used to treat CSFV-infected PK-15 or 3D4/2 cells, respectively, and DMSO treatment was used as a negative control. After treatment for 24 and 48 h (h), we examined the levels of FFAs in cell supernatants and analyzed the capability of CSFV replication by detecting the virus copy number and titer. Compared with

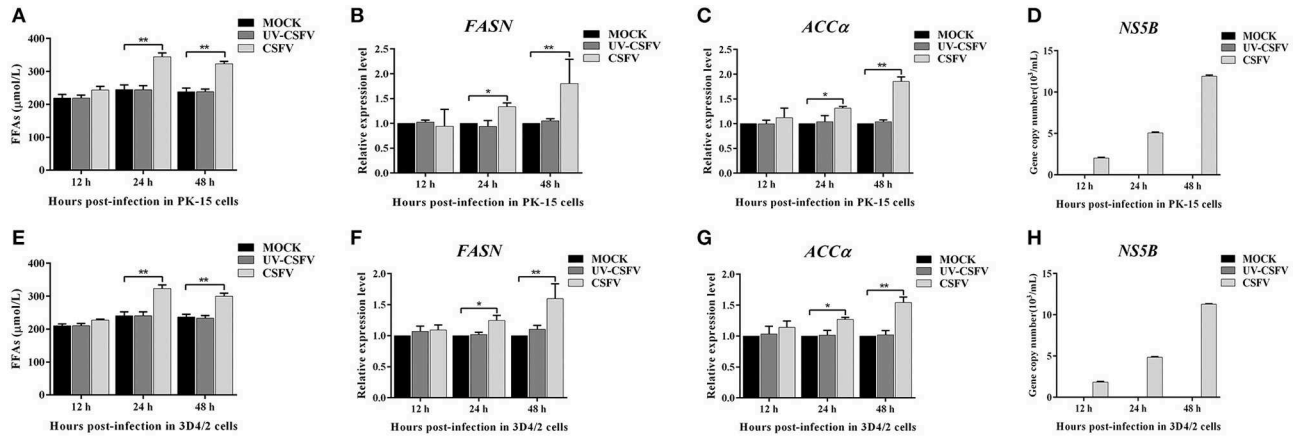

FIGURE 6 | CSFV-induced FFAs accumulation and increased fatty acid synthesis *in vitro*. PK-15 and 3D4/2 cells were mock-infected or infected with CSFV (MOI = 1.0) or UV-inactivated CSFV (MOI = 1.0) for 12, 24, and 48 h. **(A,E)** the levels of FFAs in the supernatant of PK-15 **(A)** and 3D4/2 **(E)** cells were detected by FFAs ELISA Kit. **(B,C,F,G)** The transcription levels of FASN, ACCα in PK-15 and 3D4/2 cells were detected by qRT-PCR as described in Materials and Methods. **(D,H)** CSFV protein NS5B was detected by qRT-PCR to evaluate the progression of viral infection in PK-15 **(D)** and 3D4/2 **(H)** cells. The data represent the mean ± SD of 3 independent experiments. $^{*}P < 0.05$; $^{**}P < 0.01$. *P*-values were calculated using an One-way ANOVA test.

DMSO treatment, both C75 and TOFA significantly inhibited the accumulation of FFAs (**Figures 7A,E**) and reduced CSFV copy number and titer (**Figures 7B,C,F,G**), showing that fatty acid biosynthesis inhibition reduce FFAs accumulation and CSFV production. However, when we treated cells with a mixture of FFAs (mFFAs) at a 2:1 ratio of oleic to palmitoleic (100 μM), the capability of CSFV replication increased (**Figures 7B,C,F,G**). Meanwhie, in order to exclude the effect of fatty acid biosynthesis inhibitors and mFFAs on viral replication by altering cell viability, CCK-8 Cell Counting Kit (Vazyme,A311-01) was used to evaluate the effects of C75, TOFA and mFFAs on PK-15 and 3D4/2 cells viability. Statistical analyses revealed no significant effects on the viability of cells treated with C75, TOFA or mFFAs ($P > 0.05$) (**Figures 7D,H**). Taken together, these data revealed that FFAs are required for efficient CSFV replication.

FFAs Are an Indispensable Source of ATP for CSFV Replication

FFAs not only participate in the formation of cell structure, but also provide an energy source for host cells through fatty acid beta oxidation (FAO) (Yoshida et al., 1986; Hayyan et al., 2012). Etomoxir is an inhibitor of carnitine palmitoyltransferase A (CPT1), which is required for the oxidation of long-chain acyl CoA esters. Trimetazidine (TMZ) reduces acetyl coenzyme A produced by free fatty acid metabolism, thereby stimulating pyruvate dehydrogenase and indirectly enhancing glucose oxidation. To directly analyze whether the increased FFAs during CSFV infection provides ATP for virus replication through FAO, we tested the levels of ATP in PK-15 and 3D4/2 cells and the replication ability of CSFV following etomoxir (2 μM) or TMZ (60 μM) treatment. We found that the pharmacological alteration of FAO with etomoxir and TMZ not only reduced the levels of cellular ATP (**Figures 8A,G**), but also significantly decreased the capability of CSFV replication (**Figures 8B,C,H,I**). Meanwhile, there are no significant effects on the viability of PK-15 or 3D4/2 cells treated with etomoxir or TMZ (**Figures 8D,J**). These findings suggest that CSFV-induced the accumulation of FFAs was transported to mitochondria for beta oxidation, thus providing ATP for viral replication.

As another energy source, glucose is the most widely used carbon source for energy metabolism and biosynthesis in mammalian cells. Studies have found that most viral infections cause glycolysis to provide energy for viral replication (Fontaine et al., 2014; Findlay and Ulaeto, 2015). To further determine whether FAO contribute to productive CSFV infection, CSFV-infected PK-15 and 3D4/2 cells were cultured for 48 h in glucose-free media or glucose-low media or glucose-high media, respectively, along with the treatment of etomoxir or TMZ or DMSO. As show in **Figures 8E,F,K,L**, the capability of CSFV replication is dependent on a certain glucose concentration, and the higher glucose concentration, the stronger capability of CSFV replication (**Figures 8E,F,K,L**). Interestingly, the virus still has a strong replication capacity under conditions of low glucose or glucose loss, which is significantly reduced when treated with FAO inhibitors (**Figures 8E,F,K,L**). In addition, glutamine can replace glucose in the TCA cycle to provide energy for viral replication (Sanchez et al., 2017). However, in the absence of glutamine, CSFV replication had no significant changes relative to the complete medium (**Figures 8E,F,K,L**). Together, these results suggested that ATP produced by FFAs transported to mitochondria for FAO is essential for CSFV replication.

CSFV Induced FFAs Accumulation Results in Impaired Type I IFN Signaling-Mediated Antiviral Responses

According to the current understanding of the pathogenesis of CSFV, we know that CSFV infection inhibits the production of type I IFN *in vitro*, thereby resulting in the persistent survival

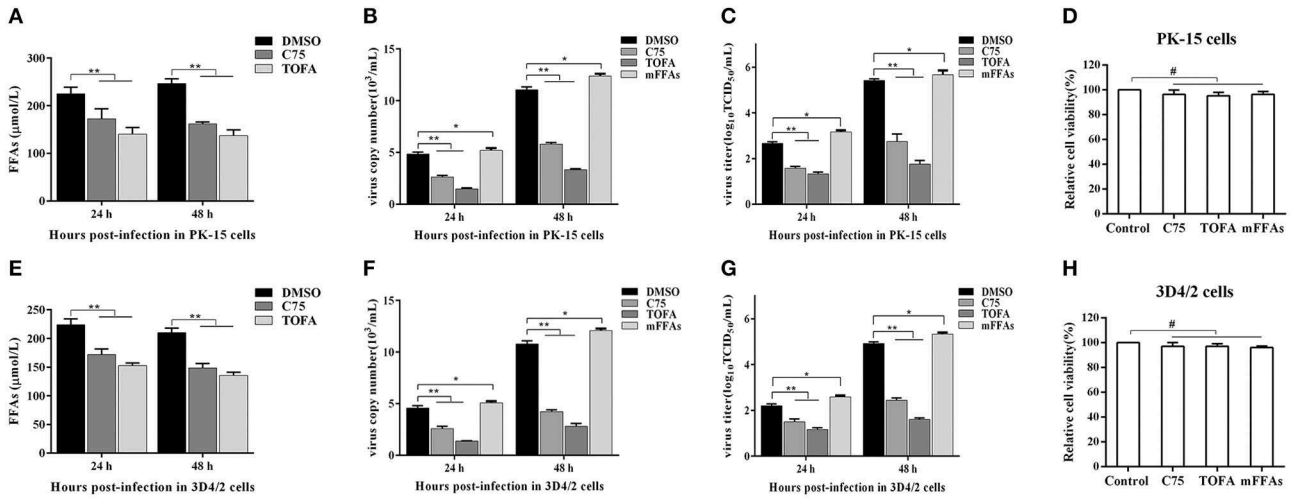

FIGURE 7 | FFAs are required for CSFV replication *in vitro*. **(A,E)** CSFV-infected PK-15 and CSFV-infected 3D4/2 cells were treated with C75 (20 μM), TOFA (30 μM) or DMSO for 24 and 48 h. The levels of FFAs in the supernatant of PK-15 **(A)** and 3D4/2 **(E)** cells were detected by FFAs ELISA Kit. **(B,C,F,G)** CSFV-infected PK-15 and CSFV-infected 3D4/2 cells were treated with mFFAs, C75 (20 μM), TOFA (30 μM), or DMSO for 24 and 48 h. The virus copy number of CSFV in PK-15 **(B)** and 3D4/2 **(F)** cells were detected by qRT-PCR. The titer of CSFV in PK-15 **(C)** and 3D4/2 **(G)** cells were detected by IFA. **(D,H)** PK-15 and 3D4/2 cells were treated with mFFAs (100 μM), C75 (20 μM), TOFA (30 μM), or DMSO for 48 h. PK-15 **(D)** and 3D4/2 **(H)** cells viability were detected by CCK-8 Cell Counting Kit. The data represent the mean ± SD of 3 independent experiments. $^{*}P < 0.05$; $^{**}P < 0.01$; $^{\#}P > 0.05$. *P*-values were calculated using an One-way ANOVA test.

of CSFV in host cells (Bensaude, 2004). Studies have shown that the accumulation of FFAs in HCV-infected cells inhibits the activation of type I IFN signaling pathway, resulting in impaired antiviral response (Gunduz et al., 2012). To further understand the mechanism of FFAs affecting the replication of CSFV, mFFAs and fatty acid biosynthesis inhibitors were used to regulate the production of FFAs in CSFV-infected or mock-infected PK-15 and 3D4/2 cells, and the mRNA expression levels of IFN-α and IFN-β were detected by qRT-PCR to verify if alteration of cellular FFAs production has an effect on the IFN signaling pathway. Results showed a significant decrease in mRNA expression of IFN-α and IFN-β genes in mFFAs treated CSFV-infected PK-15 and 3D4/2 cells for 24 and 48 hpi, and a increase in C75 or TOFA treated CSFV-infected cells, compared with DMSO treated CSFV-infected cells (**Figures 9A,B,D,E**), suggesting that CSFV-induced FFAs accumulation may affect viral replication by suppressing type I IFN production. CSFV can be recognized by the members of the RIG-I-like receptors (RLRs) in cells, such as melanoma differentiation-associated gene 5 (MDA5) and retinoic acid-inducible gene I (RIG-I), which mediate type I IFN production by NF-κB and phosphorylation of IRF3 (Dong et al., 2013). Based on this, we suspect that FFAs may suppress type I IFN production by affecting the activation of RLRs signaling pathway. To test this conjecture, key markers of RLRs signaling pathway, including RIG-I, MDA5 NF-κB and p-IRF3 (phosphorylated IRF3), were examined by western blot in CSFV-infected or MOCK-infected PK-15 or 3D4/2 cells treated with mFFAs, C75, TOFA, or DMSO for 48 hpi. Surprisingly, our results showed that the expression of RIG-I and MDA5 proteins in CSFV-infected PK-15 and 3D4/2 cells were significantly increased in C75 or TOFA treated CSFV-infected cells, and NF-κB and p-IRF3 was activated, contrary to the results of mFFAs treated CSFV-infected cells, compared with DMSO treated CSFV-infected cells (**Figures 9C,F**). However, there is no significant difference in expression of these proteins in mock-infected cells treated with mFFAs, C75 or TOFA, compared with DMSO treated mock-infected cells (**Figures 9C,F**). Meanwhile, CSFV non-structural protein Npro, which is associated with virus replication, was detected by western blot to estimate the progression of infection, we found that Npro protein displayed a higher level in FFAs treated CSFV-infeted cells than in DMSO treated CSFV-infeted cells, whereas Npro protein in C75 or TOFA treated CSFV-infected cells showed a lower Level (**Figures 9C,F**). These findings indicate that CSFV-induced FFAs accumulation suppressed type I IFN production by down-regulating RLR signaling, thereby resulting in the persistent survival of CSFV in host cells.

DISCUSSION

It is well-known that viruses alter host metabolism, especially lipid metabolism, to facilitate their infection and replication (Heaton and Randall, 2011). Like other members of the *Flaviviridae* family, CSFV can also cause cellular metabolic disorders and lead to a series of pathological reactions, such as high fever, multiple hemorrhage, leukopenia and inflammation (Kleiboeker, 2002; Lohse et al., 2012; Hongchao et al., 2017). In the current study, we provided for the first time observations on the lipids changes in the serum of CSFV-infected piglets based on UHPLC-QTOF-MS, which might provide suitable targets for drug intervention and therapeutic vaccines. More

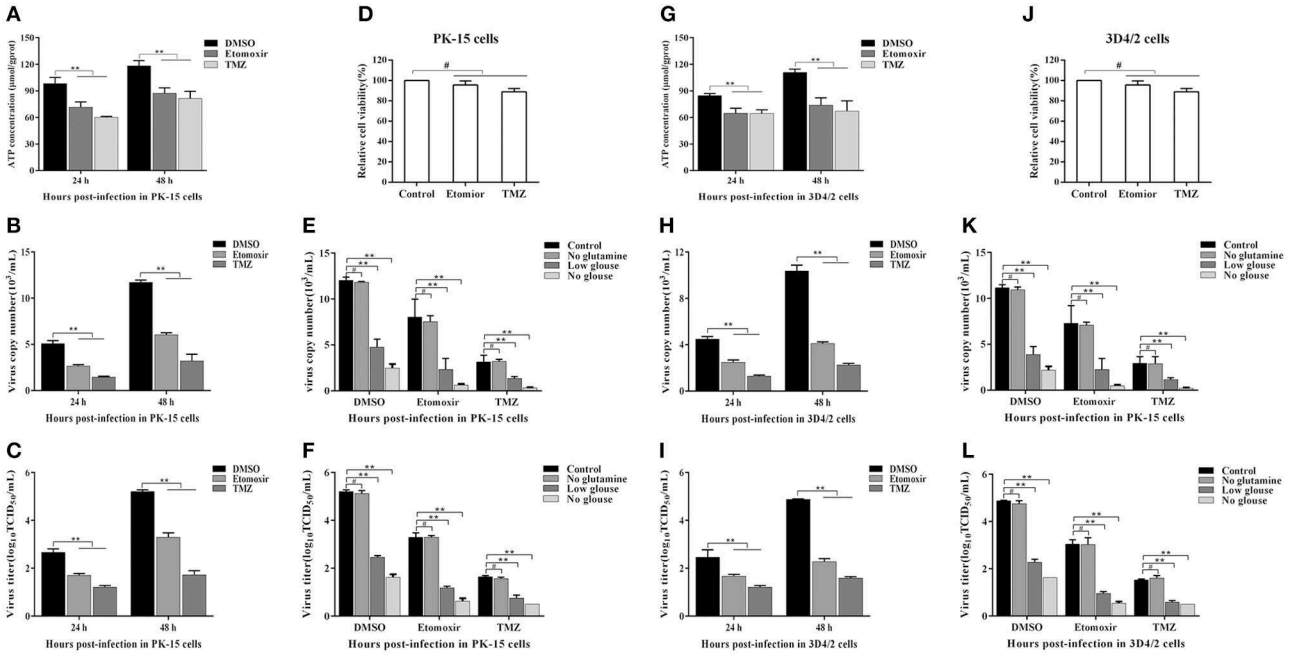

FIGURE 8 | Free fatty acid is an indispensable source of ATP for CSFV replication *in vivo*. **(A–D,G–J)** CSFV-infected PK-15 and CSFV-infected 3D4/2 cells were treated with etomoxir (2 μM), TMZ (60 μM), or DMSO for 24 and 48 h. The levels of ATP in PK-15 **(A)** and 3D4/2 **(G)** cells were detected by ATP assays Kit. The virus copy number of CSFV in PK-15 **(B)** and 3D4/2 **(H)** cells were detected by qRT-PCR. The titer of CSFV in PK-15 **(C)** and 3D4/2 **(I)** cells were detected by IFA. PK-15 **(D)** and 3D4/2 **(J)** cells viability were detected by CCK-8 Cell Counting Kit. **(E,F,K,L)** CSFV-infected PK-15 and 3D4/2 cells were cultured for 48 h in glucose-free media or glucose-low media or glutamine-free media or complete media, respectively, along with the treatment of etomoxir (2 μM) or TMZ (60 μM) or DMSO. The virus copy number of CSFV in PK-15 **(E)** and 3D4/2 **(F)** cells were detected by qRT-PCR. The titer of CSFV in PK-15 **(K)** and 3D4/2 **(L)** cells were detected by IFA. The data represent the mean ± SD of 3 independent experiments. $^{**}P < 0.01$; $^{\#}P > 0.05$. *P*-values were calculated using an One-way ANOVA test.

importantly, we found that FFAs accumulation plays a positive role in CSFV infection *in vitro,* which may reveal a new view for the pathogenesis and immune escape mechanism of CSFV.

Interestingly, viruses from same family induce some similar lipids changes. During CSFV infection, the increased lipids were mainly classified as FFAs and sphingolipids, while the reduced lipids were mainly classified as glycerolipids and glycerophospholipids (**Figures 2**–**5**) (**Tables S1, S2**). The accumulation of FFAs caused by viral infection contributes to the formation of membrane viral replication complexes and promotes the transmission of viruses, which have been confirmed in DENV and HCV (Kapadia and Chisari, 2005; Heaton and Randall, 2010). Sphingolipids, including sphingomyelin and ceramide, play an important role in the adsorption, assembly and intracellular transport of HCV and HBV, and are essential for HCV and HBV replication (Merrill et al., 2001). Glycerolipids, are an important component of cell membrane and participates in virus infection and release. Removal of cell membrane cholesterol can promote the release of virus from infected cells, but the infectivity of released virus particles is reduced (Popescu and Dubuisson, 2010). Gglycerophospholipids is considered to be an important regulator of inflammation and cell proliferation (Popescu and Dubuisson, 2010). However, whether these changed lipids play the same role in the infection of CSFV and other *Flaviviridae* family viruses still needs further confirmation.

FFAs are the major constituents of many complex lipids and are essential substrates for energy metabolism. To better understand the roles of cellular FFAs in CSFV infection, we analyzed the physiological significance of FFAs in PK-15 and 3D4/2 cells *in vitro*. The PK-15 cell line is usually used as the model cell for studying CSFV infection (Grummer et al., 2006; Sun et al., 2008), while 3D4/2 cell line is representative of the macrophage that is the target for CSFV infection (Knoetig et al., 1999). When the target cells were infected with CSFV, we found that CSFV infection promoted FAAs accumulation (**Figures 6A,E**). This observation was consistent with a previous report that CSFV infection promotes the substantial accumulation of long chain saturated and unsaturated fatty acids (Wenjie et al., 2017). In pathological cases, FFAs in some envelope virus-infeted cells are derived from fatty acid biosynthesis (Yang et al., 2008; Miguel et al., 2011; Gaunt et al., 2013; Tang et al., 2014; Ohol et al., 2015). From gene expression analysis, FASN and ACCα expression levels, as the key enzymes regulating fatty acid synthesis, were found markedly increased in CSFV-infected cells (**Figures 6B,C,F,G**), which was consistent with the reports of HCV, HCMV, and DENV (Kapadia and Chisari, 2005; Heaton and Randall, 2010; Spencer et al., 2011),

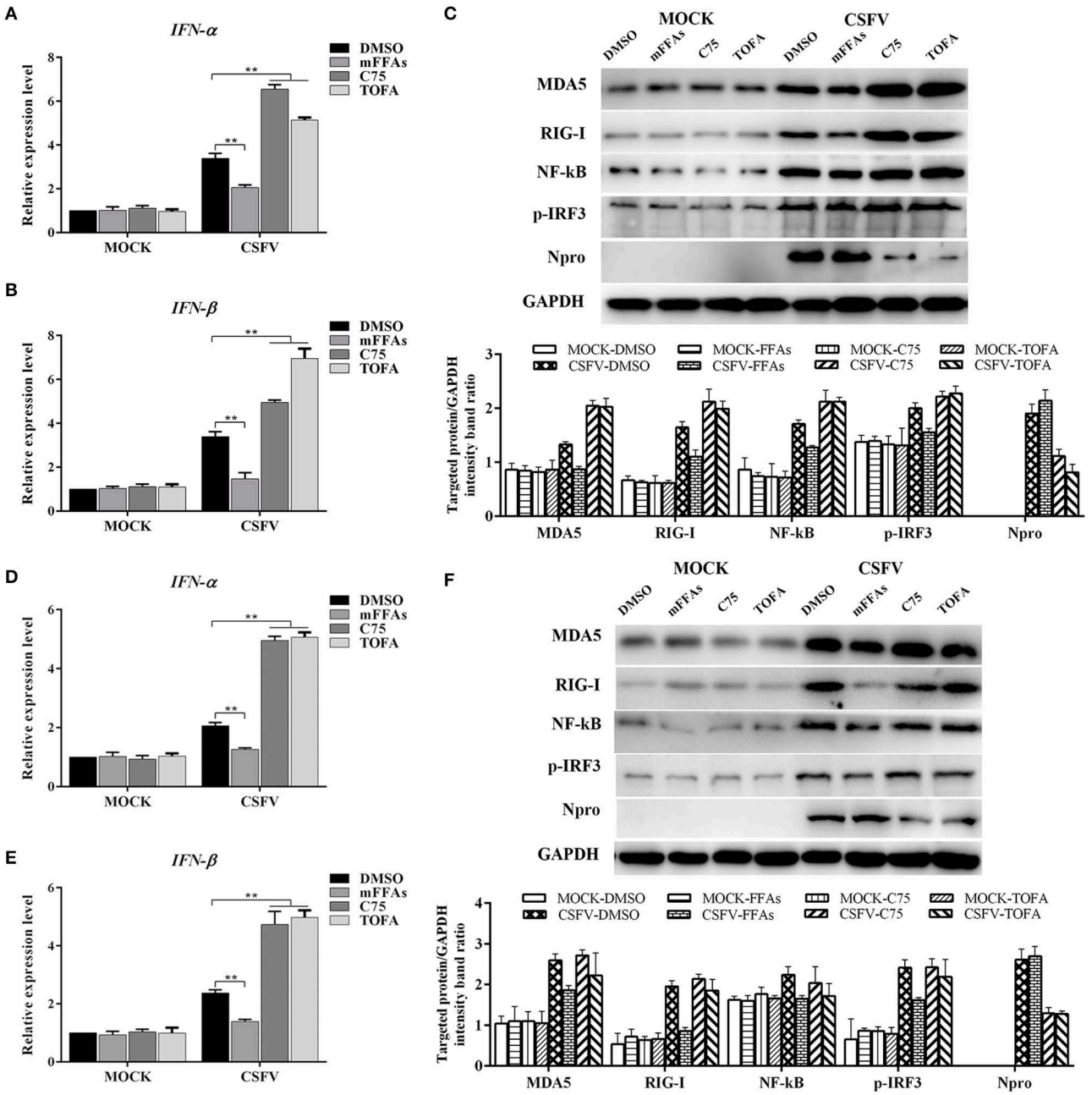

FIGURE 9 | CSFV induced FFAs accumulation suppressed type I IFN expression by down-regulating RLR signaling pathway. CSFV-infected or mock-infected PK-15 and 3D4/2 cells were treated with mFFAs (100 μM), C75 (20 μM), TOFA (30 μM) or DMSO for 48 h. **(A,B,D,E)** The transcription levels of IFNα and IFN-β in PK-15 and 3D4/2 cells were detected by qRT-PCR as described in Materials and Methods. **(C,F)** The protein expression levels of MDA5, RIG-I, NF-kB, p-IRF3, Npro and GAPDH (control) in PK-15 **(C)** and 3D4/2 **(F)** cells were examined by western blot. The relative levels of the targeted proteins were estimated by densitometric scanning, and the ratios were calculated relative to the GAPDH control. The data represent the mean ± SD of 3 independent experiments. $^{**}P < 0.01$. *P*-values were calculated using an One-way ANOVA test.

but contrary to WNV and KSHV (Delgado et al., 2012; Martin-Acebes et al., 2014).

Recent advances indicated that several members of the *Flaviviridae* family utilize host-cell machinery to create a specific optimal lipid microenvironment for assembly of their replication complex, where FFAs seems to play an essential role (Heaton and Randall, 2011). To further determine whether the accumulation of FFAs play a prominent role in the replication of CSFV, we explored the effect of the FFAs on CSFV replication by adding a mixture of FFAs (oleic:

palmitoleic=2:1) or disturbing the fatty acid biosynthase pathway with C75 and TOFA in CSFV-infected PK-15 and 3D4/2 cells. As showed in **Figure 7**, we revealed that the accumulation of FFAs and the activation of fatty acid biosynthesis are required for effective CSFV replication (**Figure 7**). It should be noted that fatty acid biosynthesis inhibitors of C75 and TOFA may provide novel drug targets for the treatment of CSFV as they inhabit CSFV replication. Available evidence suggests that FFAs can be transferred to mitochondria for beta-oxidation to produce acetyl CoA, which is a key component of the TCA cycle, thus driving oxidative phosphorylation and ATP production (Yoshida et al., 1986; Hayyan et al., 2012). In addition, glucose and glutamine, as the main carbon and nitrogen sources, can also provide the necessary energy for virus replication. Recent studies showed that glycolysis, glutaminolysis, and FAO are all required for maximal KSHV virus production (Sanchez et al., 2017). However, the presence of glucose is not important for vaccinia virus replication unless beta-oxidation of fatty acids is inhibited, whereas glutamine is essential (Greseth and Traktman, 2014). In our study, we showed that the process of FFAs enter the mitochondria for beta oxidation to produce ATP is necessary for CSFV replication (**Figure 8**). Meanwhile, We also found that glucose appears to be very important for CSFV replication, whereas glutamine is dispensable (**Figure 8**). These studies suggest that significant differences between the energy sources for viral replication exist between different viruses, which may be related to host specificity and different pathogenic mechanisms of infections.

It is worth mentioning that FFAs production is part of many signal transduction pathways in the cell, including regulating the IFN response (Schoggins and Randall, 2013). Previous studies have shown that CSFV infection can lead to impaired interferon response, which is beneficial to the sustained survival of the virus in host cells (Bensaude, 2004). To this end, we asked whether CSFV-induced FFAs accumulation modulates type I IFN production, this was important to reveal the molecular mechanism of FFAs affecting the replication of CSFV. As showed in **Figure 9**, we have documented an decrease in the mRNA level of IFN-α and IFN-β in mFFAs treated CSFV-infected PK-15 and 3D4/2 cells, but a significant increase in C75 or TOFA treated CSFV-infected cells, compared with DMSO treated CSFV-infected cells (**Figures 9A,B,D,E**). This result was consistent with a previous study, in which the accumulation of FFAs in HCV-infected cells inhibits the activation of type I IFN signaling pathway, resulting in impaired antiviral response (Gunduz et al., 2012). Importantly, CSFV can be recognized by the members of the RLRs in cells, such as RIG-I and MDA5, which mediate type I IFN production by phosphorylation of IRF3 or activation of NF-κB (Dong et al., 2013). Further, key markers of RLRs signaling pathway, including RIG-I, MDA, NF-κB and p-IRF3, were examined by western blot. We demonstrated that the expression of RIG-I and MDA5 proteins in CSFV-infected PK-15 and 3D4/2 cells were significantly decreased in C75 or TOFA treated cells, and NF-κB and p-IRF3 were activated, contrary to the results of mFFA treated CSFV-infected cells, compared with DMSO treated CSFV-infected cells (**Figures 9C,F**). Together, these findings suggest that CSFV-induced FFAs accumulation suppressed type I IFN production by inhibiting RLR signaling, thereby resulting in the persistent survival of CSFV in host cells.

In conclusion, our study demonstrated CSFV infection causes lipid metabolism disorders in host cells and provided the first data regarding the lipid metabolites during CSFV infection, which may provide a scientific basis for the study of potential antiviral drug targets. At the same time, we proved that CSFV-induced FFAs accumulation is beneficial to virus infection, which can provide the necessary ATP for virus replication and suppressed type I IFN production by inhibiting RLR signaling, thereby resulting in the persistent survival of CSFV in host cells. All these findings contribute to our understanding of the critical role of lipids in CSFV infection, but are still insufficient. It is still necessary to explore the molecular mechanisms of the interplay between CSFV and lipids, so as to understand the pathogenic mechanism of CSFV more comprehensively, and provide a solid scientific basis for the treatment and prevention of CSFV.

MATERIALS AND METHODS

Reagents and Antibodies

4-Methylene-2-octyl-5-oxotetrahydrofuran-3-carboxylic acid (C75) (sc-202511), 5-Tetradecyloxy-2-furonic acid (TOFA) (sc-200653), and etomoxir (sc-208284) were purchased from Santa Cruz Biotechnology. Trimetazidine (TMZ) (S61054) was purchased from Shyuanye Biotechnology. High glucose dulbecco's modified eagle medium (DMEM) (11995040), low glucose DMEM (11885084), no glucose DMEM (11885084), high glucose DMEM with no glutamine (11960069), RPMI 1640 medium (21875091), glucose free RPMI 1640 medium (11879020), and glutamine free RPMI 1640 medium (21870076) were obtained from Gibco. The following primary antibodies were used in the study: rabbit monoclonal anti-MDA5 (Sigma-Aldrich, SAB2101127), rabbit polyclonal anti-RIG-I (Cell Signaling Technology, 3743), rabbit polyclonal anti-NF-κB (Beyotime, AF0246), rabbit monoclonal anti-Phospho-IRF3 (Beyotime, AF1594), and mouse monoclonal anti-GAPDH (Beyotime, AG019) and mouse monoclonal anti-CSFV E2 (WH303) (JBT, 9011). Mouse polyclonal anti-CSFV Npro was kindly provided by Dr. Xinglong Yu (Veterinary Department, Hunan Agricultural University, China). Te secondary antibodies were used in the study: HRP-conjugated goat anti-mouse IgG (Beyotime, A0192), HRP-conjugated goat anti-rabbit IgG (Beyotime, A0208) and Alexa Fluor 488-labeled Goat Anti-Mouse IgG (Beyotime, A0428).

Cell Culture and Virus Infection

The swine kidney cell line PK-15 (ATCC, CCL-33) and porcine macrophage cell line 3D4/2 (ATCC, CRL-2845) were cultured in this study. PK-15 cells were maintained in DMEM containing with 10% fetal bovine serum (FBS, Gibco) 1% penicillin-streptomycin solution. 3D4/2 cells were grown in RPMI 1640 media supplemented with 10% FBS and 1% penicillin-streptomycin solution. The cells were cultured at 37°C with

5% CO_2. The virulent CSFV strain Shimen was used in the present study and tittered as described previously (Hongchao et al., 2017). All cells with 80% confluences in cell culture plates were infected in serum-free DMEM medium with CSFV at a multiplicity of infection (MOI) of 1 for 2 h, after which the medium was replaced with complete DMEM or RPMI 1640 containing 2% FBS. The cells were then cultured at 37°C with 5% CO_2 for a different hour post infection (hpi).

Animal Experiments

All procedures were conducted following regulations of the Laboratory Animal Ethics Committee of South China Agricultural University. Briefly, a total of ten 2-month-old piglets, without PRRSV, PRV, PPV infection, were randomly divided into two groups, one challenged with 10^5 $TCID_{50}$ of CSFV (Group S) and one inoculated with an equal volume of normal PK-15 cell-culture supernatant served as negative controls (Group C) ($n = 5$ each). Two groups were separately maintained in isolators with filtered air of positive pressure in a SPF animal facility. Rectal temperatures were recorded each morning and animals were observed daily for clinical signs. After CSFV infection, the anterior vena cava blood of piglets was sterilely collected into heparin sodium anticoagulant tubes every other day. Then, the blood samples were centrifuged immediately and serum was harvested and stored at −80°C for further study.

Serum Lipidomics Analysis With UHPLC-QTOF-MS

All samples were analyzed based on UHPLC-QTOF-MS non-targeted lipidomics platform. The project includes sample preparation, UHPLC-QTOF-MS analysis, raw data preprocessing, univariate and multivariate statistical analysis, and identification of differential lipids. UHPLC-QTOF-MS analysis was carried out in positive and negative ion mode, i.e., positive and negative electrospray ionization (ESI) mode. ESI is a fixed ionization mode. Positive (ESI+) and negative ions (ESI-) are our scanning mode for ions. In the process of ionization, both positive and negative ions are produced simultaneously. The selection of scanning mode (as in the range of m/z, can play a screening role). If ESI+ mode is selected, negative ions will be filtered out and can not be collected by the monitor. On the contrary, ESI- mode is adopted. Positive ions are filtered out, and the combination of the two modes will widen the range of metabolites detected and screened.

A total of 50 μL serum sample was mixed with 230 μL of ice-cold methanol/water (8:15, v/v) and 400 μL MTBE (methyl tert-butyl ether). The mixtures were vortexed for 1 min and standing for 2 h at 4°C. Then it was centrifugated at 3,000 rpm for 15 min. A 260 μL of supernatant was dried under gentle nitrogen stream, and re-dissolved in 100 μL of dichloromethane/methanol (1:1, v/v) before UHPLC-QTOF-MS analysis. The injection volume is 2 μL(ESI+)/6 μL(ESI-). Quality control (QC) sample pooled from the extractions of all samples were prepared and analyzed with the same procedure as that for the experiment samples.

Chromatographic separation was performed on an Agilent UHPLC system (1290) with a Phenomenex Kinetex C18 column (2.1 × 100 mm, 1.7 μm) at a flow rate of 0.3 mL/min and 40°C column temperature. The mobile phases consisted of water (phase A) and acetonitrile (phase B), both with 0.1% formic acid (v/v). A linear gradient elution was performed with the following program: 0 min, 40% B; 12 min, 100% B; 13.5 min, 100% B; 13.7 min, 40% B and held to 18 min.

The eluents were analyzed in positive ion mode on a hybrid quadrupole time-of-light mass spectrometer (Triple TOF 5600 system, AB Sciex, Comcord, ON, Canada) equipped with a DuoSpray ion source. A typical information dependent acquisition comprising the acquisition of a survey TOF MS spectrum and then a MS/MS experiment was applied in the analysis. The TOF MS scan was operated under the high-resolution settings with a range of 60–1,000 m/z and an accumulation time of 200 ms. The software for controlling instrument and collecting data was Analyst TF 1.7 (AB Sciex, Comcord, ON, Canada).

The raw data of UPLC-QTOF-MS were firstly transformed to mzXML format by ProteoWizard and then processed by XCMS and CAMERA packages in R software platform. The final data was exported as a peak table file, including observations (sample name), variables (rt_mz), and peak areas. The data was normalized against total peak areas before performing univariate and multivariate statistics.

For multivariate statistical analysis, the normalized data were imported to SIMCA software (version 13.0, Umetrics, Umeå, Sweden), where the data were preprocessed by Pareto scaling and mean centering before performing PCA, PLS-DA, and OPLS-DA. For univariate statistical analysis, the normalized data were analyzed by Welch's t test on the variables of normal distribution, or by Wilcoxon Mann-Whitney test on the variables of abnormal distribution. The variables with VIP values of PLS-DA or OPLS-DA model larger than 1 and p values of univariate statistical analysis lower than 0.05 were identified as potential differential metabolites.

Quantitative Real-Time PCR

The expression levels of FASN, ACCα, and NS5B were determined by qRT-PCR. According to the manufacturer's protocol of TRIzol RNA extraction kit (Life Technologies, USA), total RNA from serum samples of group S and group C piglets and CSFV-infected PK-15 and 3D4/2 cells cultured in different environments were extracted. And synthesis of cDNA was performed using the PrimeScriptTM RT reagent Kit with gDNA Eraser (TAKARA, DRR036). The primer pairs specific for pigs FASN, ACCα, IFNα, IFN-β, β-actin, and CSFV NS5B genes (**Table 1**) were used for the qPCR amplifications utilizing iQ5 iCycler detection system (Bio-Rad) following the instructions of SYBR® Premix Ex TaqTM II (Tli RNaseH Plus) (TAKARA, DRR082). Relative quantification of the FASN, ACCα, IFNα and IFN-β expression were calculated using $2^{-\Delta\Delta ct}$ method. The viral copy number was calculated using absolute quantification method by constructing a standard curve of recombinant plasmid containing CSFV NS5B Gene. Three biological replicates were used for each cell sample, and three qPCR reactions were performed for each replicate sample and the average value was obtained.

TABLE 1 | Oligonucleotide primer sequences for real-time qRT-PCR.

No.	Target gene	Genbank Acc. No.	Primer name	Type	Sequence(5′-3′)	Amplicon (bp)
1	FASN	NM_001099930.1	qRT-PCR-FASN-F	5′	CCAGCATCACCATAGACACGG	146
			qRT-PCR-FASN-R	3′	CATGAATTGCAGCGAGGAGTTAG	
2	ACCα	NM_001114269.1	qRT-PCR-ACCα-F	5′	GAATACCCGTGGGAGTAGTTGC	266
			qRT-PCR-ACCα-R	3′	CACGATGTAAGCGCCGAAC	
3	NS5B	EF026757.1	qRT-PCR-NS5B-F	5′	ACTCATCAGGATCCCCCTCAC	254
			qRT-PCR-NS5B-R	3′	CTTACTTGTATTGGTGTATGGGAGC	
4	IFN-α	NM_214393.1	qRT-PCR-IFN-α-F	5′	CTCAGCCAGGACAGAAGCA	108
			qRT-PCR-IFN-α-R	3′	TCACAGCCCAGAGAGCAGA	
5	IFN-β	NM_001003923.1	qRT-PCR-IFN-β-F	5′	TCGCTCTCCTGATGTGTTTCTC	82
			qRT-PCR-IFN-β-R	3′	AAATTGCTGCTCCTTTGTTGGT	
6	GAPDH	NM_001206359.1	qRT-PCR-GAPDH-F	5′	TGGAGTCCACTGGTGTCTTCAC	121
			qRT-PCR-GAPDH-R	3′	TTCACGCCCATCACAAACA	

Free Fatty Acids Assay

According to the manufacturer's protocol of free fatty acids assay kit (Nanjing Jiancheng Bioengineering Institute, A042-2-1), centrifuge cell culture supernates samples for 20 min at 1,000 g and remove particulates. And then, add 50 μl of Standard or Sample to the appropriate wells. Blank well doesn't add anything. Next, add 100 μl of Enzymeconjugate to standard wells and sample wells except the blank well, cover with an adhesive strip and incubate for 60 min at 37°C. Wash the Microtiter Plate 4 times. Then, add Substrate A 50 μl and Substrate B 50 μl to each well. Gently mix and incubate for 15 min at 37°C. Protect from light. Add 50 μl Stop Solution to each well. Read the Optical Density (OD) at 450 nm using a microtiter plate reader within 15 min. Finally, the measured OD value is substituted into the curve drawn by the standard to represent the FFAs concentration of each hole. Statistical analysis and comparison were made between the two groups, $P < 0.05$ was the statistical difference.

ATP Assays

PK-15 or 3D4/2 cells were infected with CSFV or mock infected and treated with etomoxir, TMZ, or DMSO control. According to the manufacturer's protocol of enhanced ATP assay kit (Beyotim, S0027), cells were washed twice in PBS and then incubated in ATP lysis buffer for 20 min. After pyrolysis, the supernatant was centrifuged at 12,000 rpm for 20 min at 4°C for subsequent determination. Next, ATP standard solution with appropriate concentration gradient and ATP detection solution was prepared. Then, the RLU value was determined by chemiluminometer after mixing 20 μL of test sample or ATP standard in the test tube containing 100 μL of ATP detection working fluid with a gun (micro-pipette) at least 2 s apart. Finally, the measured RLU value was substituted into the curve drawn by the standard solution to represent the ATP concentration of each hole. Statistical analysis and comparison were made between the two groups, with $P < 0.05$ as the statistical difference.

Western Blot Analysis

Different cell samples were washed twice in cold phosphate-buffered saline (PBS) and then incubated in RIPA lysis buffer (Beyotim, P0013B) containing 1 mM PMSF (Beyotim, ST506) for 20 min. The extracted proteins were quantified by the BCA protein assay kit (Beyotim, P0012) and boiled for 10 min in 5 × SDS-PAGE sample loading buffer (Beyotim, P0015L). Equal amounts of protein samples were separated on 10% SDS-PAGE and transferred onto a polyvinylidene difluoride (PVDF) membrane. The PVDF membranes were first blocked in PBS containing 2% non-fat milk powder and 0.05% Tween 20 at 37°C for 1 h, which were then incubated with primary antibodies at 4°C overnight and then with the corresponding secondary antibodies conjugated to HRP at 37°C for 2 h. The immunolabeled protein complexes were visualized using ECL Plus kit (Beyotim, P0018), using the CanoScan LiDE 100 scanner system (Canon).

Statistical Analysis

The data are expressed as the mean ± standard deviation (SD) and were analyzed by two-way ANOVA using the GraphPad Prism 6 software. Value of P lesser than 0.05 was considered statistically significant.

DATA AVAILABILITY STATEMENT

All datasets generated for this study are included in the article/**Supplementary Material**.

ETHICS STATEMENT

The authors declare that the animal breeding, care and all experiments were conducted following regulations of the Laboratory Animal Center of South China Agricultural University and approved by the Laboratory Animal Ethics Committee of South China Agricultural University. The waste generated during the whole experimental period, including CSFV-infected cells and piglets, biochemical reagent waste liquid and other toxic substances, is uniformly recycled and harmlessly processed by South China Agricultural University.

AUTHOR CONTRIBUTIONS

SM designed the experiment and drafted the manuscript. QM and WC performed experiments and analyzed lipidomics data. MeZ, KW, DS, and XL carried out animal experiments. EZ, SF, LY, and HD analyzed experimental results and data. MiZ and JC guided the design of the study and revised the manuscript. All authors read and approved the final manuscript.

FUNDING

This work was financially supported by grants from the National Key Research & Development Program of China (No. 2017YFD0500600), the National Natural Science Foundation of China (No. 31672590), and the Science and Technology Program of Guangzhou, China (No. 201803020005).

ACKNOWLEDGMENTS

The authors thank Shanghai Prof. Leader Biotech Co., Ltd. for assistance with the UHPLC-QTOF-MS metabolomics experiments.

SUPPLEMENTARY MATERIAL

The Supplementary Material for this article can be found online at: https://www.frontiersin.org/articles/10.3389/fcimb.2019.00410/full#supplementary-material

REFERENCES

Becher, P., Ramirez, R. A., Orlich, M., Rosales, S. C., König, M., and Schweizer, M., et al. (2003). Genetic and antigenic characterization of novel pestivirus genotypes: implications for classification. *Virology* 311, 96–104. doi: 10.1016/S0042-6822(03)00192-2

Bensaude, E. (2004). Classical swine fever virus induces proinflammatory cytokines and tissue factor expression and inhibits apoptosis and interferon synthesis during the establishment of long-term infection of porcine vascular endothelial cells. *J. General Virol.* 85, 1029–1037. doi: 10.1099/vir.0.19637-0

Bramhall, J., and Wisnieski, B. (1981). The role of lipids in virus—cell interactions. *Virus Receptors.* Dordrecht: Springer Netherlands. doi: 10.1007/978-94-011-8022-1_7

Christie, W. W. (1978). The composition, structure and function of lipids in the tissues of ruminant animals. *Progr. Lipid Res.* 17, 111–205. doi: 10.1016/0079-6832(78)90007-1

Delgado, T., Sanchez, E. L., Camarda, R., Lagunoff, M., and Feng, P. (2012). Global metabolic profiling of infection by an oncogenic virus: kshv induces and requires lipogenesis for survival of latent infection. *PLoS Pathog.* 8:e1002866. doi: 10.1371/journal.ppat.1002866

Dong, X. Y., Liu, W. J., Zhao, M. Q., Wang, J. Y., Pei, J. J., and Luo, Y. W., et al. (2013). Classical swine fever virus triggers rig-i and mda5-dependent signaling pathway to irf-3 and nf-κb activation to promote secretion of interferon and inflammatory cytokines in porcine alveolar macrophages. *Virol. J.* 10, 286–286. doi: 10.1186/1743-422X-10-286

Edwards, S., Fukusho, A., Lefèvre, P. C., Lipowski, A., Pejsak, Z., and Roehe, P., et al. (2000). Classical swine fever: the global situation. *Vet. Microbiol.* 73, 103–119. doi: 10.1016/S0378-1135(00)00138-3

Findlay, J. S., and Ulaeto, D. (2015). Semliki forest virus and sindbis virus, but not vaccinia virus, require glycolysis for optimal replication. *J. General Virol.* 96, 2693–2696. doi: 10.1099/jgv.0.000226

Fontaine, K. A., Sanchez, E. L., Camarda, R., and Lagunoff, M. (2014). Dengue virus induces and requires glycolysis for optimal replication. *J. Virol.* 89, 2358–2366. doi: 10.1128/JVI.02309-14

Gaunt, E. R., Cheung, W., Richards, J. E., Lever, A., and Desselberger, U. (2013). Inhibition of rotavirus replication by downregulation of fatty acid synthesis. *J. General Virol.* 94(Pt_9), 2140–2140. doi: 10.1099/vir.0.057331-0

Greseth, M. D., and Traktman, P. (2014). *De novo* fatty acid biosynthesis contributes significantly to establishment of a bioenergetically favorable environment for vaccinia virus infection. *PLOS Pathog.* 10:e1004021. doi: 10.1371/journal.ppat.1004021

Grummer, B., Fischer, S., Depner, K., Riebe, R., Blome, S., and Greiserwilke, I. (2006). Replication of classical swine fever virus strains and isolates in different porcine cell lines. *Dtw Deutsche Tierarztliche Wochenschrift*, 113, 138–142.

Gunduz, F., Aboulnasr, F. M., Chandra, P. K., Hazari, S., Poat, B., and Baker, D. P., et al. (2012). Free fatty acids induce er stress and block antiviral activity of interferon alpha against hepatitis c virus in cell culture. *Virol. J.* 9:143. doi: 10.1186/1743-422X-9-143

Hadley, N. F. (1991). Integumental lipids of plants and animals: comparative function and biochemistry. *Adv. Lipid Res.* 24, 303–320. doi: 10.1016/B978-0-12-024924-4.50014-6

Hayyan, A., Mjalli, F. S., Hayyan, M., Alnashef, I. M., and Mirghani, M. E. S. (2012). Utilizing ultrasonic energy for reduction of free fatty acids in crude palm oil. *Afr. J. Biotechnol.* 11, 12510–12517. doi: 10.5897/AJB12.1709

Heaton, N. S., and Randall, G. (2010). Dengue virus-induced autophagy regulates lipid metabolism. *Cell Host Microbe* 18, 422–432. doi: 10.1016/j.chom.2010.10.006

Heaton, N. S., and Randall, G. (2011). Multifaceted roles for lipids in viral infection. *Trends Microbiol.* 19, 368–375. doi: 10.1016/j.tim.2011.03.007

Hilmarsson, H., Traustason, B. S., Kristmundsdóttir, T., and Thormar, H. (2007). Virucidal activities of medium- and long-chain fatty alcohols and lipids against respiratory syncytial virus and parainfluenza virus type 2: comparison at different ph levels. *Arch. Virol.* 152, 2225–2236. doi: 10.1007/s00705-007-1063-5

Hongchao, G., Mingqiu, Z., Jin, Y., Hailuan, X., Hongxing, D., and Jinding, C. (2017). Metabolic profiles in cell lines infected with classical swine fever virus. *Front. Microbiol.* 8:691. doi: 10.3389/fmicb.2017.00691

Kapadia, S. B., and Chisari, F. V. (2005). Hepatitis c virus rna replication is regulated by host geranylgeranylation and fatty acids. *Proc. Natl. Acad. Sci. U.S.A.* 102, 2561–2566. doi: 10.1073/pnas.0409834102

Kleiboeker, S. B. (2002). Swine fever: classical swine fever and african swine fever. *Vet. Clin. North Am. Food Anim. Pract.* 18, 431–451. doi: 10.1016/S0749-0720(02)00028-2

Knoetig, S. M., Summerfield, A., Spagnuolo-Weaver, M., and Mccullough, K. C. (1999). Immunopathogenesis of classical swine fever role of monocytic cells. *Immunology* 97, 359–366. doi: 10.1046/j.1365-2567.1999.00775.x

König, M., Lengsfeld, T., Pauly, T., Stark, R., Thiel, H. J., and Virol, J., et al. (1995). Classical swine fever virus: independent induction of protective immunity by two structural glycoproteins. *J. Virol.* 69, 6479–6486.

Kulkarni, M. M., Ratcliff, A. N., Bhat, M., Alwarawrah, Y., Hughes, P., and Arcos, J., et al. (2017). Cellular fatty acid synthase is required for late stages of hiv-1 replication. *Retrovirology* 14:45. doi: 10.1186/s12977-017-0368-z

Lohse, L., Nielsen, J., and Uttenthal, A. (2012). Early pathogenesis of classical swine fever virus (csfv) strains in danish pigs. *Vet. Microbiol.* 159, 327–336. doi: 10.1016/j.vetmic.2012.04.026

Lorizate, M., and Krausslich, H. G. (2011). Role of lipids in virus replication. *Cold Spring Harbor Perspect. Biol.* 3, a004820–a004820. doi: 10.1101/cshperspect.a004820

Luchessi, A. D. (2010). Effect of fatty acids on translational control of leukocytes infected with HIV-1. *FASEB J.* 24(Suppl. 1):656.2. doi: 10.1096/fasebj.24.1_supplement.656.2

Martin-Acebes, M. A., Merino-Ramos, T., Blazquez, A. B., Casas, J., Escribano-Romero, E., and Sobrino, F., et al. (2014). The composition of west nile virus lipid envelope unveils a role of sphingolipid metabolism in flavivirus biogenesis. *J. Virol.* 88, 12041–12054. doi: 10.1128/JVI.02061-14

Melanie (2014). *Hepatocellular Lipid Metabolism in Hepatitis c Virus Infection*. University of Oxford.

Menendez, J. A., and Lupu, R. (2007). Fatty acid synthase and the lipogenic phenotype in cancer pathogenesis. *Nat. Rev. Cancer* 7, 763–777. doi: 10.1038/nrc2222

Mercer, J., and Helenius, A. (2008). Vaccinia virus uses macropinocytosis and apoptotic mimicry to enter host cells. *Science* 320, 531–535. doi: 10.1126/science.1155164

Merrill, A. H., Sullards, M. C., Wang, E., Voss, K. A., and Riley, R. T. (2001). Sphingolipid metabolism: roles in signal transduction and disruption by fumonisins. *Environ. Health Perspect.* 109(Suppl 2), 283–289. doi: 10.1289/ehp.01109s2283

Miguel, A., Martín-Acebes, A. B., Jiménez de Oya, N., Escribano-Romero, E., and Saiz, J. C. (2011). West nile virus replication requires fatty acid synthesis but is independent on phosphatidylinositol-4-phosphate lipids. *PLoS ONE* 6:e24970. doi: 10.1371/journal.pone.0024970

Moennig, V. (2000). Introduction to classical swine fever: virus, disease and control policy. *Vet. Microbiol.* 73, 93–102. doi: 10.1016/S0378-1135(00)00137-1

Moormann, R. J., Bouma, A., Kramps, J. A., et al. (2000). Development of a classical swine fever subunit marker vaccine and companion diagnostic test.[J]. *Vet. Microbiol.* 73, 209–219. doi: 10.1016/S0378-1135(00)00146-2

Nagy, P., Pogany, J., and Xu, K. (2016). Cell-free and cell-based approaches to explore the roles of host membranes and lipids in the formation of viral replication compartment induced by tombusviruses. *Viruses* 8:68. doi: 10.3390/v8030068

Ohol, Y. M., Zhaoti, W., George, K., Gregory, D., and Santanu, B. (2015). Direct inhibition of cellular fatty acid synthase impairs replication of respiratory syncytial virus and other respiratory viruses. *PLoS ONE* 10:e0144648. doi: 10.1371/journal.pone.0144648

Popescu, C. I., and Dubuisson, J. (2010). Role of lipid metabolism in hepatitis c virus assembly and entry. *Biol. Cell* 102, 63–74. doi: 10.1042/BC20090125

Sanchez, E. L., Pulliam, T. H., Dimaio, T. A., Thalhofer, A. B., Delgado, T., and Lagunoff, M. (2017). Glycolysis, glutaminolysis, and fatty acid synthesis are required for distinct stages of kaposi's sarcoma-associated herpesvirus lytic replication. *J. Virol.* 91:e02237–16. doi: 10.1128/JVI.02237-16

Schoggins, J., and Randall, G. (2013). Lipids in innate antiviral defense. *Cell Host Microbe* 14, 379–385. doi: 10.1016/j.chom.2013.09.010

Scott, K. W., Eve, J., Russell, P., Ying, H., Ahmed, R. M., and Olivier, P., et al. (2018). Lipidomics analysis of behavioral variant frontotemporal dementia: a scope for biomarker development. *Front. Neurol.* 9:104. doi: 10.3389/fneur.2018.00104

Seo, J. Y., and Cresswell, P. (2013). Viperin regulates cellular lipid metabolism during human cytomegalovirus infection. *PLOS Pathog.* 9:e1003497. doi: 10.1371/journal.ppat.1003497

Sethi, S., and Brietzke, E. (2017). Recent advances in lipidomics: analytical and clinical perspectives. *Prostagl. Other Lipid Mediat.* 128–129, 8–16. doi: 10.1016/j.prostaglandins.2016.12.002

Spencer, C. M., Schafer, X. L., Moorman, N. J., and Munger, J. (2011). Human cytomegalovirus induces the activity and expression of acetyl-coenzyme a carboxylase, a fatty acid biosynthetic enzyme whose inhibition attenuates viral replication. *J. Virol.* 85, 5814–5824. doi: 10.1128/JVI.02630-10

Stegeman, A., Elbers, A., Smit, M. H., and Pluimers, F. (2000). The 1997-1998 epidemic of classical swine fever in the netherlands. *Vet. Microbiol.* 73, 183–196. doi: 10.1016/S0378-1135(00)00144-9

Strating, J. R., and Van Kuppeveld, F. J. (2017). Viral rewiring of cellular lipid metabolism to create membranous replication compartments. *Curr. Opin. Cell Biol.* 47, 24–33. doi: 10.1016/j.ceb.2017.02.005

Strating, J. R. P. M. (2012). *Greasing the Viral Life-Cycle: the Role of Lipids in Picornavirus Replication*.

Sun, J., Jiang, Y., Shi, Z., Yan, Y., Guo, H., and He, F. et al. (2008). Proteomic alteration of pk-15 cells after infection by classical swine fever virus. *J. Proteome Res.* 7, 5263–5269. doi: 10.1021/pr800546m

Superti, F., Marziano, M. L., Donelli, G., Marchetti, M., and Seganti, L. (1995). Enhancement of rotavirus infectivity by saturated fatty acids. *Comparat. Immunol. Microbiol. Infect. Dis.* 18, 129–135. doi: 10.1016/0147-9571(95)98854-B

Tang, W. C., Lin, R. J., Liao, C. L., and Lin, Y. L. (2014). Rab18 facilitates dengue virus infection by targeting fatty acid synthase to sites of viral replication. *J. Virol.* 88, 6793–6804. doi: 10.1128/JVI.00045-14

Watkins, P. A. (2013). Fatty acids: metabolism. *Encycloped. Hum. Nutri.* 10, 220–230. doi: 10.1016/B978-0-12-375083-9.00103-3

Wenjie, G., Junjie, J., Bikai, Z., Shijiang, M., Li, Z., and Xiaoming, X., et al. (2017). Serum metabolomic profiling of piglets infected with virulent classical swine fever virus. *Front. Microbiol.* 8:731. doi: 10.3389/fmicb.2017.00731

Wenk and Markus, R. (2005). The emerging field of lipidomics. *Nat. Rev. Drug Discov.* 4, 594–610. doi: 10.1038/nrd1776

Yang, W., Hood, B. L., Chadwick, S. L., Liu, S., and Wang, T. (2008). Fatty acid synthase is up-regulated during hepatitis c virus infection and regulates hepatitis c virus entry and production. *Hepatology* 48, 1396–1403. doi: 10.1002/hep.22508

Yoshida, S., Ikeda, M., Busto, R., Santiso, M., Martinez, E., and Ginsberg, M. D. (1986). Cerebral phosphoinositide, triacylglycerol, and energy metabolism in reversible ischemia: origin and fate of free fatty acids. *J. Neurochem.* 47, 744–757. doi: 10.1111/j.1471-4159.1986.tb00675.x

Conflict of Interest: The authors declare that the research was conducted in the absence of any commercial or financial relationships that could be construed as a potential conflict of interest.

Copyright © 2019 Ma, Mao, Chen, Zhao, Wu, Song, Li, Zhu, Fan, Yi, Ding, Zhao and Chen. This is an open-access article distributed under the terms of the Creative Commons Attribution License (CC BY). The use, distribution or reproduction in other forums is permitted, provided the original author(s) and the copyright owner(s) are credited and that the original publication in this journal is cited, in accordance with accepted academic practice. No use, distribution or reproduction is permitted which does not comply with these terms.

frontiers in Cellular and Infection Microbiology

MINI REVIEW
published: 04 December 2019
doi: 10.3389/fcimb.2019.00412

Mechanisms of Oral Bacterial Virulence Factors in Pancreatic Cancer

*Zhong Sun[1], ChengLong Xiong[2], Seoh Wei Teh[3], Jonathan Chee Woei Lim[4], Suresh Kumar[3,5,6] and Karuppiah Thilakavathy[1,5]**

[1] Department of Biomedical Science, Universiti Putra Malaysia, Serdang, Malaysia, [2] Department of Public Health Microbiology, School of Public Health, Fudan University, Shanghai, China, [3] Department of Medical Microbiology and Parasitology, Universiti Putra Malaysia, Serdang, Malaysia, [4] Pharmacotherapeutics Unit, Department of Medicine, Faculty of Medicine and Health Sciences, Universiti Putra Malaysia, Serdang, Malaysia, [5] Genetics and Regenerative Medicine Research Centre, Universiti Putra Malaysia, Serdang, Malaysia, [6] UPM-MAKNA Cancer Research Laboratory, Institute of Bioscience, Universiti Putra Malaysia, Serdang, Malaysia

Pancreatic cancer is a highly lethal disease, and most patients remain asymptomatic until the disease enters advanced stages. There is lack of knowledge in the pathogenesis, effective prevention and early diagnosis of pancreatic cancer. Recently, bacteria were found in pancreatic tissue that has been considered sterile before. The distribution of flora in pancreatic cancer tissue was reported to be different from normal pancreatic tissue. These abnormally distributed bacteria may be the risk factors for inducing pancreatic cancer. Therefore, studies on combined effect of multi-bacterial and multi-virulence factors may add to the knowledge of pancreatic cancer pathogenesis and aid in designing new preventive and therapeutic strategies. In this review, we outlined three oral bacteria associated with pancreatic cancer and their virulence factors linked with cancer.

Keywords: oral bacteria, pancreatic cancer, virulence factors, CDT, FadA, NDK, Gingipains

OPEN ACCESS

Edited by:
Sigrun Lange, University of Westminster, United Kingdom

Reviewed by:
Jorg Kleeff, Martin Luther University of Halle-Wittenberg, Germany
Xingmin Sun, University of South Florida, United States

***Correspondence:**
Karuppiah Thilakavathy
thilathy@upm.edu.my

Specialty section:
This article was submitted to Bacteria and Host, a section of the journal Frontiers in Cellular and Infection Microbiology

Received: *27 September 2019*
Accepted: *19 November 2019*
Published: *04 December 2019*

Citation:
Sun Z, Xiong C, Teh SW, Lim JCW, Kumar S and Thilakavathy K (2019) Mechanisms of Oral Bacterial Virulence Factors in Pancreatic Cancer. Front. Cell. Infect. Microbiol. 9:412. doi: 10.3389/fcimb.2019.00412

INTRODUCTION

Pancreatic cancer is considered as one of the deadliest cancers, since its onset is occult and the early symptoms are not typical (Kamisawa et al., 2016). Although the detection and treatment of pancreatic cancer has progressed, the 5-year survival rate of pancreatic cancer is only 9%, which is the lowest among all cancers (Siegel et al., 2019). Worldwide, the incidence of pancreatic cancer is increasing year by year. There are 458,918 new cases in 2018, which means more than 1,250 people are told to have pancreatic cancer every day. In the same year, 432,242 patients died of pancreatic cancer, therefore, it has become the seventh leading cause of cancer-related deaths (Rawla et al., 2019). The reason for this situation is that researchers do not know enough about the pathogenesis of pancreatic cancer.

According to the 2018 International Agency for Research on Cancer (IARC) ∼18% of cancers are associated with infectious diseases caused by bacteria, viruses and parasites (Rawla et al., 2019). Bacterial infections promote the formation of inflammatory microenvironment, which is a critical regulator of carcinogenesis (Coussens and Werb, 2002). Persistent infections will induce epigenetic modification of the somatic cells and lead to the production of a large amount of reactive oxygen species (ROS) and reactive nitrogen (RNS), that eventually cause DNA damage, oncogene activation or tumor suppressor genes inactivation (Cuevas-Ramos et al., 2010; Sahan et al., 2018).

BACTERIA AND PANCREATIC CANCER

The pancreas has been considered as sterile for a long time due to presence of highly alkaline pancreatic enzymes. However, it was found that microorganisms can reach pancreas through blood and digestive systems (Michaud, 2013). Recent studies have reported that the content and composition of bacteria and fungi in pancreatic cancer tissues are different from normal pancreatic tissues. Their presence not only promote the occurrence of pancreatic cancer, but also affects its prognosis (Pushalkar et al., 2018; Aykut et al., 2019; Riquelme et al., 2019). Pushalkar et al. reported that *Bacteroidetes* (31%) and *Firmicutes* (22%) dominated the healthy pancreas, whereas *Proteobacteria* found to be abundant in pancreatic cancer tissues and was associated with advanced disease. *Actinobacteria* (1%) was also reported present in pancreatic cancer tissue although the abundance was low (Pushalkar et al., 2018). On the same year, Fan et al. conducted prospective study on the relationship between oral microbes and pancreatic cancer, and found that *Aggregatibacter actinomycetemcomitans* (*A. actinomycetemcomitans*) and *Porphyromonas gingivalis* (*P. gingivalis*), and decreased relative abundance of *Fusobacterium nucleatum* (*F. nucleatum*) are associated with onset risk of pancreatic cancer (Fan et al., 2018). However, in another study, *F. nucleatum* was independently associated with a poor prognosis for pancreatic cancer (Mitsuhashi et al., 2015). The results of these experiments showed that the abundance variation of these three bacteria were associated with increased risk of pancreatic cancer. In recent years, prospective cohort studies and case-control studies could not conclude that *Helicobacter pylori* (*H. pylori*) is associated with increased risk of pancreatic cancer (Wei et al., 2019). Moreover, *H. pylori* cannot be detected in chronic pancreatitis and pancreatic cancer tissues, which proved that it could not directly participate in the development of cancer (Jesnowski et al., 2010). However, the effect of *H. pylori* on gastric mucosa and suppression of gastric acid secretion, which resulting low acidity in the stomach may provide other oral bacteria an opportunity to enter the pancreas (Michaud, 2013). Since there is association among bacteria in cancer development, Tjaslsma et al. proposed a "driver-passenger" model according to characteristics of the participating microbes (Tjalsma et al., 2012). Based on these studies, we have selected several digestive tract bacteria that may be involved in the pathogenesis of pancreatic cancer (**Table 1**).

ORAL BACTERIAL VIRULENCE FACTORS AND CANCER

Virulence factors produced by oral bacteria assist them to invade the host and cause diseases. Primarily, they are causal agents of periodontitis (Shang et al., 2019). However, studies have also identified pathogenic components of oral bacteria as significant risk factors for developing other diseases. For example, *A. actinomycetemcomitans* is associated with endocarditis, rheumatoid arthritis (Paturel et al., 2004; Mukherjee et al., 2018), *F. nucleatum* is associated with colorectal carcinoma (Repass et al., 2018), and *P. gingivalis* is associated with the onset of Alzheimer disease, atherosclerosis and diabetes (Sugiyama et al., 2012; Velsko et al., 2014; Laugisch et al., 2018). This paper reviews the virulence factors of the three oral bacteria and their mechanisms of action associated with cancer, particularly pancreatic cancer.

Aggregatibacter actinomycetemcomitans

Aggregatibacter actinomycetemcomitans is a Gram-negative, facultative anaerobe, non-motile bacterium which can enter the host cells by endocytosis, and then secrete phospholipase C to destroy membrane vesicles and release themselves into the cytoplasm. However, the invasion is a dynamic process, after growth and division, which anchors to the host cell membrane and enters adjacent epithelial cells or deep cells through microtubules. This process benefits *A. actinomycetemcomitans* to infect deep cells and escape from immune system (Henderson et al., 2010).

Aggregatibacter actinomycetemcomitans can secrete a variety of toxins, of which the following three are most studied. The first variety is Leukotoxin (LtxA), a lipoprotein belonging to the RTX family of toxins, attached to neutroplils, monocytes and lymphocytes. It will form pores on their cell membrane, thereby altering its function of osmotic homeostasis, leading to cell death (Johansson, 2011).

The second type is cell cytolethal distending toxins (CDT), a bacterial toxin of AB2 trimer, which is made of the active subunit (CdtB) and two binding subunits (CdtA and CdtC). The enzymatically active subunit CdtB has structural and functional homology similar with mammalian deoxyribonuclease I (DNase I). CDTis the only member of AB toxin family with DNase enzyme activity. The role of CdtA and CdtC is to anchor CdtB on host cell membrane, in which CdtC is considered to be a chaperone for CdtB. After entering cell by endocytosis, CdtB undergoes retrograde translocate to endoplasmic reticulum (ER) via Golgi complex, then directly trans from ER to nucleus (Frisan, 2015). Due to its potent DNase activity, CDT is sufficient to induce DNA damage at very low doses (50 pg / mL). Single-strand breaks (SSB) can be induced after CDT intervention in 3 h. SSB causes replication forks (RFs) to stall, producing replication stress response, that ultimately leads to double-strand breaks (DSB) and cell cycle arrest. However, high doses (4 μg/ mL) of CDT can directly lead to important levels of DSB (Jinadasa et al., 2011).

DSB in host cells can be recognized by MRN complex (composed of MRE11, RAD50, and NBS1). The latter recruits ATM (ataxia-telangiectasia mutated) kinase to DNA injury sites, then ATM phosphorylates the CHK2 transduction proteins (Lee and Paull, 2005). Activated ATM and CHK2 phosphorylate a variety of substrates, including the p53 and CDC25 phosphatase families, while effector protein (p53, CDC25) activates appropriate cellular response (Jazayeri et al., 2006). These cellular responses include the following: (1) ATM-dependent DNA damage response (DDR): With the advent of DBS, DNA repair mechanisms are initiated, DDR is activated, including homologous recombination (HR)

TABLE 1 | The characteristics of cancer causing digestive tract bacteria and their correlation with pancreatic cancer.

	H. pylori	*A. actinomycetemcomitans*	*F. nucleatum*	*P. gingivalis*
Phylum	*Proteobacteria*	*Proteobacteria*	*Fusobacteria*	*Bacteroidetes*
Gram stain	Negative	Negative	Negative	Negative
Respiration characteristic	Microaerophilic	Facultative anaerobe	Anaerobic	Anaerobic
Location	Stomach	Oral	Oral	Oral
Pancreatic tissue	Absence	Presence	Presence	Presence
Correlation with pancreatic cancer	Poor	High	High	High

and non-homologous end joining (NHEJ) repair mechanism (Goodarzi and Jeggo, 2013). (2) ATM-dependent cell cycle arrest: Activated ATM phosphorylates p53, resulting p21 upregulates cytosine E-CDK2, which blocks cells from entering the S phase (Mediates G1/S blockade). Activated Chk2 phosphorylates and inactivates cell division cycle 25 (CDC25) C phosphatase, resulting accumulation of phosphorylated cyclin B-CDK1 complex, which prevents cells from entering the M phase (Mediated G2/M blockade) (Jinadasa et al., 2011). These can lead to cell cycle arrest, resulting in the formation of corresponding tissue microenvironment, that not only promotes survival and proliferation of transformed cells through by senescence-associated secretory phenotype (SASP) but also promote cancer occurrence (Coppé et al., 2010; Campisi, 2013).

In some cases, genetic instability caused by improper DNA damage repair is a significant reason of cancer development. In the other cases, CDT can also induce apoptosis. When DDR systems fail to properly repair DNA damage, thereby activating p53, leading to activation of intrinsic apoptotic pathway, which ultimately leads apoptotic cell to death (Jinadasa et al., 2011). At the same time, CdtB has phosphatase activity, which can decompose PI-3,4,5-P_3 (PIP3) to PI-3,4-P_2, thereby changing pathway of PI-3K/PIP_3/AKT/pGSK3β signaling, leading inactivation of the downstream Akt pathway, which ultimately leads to cell cycle arrest and activation of the apoptosis cascade (Shenker et al., 2007). The PIP3 is mainly synthesized by PI-3Ks intracellular. Accompanied by a large consumption of PIP3, which leads to excessive activation of PI-3K. Since PI-3K is one of the major effectors of KRAS, activation of KRAS signaling by RAC1 via PI-3K is required for KRAS mutation. It is well-known that almost all pancreatic ductal adenocarcinoma (PDA) has mutations in the KRAS gene (Wu et al., 2014). Therefore, CDT can also modulate cyclomodulin in addition to genotoxin.

The fate of cells after CDT infection seems to depend on the cell type. When lymphocytes are present due to antigen presentation or mitosis, the PIP3 content is increased. The phosphatase activity of CdtB is enhanced with the increase of intracellular PIP3 concentration. Lymphocytes undergo cell cycle arrest or apoptosis, which ultimately impair host immunity and conducive to the formation of chronic infection microenvironment (Shenker et al., 2007). In fact, almost all the host cells will undergo cell cycle arrest after infection with CDT. Among them, hematopoietic cell lineage will progress toward apoptosis, while epithelial and mesenchymal cell lineages will remain alive, which is associated with activation of the survival signal transduction pathway in these adherent cells. In order to resist the toxin action of CDT, Net1 (transforming gene 1) regulates the activation of ras homolog family member A (RhoA) and p38 mitogen-activated protein kinase (MAPK). Activation of the survival signal causes these cells to survive, and also allows cells with incorrect DNA repair to survive, thereby promoting tumorigenesis and progression (Guerra et al., 2008) (**Figure 1A**).

Based on the above CDT mechanism of actions some researches have confirmed that CDT can promote the occurrence of liver cancer and colorectal cancer (Ge et al., 2007; Graillot et al., 2016).

The third type of cytotoxin is cytotoxin-associated gene E (CagE). CagE may have helicase activity due to the presence of DEAD cassette, and its role in regulating DNA methylation expression is considered as possible mechanisms of tumorigenesis. Because of above functions, CagE can participate in a variety of cellular activities, including mutagenesis, senescence and regulation of tissue-specific gene expression. Therefore, the CagE gene can be widely expressed in various cancer cell lines and cancer tissues including pancreatic cancer (Kim and Jeoung, 2008). In fact, it shares homology with the carcinogenic factors secreted by *H. pylori* (Henderson et al., 2010).

Fusobacterium nucleatum

F. nucleatum is a Gram-negative anaerobic bacterium, but unlike many strict anaerobic bacteria, possess NADH oxidase, endowing them with a limited ability to respire oxygen (Kapatral et al., 2002). *F. nucleatum* is an adherent bacterium that encodes a variety of adhesins so that it can copolymerize various microorganisms. At the same time, its main virulence factors are also adhesion proteins from the outer membrane. Among all the adhesins, only *Fusobacterium* adhesin A (FadA), was identified as capable of binding to host cells and is also the most characteristic virulence factor of *F. nucleatum*. FadA exists in two forms, non-secretory intact pre-FadA and secreted mature FadA (mFadA). When pre-FadA mixed with mFadA, they form activity complexes, FadAc, which binds to host's receptor for attachment and invasion. The host receptors for FadA are members of the cadherin family, mainly E-cadherin and vascular endothelial (VE) cadherin (CDH5), which are required for *F. nucleatum* adhesion and invasion (Fardini et al., 2011; Rubinstein

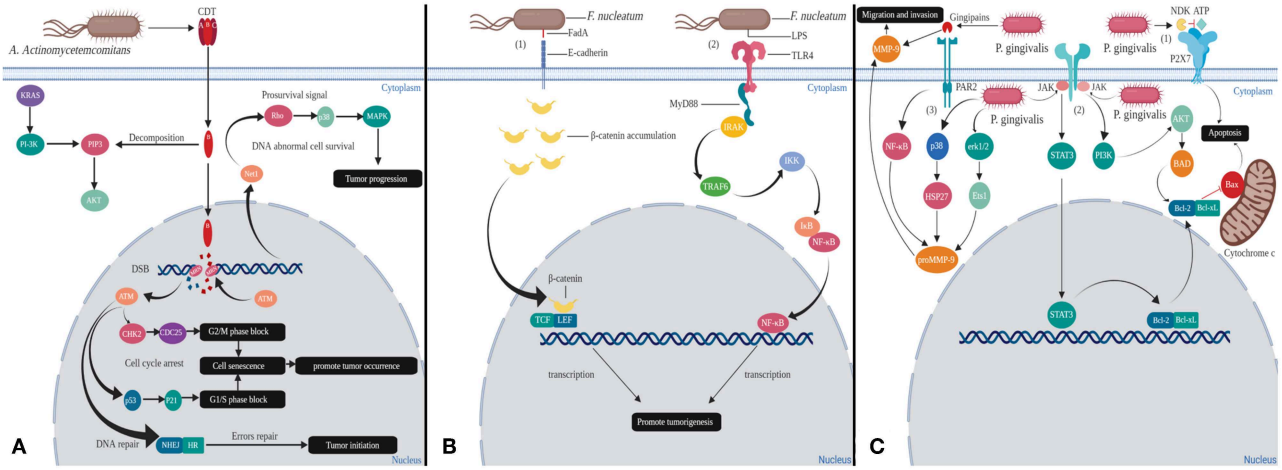

FIGURE 1 | Mechanisms of oral bacteria virulence factors inducing changes in host cells. **(A)** Cytolethal distending toxins (CDT) are the virulence factors released by *A. actinomycetemcomitans*: In the cytoplasm, the phosphatase activity of CdtB can decompose PIP3, thereby over-activating PI-3K, which is one of effectors of KRAS. This process may cause KRAS mutation that leads to cancer. In the nucleus, CdtB causes double strand break (DSB), which activates ataxia telangiectasia mutated (ATM) kinase. Activation of ATM kinase blocks G1/S and G2/M phases promoting tumor occurrence through cell senescence. Tumor initiation also could occur in the instance of erroneous in homologous recombination (HR) and non-homologous end joining (NHEJ) repair mechanisms. In order for the cells to survive, RhoA and p38 MAPK will get activated, thereby promoting tumorigenesis. **(B)** FadA and LPS are the significant virulence factors of *F. nucleatum*. (1) Binding of FadA to host cell E-cadherin causes accumulation of β-catenin in cytoplasm that eventually enters into nucleus. β-catenin will act together with LEF/TCF and produce abnormal proteins, which ultimately leads to cancer. (2) LPS binds to host cell TLR4 receptor and induces MyD88 recruitment. These will activate NF-κB signaling pathway to direct cell proliferation and cancer development. **(C)** Gingipains and NDK are the virulence factors secreted by *P. gingivalis*. (1) NDK can decompose ATP and inhibit p2x7-mediated apoptosis. (2) Gingipains able to upregulate matrix metalloproteinase 9 (MMP-9) outside the cells and proMMP-9 via NF-kB pathways in the cytoplasm that contribute to the metastasis of cancer cells. (3) *P. gingivalis* also could enter the cells and increase the expression of proMMP-9 by activating erk1/2-ets1, p38/HSP27. Moreover, *P. gingivalis* invasion could inhibit release of cytochrome c and activate caspase-9 and caspase-3 by dual JAK/Stat and Akt signaling, thereby allowing damaged or diseased cells to survive.

et al., 2013). FadA binds to E-cadherin of epithelial cells, resulting in phosphorylation and internalization of E-cadherin on the membrane. Subsequently, canonical Wnt pathway is activated, accompanied by decreased phosphorylation of β-catenin, which accumulates in the cytoplasm and translocates to the nucleus (Rubinstein et al., 2013). This process results in activation of β-catenin-regulated transcription (CRT), which interacts with transcription factors lymphoid enhancer factor (LEF)/T-cell factor (TCF). Eventually the Wnt target gene *c-myc* and *cyclin D1* are transcribed (**Figure 1B**). In general, Wnt signaling pathways can regulate cell differentiation and proliferation, thus also involve many aspects of pancreatic biology. Studies have shown that during the development of pancreatic cancer, Wnt signaling activity is gradually increased, and activation of the Wnt/β-catenin pathway is necessary for the initiation of pancreatic cancer (Rubinstein et al., 2013; Zhang et al., 2013). In addition, FadA binds to VE-cadherin on vascular endothelial cells, causing the latter to migrate from cell-cell junction to intracellular compartment, increasing endothelial permeability. Therefore, FadA not only directly invades host cells but also allow invasion of itself and other bacteria into blood by increasing endothelial permeability, which is conducive to spread of infection and immune escape (Fardini et al., 2011; Rubinstein et al., 2013).

Another virulence factor of *F. nucleatum* is familial adenomatous polyposis 2 (Fap2), which is an outer membrane protein. Fap2 binds and interacts to human inhibitory receptor T cell immunoreceptor with Ig and ITIM domains (TIGIT), that is present on human natural killer (NK) cells and lymphocytes. The cytotoxic effects of NK cells and lymphocytes are suppressed, which ultimately protecting tumor from immune system and promoting the formation of inflammatory microenvironment (Gur et al., 2015).

Moreover, during the infection invasion of *F. nucleatum*, after binding with host cell toll-like receptor 4 (TLR4) receptor, lipopoly-saccharide (LPS) of *F. nucleatum* interacts with Toll/il-1 receptor (TIR) domain-containing adaptor inducing IFN-beta (TRIF) to induce myeloid differentiation primary response protein 88 (MyD88) recruitment. MyD88 induces IRAK (IL-1 receptor–associated kinase) phosphorylation, which dissociates from the receptor, interacts with adaptor proteins TNFR-associated factor 6 (TRAF6) and TAK1 -binding proteins 2 (TAB2) on the membrane, and regulates their transport to the cytosol. Subsequently, TRAF6 becomes ubiquitinated (Ub) and activates TAK1 (TGF-β-activated kinase 1), the latter phosphorylates and activates the IκB kinase (IKK) complex. IKK phosphorylates IκB, an inhibitor of nuclear factor kappa B (NF-κB), which allows NF-κB to be rapidly activated and transferred to nucleus, promoting expression of related genes by binding to κB (Janssens and Beyaert, 2002; Wu et al., 2018). NF-κB is a multifunctional dimeric transcription factor that coordinates cell proliferation and closely related to cancer development and

progression (Yang et al., 2017) (**Figure 1B**). In addition, it has been reported that high levels of MyD88 promote PDAC cell growth and are associated with low survival in patients with PDAC (Yang et al., 2017).

Porphyromonas gingivalis

P. gingivalis, a Gram negative anaerobeis, can replicate to high levels after invading host cells without inducing host cell death, thereby contributing to extend their common survival time (Yang et al., 2017). The major virulence mechanism of *P. gingivalis* involve three pathways as follows:

In the first pathway, the nucleoside diphosphate kinase (NDK) secreted by *P. gingivalis* can act as an ATPase to reduce ATP concentration and inhibit apoptosis (Yilmaz et al., 2008) (**Figure 1C**). The purinergic receptor P2X7, located in cell membrane, mediates ATP-dependent apoptosis, which is considered to be a cytotoxic receptor. Actually, low levels of ATP promote cell growth and proliferation, high doses of ATP cause cell death (Adinolfi et al., 2005).

In the second pathway, *P. gingivalis* activates various anti-apoptotic/pro-survival pathways and keeps host cells survival by partially blocking mitochondrion-dependent apoptosis. These activation pathways include both of JAK/PI3K/Akt and JAK/STAT3. When cells are stimulated by canceration, dephosphorylated, Bcl-2-antagonist of cell death (BAD) forms a heterodimer with B-cell lymphoma 2 (Bcl-2) and B-cell lymphoma-extra large (Bcl-xL), thereby inactivate the latter, allowing Bax/Bak to form pores in the outer membrane of mitochondria. The above process causes cytochrome c (Cyt c) to leak from the mitochondria into cytoplasm and activate the pro-apoptotic caspase cascade to initiate apoptosis. *P. gingivalis* can activate the JAK/PI3K/Akt signaling pathway, in which Akt can phosphorylate BAD and forms a BAD-(14-3-3) protein heterodimer. This process allows Bcl-2 to freely inhibit Bax-triggered apoptosis (Yilmaz et al., 2004; Mao et al., 2007). In addition, *P. gingivalis* can simultaneously activate JAK/STAT3 signaling pathway and up-regulate miR-203, which inhibits the negative regulatory factor suppressor of cytokine signaling 3 (SOCS3). When SOCS3 is inhibited, STAT3 activity is significantly enhanced, that targets mainly anti-apoptotic genes (such as Bcl-2, Bcl-XL) (Yasukawa et al., 2003; Moffatt and Lamont, 2011; Bousoik and Aliabadi, 2018). Thus, the combination of these pathways results in up-regulation of anti-apoptotic Bcl-2 and down-regulation of pro-apoptotic Bax. Anti-apoptotic Bcl-2 and Bcl-xL proteins not only inhibit Cyt c release through mitochondrial pores, but also inhibit Cyt c activation of the cytoplasmic caspase cascade, ultimately promoting host cell survival and proliferation (Mao et al., 2007) (**Figure 1C**). Ikezawa *et al.* showed that overexpression of Bcl-xL is present in 90% of pancreatic ductal adenocarcinoma (PDAC) (Ikezawa et al., 2017).

Additionally, gingipains secreted by *P. gingivalis* stimulate proteinase-activated receptor 2 (PAR2) and then activate the pathway of PAR2/NF-κB. Meanwhile, *P. gingivalis* can activate erk1/2 -Ets1 and p38/HSP27 pathways after invading host cells. The above three pathways jointly induce the expression of promatrix metalloproteinase (proMMP-9). Thereafter, proMMP9 is released into extracellular environment by host cells via PAR2 activated by gingipains. Activated MMP-9 can degrade a variety of extracellular matrices (ECM) by proteolytic cleavage. Destruction of ECM is often a necessary step during tumor invasion and metastasis (Inaba et al., 2014; Whitmore and Lamont, 2014). Studies have shown that MMP-9 is overexpressed in PDAC and plays an important role in the invasion and metastasis (Ikezawa et al., 2017) (**Figure 1C**).

CONCLUSION

In the process of inducing cancer, bacteria act as a team. This mode of cooperation has been summarized as bacterial driver-passenger model, where the initial pathogen known as "driver," e.g., *A. actinomycetemcomitans*, induce DNA damage in host cells. This driver pathogen causes microenvironment changes around the host cell, which facilitates proliferation and survival of other pathogens resulting in a more stable ecosystem. Then the "passenger" bacteria, e.g., *F. nucleatum* will locate the cancer cells and act as bridging organism between the early (*A. actinomycetemcomitans*) and late colonizing microbes (*P. gingivalis*). *P. gingivalis* can inhibit cancer cell apoptosis and promote tumor development. The three bacteria may play an important synergistic role in the occurrence and development of cancer. Therefore, the diverse microbial ecosystem is not only more stable than single type of bacteria but also more toxic, which might be one of the important factors in inducing cancer. In conclusion, with deepening of research on relationship between bacteria and cancer, uncovering the mechanisms of bacterial cooperation may bring new dawn to early diagnosis and treatment of pancreatic cancer.

AUTHOR CONTRIBUTIONS

All authors have made a significant, direct and intellectual contribution to this manuscript. ZS designed, drafted and edited the manuscript. CX revised the figures and the manuscript. JL revised and edited the manuscript. ST edited the manuscript. SK conceptualized the study, reviewed and edited the manuscript. KT conceptualized and designed the study and reviewed and edited the manuscript. All authors approved the final manuscript as well as the authorship list.

FUNDING

This publication fee was supported by Universiti Putra Malaysia.

REFERENCES

Adinolfi, E., Pizzirani, C., Idzko, M., Panther, E., Norgauer, J., Di Virgilio, F., et al. (2005). P2X(7) receptor: death or life? *Purinergic Signal.* 1, 219–227. doi: 10.1007/s11302-005-6322-x

Aykut, B., Pushalkar, S., Chen, R., Li, Q., Abengozar, R., Kim, J. I., et al. (2019). The fungal mycobiome promotes pancreatic oncogenesis via activation of MBL. *Nature* 574, 264–267. doi: 10.1038/s41586-019-1608-2

Bousoik, E., and Aliabadi, H. M. (2018). 'Do we know Jack' about JAK? A closer look at JAK/STAT signaling pathway. *Front. Oncol.* 8:287. doi: 10.3389/fonc.2018.00287

Campisi, J. (2013). Aging, cellular senescence, and cancer. *Annu. Rev. Physiol.* 75, 685–705. doi: 10.1146/annurev-physiol-030212-183653

Coppé, J.P., Desprez, P.Y., Krtolica, A., and Campisi, J. (2010). The senescence-associated secretory phenotype: the dark side of tumor suppression. *Annu. Rev. Pathol. Mech. Dis.* 5, 99–118. doi: 10.1146/annurev-pathol-121808-102144

Coussens, L. M., and Werb, Z. (2002). Inflammation and cancer. *Nature* 420, 860–867. doi: 10.1038/nature01322

Cuevas-Ramos, G., Petit, C. R., Marcq, I., Boury, M., Oswald, E., and Nougayrède, J.P. (2010). *Escherichia coli* induces DNA damage *in vivo* and triggers genomic instability in mammalian cells. *Proc. Natl. Acad. Sci. U.S.A.* 107, 11537–11542. doi: 10.1073/pnas.1001261107

Fan, X., Alekseyenko, A. V., Wu, J., Peters, B. A., Jacobs, E. J., Gapstur, S. M., et al. (2018). Human oral microbiome and prospective risk for pancreatic cancer: a population-based nested case-control study. *Gut* 67, 120–127. doi: 10.1136/gutjnl-2016-312580

Fardini, Y., Wang, X., Témoin, S., Nithianantham, S., Lee, D., Shoham, M., et al. (2011). *Fusobacterium nucleatum* adhesin fada binds vascular endothelial cadherin and alters endothelial integrity. *Mol. Microbiol.* 82, 1468–1480. doi: 10.1111/j.1365-2958.2011.07905.x

Frisan, T. (2015). "Bacterial genotoxins," in *The Comprehensive Sourcebook of Bacterial Protein Toxins*, eds J. Alouf, D. Ladant, and M. R. Popoff (Boston, MA: Elsevier), 558–602. doi: 10.1016/B978-0-12-800188-2.00020-3

Ge, Z., Rogers, A. B., Feng, Y., Lee, A., Xu, S., Taylor, N. S., et al. (2007). Bacterial cytolethal distending toxin promotes the development of dysplasia in a model of microbially induced hepatocarcinogenesis. *Cell. Microbiol.* 9, 2070–2080. doi: 10.1111/j.1462-5822.2007.00939.x

Goodarzi, A. A., and Jeggo, P. A. (2013). The Repair and signaling responses to DNA double-strand breaks. *Adv. Genet.* 82, 1–45. doi: 10.1016/B978-0-12-407676-1.00001-9

Graillot, V., Dormoy, I., Dupuy, J., Shay, J. W., Huc, L., Mirey, G., et al. (2016). Genotoxicity of cytolethal distending toxin (CDT) on isogenic human colorectal cell lines: potential promoting effects for colorectal carcinogenesis. *Front. Cell. Infect. Microbiol.* 6: 34. doi: 10.3389/fcimb.2016.00034

Guerra, L., Carr, H. S., Richter-Dahlfors, A., Masucci, M. G., Thelestam, M., Frost, J. A., et al. (2008). A bacterial cytotoxin identifies the RhoA exchange factor Net1 as a key effector in the response to DNA damage. *PLoS ONE* 3:e2254. doi: 10.1371/journal.pone.0002254

Gur, C., Ibrahim, Y., Isaacson, B., Yamin, R., Abed, J., Gamliel, M., et al. (2015). Binding of the Fap2 protein of *Fusobacterium nucleatum* to human inhibitory receptor TIGIT protects tumors from immune cell attack. *Immunity* 42, 344–355. doi: 10.1016/j.immuni.2015.01.010

Henderson, B., Ward, J. M., and Ready, D. (2010). Aggregatibacter (Actinobacillus) Actinomycetemcomitans: a triple A* Periodontopathogen? *Periodontol2000* 54, 78–105. doi: 10.1111/j.1600-0757.2009.00331.x

Ikezawa, K., Hikita, H., Shigekawa, M., Iwahashi, K., Eguchi, H., Sakamori, R., et al. (2017). Increased Bcl-XL expression in pancreatic neoplasia promotes carcinogenesis by inhibiting senescence and apoptosis. *Cell. Mol. Gastroenterol. Hepatol.* 4, 185–200.e1. doi: 10.1016/j.jcmgh.2017.02.001

Inaba, H., Sugita, H., Kuboniwa, M., Iwai, S., Hamada, M., Noda, T., et al. (2014). *Porphyromonas gingivalis* promotes invasion of oral squamous cell carcinoma through induction of ProMMP9 and its activation. *Cell. Microbiol.* 16, 131–145. doi: 10.1111/cmi.12211

Janssens, S., and Beyaert, R. (2002). A universal role for MyD88 in TLR/IL-1R-mediated signaling. *Trends Biochem. Sci.* 27, 474–482. doi: 10.1016/S0968-0004(02)02145-X

Jazayeri, A., Falck, J., Lukas, C., Bartek, J., Smith, G. C., Lukas, J., et al. (2006). ATM- and cell cycle-dependent regulation of ATR in response to DNA double-strand breaks. *Nat. Cell Biol.* 8, 37–45. doi: 10.1038/ncb1337

Jesnowski, R., Isaksson, B., Möhrckea, C., Bertsch, C., Bulajic, M., Schneider-Brachert, W., et al. (2010). *Helicobacter pylori* in autoimmune pancreatitis and pancreatic carcinoma. *Pancreatology* 10, 462–466. doi: 10.1159/000264677

Jinadasa, R. N., Bloom, S. E., Weiss, R. S., and Duhamel, G. E. (2011). Cytolethal distending toxin: a conserved bacterial genotoxin that blocks cell cycle progression, leading to apoptosis of a broad range of mammalian cell lineages. *Microbiology* 157, 1851–1875. doi: 10.1099/mic.0.049536-0

Johansson, A. (2011). *Aggregatibacter actinomycetemcomitans* leukotoxin: a powerful tool with capacity to cause imbalance in the host inflammatory response. *Toxins* 3, 242–259. doi: 10.3390/toxins3030242

Kamisawa, T., Wood, L. D., Itoi, T., and Takaori, K. (2016). Pancreatic cancer. *Lancet* 388, 73–85. doi: 10.1016/S0140-6736(16)00141-0

Kapatral, V., Anderson, I., Ivanova, N., Reznik, G., Los, T., Lykidis, A., et al. (2002). Genome sequence and analysis of the oral bacterium *Fusobacterium nucleatum* strain ATCC 25586. *J. Bacteriol.* 184, 2005–2018. doi: 10.1128/JB.184.7.2005-2018.2002

Kim, Y., and Jeoung, D. (2008). Role of CAGE, a novel cancer/testis antigen, in various cellular processes, including tumorigenesis, cytolytic T lymphocyte induction, and cell motility. *J. Microbiol. Biotechnol.* 18, 600–610.

Laugisch, O., Johnen, A., Maldonado, A., Ehmke, B., Bürgin, W., Olsen, I., et al. (2018). Periodontal pathogens and associated intrathecal antibodies in early stages of Alzheimer's disease. *J Alzheimers Dis.* 66, 105–114. doi: 10.3233/JAD-180620

Lee, J.H., and Paull, T. T. (2005). Direct activation of the ATM protein kinase by the Mre11/Rad50/Nbs1 complex. *Science* 304, 93–96. doi: 10.1126/science.1091496

Mao, S., Park, Y., Hasegawa, Y., Tribble, G. D., James, C. E., Handfield, M., et al. (2007). Intrinsic apoptotic pathways of gingival epithelial cells modulated by *Porphyromonas gingivalis*. *Cell. Microbiol.* 9, 1997–2007. doi: 10.1111/j.1462-5822.2007.00931.x

Michaud, D. S. (2013). Role of bacterial infections in pancreatic cancer. *Carcinogenesis* 34, 2193–2197. doi: 10.1093/carcin/bgt249

Mitsuhashi, K., Nosho, K., Sukawa, Y., Matsunaga, Y., Ito, M., Kurihara, H., et al. (2015). Association of Fusobacterium species in pancreatic cancer tissues with molecular features and prognosis. *Oncotarget* 6, 7209–7220. doi: 10.18632/oncotarget.3109

Moffatt, C. E., and Lamont, R. J. (2011). *Porphyromonas gingivalis* induction of microRNA-203 expression controls suppressor of cytokine signaling 3 in gingival epithelial cells. *Infect. Immun.* 79, 2632–2637. doi: 10.1128/IAI.00082-11

Mukherjee, A., Jantsch, V., Khan, R., Hartung, W., Fischer, R., Jantsch, J., et al. (2018). Rheumatoid arthritis-associated autoimmunity due to aggregatibacter actinomycetemcomitans and its resolution with antibiotic therapy. *Front. Immunol.* 9:2352. doi: 10.3389/fimmu.2018.02352

Paturel, L., Casalta, J. P., Habib, G., Nezri, M., and Raoult, D. (2004). Actinobacillus actinomycetemcomitans endocarditis. *Clin. Microbiol. Infect.* 10, 98–118. doi: 10.1111/j.1469-0691.2004.00794.x

Pushalkar, S., Hundeyin, M., Daley, D., Zambirinis, C. P., Kurz, E., Mishra, A., et al. (2018). The pancreatic cancer microbiome promotes oncogenesis by induction of innate and adaptive immune suppression. *Cancer Discov.* 8, 403–416. doi: 10.1158/2159-8290.CD-17-1134

Rawla, P., Sunkara, T., and Gaduputi, V. (2019). Epidemiology of pancreatic cancer: global trends, etiology and risk factors. *World J. Oncol.* 10, 10–27. doi: 10.14740/wjon1166

Repass, J., Iorns, E., Denis, A., Williams, S. R., Perfito, N., and Errington, T. M. (2018). Replication study: Fusobacterium nucleatum infection is prevalent in human colorectal carcinoma. *eLife* 7:e25801. doi: 10.7554/eLife.25801

Riquelme, E., Zhang, Y., Zhang, L., Montiel, M., Zoltan, M., Dong, W., et al. (2019). Tumor microbiome diversity and composition influence pancreatic cancer outcomes. *Cell* 178, 795–806.e12. doi: 10.1016/j.cell.2019.07.008

Rubinstein, M. R., Wang, X., Liu, W., Hao, Y., Cai, G., and Han, Y. W. (2013). *Fusobacterium nucleatum* promotes colorectal carcinogenesis by modulating E-cadherin/β-catenin signaling via its FadA adhesin. *Cell Host Microbe* 14, 195–206. doi: 10.1016/j.chom.2013.07.012

Sahan, A. Z., Hazra, T. K., and Das, S. (2018). The pivotal role of DNA repair in infection mediated-inflammation and cancer. *Front. Microbiol.* 9:663. doi: 10.3389/fmicb.2018.00663

Shang, L., Deng, D., Buskermolen, J. K., Roffel, S., Janus, M. M., et al. (2019). Commensal and pathogenic biofilms alter toll-like receptor signaling in reconstructed human gingiva. *Front. Cell. Infect. Microbiol.* 9:282. doi: 10.3389/fcimb.2019.00282.

Shenker, B. J., Dlakic, M., Walker, L. P., Besack, D., Jaffe, E., LaBelle, E., et al. (2007). A novel mode of action for a microbial-derived immunotoxin: the cytolethal distending toxin subunit B exhibits phosphatidylinositol 3,4,5-triphosphate phosphatase activity. *J. Immunol.* 178, 5099–5108. doi: 10.4049/jimmunol.178.8.5099

Siegel, R. L., Miller, K. D., and Jemal, A. (2019). Cancer Statistics, 2019. *CA Cancer J. Clin.* 69, 7–34. doi: 10.3322/caac.21551

Sugiyama, S., Takahashi, S., Tokutomi, F., Yoshida, A., Kobayashi, K., Yoshino, F., et al. (2012). Gingival vascular functions are altered in type 2 diabetes mellitus model and/or periodontitis model. *J. Clin. Biochem. Nutr.* 51, 108–113. doi: 10.3164/jcbn.11-103

Tjalsma, H., Boleij, A., Marchesi, J. R., and Dutilh, B. E. (2012). A bacterial driver–passenger model for colorectal cancer: beyond the usual suspects. *Nat. Rev. Microbiol.* 10, 575–582. doi: 10.1038/nrmicro2819

Velsko, I. M., Chukkapalli, S. S., Rivera, M. F., Lee, J. Y., Chen, H., Zheng, D., et al. (2014). Active invasion of oral and aortic tissues by *Porphyromonas gingivalis* in mice causally links periodontitis and atherosclerosis. *PLoS ONE* 9:e97811. doi: 10.1371/journal.pone.0097811

Wei, M.Y., Shi, S., Liang, C., Meng, Q.C., Hua, J., Zhang, Y.Y., et al. (2019). The microbiota and microbiome in pancreatic cancer: more influential than expected. *Mol Cancer* 18:97. doi: 10.1186/s12943-019-1008-0

Whitmore, S. E., and Lamont, R. J. (2014). Oral bacteria and cancer. *PLoS Pathog.* 10:e1003933. doi: 10.1371/journal.ppat.1003933

Wu, C.Y. C., Carpenter, E. S., Takeuchi, K. K., Halbrook, C. J., Peverley, L. V., Bien, H., et al. (2014). PI3K regulation of RAC1 is required for KRAS-induced pancreatic tumorigenesis in mice. *Gastroenterology* 147, 1405–1416.e7. doi: 10.1053/j.gastro.2014.08.032

Wu, J., Ding, J., Yang, J., Guo, X., and Zheng, Y. (2018). MicroRNA roles in the nuclear factor kappa B signaling pathway in cancer. *Front. Immunol.* 9:546. doi: 10.3389/fimmu.2018.00546

Yang, Y., Weng, W., Peng, J., Hong, L., Yang, L., Toiyama, Y., et al. (2017). *Fusobacterium nucleatum* increases proliferation of colorectal cancer cells and tumor development in mice by activating toll-like receptor 4 signaling to nuclear factor–κB, and up-regulating expression of microRNA-21. *Gastroenterology* 152, 851–866.e24. doi: 10.1053/j.gastro.2016.11.018

Yasukawa, H., Ohishi, M., Mori, H., Murakami, M., Chinen, T., Aki, D., et al. (2003). IL-6 induces an anti-inflammatory response in the absence of SOCS3 in macrophages. *Nat. Immunol.* 4, 551–556. doi: 10.1038/ni938

Yilmaz, O., Jungas, T., Verbeke, P., and Ojcius, D. M. (2004). Activation of the phosphatidylinositol 3-kinase/Akt pathway contributes to survival of primary epithelial cells infected with the periodontal pathogen *Porphyromonas gingivalis*. *Infect. Immun.* 72, 3743–3751. doi: 10.1128/IAI.72.7.3743-3751.2004

Yilmaz, Ö., Yao, L., Maeda, K., Rose, T. M., Lewis, E. L., Duman, M., et al. (2008). ATP scavenging by the intracellular pathogen *Porphyromonas gingivalis* inhibits P2X $_7$ -mediated host-cell apoptosis. *Cell. Microbiol.* 10, 863–875. doi: 10.1111/j.1462-5822.2007.01089.x

Zhang, Y., Morris, J. P., Yan, W., Schofield, H. K., Gurney, A., Simeone, D. M., et al. (2013). Canonical Wnt signaling is required for pancreatic carcinogenesis. *Cancer Res.* 73, 4909–4922. doi: 10.1158/0008-5472.CAN-12-4384a

Conflict of Interest: The authors declare that the research was conducted in the absence of any commercial or financial relationships that could be construed as a potential conflict of interest.

Copyright © 2019 Sun, Xiong, Teh, Lim, Kumar and Thilakavathy. This is an open-access article distributed under the terms of the Creative Commons Attribution License (CC BY). The use, distribution or reproduction in other forums is permitted, provided the original author(s) and the copyright owner(s) are credited and that the original publication in this journal is cited, in accordance with accepted academic practice. No use, distribution or reproduction is permitted which does not comply with these terms.

frontiers in Cellular and Infection Microbiology

ORIGINAL RESEARCH
published: 17 January 2020
doi: 10.3389/fcimb.2019.00451

Association of *Plasmodium berghei* With the Apical Domain of Hepatocytes Is Necessary for the Parasite's Liver Stage Development

*Lakshmi Balasubramanian[1], Vanessa Zuzarte-Luís[2], Tabish Syed[3], Debakshi Mullick[1], Saptarathi Deb[1], Harish Ranga-Prasad[1], Jana Meissner[4], Ana Almeida[2], Tobias Furstenhaupt[4], Kaleem Siddiqi[3], Miguel Prudêncio[2], Cecilia M. P. Rodrigues[5], Maria Mota[2] and Varadharajan Sundaramurthy[1]**

[1] National Center for Biological Sciences, Bangalore, India, [2] Instituto de Medicina Molecular, Faculdade de Medicina, Universidade de Lisboa, Lisbon, Portugal, [3] School of Computer Science and Centre for Intelligent Machines, McGill University, Montreal, QC, Canada, [4] Max Planck Institute of Molecular Cell Biology and Genetics, Dresden, Germany, [5] Research Institute for Medicines, University of Lisbon, Lisbon, Portugal

OPEN ACCESS

Edited by:
Marcel I. Ramirez,
Oswaldo Cruz Foundation (Fiocruz), Brazil

Reviewed by:
Gaoqian Feng,
Burnet Institute, Australia
Fred David Mast,
Seattle Children's Research Institute, United States

***Correspondence:**
Varadharajan Sundaramurthy
varadha@ncbs.res.in

Specialty section:
This article was submitted to Parasite and Host, a section of the journal Frontiers in Cellular and Infection Microbiology

Received: 02 September 2019
Accepted: 12 December 2019
Published: 17 January 2020

Citation:
Balasubramanian L, Zuzarte-Luís V, Syed T, Mullick D, Deb S, Ranga-Prasad H, Meissner J, Almeida A, Furstenhaupt T, Siddiqi K, Prudêncio M, Rodrigues CMP, Mota M and Sundaramurthy V (2020) Association of Plasmodium berghei With the Apical Domain of Hepatocytes Is Necessary for the Parasite's Liver Stage Development. Front. Cell. Infect. Microbiol. 9:451. doi: 10.3389/fcimb.2019.00451

Plasmodium parasites undergo a dramatic transformation during the liver stage of their life cycle, amplifying over 10,000-fold inside infected hepatocytes within a few days. Such a rapid growth requires large-scale interactions with, and manipulations of, host cell functions. Whereas hepatocyte polarity is well-known to be critical for liver function, little is presently known about its involvement during the liver stage of *Plasmodium* development. Apical domains of hepatocytes are critical components of their polarity machinery and constitute the bile canalicular network, which is central to liver function. Here, we employed high resolution 3-D imaging and advanced image analysis of *Plasmodium*-infected liver tissues to show that the parasite associates preferentially with the apical domain of hepatocytes and induces alterations in the organization of these regions, resulting in localized changes in the bile canalicular architecture in the liver tissue. Pharmacological perturbation of the bile canalicular network by modulation of AMPK activity reduces the parasite's association with bile canaliculi and arrests the parasite development. Our findings using *Plasmodium*-infected liver tissues reveal a host-*Plasmodium* interaction at the level of liver tissue organization. We demonstrate for the first time a role for bile canaliculi, a central component of the hepatocyte polarity machinery, during the liver stage of *Plasmodium* development.

Keywords: plasmodium liver stage, hepatocyte polarity, ultrastructure, 3D image analysis, liver tissue, bile canaliculi

INTRODUCTION

Plasmodium parasites undergo a dramatic amplification during the liver stage of their life cycle, when an individual sporozoite infecting a hepatocyte multiplies inside a parasitophorous vacuole (PV) to produce several thousand infective merozoites (Prudencio et al., 2006; Vaughan and Kappe, 2017). This rapid intra-hepatic growth requires extensive networking and interactions with the

host's liver cells, at both the sub-cellular and molecular levels (Agop-Nersesian et al., 2018; Nyboer et al., 2018). Pioneering ultrastructure studies employing sporozoite infection of a restricted area of rat livers have suggested extensive interactions of the PV membrane (PVM) with different host organelles during parasite development (Meis et al., 1981, 1983a,b; Shin et al., 1982). Some of these interactions, such as those with the autophagosome, late endosomes, lysosomes and the endoplasmic reticulum, play central roles in nutrient acquisition and immune evasion, and are necessary for supporting parasite development inside hepatocytes (Bano et al., 2007; Lopes da Silva et al., 2012; Thieleke-Matos et al., 2016; Coppens, 2017; Evans et al., 2018).

One of the defining features of hepatocyte function is their unique polarity. Unlike a columnar epithelial cell, where the entire surface facing a luminal cavity is apical, hepatocytes have apical domains spanning the cell as "bands" that connect in 3 dimensions to form the highly ramified bile canalicular (BC) network. This network constitutes the first level of branching in the complex bile duct tree, which eventually drains into the gall bladder (Elias, 1949; Treyer and Musch, 2013; Gissen and Arias, 2015). The geometry of the bile duct tree plays a crucial role in the production, flux, and storage of bile (Meyer et al., 2017). Correct polarization of hepatocytes and organization of the apical domains are essential for bile secretion and flow (Arias et al., 1993; Turumin et al., 2013), while loss of polarity is associated with several liver diseases (Gissen and Arias, 2015). The velocity of the bile flow depends on the secretion of bile by hepatocytes into their apical domain and on the geometric features of the bile canalicular network (Meyer et al., 2017). Thus, apical domain organization is a critical aspect of hepatocyte function. Whether these processes are involved in the liver stage of *Plasmodium* infection is not presently known.

The critical role of polarity for hepatocyte function, and the specific tropism of *Plasmodium* sporozoites for hepatocytes, motivated us to explore the connection between hepatocyte polarity and *Plasmodium* development during the liver stage of infection. Hepatoma cells in 2D culture systems typically lose the characteristic hepatocyte polarity (Treyer and Musch, 2013; Musch, 2014; Gissen and Arias, 2015), and are hence unsuitable models to address this question. We therefore departed from the classical approach, by studying the development of the *Plasmodium* parasite in its native three-dimensional tissue environment. To that end, we employed high resolution 3D imaging and advanced and customized quantitative image analysis of infected liver tissues to show that the parasite makes preferential contacts with the hepatocyte's apical domain during its development in the liver. Furthermore, these apical domains are themselves re-organized during the liver stage of *Plasmodium* development, resulting in localized alterations in bile canalicular architecture. Finally, we show that pharmacological manipulation of hepatocyte polarity alters the bile canalicular architecture, preventing the contact of the hepatocyte's apical domain with the parasite vacuole membrane and arresting its development.

MATERIALS AND METHODS

Mice and *Plasmodium berghei* Liver Infection

All mice used in this study were C57BL/6J mice purchased from Charles River Laboratories (L'Arbresle, France), housed in the facilities of the Instituto de Medicina Molecular and allowed free access to water and food. Infections were performed using a GFP-expressing *P. berghei* ANKA parasite line (259cl2). Mice were infected by intravenous injection of 10^5 sporozoites obtained through dissection of the salivary glands of infected female *Anopheles stephensi* mosquitoes bred at the Instituto de Medicina Molecular. Hepatic infection was determined by microscopy analysis of liver sections or by quantitative RT-PCR amplification of *Plasmodium* 18S rRNA, at specific times of infection. Salicylate (Calbiochem 71945) was administered by intraperitoneal injection of 300 mg/kg in NaCl 0.9% at 2 and 24 h post infection (hpi). All experiments were approved by the animal ethics committee at Instituto de Medicina Molecular and performed in strict compliance with the guidelines of National and European regulations.

Bile Acid Analysis

Bile acids were extracted from 5 µl of gallbladder bile by liquid-solid extraction using Sep Pak C18 cartridges (Waters, Milford, MA, USA). The samples were diluted in 0.1 M Tris HCl, pH 9.0, passed through activated cartridges, eluted with methanol, taken to dryness under an N2 stream, re-dissolved in methanol and saline (1:10, v/v) and then subjected to an enzymatic colorimetric assay. The total volume of bile acids in gallbladder bile and serum (150–200 µl) was determined using the 5th Generation Enzymatic Colorimetric RX Series kit (Randox Laboratories Ltd, Crumlin, UK) and the HORIBA Medical Clinical Chemistry Analysis Pentra C200 (Kyoto, Japan).

Fixation, Staining, and Immunofluorescence Microscopy Analysis of Liver Tissues

At selected time points after sporozoite infection, livers were perfused through the portal vein with 4% PFA and further fixed by overnight incubation in 4% PFA at 4°C. One-hundred micrometer thick sections were prepared from perfusion-fixed infected mouse liver using a vibratome (Leica VT1200S). The sections were immuno-stained using standard methods (Meyer et al., 2017) to mark the parasitophorous vacuole membrane (PVM) using a UIS4 antibody (Sicgen, dilution 1:500), and the apical domain using a CD13 antibody (Novus biologicals, dilution 1:200). Nuclei and cell boundaries were visualized using DAPI (Invitrogen) and Phalloidin (Invitrogen, dilution 1:250), respectively. Briefly, floating sections were permeabilized by incubation in 0.5% Triton X-100 in PBS for 60 min, washed thrice in 0.2% fish gelatin, 300 mM NaCl and 0.3% Triton-X100 in PBS, and then incubated in a primary antibody in the same buffer for two overnight incubations with the section flipped once in between. Sections were then washed extensively (5 changes of 15 min each) followed by two overnight incubations with a

secondary antibody in the same buffer, with the section flipped after 1 day. Typically DAPI and Phalloidin were added along with this mix. The stained sections were cleared by SeeDB using standard methods (Ke et al., 2013). Briefly, immunostained sections were washed 5 × 15 min with 0.3% Triton X-100, followed by a 3 × 1 min wash in PBS. They were then incubated in progressively increasing concentrations of fructose solutions (25, 50, 75, and 100%) for 8–12 h at room temperature for each concentration of fructose, until the floating sections sank to the bottom. Finally, the sections were incubated with SeeDB overnight at room temperature and mounted on a glass slide in SeeDB with a coverslip of 0.17 ± 0.005 mm thickness. The slides were imaged using a Zeiss LSM780 confocal microscope using a 63x objective, NA 1.4 with four lasers, 405 nm to detect DAPI, 488 nm for CD13, 568 nm for UIS4 and 647 nm for Phalloidin-647. The images were typically acquired up to a z-depth of 75–90 μm with a voxel size of either 0.3 or 0.5 μm^3, with pinhole set to 1 Airy unit. Typically, the x-y area covered a field of 134.95 μm^2.

Image Analysis

Image analysis was carried out using either CellProfiler (Carpenter et al., 2006; Lamprecht et al., 2007; Kamentsky et al., 2011) or customized macros in Fiji (Schindelin et al., 2012). The Fiji macros were semi-automated and were used to segment the cellular organelles from the infected liver tissue and to estimate the tubular and network features of the bile canaliculi. Details on the macros and the processing steps are provided in **Supplementary Material**. A fully automated geometric flow-based segmentation method (Vasilevskiy and Siddiqi, 2002) using customized Matlab codes was also employed to independently segment the BC and PVM in 3D, and the results were compared against those obtained using intensity threshold based segmentation with manual interaction.

EM Sample Preparation

One hundred micrometer thick vibratome sections were cut from perfusion-fixed (2% formaldehyde, 2.5% glutaraldyhde in PBS) *P. berghei*-infected livers (Leica, Vienna 1200S) and stored in 1xPBS at 4°C. A Zeiss Axioplan2 upright epifluorescence microscope with an RTSPOT monochrome camera was used to locate the parasites within the sections. The region of interest containing the parasite was cut with a razor blade and placed into 3 × 0.1 mm gold-coated sample carriers (Leica) for high pressure freezing. The carrier was filled with 20% BSA in a 0.1 M phosphate buffer for cryo protection. The liver tissue pieces were high pressure frozen (Leica EM ICE) and freeze substituted (Leica EM/AFS2) in 1% osmium tetroxide, 0.1% uranyl acetate in acetone, rinsed in acetone at RT and then flat-embedded in epoxy resin (EMBed 812, EMS). Three hundred or seventy nanometer thick sections were cut from the polymerized tissue blocks for tomogram and ultrastructure imaging, respectively. The grids were stained with uranyl acetate and lead citrate according to standard protocols. Gold fiducials were added prior to imaging for the tomograms.

Transmission Electron Tomography was performed using a Tecnai TF30 G2 FEG-TEM (Thermo Fisher Scientific Electron Microscopy, Hillsboro, Oregon, USA) with a Fischione 2040 Dual-Axis Tomography Holder (Fischione Instruments, Pennsylvania, USA). All images were acquired on a Gatan UltraScan 1,000 CCD (Gatan, Pleasanton, California, USA) at 2,048 × 2,048 pixels at a microscope magnification of 4,700. The acceleration voltage was 300 kV with 4,500 V extraction voltage at the Field Effect Gun at spot size 1 and gunlens 1. Dual axis tomography was carried out by taking one image every degree, for a tilt range between 120 and 130 degrees, with the program SerialEM (Mastronarde, 2005), with exposure times between 0.8 and 1.3 s. The tomographic reconstruction was performed by weighted back-projection with the IMOD software package (Kremer et al., 1996; Mastronarde, 1997). The same software was used for visualization and analysis, including 3D rendering.

RESULTS

In order to comprehensively characterize hepatic *P. berghei* development in its native liver tissue environment, 100 μm-thick sections of mouse livers collected 24, 33, and 48 h post-infection (hpi) were immunostained with UIS4 to mark the PVM and stained with DAPI and phalloidin, to label the nuclei and host cell boundaries, respectively. These time points were selected to specifically study *Plasmodium* hepatic schizogony following the successful completion of the initial invasion and dedifferentiation steps. For the purpose of this study, we consider the selected time points to correspond roughly to "early," "mid," and "late" stages of parasite schizogony. We performed high resolution 3D imaging at isometric sub-micron resolution (**Figures 1A,B**, **Movie S1A**), and acquired 3D images of the entire volume of the infected cell. The PV volume was quantified by segmenting the vacuole in 3D using an intensity thresholding method and compared across the different time points. Our results show that parasite growth *in vivo* is not linear, displaying only a modest increase in PV volume between 24 and 33 hpi, followed by a steep increase between 33 and 48 hpi (**Figure 1C**), showing that the period between 33 and 48 hpi marks a phase of rapid parasite development *in vivo*. We modified a flow-based segmentation method (Vasilevskiy and Siddiqi, 2002) to establish an automated method for object segmentation in 3D on this dataset (**Movies S1C,S1D**, **Figure 1D**). Next, we measured the changes in hepatocyte volume accompanying parasite growth at these time points, by segmenting infected and uninfected hepatocytes from the same tissue (**Movie S1B**). Our results show that the volume of the infected cell was comparable to that of non-infected cells at 24 hpi, but showed a modest increase at 33 hpi (**Figure 1E**). Most strikingly, at 48 hpi, the volume of the infected cell increased 6–8-fold relative to that of the non-infected cells (**Figure 1E**). The fraction of the cell volume occupied by the parasite increased from 10 to 35% between 24 and 33 hpi, and reached almost 90% by 48 hpi (**Figure 1F**), in agreement with the dramatic parasite growth observed *in vivo*. The large increase in the volume of the infected hepatocyte observed at late stages of infection is likely to influence neighboring cells. Given that the number of uninfected cells far outnumbers that of infected cells, these data suggest

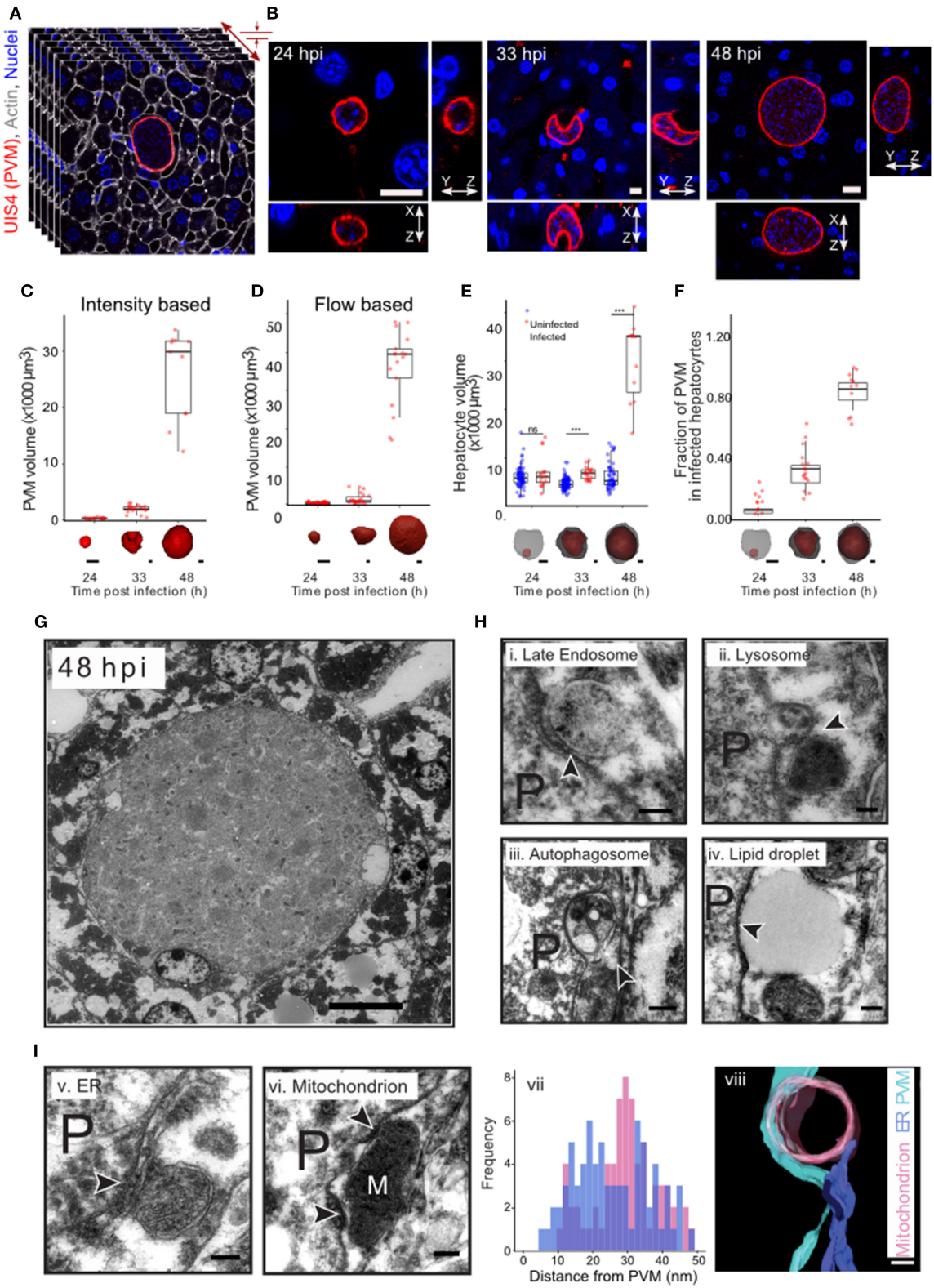

FIGURE 1 | Plasmodium liver stage development *in vivo* in 3d. **(A)** 3D imaging and analysis of *Plasmodium berghei* development during the liver stage of infection. One hundred µm liver sections from *P. berghei* infected mice were sectioned and stained for PVM using an anti-UIS4 antibody. Nuclei and cell membranes are

(Continued)

FIGURE 1 | visualized by DAPI and Phalloidin staining, respectively. Imaging was carried out using confocal microscopy at a resolution of 0.3 μm voxel. **(B)** Representative images from *P. berghei*-infected liver sections collected 24, 33, and 48 hpi, showing the PVM and nucleus in x-y, x-z, and y-z views. The scale bar is 10 μm. **(C)** Quantification of volume changes in the parasitophorous vacuole during *P. berghei* development *in vivo*. Images from B were segmented using an intensity thresholding method. **(D)** Quantification of volume changes in the parasitophorous vacuole during *P. berghei* development *in vivo*. Images from B were segmented using an automated geometric flow based segmentation method. **(E)** Quantification of volume changes at the indicated time points post infection in the infected and nearby uninfected hepatocytes. ***denote a $p < 0.001$ by Student's *t*-test. **(F)** Proportion of host cell volume occupied by the parasite during liver stage development *in vivo*. For **(C–F)**, a representative image of the model for the segmented parasite (red) and the host hepatocyte (gray) in 3d, for the time points indicated, is shown along the x-axis. The scale bar is 10 μm. **(G)** Ultrastructure of *P. berghei*-infected cell at 48 hpi *in vivo*. The scale bar is 10 μm. **(H)** Selected regions from a *P. berghei* infected hepatocyte *in vivo* showing close association of the PVM with late endosome (i), lysosome (ii), autophagosome (iii), and a lipid droplet (iv). **(I)** Selected regions from a *P. berghei* infected hepatocyte *in vivo* showing close association of the PVM with ER (v) and a mitochondrion (vi). Distance distribution of PVM with ER (purple) and mitochondria (pink) (vii). Data is from at least 5 infected cells. (viii) shows a representative tomogram reconstruction of a close interaction of the PVM (cyan) with a mitochondrion (pink) and ER (purple). For **(H,I)**, P denotes the parasite and the arrowheads point to the apposition of PVM with the indicated organelles. The scale bar is 200 nm.

that the intrahepatic development of *Plasmodium* parasites likely results in highly localized changes to liver tissue, specifically around the infected cells.

The striking changes observed in intracellular *Plasmodium* development during the liver stage of infection likely necessitate extensive interactions with the host cells at a sub-cellular level. In order to systematically explore these interactions during parasite development *in vivo*, we optimized methods for ultrastructural observation of infected cells in the liver tissue at 33 and 48 hpi (**Figures 1G,H**). We observed close interaction of PVM with late endosomes, lysosomes, autophagosomes, lipid droplet, ER and mitochondria (**Figures 1H,I**). Late endosomes and lysosomes were identified based on their characteristic morphology (Zeigerer et al., 2012), autophagosomes were distinguished by the presence of double membrane, and the ER was identified based on its characteristic tubular structure. In particular, contacts with mitochondria and ER were proximal and frequent, as shown by a representative tomogram (**Figure 1I,viii**) and by distance distribution plots (**Figure 1I,vii**), respectively. Thus, extensive contacts with diverse host cellular organelles are established and maintained during liver stage infection *in vivo*. Collectively, these observations exemplify the interactions occurring between *Plasmodium* and the host cell during the parasite's liver stage development.

In addition, we also observed that the PVM is often in close contact with the apical domain of the hepatocyte, as illustrated by EM imaging of 70 nm thick serial liver sections (**Figure 2A**). Apical membranes are defined by the electron dense tight junction and the characteristic involutions of the bile canaliculi (BC)(Goldblatt and Gunning, 1984). In order to study this association further, we measured the distance from regularly spaced points in the PVM to the closest point in the hepatocyte plasma membrane, and further categorized the hepatocyte membrane as either apical or basolateral. Frequency plots of these measurements from five infected cells using ultrastructural EM show that the PVM tends to be closer to the apical membranes than the baso-lateral ones (**Figure 2B**). We confirmed this result by electron microscopy tomogram analysis of a 300 nm thick section of an infected cell (**Figure 2C**, **Movie S2A**). EM analysis of a limited number of infected cells suggested an interaction between the PVM and the host hepatocyte's apical domain. Apical domains are a central feature of the unique hepatocyte polarity, as apical regions from the plasma membrane of adjacent cells connect in 3 dimensions to form the bile canaliculi, which represents the first level of organization in the complex 3 dimensional bile network geometry (Arias et al., 1993; Treyer and Musch, 2013; Gissen and Arias, 2015).

We sought to confirm this potentially novel interaction by an independent method and substantiate it with quantitation from several infected cells. To this end, high resolution 3D imaging and image analysis of infected mouse liver tissues were performed using customized platforms on infected liver sections stained for the apical domain marker CD13 and imaged using confocal microscopy at isometric voxels size of 0.3 μm (**Figure 2D**). Images were reconstructed in 3D to visualize the PVM in conjunction with the apical domain of the infected hepatocytes. Two independent customized image analysis workflows were employed to analyze the PVM-BC association (**Figures S2, S3**). The first method employed customized macros in Fiji to subtract the BC image from the PVM in 3D, in order to identify and quantify the total intensity of the BC regions overlapping with the PVM (method outlined in **Figure S2**). The surface voxels of BC on the PVM were quantified as a measure of the PVM-BC association. These voxels represent parts of the BC that are in direct contact with the PVM; values higher than zero denote juxtaposition and are proportional to the extent of the overlap. The second method employed CellProfiler to segment the PVM and BC in individual slices, and extract the intensity of BC that specifically overlaps the BC. The intensity values, extracted for each slice, were added over all the 3D stacks to generate a single value that represents the total fluorescence intensity of PVM on BC for the entire 3D volume of a given PVM. Both methods yielded consistent results (**Figures 2E,F**), showing that the PVM-BC associations are formed early during parasite development and expand over time, to mirror the growth pattern of the parasite development *in vivo*. The appositions at 48 hpi could be due to the PVM occupying up to 90% of hepatocyte volume so that such contacts are a consequence of the large parasite size. For this reason, we also quantified associations at 24 and 33 hpi, when both the infected cell size and the PVM size are not likely to be confounding factors. Our analysis at 24 hpi shows that, even at this time point, when the parasite is about the size of the hepatocyte nucleus, the PVM is in close proximity to the BC (denoted by non-zero values) and these associations increase considerably at 33 hpi (**Figures 2E,F**), suggesting that the PVM has a spatial preference within the infected cell as

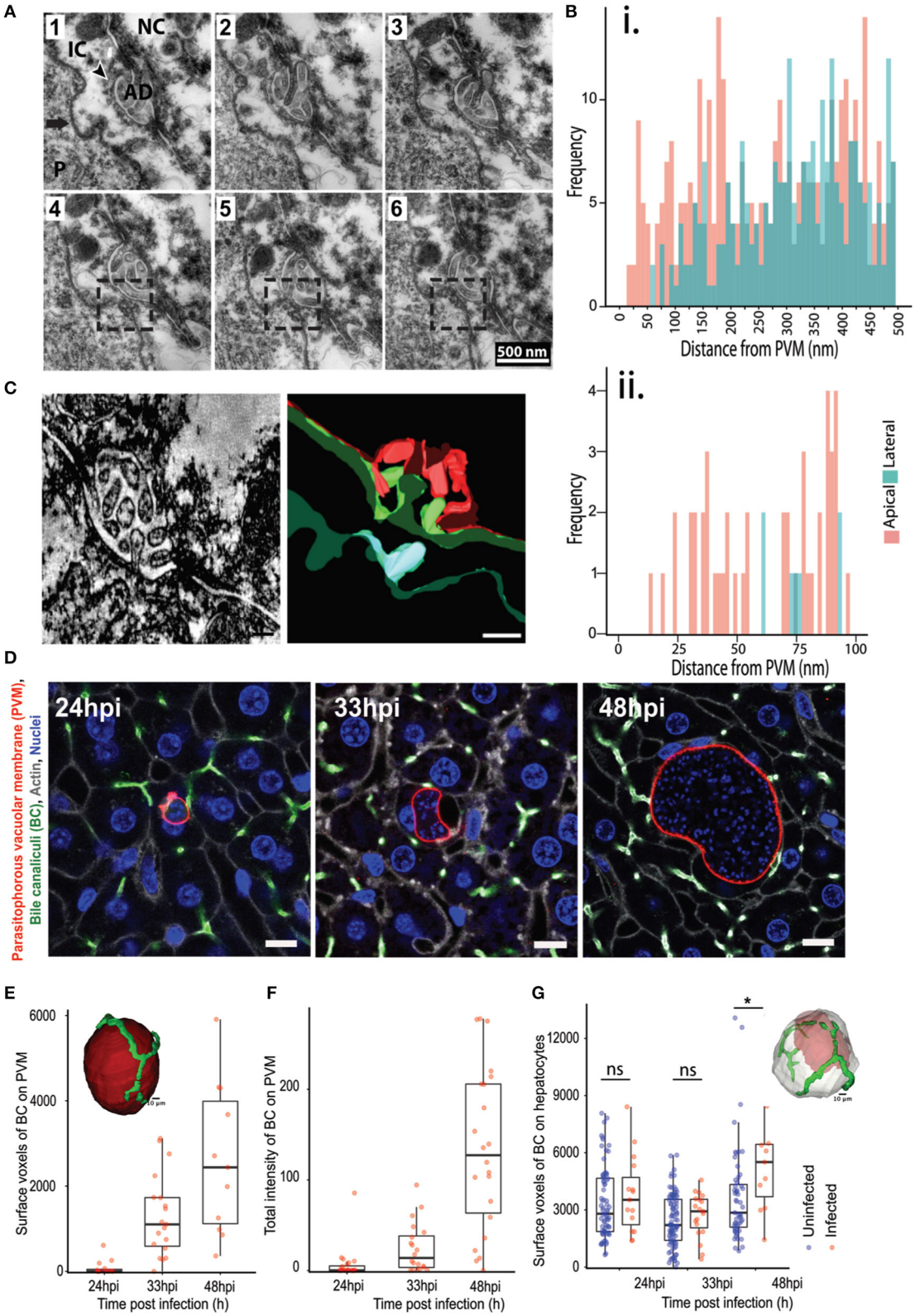

FIGURE 2 | Association of *P. berghei* with hepatocyte apical domains during liver stage development. **(A)** Serial EM sections showing the PVM in close proximity to the apical domains of the hepatocyte plasma membrane. The sections are 70 nm apart, with the boxed region highlighting the juxtaposition of the PVM with the apical

(Continued)

FIGURE 2 | region. The arrow points to the PVM, with the arrowhead showing the apical domain (AD). P indicates the parasite. **(B)** Quantification of the distance between the PVM and apical (pink) or basolateral (green) regions of the hepatocyte plasma membrane. Data is combined from distance measurements from at least five infected cells. (ii) highlights a region from (i) showing spatial proximity of the PVM to apical domains. **(C)** A section of a tomogram of the PVM associated with an apical region (left) and the corresponding reconstruction (right). The PVM is in cyan, the plasma membrane of the infected hepatocyte in green, and the plasma membrane of the adjacent non-infected hepatocyte in red. **(D)** Representative confocal images of infected liver sections at 24, 33, and 48 hpi, showing PVM (red), bile canaliculi (green), cell boundaries (gray), and nuclei (blue). The UIS4 and CD13 antibodies were used to mark the PVM and apical domains, respectively. The scale bar is 10 μm. **(E)** Quantification of surface voxels of the apical domain (CD13) on the PVM at different time points post infection. The inset figure shows the segmented model of apical domains (green) in proximity with the PVM (red). The scale bar is 10 μm. **(F)** Quantification of the total intensity of CD13 (apical domain/bile canaliculi marker) on the PVM at different time points post infection. The inset shows a schematic of the pipeline used for quantitative analysis. **(G)** Quantification of the alteration in hepatocyte polarity during *P. berghei* infection *in vivo*. Surface voxels of the apical domain on the infected hepatocyte surface in comparison with an uninfected hepatocyte at different time points post infection are shown. n.s and *denote *p* values that are non-significant and < 0.01 respectively, based on Student's *t*-test. The inset shows a model of 3D segmentation of an infected hepatocyte (gray) containing a parasite (red), with the apical domains (green).

the infection proceeds. We tested if the apical domain contact scales with the PVM volume using scatter plot analysis. The results (**Figure S5**) show a positive correlation at 33 hpi, but not at 24 or 48 hpi, suggesting that the apical domain contact scales with parasite volume during the expansion phase of the parasite. At 24 hpi it is likely that the contacts are starting to form and at 48 hpi, the correlation could be lost due to the large volume the parasite attains. Finally, we tested the specificity of the PVM-BC association by using the flow based method to assess the chances of a randomly placed sphere of volume equivalent to the PVM to form similar associations with the BC network (Supplementary Method, **Figure S6**). The results show that an inert bead randomly placed at a distance "r" from the BC network would be more likely to not intersect the BC network than to intersect it.

We then assessed whether the close association of the PVM with BC, together with the massive increase in the parasite and host cell volume, result in alterations in the apical domain organization around the infected cell. To this end, we quantified the total apical domain of the infected cells and compared it with that of the uninfected cells. In order to preclude any proximity effects on uninfected cells due to close positioning with infected cells, we selected uninfected cells at least two cell layers away from the infected cells for this analysis. Our data show that, at 48 hpi, there is a significant increase in the apical surface area of the infected cells compared to uninfected cells (**Figure 2G**). These changes may be due to the massive increase seen in the infected cell volume at this time point. Nevertheless, since apical domains from adjacent cells connect in 3D to form the bile canaliculi, this result suggests that localized alterations in the BC network geometry occurs during the liver stage of *Plasmodium* development.

Bile acids are secreted into bile canaliculi through transporters localized on the apical domains of hepatocytes and are transported through the bile canalicular network to eventually drain into the gallbladder (Turumin et al., 2013). We reasoned that alterations in bile canalicular network could impact this process and possibly reflect in the gallbladder bile acid levels. To test this, we measured bile acid levels in the gallbladder during the liver stage of infection. Surprisingly, we found that the bile acid levels are significantly higher in infected mice than in uninfected controls (**Figure 3**). Moreover, bile acid levels increased with increasing dose of sporozoites injected, correlating with the ensuing hepatic parasite burden at 40 hpi

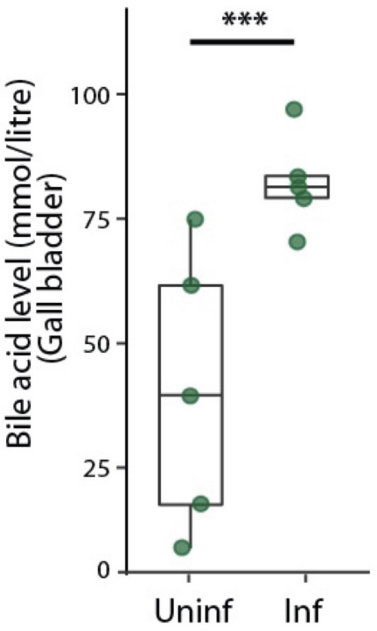

FIGURE 3 | Infected mice show higher levels of bile acid levels in the gallbladder. Total bile acid levels in gallbladders of *P. berghei*-infected and uninfected mice at 48 hpi. Result representative of two biological replicates. ***denotes $p < 0.001$ from Student's *t*-test.

(**Figure S7**). Since biliary secretion is a major function of liver that requires hepatocyte polarization, this result suggest that Plasmodium liver stage infections impact liver function, possibly by impacting the apical domain organization.

Next, we explored the relevance of the localized alteration in apical domain organization for *Plasmodium* development in the liver. The AMPK pathway is a key regulator of tight junction formation and apical trafficking, thereby influencing apical domain organization and hepatocyte polarity (Treyer and Musch, 2013; Musch, 2014; Gissen and Arias, 2015). Hence, we wondered whether pharmacological modulation of the AMPK pathway would alter bile canalicular geometry *in vivo*. To evaluate this, mice were treated with a well-known AMPK modulator, salicylate (Hawley et al., 2012), and 100 μm-thick liver sections were collected from both salicylate-treated and

untreated control mice, and stained for the bile canalicular marker, CD13. The bile canalicular network was then imaged at isometric voxels at 0.5 μm resolution. The images were segmented in 3D using intensity-based thresholding as well as automated flow-based methods (**Movies S4A, S4B**, **Figure 4A**), and the total length of the BC network was calculated for the salicylate-treated and untreated conditions. The result shows significant alterations in the bile canalicular network upon salicylate treatment (**Figure 4B**), confirming that BC geometry is indeed altered *in vivo* upon AMPK activation. We next assessed the effect of pharmacological activation of AMPK on *P. berghei* hepatic development *in vivo*. To this end, parasite size in the livers of salicylate-treated and untreated control mice was quantified at 24, 33, and 48 hpi. While no significant differences in parasite volume were observed upon salicylate treatment at 24 and 33 hpi (**Figure 4C**), parasite growth was significantly attenuated in salicylate-treated mouse livers at 48 hpi (**Figure S8**), in agreement with a previous report (Ruivo et al., 2016). This suggests that salicylate treatment does not have an effect on the initial growth phase of the parasite but impacts its subsequent rapid expansion phase. Our data (**Figures 2E,F**) shows that the association of PVM with the BC mirrors the parasite growth dynamics *in vivo*. Since the parasite volume is not affected up to 33 hpi upon salicylate treatment but is arrested at 48 hpi, we hypothesized that salicylate-mediated global alteration in BC geometry locally affects the PVM contact with the apical domain in the infected cell. Since the salicylate-mediated alteration in BC geometry is global, whereas parasite-mediated alteration is localized to the infected cells, we also reasoned that the apical domain fraction of hepatocytes would not be altered upon salicylate treatment, i.e., the perturbation would specifically affect the PVM-BC association. In order to assess this, we analyzed the voxels of apical domains juxtaposed with the surface of hepatocytes, as well as with the PVM, in sections from infected animals treated or not with salicylate. The results show that salicylate treatment does not result in a relative alteration of the apical domain organization on the hepatocyte surface in infected or uninfected cells (**Figure 4D**). In contrast, salicylate treatment significantly decreases the contact of the apical domain with the PVM at 33 hpi, as shown by the reduced surface voxels of CD13 on the PVM (**Figure 4E**), indicating that the contact between the apical domain and the PVM is decreased during AMPK activation. In view of these results, we propose that the salicylate-mediated reduction in the contact of the PVM with the hepatocyte apical domain contributes to the arrest of parasite growth *in vivo*.

DISCUSSION

The data presented in this manuscript suggests that in infected liver tissues, *Plasmodium* parasites associate with the apical domain of hepatocytes and influence the bile canalicular geometry around the infected cells, alterations that may impact liver function. Modulation of bile canalicular organization by pharmacological activation of AMPK results in abrogation of the localized PVM-BC apposition, and correlate with a significant reduction in the parasite development (**Figure 5**). Our results provide the first report of the involvement of the hepatocyte apical domain and bile canaliculi organization, crucial components of hepatocyte polarity, in the development of *P. berghei* parasites. Further studies will be needed to confirm these findings in human *Plasmodium* infections.

Hepatocytes have a complex and unique polarity that is central to their function (Elias, 1949; Arias et al., 1993; Treyer and Musch, 2013; Musch, 2014; Gissen and Arias, 2015). A major component of hepatocyte polarity is the organization of the apical domains. Our EM observations show a preferential association of PVM with the apical domains at 48 hpi. These results are further confirmed by high resolution fluorescence imaging in 3D at 48 hpi, as well as at earlier time points where the parasite size is not a confounding factor. Our analysis in 3D using two independent methods validate the preferential association of PVM with the apical domains of the hepatocyte. In order to establish a functional link for this association, further studies aimed at detecting features of functional contact sites such as tethering or lack of fusion, or at identifying the proteome/lipidome of the contact site are required.

It is well-known that the hepatocyte's apical domain has higher cholesterol, phospholipids and sphingomyelin content than the basolateral membrane (Meier et al., 1984; Godoy et al., 2013). Apical membranes are also highly convoluted, hence offering more membrane surface per unit volume. Hence it is tempting to speculate that the apical membrane is a potential source for membranes/lipids employed by the parasite during its rapid expansion phase in the liver. Additionally, apposition with the apical domain could provide the parasite with access to the extracellular environment and, possibly, to additional sources of nutrients. Indeed, phosphatidylcholine, one of the major phospholipids required for parasite survival in liver (Itoe et al., 2014), is actively transported to the bile canaliculi through the transporters present specifically in the apical domains (Gissen and Arias, 2015). Alternatively, the parasite could manipulate the trafficking of specific transporters such as an apical domain bound PC transporter to access such polarized nutrients. A comprehensive characterization of host proteins on the PVM will be important to address such questions.

The gallbladder is a crucial component of the entero-hepatic system which stores the biliary secretions from liver. Hepatocyte polarity is central to the biliary secretion of liver, since bile acids are absorbed from the sinusoids through the basal side of hepatocytes and secreted into the bile canaliculi on the apical side (Reshetnyak, 2013; Gissen and Arias, 2015). The etiology of the increased gall bladder bile acid levels during the liver stage of *Plasmodium* infection is therefore complex. Alterations in bile canalicular geometry could influence BC contractions and bile acid transport activity, which, in turn influence bile transport and clearance to the gall bladder (Layden and Boyer, 1978; Baumgartner et al., 1986, 1987; Morales-Navarrete et al., 2015; Sharanek et al., 2016). Pharmacological modulation of bile canalicular geometry indeed alters the bile flow/velocity along the central vein—portal vein axis (Meyer et al., 2017). In support of this, alterations in bile canalicular geometry and contractility during drug-induced cholestasis (Sharanek et al., 2016) correlate with increased levels of bile acids (Fattinger et al.,

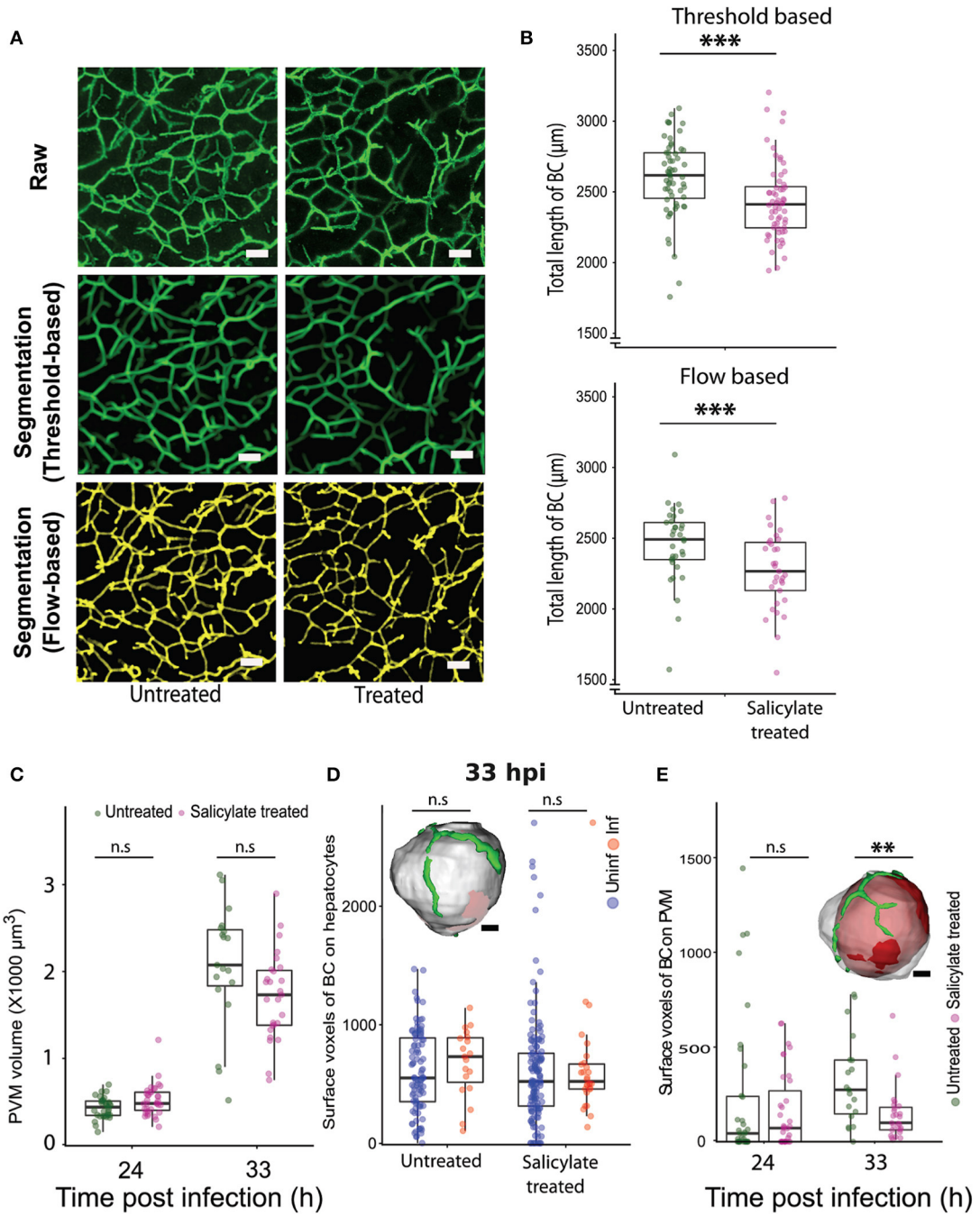

FIGURE 4 | Pharmacological modulation of hepatocyte polarity *in vivo* arrests *P. berghei* development in liver tissues. **(A)** Representative images of maximum intensity projections of liver sections from untreated and salicylate-treated mice, stained with the apical domain marker CD13. One hundred µm thick liver sections were imaged with a voxel size of 0.5 μm^3. The scale bar is 10 µm. The top panel shows the raw image, the middle panel shows segmentation based on thresholding and the lower panel shows segmentation using an automated flow based method. **(B)** Quantification of total length of bile canaliculi (BC) between untreated and Salicylate treated mice. The top and bottom panels show quantifications from threshold based and flow based segmentation, respectively. **(C)** PVM volume changes upon salicylate treatment at 24 and 33 hpi. n.s. denotes the differences between treated and untreated conditions that are not statistically significant at these time points. **(D)** A comparison of surface voxels of bile canaliculi (BC) on hepatocytes between uninfected and infected hepatocytes, with and without salicylate treatment. The inset shows a representative segmented model of infected hepatocyte (gray) and bile canaliculi (green). The scale bar is 10 µm. n.s denotes the differences are not statistically significant. **(E)** Surface voxels of bile canaliculi on the PVM between Salicylate treated and untreated conditions. The inset shows a representative segmented model of PVM (red) within an infected hepatocyte (gray) with surrounding bile canaliculi (green). The scale bar is 10 µm. **(A–E)** Are representative of two biological replicates, n.s. denotes the differences are not statistically significant, ** and ***denote $p < 0.01$ and < 0.001, respectively. Statistical significance is assessed using Student's *t*-test.

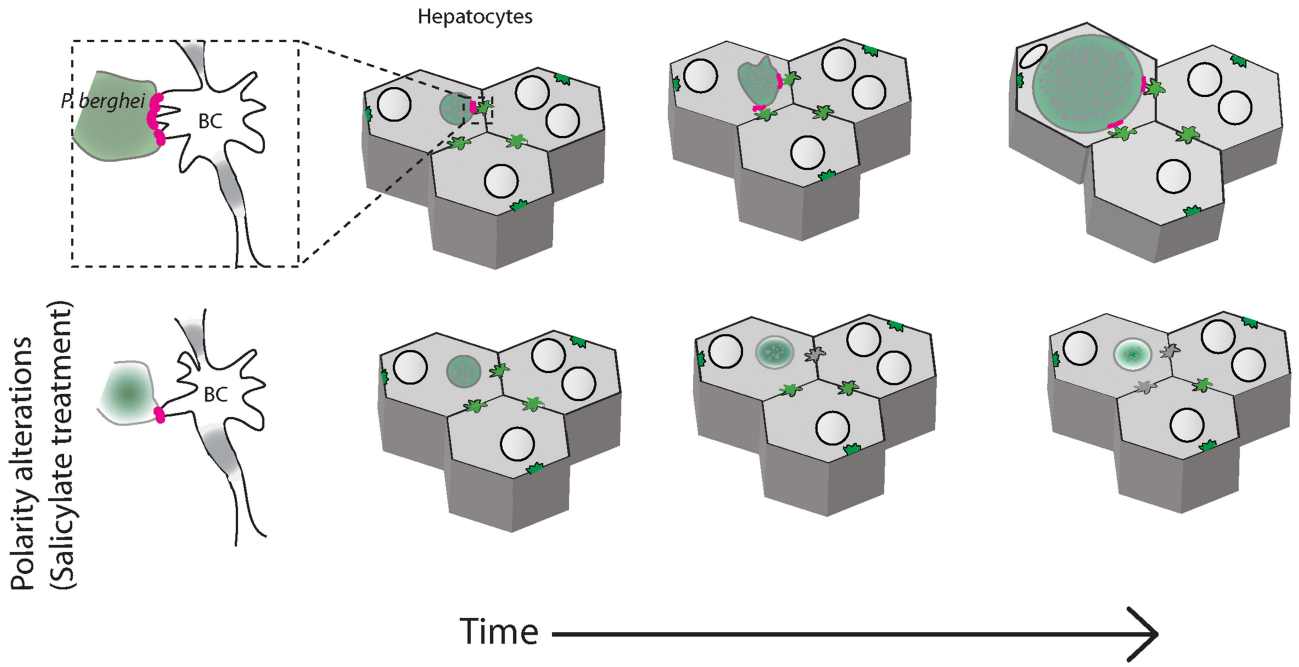

FIGURE 5 | Schematic of *P. berghei* interacting with the apical domains of hepatocytes during liver stage development in the liver tissue. *Plasmodium berghei* (green) development within hepatocytes (gray) requires interaction of the parasite vacuole membrane with the hepatocyte apical domain, or bile canaliculi (BC). When hepatocyte polarity is altered by salicylate treatment, the interaction is reduced and the parasite growth is arrested (bottom panels).

2001), while, in turn, bile acids promote hepatocyte polarity (Fu et al., 2010, 2011a,b). The dose dependency of bile acid levels with increasing parasite load suggests a possible cumulative effect resulting from several localized alterations around the sites of individual infected cells. Detailed investigations on the localization of different bile acid transporters during Plasmodium infections could shed further light into the mechanisms involved.

Pharmacological manipulation of bile canalicular geometry by well-tolerated drugs like salicylate, as reported here, opens up the possibility of controlled manipulation of polarity. The effect of AMPK on polarity is documented in different contexts, including Drosophila, neurons and polarized cell lines (Shackelford and Shaw, 2009). In a collagen sandwich model for polarized hepatocytes, AMPK activation results in acceleration of bile canalicular formation (Fu et al., 2010), through mechanisms that are not well-characterized (Gissen and Arias, 2015). Here, we show that in adult liver tissues, salicylate, a well-known AMPK modulator, alters the geometry of the bile canaliculi, with a concomitant decrease in the BC association with the PVM and the arrest of parasite growth. However, potential off-target and pleiotropic effects of salicylate cannot be ruled out entirely. It will be important to evaluate whether other well-known AMPK activators, including widely used drugs like metformin, show similar effects on AMPK modulation, hepatocyte polarity, and parasite development *in vivo*.

The idea of targeting the host to tackle infectious diseases, including malaria, has gained significant traction in recent years (Collier et al., 2013; Zumla et al., 2016; Glennon et al., 2018). Our results provide an example of a host process that is amenable to therapeutic intervention against malaria. Pharmacological modulation of hepatocyte polarity by well-tolerated widely used drugs might fast track approaches to host-directed prophylactic therapeutics. Hepatic dysfunction is strongly associated with malaria (Reuling et al., 2018), with a significant number of malaria patients showing impaired liver functions including hyperbilirubinemia, and jaundice (Joshi et al., 1986; Kaeley et al., 2017). While the pathological basis of hepatic dysfunction during malaria is not clear, drug-induced hepatotoxicity and clearance of infected RBC's have been proposed to play major roles in hepatic pathology (Reuling et al., 2018). Our results suggest that primary modulation of hepatocyte function during liver stage infection could have a direct but subtle effect on liver function. The contribution of these liver stage-specific alterations to the overall hepatic dysfunction observed during malaria remains to be determined.

DATA AVAILABILITY STATEMENT

The datasets generated for this study are available on request to the corresponding author.

ETHICS STATEMENT

The animal study was reviewed and approved by Animal ethics committee at Instituto de Medicina Molecular, Lisbon.

AUTHOR CONTRIBUTIONS

LB, TS, SD, and KS were responsible for image analysis algorithms and performing analysis. VZ-L, VS, DM, AA, HR-P, and CR worked on animal infections, experimentation, image acquisition, and analysis. DM, TF, and JM worked on electron microscopy, sample preparation, and imaging. MP, MM, VZ-L, and VS conceptualized the study and edited the manuscript. VS was responsible for the study direction, funding, and manuscript draft.

FUNDING

This study was funded by core funds from TIFR-NCBS and Max Planck Partner Group (VS). LB was a recipient of a SERB N-PDF and Max Planck Mobility fellowship.

ACKNOWLEDGMENTS

We thank Christian Tischer (EMBL, Heidelberg) for advice with image analysis, Michaela Wilsch-Brauninger (MPI-CBG, Dresden) for advise with EM; Arjun Guha (inStem, Bangalore) for critical reading of the manuscript; Gopal Das, Shadab Nizam, and Maruthi Mulaka for help with imaging, and Vanda Marques and Maria Elisa Alves for help with bile acid analysis. We acknowledge the Central Imaging and Flow Cytometry (CIFF) facility in NCBS for their support.

SUPPLEMENTARY MATERIAL

The Supplementary Material for this article can be found online at: https://www.frontiersin.org/articles/10.3389/fcimb.2019.00451/full#supplementary-material

REFERENCES

Agop-Nersesian, C., Niklaus, L., Wacker, R., and Theo Heussler, V. (2018). Host cell cytosolic immune response during Plasmodium liver stage development. *FEMS Microbiol. Rev.* 42, 324–334. doi: 10.1093/femsre/fuy007

Arias, I. M., Che, M., Gatmaitan, Z., Leveille, C., Nishida, T., and St Pierre, M. (1993). The biology of the bile canaliculus, 1993. *Hepatology* 17, 318–329. doi: 10.1002/hep.1840170225

Bano, N., Romano, J. D., Jayabalasingham, B., and Coppens, I. (2007). Cellular interactions of Plasmodium liver stage with its host mammalian cell. *Int. J. Parasitol.* 37, 1329–1341. doi: 10.1016/j.ijpara.2007.04.005

Baumgartner, U., Miyai, K., and Hardison, W. G. (1986). Greater taurodeoxycholate biotransformation during backward perfusion of rat liver. *Am. J. Physiol.* 251(4 Pt 1), G431–435. doi: 10.1152/ajpgi.1986.251.4.G431

Baumgartner, U., Miyai, K., and Hardison, W. G. (1987). Modulation of hepatic biotransformation and biliary excretion of bile acid by age and sinusoidal bile acid load. *Am. J. Physiol.* 252(1 Pt 1), G114–119. doi: 10.1152/ajpgi.1987.252.1.G114

Carpenter, A. E., Jones, T. R., Lamprecht, M. R., Clarke, C., Kang, I. H., Friman, O., et al. (2006). CellProfiler: image analysis software for identifying and quantifying cell phenotypes. *Genome Biol.* 7:R100. doi: 10.1186/gb-2006-7-10-r100

Collier, M. A., Gallovic, M. D., Peine, K. J., Duong, A. D., Bachelder, E. M., Gunn, J. S., et al. (2013). Delivery of host cell-directed therapeutics for intracellular pathogen clearance. *Exp. Rev. Anti. Infect. Ther.* 11, 1225–1235. doi: 10.1586/14787210.2013.845524

Coppens, I. (2017). How Toxoplasma and malaria parasites defy first, then exploit host autophagic and endocytic pathways for growth. *Curr. Opin. Microbiol.* 40, 32–39. doi: 10.1016/j.mib.2017.10.009

Elias, H. (1949). A re-examination of the structure of the mammalian liver; the hepatic lobule and its relation to the vascular and biliary systems. *Am. J. Anat.* 85, 379–456. doi: 10.1002/aja.1000850303

Evans, R. J., Sundaramurthy, V., and Frickel, E. M. (2018). The interplay of host autophagy and eukaryotic pathogens. *Front. Cell Dev. Biol.* 6:118. doi: 10.3389/fcell.2018.00118

Fattinger, K., Funk, C., Pantze, M., Weber, C., Reichen, J., Stieger, B., et al. (2001). The endothelin antagonist bosentan inhibits the canalicular bile salt export pump: a potential mechanism for hepatic adverse reactions. *Clin. Pharmacol. Ther.* 69, 223–231. doi: 10.1067/mcp.2001.114667

Fu, D., Lippincott-Schwartz, J., and Arias, I. M. (2011a). Cellular mechanism of bile acid-accelerated hepatocyte polarity. *Small GTPases* 2, 314–317. doi: 10.4161/sgtp.18087

Fu, D., Wakabayashi, Y., Ido, Y., Lippincott-Schwartz, J., and Arias, I. M. (2010). Regulation of bile canalicular network formation and maintenance by AMP-activated protein kinase and LKB1. *J. Cell Sci.* 123(Pt 19), 3294–3302. doi: 10.1242/jcs.068098

Fu, D., Wakabayashi, Y., Lippincott-Schwartz, J., and Arias, I. M. (2011b). Bile acid stimulates hepatocyte polarization through a cAMP-Epac-MEK-LKB1-AMPK pathway. *Proc. Natl. Acad. Sci. U.S.A.* 108, 1403–1408. doi: 10.1073/pnas.1018376108

Gissen, P., and Arias, I. M. (2015). Structural and functional hepatocyte polarity and liver disease. *J. Hepatol.* 63, 1023–1037. doi: 10.1016/j.jhep.2015.06.015

Glennon, E. K. K., Dankwa, S., Smith, J. D., and Kaushansky, A. (2018). Opportunities for host-targeted therapies for Malaria. *Trends Parasitol.* 34, 843–860. doi: 10.1016/j.pt.2018.07.011

Godoy, P., Hewitt, N. J., Albrecht, U., Andersen, M. E., Ansari, N., Bhattacharya, S., et al. (2013). Recent advances in 2D and 3D in vitro systems using primary hepatocytes, alternative hepatocyte sources and non-parenchymal liver cells and their use in investigating mechanisms of hepatotoxicity, cell signaling and ADME. *Arch. Toxicol.* 87, 1315–1530. doi: 10.1007/s00204-013-1078-5

Goldblatt, P. J., and Gunning, W. T. 3rd (1984). Ultrastructure of the liver and biliary tract in health and disease. *Ann. Clin. Lab. Sci.* 14, 159–167.

Hawley, S. A., Fullerton, M. D., Ross, F. A., Schertzer, J. D., Chevtzoff, C., Walker, K. J., et al. (2012). The ancient drug salicylate directly activates AMP-activated protein kinase. *Science* 336, 918–922. doi: 10.1126/science.1215327

Itoe, M. A., Sampaio, J. L., Cabal, G. G., Real, E., Zuzarte-Luis, V., March, S., et al. (2014). Host cell phosphatidylcholine is a key mediator of malaria parasite survival during liver stage infection. *Cell Host Microbe* 16, 778–786. doi: 10.1016/j.chom.2014.11.006

Joshi, Y. K., Tandon, B. N., Acharya, S. K., Babu, S., and Tandon, M. (1986). Acute hepatic failure due to *Plasmodium falciparum* liver injury. *Liver* 6, 357–360. doi: 10.1111/j.1600-0676.1986.tb00304.x

Kaeley, N., Ahmad, S., Shirazi, N., Bhatia, R., Bhat, N. K., Srivastava, S., et al. (2017). Malarial hepatopathy: a 6-year retrospective observational study from Uttarakhand, North India. *Trans. R Soc. Trop. Med. Hyg.* 111, 220–225. doi: 10.1093/trstmh/trx042

Kamentsky, L., Jones, T. R., Fraser, A., Bray, M. A., Logan, D. J., Madden, K. L., et al. (2011). Improved structure, function and compatibility for CellProfiler: modular high-throughput image analysis software. *Bioinformatics* 27, 1179–1180. doi: 10.1093/bioinformatics/btr095

Ke, M. T., Fujimoto, S., and Imai, T. (2013). SeeDB: a simple and morphology-preserving optical clearing agent for neuronal circuit reconstruction. *Nat. Neurosci.* 16, 1154–1161. doi: 10.1038/nn.3447

Kremer, J. R., Mastronarde, D. N., and McIntosh, J. R. (1996). Computer visualization of three-dimensional image data using IMOD. *J. Struct. Biol.* 116, 71–76. doi: 10.1006/jsbi.1996.0013

Lamprecht, M. R., Sabatini, D. M., and Carpenter, A. E. (2007). CellProfiler: free, versatile software for automated biological image analysis. *Biotechniques* 42, 71–75. doi: 10.2144/000112257

Layden, T. J., and Boyer, J. L. (1978). Influence of bile acids on bile canalicular membrane morphology and the lobular gradient in canalicular size. *Lab. Invest.* 39, 110–119.

Lopes da Silva, M., Thieleke-Matos, C., Cabrita-Santos, L., Ramalho, J. S., Wavre-Shapton, S. T., Futter, C. E., et al. (2012). The host endocytic pathway is essential for Plasmodium berghei late liver stage development. *Traffic* 13, 1351–1363. doi: 10.1111/j.1600-0854.2012.01398.x

Mastronarde, D. N. (1997). Dual-axis tomography: an approach with alignment methods that preserve resolution. *J. Struct. Biol.* 120, 343–352. doi: 10.1006/jsbi.1997.3919

Mastronarde, D. N. (2005). Automated electron microscope tomography using robust prediction of specimen movements. *J. Struct. Biol.* 152, 36–51. doi: 10.1016/j.jsb.2005.07.007

Meier, P. J., Sztul, E. S., Reuben, A., and Boyer, J. L. (1984). Structural and functional polarity of canalicular and basolateral plasma membrane vesicles isolated in high yield from rat liver. *J. Cell Biol.* 98, 991–1000. doi: 10.1083/jcb.98.3.991

Meis, J. F., Verhave, J. P., Jap, P. H., Hess, F., and Meuwissen, J. H. (1981). An ultrastructural study of developing stages of exo-erythrocytic *Plasmodium berghei* in rat hepatocytes. *Parasitology* 82(Pt 2), 195–204. doi: 10.1017/S0031182000056936

Meis, J. F., Verhave, J. P., Jap, P. H., Sinden, R. E., and Meuwissen, J. H. (1983a). Malaria parasites–discovery of the early liver form. *Nature* 302, 424–426. doi: 10.1038/302424a0

Meis, J. F., Verhave, J. P., Jap, P. H., Sinden, R. E., and Meuwissen, J. H. (1983b). Ultrastructural observations on the infection of rat liver by *Plasmodium berghei* sporozoites *in vivo*. *J. Protozool.* 30, 361–366. doi: 10.1111/j.1550-7408.1983.tb02931.x

Meyer, K., Ostrenko, O., Bourantas, G., Morales-Navarrete, H., Porat-Shliom, N., Segovia-Miranda, F., et al. (2017). A predictive 3D multi-scale model of biliary fluid dynamics in the liver lobule. *Cell Syst.* 4, 277–90.e279. doi: 10.1016/j.cels.2017.02.008

Morales-Navarrete, H., Segovia-Miranda, F., Klukowski, P., Meyer, K., Nonaka, H., Marsico, G., et al. (2015). A versatile pipeline for the multi-scale digital reconstruction and quantitative analysis of 3D tissue architecture. *Elife* 4:e11214. doi: 10.7554/eLife.11214.039

Musch, A. (2014). The unique polarity phenotype of hepatocytes. *Exp. Cell Res.* 328, 276–283. doi: 10.1016/j.yexcr.2014.06.006

Nyboer, B., Heiss, K., Mueller, A. K., and Ingmundson, A. (2018). The Plasmodium liver-stage parasitophorous vacuole: a front-line of communication between parasite and host. *Int. J. Med. Microbiol.* 308, 107–117. doi: 10.1016/j.ijmm.2017.09.008

Prudencio, M., Rodriguez, A., and Mota, M. M. (2006). The silent path to thousands of merozoites: the Plasmodium liver stage. *Nat. Rev. Microbiol.* 4, 849–856. doi: 10.1038/nrmicro1529

Reshetnyak, V. I. (2013). Physiological and molecular biochemical mechanisms of bile formation. *World J. Gastroenterol.* 19, 7341–7360. doi: 10.3748/wjg.v19.i42.7341

Reuling, I. J., de Jong, G. M., Yap, X. Z., Asghar, M., Walk, J., van de Schans, L. A., et al. (2018). Liver injury in uncomplicated malaria is an overlooked phenomenon: an observational study. *EBio Med.* 36, 131–139. doi: 10.1016/j.ebiom.2018.09.018

Ruivo, M. T. G., Vera, I. M., Sales-Dias, J., Meireles, P., Gural, N., Bhatia, S. N., et al. (2016). Host AMPK is a modulator of plasmodium liver infection. *Cell Rep.* 16, 2539–2545. doi: 10.1016/j.celrep.2016.08.001

Schindelin, J., Arganda-Carreras, I., Frise, E., Kaynig, V., Longair, M., Pietzsch, T., et al. (2012). Fiji: an open-source platform for biological-image analysis. *Nat Methods* 9, 676–682. doi: 10.1038/nmeth.2019

Shackelford, D. B., and Shaw, R. J. (2009). The LKB1-AMPK pathway: metabolism and growth control in tumour suppression. *Nat. Rev. Cancer* 9, 563–575. doi: 10.1038/nrc2676

Sharanek, A., Burban, A., Burbank, M., Le Guevel, R., Li, R., Guillouzo, A., et al. (2016). Rho-kinase/myosin light chain kinase pathway plays a key role in the impairment of bile canaliculi dynamics induced by cholestatic drugs. *Sci. Rep.* 6:24709. doi: 10.1038/srep24709

Shin, S. C., Vanderberg, J. P., and Terzakis, J. A. (1982). Direct infection of hepatocytes by sporozoites of *Plasmodium berghei*. *J. Protozool.* 29, 448–454. doi: 10.1111/j.1550-7408.1982.tb05431.x

Thieleke-Matos, C., Lopes da Silva, M., Cabrita-Santos, L., Portal, M. D., Rodrigues, I. P., Zuzarte-Luis, V., et al. (2016). Host cell autophagy contributes to Plasmodium liver development. *Cell Microbiol.* 18, 437–450. doi: 10.1111/cmi.12524

Treyer, A., and Musch, A. (2013). Hepatocyte polarity. *Compr. Physiol.* 3, 243–287. doi: 10.1002/cphy.c120009

Turumin, J. L., Shanturov, V. A., and Turumina, H. E. (2013). The role of the gallbladder in humans. *Rev. Gastroenterol. Mex.* 78, 177–187. doi: 10.1016/j.rgmx.2013.02.003

Vasilevskiy, A., and Siddiqi, K. (2002). Flux-maximizing geometric flows. *IEEE Transac. Pattern Anal. Mach. Intell.* 24, 1565–1578. doi: 10.1109/TPAMI.2002.1114849

Vaughan, A. M., and Kappe, S. H. I. (2017). Malaria parasite liver infection and exoerythrocytic biology. *Cold Spring Harb. Perspect Med.* 7:a025486. doi: 10.1101/cshperspect.a025486

Zeigerer, A., Gilleron, J., Bogorad, R. L., Marsico, G., Nonaka, H., Seifert, S., et al. (2012). Rab5 is necessary for the biogenesis of the endolysosomal system *in vivo*. *Nature* 485, 465–470. doi: 10.1038/nature11133

Zumla, A., Rao, M., Wallis, R. S., Kaufmann, S. H., Rustomjee, R., Mwaba, P., et al. (2016). Host-directed therapies for infectious diseases: current status, recent progress, and future prospects. *Lancet Infect. Dis.* 16:e47–63. doi: 10.1016/S1473-3099(16)00078-5

Conflict of Interest: The authors declare that the research was conducted in the absence of any commercial or financial relationships that could be construed as a potential conflict of interest.

The reviewer GF declared a past collaboration with one of the authors MP to the handling editor.

Copyright © 2020 Balasubramanian, Zuzarte-Luís, Syed, Mullick, Deb, Ranga-Prasad, Meissner, Almeida, Furstenhaupt, Siddiqi, Prudêncio, Rodrigues, Mota and Sundaramurthy. This is an open-access article distributed under the terms of the Creative Commons Attribution License (CC BY). The use, distribution or reproduction in other forums is permitted, provided the original author(s) and the copyright owner(s) are credited and that the original publication in this journal is cited, in accordance with accepted academic practice. No use, distribution or reproduction is permitted which does not comply with these terms.

frontiers in Cellular and Infection Microbiology

ORIGINAL RESEARCH
published: 29 January 2020
doi: 10.3389/fcimb.2020.00008

Kupffer Cells: Important Participant of Hepatic Alveolar Echinococcosis

Yumei Liu[1†], Fengming Tian[1†], Jiaoyu Shan[2], Jian Gao[2], Bin Li[1], Jie Lv[1], Xuan Zhou[1], Xuanlin Cai[2], Hao Wen[1] and Xiumin Ma[1,2]*

[1] State Key Laboratory of Pathogenesis, Prevention and Treatment of High Incidence Diseases in Central Asia, Clinical Medical Research Institute, First Affiliated Hospital of Xinjiang Medical University, Urumqi, China, [2] College of Basic Medicine of Xinjiang Medical University, Urumqi, China

Aims: Kupffer cells (KCs) are the liver-resident macrophages and play a leading role in the regulation of liver homeostasis in physiological conditions and in pathology. The study aims to investigate the anti-echinococcosis effect of KCs and the effects of hepatic stellate cells (HSCs) activation in the progression of liver fibrosis in hepatic alveolar echinococcosis (hepatic AE).

Methods: Hematoxylin—eosin (H&E) and Masson staining were used to assess the pathological inflammatory changes and collagen deposition, respectively. Immunohistochemistry and qRT-PCR were used to detect the number of aggregates of KCs, the expression of cytokines and activation of HSCs.

Results: In the close group, H&E staining showed that the normal lobular structure was destroyed and inflammatory infiltration around the lesion could be observed, and Masson staining showed that blue collagen fibers were clearly deposited near the portal area. IHC showed that KCs surface markers CD68 and CD163, cytokine iNOS and Arg-1 were positively expressed in the vicinity of inflammatory lesions. qRT-PCR indicated that TNF-α, IL-10, and TGF-β1 secreted by KCs were significantly higher than those in the distance group ($P < 0.01$). It is worth noticing that the expression levels of anti-inflammatory cytokines were slightly higher than that of pro-inflammatory cytokines. Both IHC and qRT-PCR results showed that HSCs activation markers, the expression of α-SMA and Desmin significantly increased.

Conclusions: Our research indicates that KCs have immune-protective effect of anti-echinococcosis and promote liver fiber repair, and it also suggests that they have potential therapeutic value for patients with hepatic AE.

Keywords: hepatic alveolar echinococcosis, liver fibrosis, KCs, HSCs, cytokine

OPEN ACCESS

Edited by:
Sigrun Lange,
University of Westminster,
United Kingdom

Reviewed by:
Yong He,
National Institutes of Health (NIH),
United States
Shanna Bitencourt,
Universidade do Vale do Taquari—Univates, Brazil

***Correspondence:**
Xiumin Ma
maxiumin1210@sohu.com

† These authors have contributed equally to this work

Specialty section:
This article was submitted to Parasite and Host, a section of the journal Frontiers in Cellular and Infection Microbiology

Received: *01 November 2019*
Accepted: *09 January 2020*
Published: *29 January 2020*

Citation:
Liu Y, Tian F, Shan J, Gao J, Li B, Lv J, Zhou X, Cai X, Wen H and Ma X (2020) Kupffer Cells: Important Participant of Hepatic Alveolar Echinococcosis. Front. Cell. Infect. Microbiol. 10:8. doi: 10.3389/fcimb.2020.00008

INTRODUCTION

Alveolar echinococcosis (AE), caused by *Echinococcus multilocularis.* is characterized by a large multilocular cyst with a jelly-like substance, instead of clear hydatid fluid. As most cases involve the liver, patients may suffer from hepatomegaly and recurrent jaundice (Menghi et al., 2017). Cysts localize first in the liver, and in the early stages, the infection is generally asymptomatic (Arrechea Irigoyen et al., 2008). As the growth pattern of the cyst is similar to a malignant tumor, the WHO has proposed that a clinical classification that is similar to TNM (Tumor, Node,

Metastases) classification of tumors. Such classification is a necessary tool when making therapeutic decisions for the treatment of this disease (Kern et al., 2006). AE is a serious life-threatening chronic helminthiasis caused by *E. multilocularis*. It mostly occurs in the liver and is known to be slowly progressive but often, a fatal disease. It is estimated that nearly 2 billion people worldwide are infected with worms (Hotez et al., 2008) and about 200 million cases are *echinococcosis*, of which, 0.3% are caused by AE (Craig et al., 2017). Some experimental studies, including experimental studies on infected mice and immunological studies on AE patients, have revealed that complex host-parasite interaction occurs in the process of *E. multilocularis* infection (Wang and Gottstein, 2016). The variability and severity of the clinical manifestations of this parasitic disease are related to the duration and degree of infection (Mezioug and Touil-Boukoffa, 2012).

Liver fibrosis is one of the main pathological changes in the progression of hepatic AE. When acute liver injury occurs, the accumulation of extracellular matrix (ECM) secreted by fibroblasts is a normal feature of wound healing during acute inflammation. However, under most chronic or persistent inflammatory injuries, such as alcoholic hepatitis, viral hepatitis, autoimmune liver disease, and parasitic diseases, this mechanism of liver tissue repair is abnormally regulated and leads to irreversible fibrosis, even eventually develops into cirrhosis and liver cancer.

The inflammatory stimulation of *E. multilocularis*, an invader of the liver environment, promotes the activation and proliferation of a large number of Kupffer cells (KCs). KCs are specialized macrophages that reside in the liver and belong to the mononuclear phagocyte system. In addition to the phagocytic capacity, they can immediately respond to non-specific defense responses and have the ability to recruit other immune cells. These cells are highly malleable and can be altered according to changes in the microenvironment of the liver, both in morphology and function (Tacke and Zimmermann, 2014; Wynn and Vannella, 2016). In acute hepatic inflammatory injury, KCs release the pro-inflammatory cytokine inducible nitric oxide synthase (iNOS) through direct contact between cells and hepatocytes, and then release NO to effectively kill pathogens (Elchaninov et al., 2019). In order to limit the continuous stimulation of *E. multilocularis* and protect the stability of the liver environment, KCs secrete a large amount of profibrogenic cytokine transforming growth factor-β1 (TGF-β1), to promote the activation and proliferation of hepatic stellate cells (HSCs), a marker of liver fibrosis activation and leading to the occurrence and development of liver fibrosis (Lee and Friedman, 2011; Tosello-Trampont et al., 2011; Beljaars et al., 2014; Sica et al., 2014). In turn, HSCs further promote the proliferation and differentiation of KCs through paracrine effects. When patients with hepatic AE show clinical symptoms, most of them are in the middle or late stages of the disease, often accompanied with liver fibrosis and it is irreversible. Therefore, in the middle or late stages of tissue repair, KCs highly express anti-inflammatory surface marker CD163, upregulate the secretion of cytokine Interleukin-10 (IL-10), arginasing synthesis of polyamines (Arg-1), and promoting angiogenesis etc. to show its anti-inflammatory influence and repair effects (Fabriek et al., 2009). The main purpose of this study is to investigate the anti-*alveolar echinococcosis* effect of KCs in hepatic AE accompanied with liver fibrosis, and aims to evaluate KCs' potential therapeutic value in the treatment of liver fibrosis caused by persistent AE infection.

MATERIALS AND METHODS

Patients

A total of 33 diagnosed hepatic AE patients were enrolled in the First Affiliated Hospital of Xinjiang Medical University from March 2017 to March 2019, including 17 males and 16 females with an average age of 40.61 years old (9–65 years old). Inclusion criteria was: The diagnosis of AE was in accordance with the classification criteria established by the World Health Organization (WHO) unofficial working group (Kern et al., 2006), confirmed by surgery and post-operative pathology. Patients with infectious diseases (bacteria, viruses, etc.), malignant tumors, rheumatic immune diseases, *cystic echinococcosis* or other parasitic diseases, and who took non-caries Body anti-inflammatory drugs, hormone drugs, psychotropic drugs, etc. were excluded (Kern et al., 2006). At the same time, 33 healthy age-matched controls from blood bank donors in the hospital were selected, including 17 males and 16 females, with an average age of 41.50 years (19–56 years old). Blood tests, electrocardiogram and B-ultrasound all showed no obvious abnormalities. Prior written and informed consent were obtained from patients, the minors (<18 years old) who participated in the study, had informed consent signed by their parents/legal guardians. This study conformed to the approved institutional guidelines and was approved by the Ethical Committee of Xinjiang Medical University.

Tissue Collection and Biochemical Analysis

In hepatic AE patients, the liver tissues were taken within 2 cm of the lesion by surgery for the close group, whereas the liver tissues were taken 2 cm outside the lesion for the distance group. Part of the liver tissues were fixed with 10% formaldehyde, paraffin-embedded and sectioned for 3 um successively for H&E staining, Masson staining and immunohistochemistry. The other part of liver tissue was frozen in the refrigerator at −80°C for qRT-PCR detection. Blood, both in hepatic patients and healthy age-matched controls, was obtained for the measurement of biochemical parameters using standard methods. Serum levels of alanine aminotransferase (ALT), aspartate aminotransferase (AST), alkaline phosphatase (ALP), glutamyl transpeptidase (GGT), total bilirubin (TBIL), indirect bilirubin (IBIL), and direct bilirubin (DBIL) were determined by an automatic blood biochemical analyzer (Beckman Counter LX20, USA).

H&E, Masson Staining, and Immunohistochemistry

Tissue slices were prepared at a 3 μm thickness and stained with hematoxylin-eosin(H&E), Masson's trichrome, or immunohistochemically (IHC) according to standard

procedures. After H&E staining, observations were made and pictures were taken under the microscope (OLYMPUS BX43, Japan). In reference to the chronic hepatitis GS score, two experienced pathologists blindly developed a pathology score to assess the severity of liver inflammatory lesions in patients with hepatic AE by a microscope (OLYMPUS BX43). After Masson staining, observations were made and pictures were taken under the microscope (OLYMPUS BX43) Afterwards, the sections were assessed for the METAVIR fibrosis score, as adapted from the study by Zhang et al. (2016). Detailed as follows,

- 0 score: Fibrosis free;
- 1 score: fibrosis is limited to the portal area;
- 2 score: fibrosis is not limited to the portal area, a small part of the development to the hepatic lobules;
- 3 score: fibrosis into the central vein of the hepatic lobules;
- 4 score: false Lobular formation, lesions even develop into cirrhosis.

For immunohistochemistry, the sections were incubated with primary antibodies at 4°C overnight. The sections were then incubated with the secondary antibody (biotinylated goat anti-rabbit IgG) (Mavision™, Maxim, China) for 30 min. The signal was amplified using either streptavidin—biotin complexes conjugated with peroxidase and 3, 3′ diaminobenzidine, or aminoethyl carbazole (Mavision™, Maxim, China). Next, the sections were counterstained with hematoxylin and mounted using cover slips. Observations were made and pictures were taken under the microscope (OLYMPUS BX43, Japan).

RNA Extraction and Real-Time PCR

Total RNA was isolated from homogenized liver tissues using a TRIzol™ isolation kit (Takara Bio, Dalian, China) following the manufacturer's protocol. The cDNA was synthesized by using Primer Script RT kit (Takara Bio, Dalian, China). Prime Script™ RT reagent kits, along with SYBR Green Realtime PCR Master Mix and Permix Ex Taq (Takara Bio), according to the manufacturer's instructions. The primers for GAPDH, TNF-α, IL-10, TGF-β1, α-SMA, and Desmin were synthesized by Sangon Biotech (Shanghai, China). Real-Time PCR was operated on ABI Prism 7500 Sequence Detection System (BioRad, Life Science Research, Hercules, CA, USA). PCR conditions were as follows: one cycle at 95°C for 30 s, 40 cycles at 95°C for 5 s, at 64°C for 30 min. All reactions were performed in triplicate for each sample. The $2^{-\Delta\Delta CT}$ method was used to calculate relative concentration of each target by standardizing to internal GAPDH level.

Statistical Analysis

Data was shown as the means ± standard error of mean (SEM). They were analyzed by SPSS 21.0 (IBM, Chicago, IL, USA) or GraphPad Prism 7.0 software (GraphPad Software, San Diego, CA, USA). Student's *t*-test was performed to determine differences between two groups. $P < 0.05$ indicated statistical significance.

TABLE 1 | Biochemical parameters in Hepatic AE group and Healthy control group (Mean ± SD).

Index	HAE ($n = 33$)	Control ($n = 33$)
Age (average)	40.61	41.50
Sex (male:female)	1.06:1	1.06:1
ALT (U/L)	65.21 ± 44.12****	23.96 ± 10.48
AST (U/L)	47.36 ± 27.52****	23.87 ± 5.72
ALP (U/L)	139.77 ± 60.74****	65.38 ± 13.27
GGT (U/L)	82.66 ± 56.76****	26.59 ± 12.69
TBIL (umol/L)	15.14 ± 8.26	14.83 ± 4.37
I-BIL (umol/L)	9.02 ± 4.99**	12.13 ± 3.71
DBIL (umol/L)	6.70 ± 5.15***	2.70 ± 0.77

****$P < 0.0001$, ***$P < 0.001$, **$P < 0.01$.

RESULTS

Biochemical Parameters in Patients With Hepatic AE

Notably, serum levels of ALT, AST, GGT, ALP, IBIL, and DBIL were significantly higher in patients with hepatic AE than those in healthy controls (shown in **Table 1**). It indicated that the normal function of hepatocytes was impaired, and the liver microenvironment was severely imbalanced in patients with hepatic AE.

Pathological Changes Were Observed in Liver Lesions of Patients With Hepatic AE

We have used H&E staining to observe the pathological morphology of livers. The close group showed that the normal lobular structure of liver tissue was destroyed. Cell edema, cytoplasm loose, a large amount of congestion in the central vein of the liver, and the hepatic sinus was clearly dilated, some inflammatory lesions were visible, and a large number of inflammatory cells infiltrated around them (shown in **Figure 1**). In contrast, the distance group showed that the hepatic lobule structure of the liver tissue was normal, and the central vein was visible inside. The hepatocytes were arranged radially around the central vein, the structure of the hepatic sinus was clear and there was no pathological change. Combined with the chronic hepatitis GS score, two pathologists blindly assessed the severity of liver inflammatory lesions in patients with hepatic AE (severity criteria details shown in **Table 2**, results shown in **Figure 2A**).

We have used Masson staining to observe the collagen deposition. Masson staining indicated that there was no inflammatory cell infiltration in the liver tissue portal area, and little or no collagen fiber tissue in Distance group. However, in the close group, the normal structure of the hepatic lobules disappeared, the hepatocytes were disorderly arranged, the volume became larger, nuclear dissolution occurred, and the blue collagen fibrous tissue was clearly proliferated and deposited (shown in **Figure 3**). Referring to METAVIR scoring criteria, the fibrosis score of patients with hepatic AE as shown in **Figure 2B**.

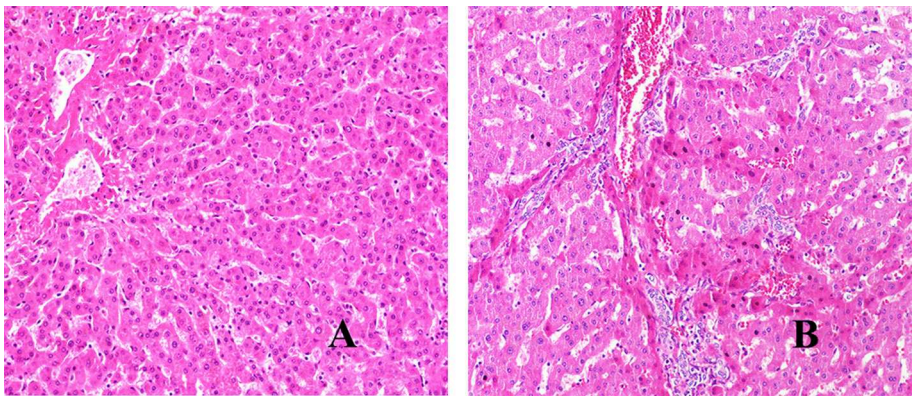

FIGURE 1 | H&E staining of liver lesions in patients with hepatic AE (magnification, ×200). **(A)** Distance group. **(B)** Close group.

TABLE 2 | Pathological scores of liver lesions' inflammatory changes in patients with hepatic AE.

Cholestasis	Calcification	Vesicles (number)	Necrotic liquefaction cavity (number)	Inflammatory cells infiltration	Scores
	Calcification zone could be observed	≥16	≥10	Confluent lesion infiltration	4
	Confluent calcification	11–15	7–9	More than 4 lesions infiltration	3
+	Irregular calcification	6–10	4–6	2–4 lesions infiltration	2
	Point calcified particles	1–5	1–3	Single lesion infiltration	1
–	No obvious change	0	0	No obvious change	0

*After H&E staining, pathological score criteria was drawn up for evaluating the inflammatory changes in liver lesions in patients with hepatic AE (results were shown in **Figure 2A**). Among them, the vesicle count was observed in at least 3 different fields and the necrotic liquefaction cavity was the sum of the entire pathological section of view under low-power microscope (magnification, ×100).*

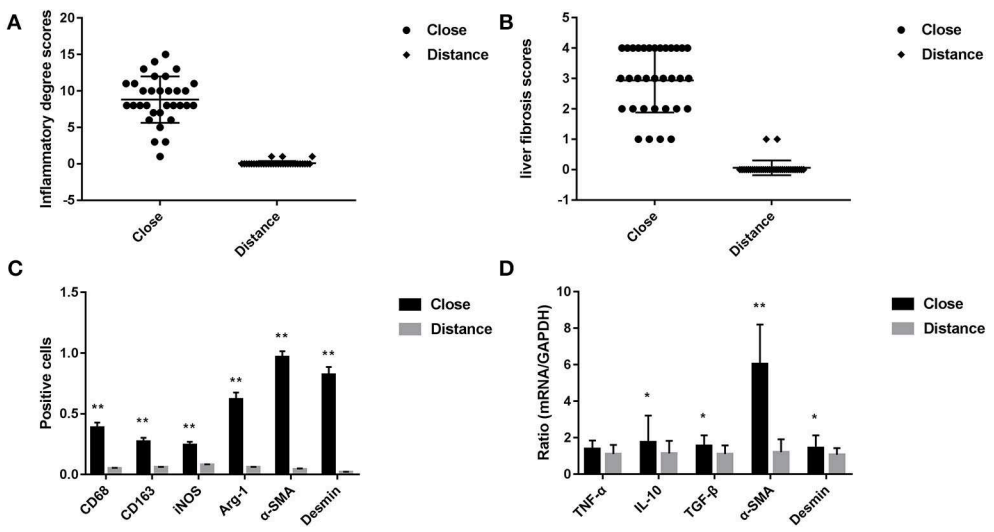

FIGURE 2 | (A) Pathological score of liver tissue inflammatory changes in patients with hepatic AE (after H&E staining, score criteria refers to the **Table 2**). **(B)** Liver fibrosis score in patients with hepatic AE (after Masson staining, refers to METAVIR scoring standard). **(C)** Immunohistochemical positive cells area of liver tissue in patients with hepatic AE (magnification, ×400). KCs surface markers CD68 and CD163, pro-inflammatory cytokine iNOS, anti-inflammatory cytokine Arg-1 were differentially expressed in immunohistochemical staining between the two groups. The difference in the HSCs activation markers α-SMA and Desmin between the two groups (**$P < 0.01$, compared with Distance group). **(D)** Gene expression levels of KCs and HSCs activation (*$P < 0.05$, **$P < 0.01$, compared with Distance group).

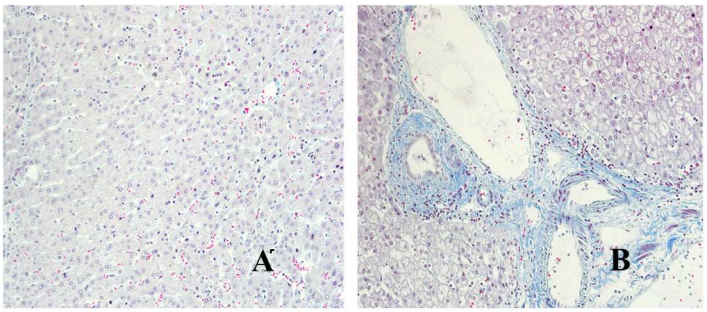

FIGURE 3 | Masson staining of liver lesions in patients with hepatic AE (magnification, ×200). **(A)** Distance group. **(B)** Close group.

KCs Secrete Some Cytokines, and Anti-inflammatory Cytokines Were Expressed at Higher Levels Than Pro-inflammatory Cytokines in Patients With Hepatic AE

CD68 is commonly used as a surface marker for KCs in human (Sica et al., 2014; Koyama and Brenner, 2017), during liver tissue self-repair stage, KCs highly express CD163 (You et al., 2013; Bala et al., 2016; Björklund et al., 2018). Patients with hepatic AE are generally in the middle, even late stages of the disease. At this point, liver fibrosis has formed and the liver is in the period of tissue repair. Therefore, CD68 and CD163 were used as surface markers for KCs in our study. In IHC (Antibodies in IHC shown in **Table 3**), CD68 showed a brown mass around the liver lesions, and the positive results were mainly expressed in the cytoplasm of KCs. Because the vesicles of the *echinococcosis* continued to expand and compress the liver tissue, the inflammation continuously stimulated the liver tissue, KCs clustered around the lesions and actively exerted anti-inflammatory effects. While the distance group showed lower expression ($p < 0.01$; Primer sequence shown in **Table 4**, results shown in **Figures 2C**, **4a,d**). Meanwhile, the positive result of CD163 was expressed as brownish yellow particles in the cytoplasm of KCs (**Figures 4b,e**), which is consistent with the results of CD68. When liver is damaged or infected, iNOS—a kind of catalytic enzyme, is released by KCs to promote the inflammatory (Anavi et al., 2015; Cinar et al., 2016). After activation, a large amount of NO is produced, which enhances the degree of oxidative stress in the body and promotes the expression of pro-inflammatory substances by inflammatory cytokines such as TNF-α etc., which simultaneously expresses and secretes pro-inflammatory substances to clear pathogens. In protein level, iNOS was positive in the cytoplasm or nucleus of KCs around the lesion while the distance group showed less positive cells ($p < 0.01$; **Figures 2C**, **4c,f**). In gene level, TNF-α was also at a high expression level than that in the distance group ($p < 0.05$; **Figure 2D**). In contrast to the pro-inflammatory effect of iNOS and TNF-α, KCs also can secrete an amount of cytokine Arg-1 and cytokine IL-10 (Altamirano-Barrera et al., 2017; Kim et al., 2017; Campana et al., 2018), they can down-regulate iNOS and TNF-α activity reducing cell apoptosis (Lisi et al., 2017).

TABLE 3 | Antibodies used for immunohistochemistry.

Antibody	Dilution factor	Company
Anti-CD68 Antibody	1:200	Bioss, Beijing, China
Anti-CD163 Antibody	1:200	Bioss, Beijing, China
Anti-iNOS antibody	1:1000	Abcam, Cambridge, UK
Rabbit Anti-Arg-1 antibody	1:200	Bioss, Beijing, China
Rabbit Anti-alpha-SMA antibody	1:400	Affinity, Cincinnati, US
Rabbit Anti-Desmin antibody	1:200	Affinity, Cincinnati, US

TABLE 4 | Primer sequence.

Gene (human)	Primer sequence
TNF-α	F: TGCTCCTCACCCACACCAT
	R: GGAGGTTGACCTTGGTCTGGTA
IL-10	F: GGGAGAACCTGAAGACCCTCA
	R: TGCTCTTGTTTTCACAGGGAAG
TGF-β1	F: CAATTCCTGGCGATACCTCAG
	R: GCACAACTCCGGTGACATCAA
α-SMA	F: TTGAGAAGAGTTACGAGTTG
	R: GGACATTGTTAGCATAGAGG
Desmin	F: AGCCAGGCCTACTCGTCCAGCCA
	R: CCGCCCGACGTGCGCGACACCTG
GAPDH	F: CATCCACTGGTGCTGCCAAGGCTGT
	R: ACA ACCTGGTCCTCAGTGTAGCCCA

F, Forward; R, Reverse.

In protein level, Arg-1 was mostly distributed in the cytoplasm of macrophages around the lesion tissue and appeared as brownish yellow particles (**Figures 4g,j**). In gene level, IL-10 was also at a high expression level than that in the distance group ($p < 0.05$; **Figure 2D**). Interestingly, we found that the anti-inflammatory cytokines were higher than pro-inflammatory cytokines both in the protein expression and gene levels. A possible reason for this could be due to the liver tissue already being at the anti-inflammatory and self-repairing stage, when the patients with hepatic AE received surgery. At the same time, liver fibrosis had already formed and gradually progressed.

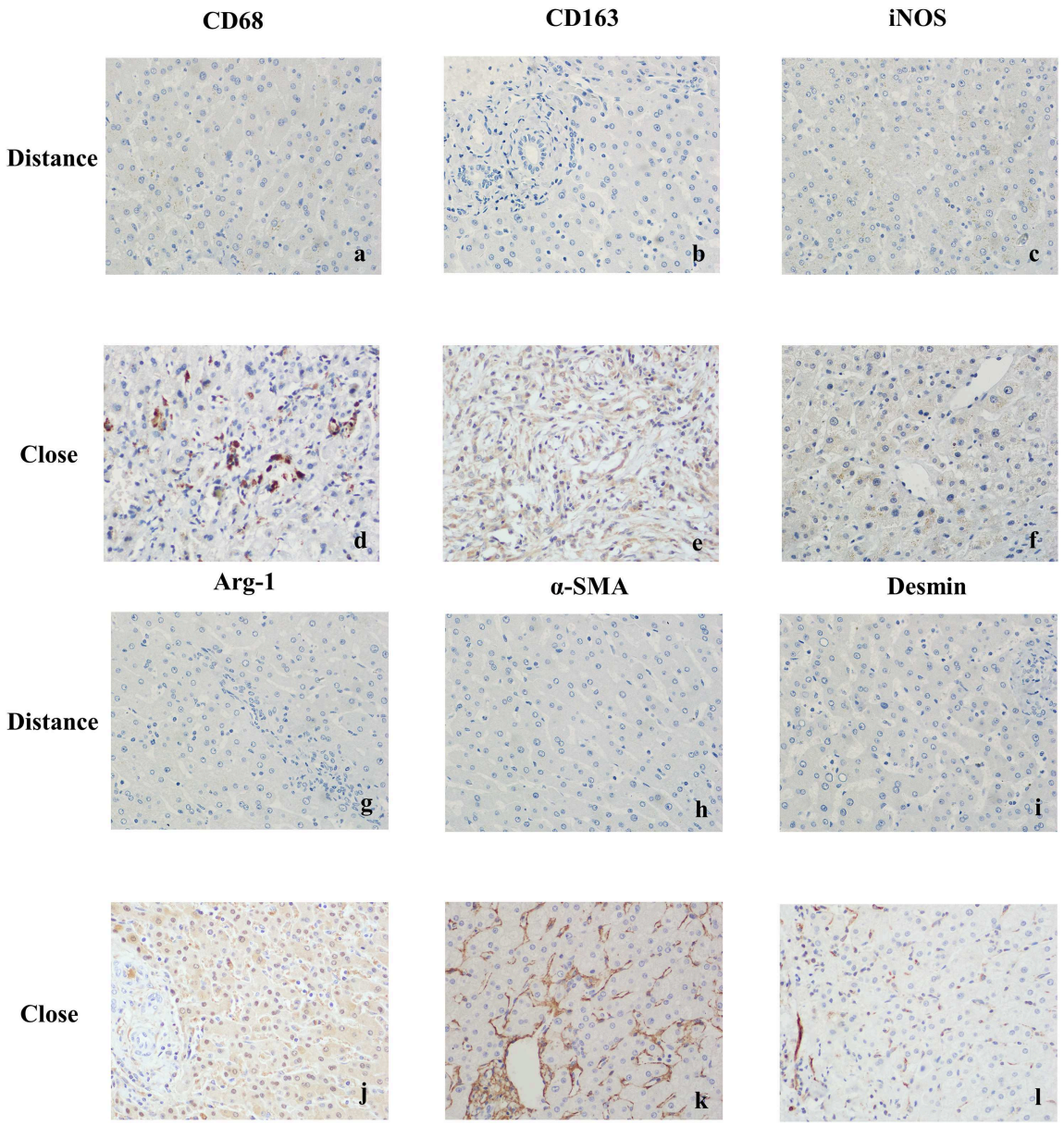

FIGURE 4 | Immunohistochemical staining results of liver tissues in patients with hepatic AE (magnification, ×400). **(a)** CD68 was weakly positive or negative in KCs cytoplasm (Distance group). **(b)** CD163 was weakly positive or negative in KCs cytoplasm (Distance group). **(c)** iNOS was weakly positive or negative in KCs cytoplasm (Distance group). **(d)** Strong positive expression of CD68 in KCs cytoplasm (Close group). **(e)** Strong positive expression of CD163 in KCs cytoplasm (Close group). **(f)** When exposed to inflammatory stimuli, KCs secreted the pro-inflammatory cytokine iNOS, strong positive expression of iNOS in KCs cytoplasm (Close group). **(g)** Arg-1 was weakly positive or negative in KCs cytoplasm (Distance group). **(h)** α-SMA was weakly positive or negative in cytoplasm of resting HSCs (Distance group). **(i)** Desmin was weakly positive or negative in cytoplasm of resting HSCs (Distance group). **(j)** In the continuous parasite stimulation, KCs secreted the anti-inflammatory cytokineArg-1, strong positive expression of Arg-1 in KCs cytoplasm (Close group). **(k)** Strong positive expression of α-SMA in cytoplasm of activated HSCs (Close group). **(l)** Strong positive expression of Desmin in cytoplasm of activated HSCs (Close group).

KCs Secrete a Large Amount of Cytokine TGF-β1 Trigger HSCs Activation and Proliferation in Liver Lesions of Hepatic AE Patients

In order to protect the stability of the liver microenvironment and repair the liver damage during the continuous stimulation of *E. multilocularis*, KCs secrete a large amount of pro-fibrogenic cytokine TGF- β1, which promotes the activation and proliferation of HSCs. The activation of HSCs is central for liver fibrogenesis, because these cells transdifferentiate into myofibroblasts and represent the major extracellular matrix producing cells in the liver (Tsuchida and Friedman, 2017). TGF-β1 positively regulates the activation of HSCs. In order to detect

the changes of TGF-β1 at mRNA level in the liver lesions of hepatic AE patients, we performed qRT-PCR assay. As shown in **Figure 2D**, the mRNA level of TGF-β1 in the liver lesions was significantly elevated in the close group than that in the distance group ($P < 0.05$). α-SMA, Desmin are the surface markers of HSCs activation (Ding et al., 2014; Zhang et al., 2018; Inzaugarat et al., 2019), mainly express in the cytoplasm of the vascular wall or in the cytoplasm of activated HSCs. We performed IHC and qRT-PCR assay to assess the protein and gene levels, respectively. In the close group, IHC indicated there was strong expression of α-SMA and Desmin reaction in lesion tissues, increased brown-yellow staining could be observed in the portal area and fiber compartment (shown in **Figures 4k,l**), it suggested that HSCs were in a proliferating stage. Compared with the distance group, the expression of α-SMA and Desmin was significantly increased (shown in **Figures 2C**, **4h,i**; $P < 0.01$). As shown in **Figure 2D**, the mRNA levels of α-SMA in the liver was significantly elevated in the close group than that in the distance group ($P < 0.01$). Meanwhile the mRNA levels of Desmin in the liver lesions was significantly elevated in the close group than that in the distance group ($P < 0.05$), the difference was statistically significant.

DISCUSSION

Liver is the main parasitic organ infected with hydatid cyst. Its pathological structure is a collection of numerous small vesicles with a diameter of 0.1–1.0 cm. Its general view is a single large block, which is a pale yellow or white vesicle-like mass, with a hard texture and unclear boundaries with surrounding tissues. Liver fibrosis is a protective pathological process triggered by continuous stimulation of *echinococcosis*. Early liver fibrosis can be reversed and collagen can limit the expansion of the worm as well as repair damaged liver tissue. The situation of fibrosis, in the middle and late stages, starts to deteriorate, reaching an irreversible level, thus can further develop into cirrhosis and liver cancer. It is currently difficult to completely remove echinococcal vesicles by surgery. Therefore, timely administration of anti-fibrosis therapy is an important measure to hinder the progress of the disease. Our study firstly performed pathological scoring on liver lesions of patients with hepatic AE, including common items such as inflammatory cell infiltration, cholestasis etc. and the number of vesicles in the disease was also included to assess the severity of liver pathological changes in patients with hepatic AE. At the same time, liver fibrosis severity was evaluated by METAVIR liver fibrosis score. Both scores indicated a high degree of liver inflammation, a severe degree of fibrosis, and a small number of patients have even reached the level of cirrhosis.

A large number of studies (Lin et al., 2009; Tacke and Kurts, 2011) suggested that bone marrow monocyte-derived macrophages (MoMFs) contributed significantly to parasitic liver fibrosis. However, KCs, the liver-resident macrophages distinguished from the macrophage recruited from peripheral blood, were also shown to contribute significantly to the progression of liver fibrosis, and macrophages recruited from peripheral blood. Wang et al. (2013) pointed out that the liver lesions of patients with echinococcosis were similar to those observed in the 180th day after infection in experimental mice. Typical chronic granuloma and fibrosis changes existed around the vesicles. In an area of the liver, far from the lesion, a large number of lymphocytes infiltrated the portal vein causing the degeneration and necrosis of some of the hepatocytes; which resulted in the proliferation and differentiation of a large number of KCs. In this study, H&E staining and Masson staining were used to evaluate the pathological changes and fibrosis of liver lesions in patients with hepatic AE. The pathologic manifestations, described in previous studies, in liver lesion tissues of patients with hepatic AE were verified. CD68 and CD163 were selected as the surface markers of KCs in immunohistochemical staining to observe the number of activated KCs proliferation (Bala et al., 2016; Björklund et al., 2018). In the distance group, a small number of cells showed yellowish clumps in cytoplasm that were weakly positive for CD68, suggesting that there was still a small amount of active KCs expression in distant liver tissue. In the close group, CD68 and CD163 were positively expressed in liver lesions. It indicated that a large number of KCs were activated to accumulate around the lesions and responded to the immune response during the process of continuous stimulation of echinococcosis in the liver.

The patients, who had no clinical manifestations in the early stage of infection, most of them had reached the middle or late stage with clear fibrosis changes in the liver with hepatic AE. In our study, the liver lesions in the patients with hepatic AE showed a clear collagen deposition, presenting the middle and late stage of liver fibrosis, that is, the liver tissues were in the anti-inflammatory and self-repairing stage.

Hashimoto et al. (2013) and Sasaki et al. (2017) found that KCs, in response to liver injury, become activated and express cytokines and signaling molecules. Additionally, activated KCs display markers of M1-like macrophages or M2-like macrophages depending on the signals that they receive from their environment. Inflammation in the liver is regulated by the balance of pro-inflammatory M1 Kupffer cells and anti-inflammatory M2 Kupffer cells which was partially self-renewing in a steady state, independent of monocyte recruitment. Interestingly, in our study, the anti-inflammatory cytokines were higher than pro-inflammatory cytokines both in the protein expression and gene levels. It suggests that KCs exhibit a similar phenotype in the late stage of hepatic AE, and moreover, KCs secreted a large amount of cytokine TGF-β1 to further promote fibrosis. However, further research is needed to investigate whether it is related to peripheral blood recruited macrophages.

It is generally accepted that α-SMA and Desmin are surface markers of HSCs activation (Gibelli et al., 2008; Novo et al., 2009; Golbar et al., 2011). There is clear evidence from *in vitro* and *in vivo* studies that KCs can activate HSCs to transdifferentiate into myofibroblasts, the major collagen-producing cell type in hepatic fibrosis (Pradere et al., 2013; Tacke and Zimmermann, 2014). KCs activate HSCs via paracrine mechanisms, likely involving the potent profibrotic and mitogenic cytokines TGF-β and PDGF (Pradere et al., 2013). These profibrotic functions of KCs during chronic hepatic injury remain functionally relevant, even if the

infiltration of additional inflammatory monocytes is blocked via pharmacological inhibition of the chemokine CCL2 (Baeck et al., 2012). Whether the mechanism of KCs in liver fibrosis caused by vesicular hydatid disease is consistent to other chronic liver disease, further research is needed. In our study, they were up-regulated at both protein and gene levels in patients with hepatic AE.

In summary, through investigating the activation and KCs' proliferation and HSCs' activation in patients with hepatic AE, it suggested that the long-term inflammatory reaction caused by the infection of the *echinococcosis* triggered the self-protection and self-repairing of the liver microenvironment. At the same time, it caused a large number of KCs to proliferate and update, and tended to be M2-like macrophages than M1-like macrophages, releasing a large number of anti-inflammatory cytokines to resist the stimulation of *echinococcosis*. Meanwhile KCs secreted a large amount of pro-fibrogenic cytokines to activate HSCs. KCs has a complex and highly flexible role in the anti-*echinococcosis* and self-repairing in patients with hepatic AE. It is potentially feasible to reduce the fibrosis activity of HSCs and improve its anti-fibrosis activity by targeting KCs (Han et al., 2019). However, this study mainly evaluated the liver pathological changes and degree of fibrosis to assess the severity of the patients with hepatic AE, and studied the role of KCs in liver fibrosis to evaluate its influence in hepatic AE. In the future, we will simulate the *in vivo* environment and co-culture the two cells *in vitro* to further clarify the mechanism of KCs regulating the activation of HSCs.

DATA AVAILABILITY STATEMENT

The data used to support the findings of this study are available from the corresponding author upon request.

ETHICS STATEMENT

The studies involving human participants were reviewed and approved by Ethical Committee of Xinjiang Medical University. The patients/participants provided their written informed consent to participate in this study.

AUTHOR CONTRIBUTIONS

XM, HW, and FT conceptualized and design the study. XM, YL, and JG were responsible for the administrative support. JS and JL worked on the provision of the study materials or patients. BL and XC collected and assembled the data. XZ was responsible for the data analysis and interpretations. All authors wrote and approved the final manuscript.

FUNDING

This work was supported by the National Natural Science Foundation (No. 81760372), the State Key Laboratory of Pathogenesis, Prevention and Treatment of High Incidence Diseases in Central Asia (No. SKL-HIDCA-2018-27), and Key Laboratory of Parasitic Pathogens and Vector Biology, Ministry of Health (No. WSBKFKT201803).

REFERENCES

Altamirano-Barrera, A., Barranco-Fragoso, B., and Méndez-Sánchez, N. (2017). Management strategies for liver fibrosis. *Ann. Hepatol.* 16, 48–56. doi: 10.5604/16652681.1226814

Anavi, S., Eisenberg-Bord, M., Hahn-Obercyger, M., Genin, O., Pines, M., and Tirosh, O. (2015). The role of iNOS in cholesterol-induced liver fibrosis. *Lab. Invest.* 95, 914–924. doi: 10.1038/labinvest.2015.67

Arrechea Irigoyen, M. A., Córdoba Iturriagagoitia, A., Tuñón Álvarez, M. T., Gómez Dorronsoro, M. L., and MartínezPeñuela Virseda, J. M. (2008). Equinococosis alveolar humana. Presentación de un caso. *Rev. Esp. Patol.* 41, 203–206. doi: 10.1016/S1699-8855(08)70122-3

Baeck, C., Wehr, A., Karlmark, K. R., Heymann, F., Vucur, M., Gassler, N., et al. (2012). Pharmacological inhibition of the chemokine CCL2 (MCP-1) diminishes liver macrophage infiltration and steatohepatitis in chronic hepatic injury. *Gut* 61, 416–426. doi: 10.1136/gutjnl-2011-300304

Bala, S., Csak, T., Saha, B., Zatsiorsky, J., Kodys, K., Catalano, D., et al. (2016). The pro-inflammatory effects of miR-155 promote liver fibrosis and alcohol-induced steatohepatitis. *J. Hepatol.* 64, 1378–1387. doi: 10.1016/j.jhep.2016.01.035

Beljaars, L., Schippers, M., Reker-Smit, C., Martinez, F. O., Helming, L., Poelstra, K., et al. (2014). Hepatic localization of macrophage phenotypes during fibrogenesis and resolution of fibrosis in mice and humans. *Front. Immunol.* 8:430. doi: 10.3389/fimmu.2014.00430

Björklund, J., Laursen, T. L., Sandahl, T. D., Møller, H. J., Vilstrup, H., Ott, P., et al. (2018). High hepatic macrophage activation and low liver function in stable Wilson patients - a Danish cross-sectional study. *Orphanet J. Rare Dis.* 13:169. doi: 10.1186/s13023-018-0910-7

Campana, L., Starkey Lewis, P. J., Pellicoro, A., Aucott, R. L., Man, J., O'Duibhir, E., et al. (2018). The STAT3-IL-10-IL-6 pathway is a novel regulator of macrophage efferocytosis and phenotypic conversion in sterile liver injury. *J. Immunol.* 200, 1169–1187. doi: 10.4049/jimmunol.1701247

Cinar, R., Iyer, M. R., Liu, Z., Cao, Z., Jourdan, T., Erdelyi, K., et al. (2016). Hybrid inhibitor of peripheral cannabinoid-1 receptors and inducible nitric oxide synthase mitigates liver fibrosis. *JCI Insight* 1:87336. doi: 10.1172/jci.insight.87336

Craig, P. S., Hegglin, D., Lightowlers, M. W., Torgerson, P. R., and Wang, Q. (2017). Echinococcosis: control and prevention. *Adv. Parasitol.* 96, 155–158. doi: 10.1016/bs.apar.2016.09.002

Ding, B. S., Cao, Z., Lis, R., Nolan, D. J., Guo, P., Simons, M., et al. (2014). Divergent angiocrine signals from vascular niche balance liver regeneration and fibrosis. *Nature* 505, 97–102. doi: 10.1038/nature12681

Elchaninov, A. V., Fatkhudinov, T. K., Vishnyakova, P. A., Lokhonina, A. V., and Sukhikh, G. T. (2019). Phenotypical and functional polymorphism of liver resident macrophages. *Cells* 8:E1032. doi: 10.3390/cells8091032

Fabriek, B. O., van Bruggen, R., Deng, D. M., Ligtenberg, A. J. M., Nazmi, K., Schornagel, K., et al. (2009). The macrophage scavenger receptor CD163 functions as an innate immune sensor for bacteria. *Blood* 113, 887–892. doi: 10.1182/blood-2008-07-167064

Gibelli, N. E., Tannuri, U., and Mello, E. S. (2008). Immunohistochemical studies of stellate cells in experimental cholestasis in newborn and adult rats. *Clinics* 63, 689–694. doi: 10.1590/S1807-59322008000500019

Golbar, H. M., Izawa, T., Yano, R., Ichikawa, C., Sawamoto, O., Kuwamura, M., et al. (2011). Immunohistochemical characterization of macrophages and myofibroblasts in α-Naphthylisothiocyanate (ANIT) - induced bile duct injury and subsequent fibrogenesis in rats. *Toxicol. Pathol.* 39, 795–808. doi: 10.1177/0192623311413790

Han, J., Zhang, X., Lau, J. K., Fu, K., Lau, H. C., Xu, W., et al. (2019). Bone marrow-derived macrophage contributes to fibrosing steatohepatitis through activating hepatic stellate cells. *J. Pathol.* 248, 488–500. doi: 10.1002/path.5275

Hashimoto, D., Chow, A., Noizat, C., Teo, P., Beasley, M. B., Leboeuf, M., et al. (2013). Tissue-resident macrophages self-maintain locally throughout adult life with minimal contribution from circulating monocytes. *Immunity* 38, 792–804. doi: 10.1016/j.immuni.2013.04.004

Hotez, P. J., Brindley, P. J., Bethony, J. M., King, C. H., Pearce, E. J., and Jacobson, J. (2008). Helminth infections: the great neglected tropical diseases. *J. Clin. Invest.* 118, 1311–1321. doi: 10.1172/JCI34261

Inzaugarat, M. E., Johnson, C. D., Holtmann, T. M., McGeough, M. D., Trautwein, C., Papouchado, B. G., et al. (2019). NLR Family Pyrin domain-containing 3 inflammasome activation in hepatic stellate cells induces liver fibrosis in mice. *Hepatology* 69, 845–859. doi: 10.1002/hep.30252

Kern, P., Wen, H., Sato, N., Vuitton, D. A., Gruener, B., Shao, Y., et al. (2006). WHO classification of alveolar echinococcosis: principles and application. *Parasitol. Int.* 55, S283–S287. doi: 10.1016/j.parint.2005.11.041

Kim, E. M., Kwak, Y. S., Yi, M. H., Kim, J. Y., Sohn, W. M., and Yong, T. S. (2017). Clonorchis sinensis antigens alter hepatic macrophage polarization *in vitro* and *in vivo*. *PLoS Negl. Trop. Dis.* 11:e0005614. doi: 10.1371/journal.pntd.0005614

Koyama, Y., and Brenner, D. A. (2017). Liver inflammation and fibrosis. *J. Clin. Invest.* 127, 55–64. doi: 10.1172/JCI88881

Lee, U. E., and Friedman, S. L. (2011). Mechanisms of hepatic fibrogenesis. *Best Pract. Res. Clin. Gastroenterol.* 25, 195–206. doi: 10.1016/j.bpg.2011.02.005

Lin, S. L., Castaño, A. P., Nowlin, B. T., Lupher, M. L. Jr., and Duffield, J. S. (2009). Bone marrow Ly6Chigh monocytes are selectively recruited to injured kidney and differentiate into functionally distinct populations. *J. Immunol.* 183, 6733–6743. doi: 10.4049/jimmunol.0901473

Lisi, L., Ciotti, G. M., Braun, D., Kalinin, S., Currò, D., Dello Russo, C., et al. (2017). Expression of iNOS, CD163 and ARG-1taken as M1 and M2 markers of microglial polarization in human glioblastoma and the surrounding normal parenchyma. *Neurosci. Lett.* 3, 106–112. doi: 10.1016/j.neulet.2017.02.076

Menghi, C., Gatta, C., and Arias, L. (2017). Human cystic and alveolar echinococcosis. *Curr. Treat. Options Infec. Dis.* 9, 210–222. doi: 10.1007/s40506-017-0121-0

Mezioug, D., and Touil-Boukoffa, C. (2012). Interleukin-17A correlates with interleukin-6 production in human cystic echinococcosis: a possible involvement of IL-17A in immune-protection against Echinococcus granulosus infection. *Eur. Cytokine Netw.* 23, 112–119. doi: 10.1684/ecn.2012.0314

Novo, E., di Bonzo, L. V., Cannito, S., Colombatto, S., and Parola, M. (2009). Hepatic myofibroblasts: a heterogeneous population of multifunctional cells in liver fibrogenesis. *Int. J. Biochem. Cell Biol.* 41, 2089–2093. doi: 10.1016/j.biocel.2009.03.010

Pradere, J. P., Kluwe, J., De Minicis, S., Jiao, J. J., Gwak, G. Y., Dapito, D. H., et al. (2013). Hepatic macrophages but not dendritic cells contribute to liver fibrosis by promoting the survival of activated hepatic stellate cells in mice. *Hepatology* 58, 1461–1473. doi: 10.1002/hep.26429

Sasaki, R., Devhare, P. B., Steele, R., Ray, R., and Ray, R. B. (2017). Hepatitis C virus-induced CCL5 secretion from macrophages activates hepatic stellate cells. *Hepatology* 66, 746–757. doi: 10.1002/hep.29170

Sica, A., Invernizzi, P., and Mantovani, A. (2014). Macrophage plasticity and polarization in liver homeostasis and pathology. *Hepatology* 59, 2034–2042. doi: 10.1002/hep.26754

Tacke, F., and Kurts, C. (2011). Infiltrating monocytes versus resident Kupffer cells: do alternatively activated macrophages need to be targeted alternatively? *Hepatology* 54, 2267–2270. doi: 10.1002/hep.24714

Tacke, F., and Zimmermann, H. W. (2014). Macrophage heterogeneity in liver injury and fibrosis. *J. Hepatol.* 60, 1090–1096. doi: 10.1016/j.jhep.2013.12.025

Tosello-Trampont, A. C., Krueger, P., Narayanan, S., Landes, S. G., Leitinger, N., and Hahn, Y. S. (2011). NKp46(+) natural killer cells attenuate metabolism induced hepatic fibrosis by regulating macrophage activation in mice. *Hepatology* 63, 799–812. doi: 10.1002/hep.28389

Tsuchida, T., and Friedman, S. L. (2017). Mechanisms of hepatic stellate cell activation. *Nat. Rev. Gastroenterol. Hepatol.* 14, 397–411. doi: 10.1038/nrgastro.2017.38

Wang, J., and Gottstein, B. (2016). Immunoregulation in larval *Echinococcus multilocularis* infection. *Parasite Immunol.* 38, 182–192. doi: 10.1111/pim.12292

Wang, J., Zhang, C., Wei, X., Blagosklonov, O., Lv, G., Lu, X., et al. (2013). TGF-lonovunol.ilocularis l ol. cell activation. ced hepatic*Echinococcus multilocularis* and its hosts. *PLoS ONE* 8:e55379. doi: 10.1371/journal.pone.0055379

Wynn, T. A., and Vannella, K. M. (2016). Macrophages in tissue repair, regeneration, and fibrosis. *Immunity* 44, 450–462. doi: 10.1016/j.immuni.2016.02.015

You, Q., Holt, M., Yin, H., Li, G., Hu, C. J., and Ju, C. (2013). Role of hepatic resident and infiltrating macrophages in liver repair after acute injury. *Biochem. Pharmacol.* 86, 836–843. doi: 10.1016/j.bcp.2013.07.006

Zhang, C. Y., Yuan, W. G., He, P., Lei, J. H., and Wang, C. X. (2016). Liver fibrosis and hepatic stellate cells: etiology, pathological hallmarks and therapeutic targets. *World J. Gastroenterol.* 22, 10512–10522. doi: 10.3748/wjg.v22.i48.10512

Zhang, D., Zhuang, R., Guo, Z., Gao, M., Huang, L., You, L., et al. (2018). Desmin- and vimentin-mediated hepatic stellate cell-targeting radiotracer (99m)Tc-GlcNAc-PEI for liver fibrosis imaging with SPECT. *Theranostics* 8, 1340–1349. doi: 10.7150/thno.22806

Conflict of Interest: The authors declare that the research was conducted in the absence of any commercial or financial relationships that could be construed as a potential conflict of interest.

Copyright © 2020 Liu, Tian, Shan, Gao, Li, Lv, Zhou, Cai, Wen and Ma. This is an open-access article distributed under the terms of the Creative Commons Attribution License (CC BY). The use, distribution or reproduction in other forums is permitted, provided the original author(s) and the copyright owner(s) are credited and that the original publication in this journal is cited, in accordance with accepted academic practice. No use, distribution or reproduction is permitted which does not comply with these terms.

frontiers in Cellular and Infection Microbiology

ORIGINAL RESEARCH
published: 29 April 2020
doi: 10.3389/fcimb.2020.00189

Defective Granuloma Formation in Elderly Infected Patients

Aurélie Daumas[1,2]*, *Benjamin Coiffard*[1], *Céline Chartier*[1], *Amira Ben amara*[1], *Julie Alingrin*[3], *Patrick Villani*[2] *and Jean-Louis Mege*[1]

[1] Aix-Marseille Univ, IRD, Assistance Publique-Hôpitaux de Marseille (APHM), MEPHI, IHU-Méditerranée Infection, Marseille, France, [2] Service de Médecine Interne, Gériatrie et Thérapeutique, Hôpital de la Timone, APHM, Marseille, France, [3] Service d'Anesthésie et de Réanimation, Hôpital Nord, APHM, Marseille, France

Granulomas are compact structures formed in tissues by the immune system in response to aggressions. The *in vitro* formation of granulomas using circulating mononuclear cells is an innovative method to easily assess the immune response of patients. Monitoring the efficiency of mononuclear cells from patients to form granulomas *in vitro* would help improve their therapeutic management. Circulating mononuclear cells from 23 elderly patients with sepsis and 24 elderly controls patients were incubated with Sepharose beads coated with either BCG or *Coxiella burnetii* extracts. The formation of granulomas was measured over 9 days. Most healthy elderly patients (92%) were able to form granulomas in response to BCG and *Coxiella burnetii* extracts compared to only 48% of infected elderly patients. Undernutrition was significantly associated with impaired granuloma formation in healthy and infected patients. Granulomas typically comprise epithelioid cells and multinucleated giant cells, however, these cells were not detected in samples obtained from patients unable to form granulomas. We also found that the impairment of granuloma formation was associated with reduced production of tumor necrosis factor without overproduction of interleukin-10. Finally, all genes specifically modulated in granulomatous cells were down-modulated in patients with defective granuloma formation. TNFSF10 was the only M1 gene markedly upregulated in patients who did not form granulomas. Our study suggest that defective granuloma formation may be a measurement of altered activation of immune cells which can predispose to nosocomial infections in elderly patients.

Keywords: sepsis, elderly patient, granuloma, tumor necrosis factor, multinucleated giant cell

OPEN ACCESS

Edited by:
Marcel I. Ramirez, Oswaldo Cruz Foundation (Fiocruz), Brazil

Reviewed by:
Don Thushara Galbadage, Biola University, United States
Shinsmon Jose, University of Cincinnati, United States

***Correspondence:**
Aurélie Daumas
aurelie.daumas@ap-hm.fr

Specialty section:
This article was submitted to Bacteria and Host, a section of the journal Frontiers in Cellular and Infection Microbiology

Received: *20 November 2019*
Accepted: *09 April 2020*
Published: *29 April 2020*

Citation:
Daumas A, Coiffard B, Chartier C, Ben amara A, Alingrin J, Villani P and Mege J-L (2020) Defective Granuloma Formation in Elderly Infected Patients. Front. Cell. Infect. Microbiol. 10:189. doi: 10.3389/fcimb.2020.00189

INTRODUCTION

Granulomas are organized collections of immune cells that reflect tissue immune response to aggressions (Saunders and Britton, 2007; Herndon and Rogers, 2013; Pagán and Ramakrishnan, 2018). They are dynamic structures based on the recruitment of monocytes, macrophages, and T lymphocytes, and the subsequent differentiation of macrophages into epithelioid cells and multinuclear giant cells (MGCs) (Saunders and Britton, 2007; Herndon and Rogers, 2013). One of the main features of the immune response to *Mycobacterium Tuberculosis* and the outcome of Q fever caused by *Coxiella burnetii* is the formation of granulomas (Saunders and Britton, 2007; Herndon and Rogers, 2013). Granulomas have a significant protective function (Ramakrishnan, 2012; Herndon and Rogers, 2013; Pagán and Ramakrishnan, 2018). Their main function is to

isolate bacteria or other pathogens from the body and facilitate their destruction by granulomatous cells (Delaby et al., 2012; Ramakrishnan, 2012; Pagán and Ramakrishnan, 2018). In tuberculosis, granuloma formation is primarily a host-defense mechanism for containing the bacteria. However, some bacilli can survive inside these structures which providing them a niche, up to a potential reactivation (Saunders and Britton, 2007; Ramakrishnan, 2012; Silva Miranda et al., 2012). Granulomas are present in patients with acute Q fever but the defective immune response observed in chronic Q fever is associated with the absence of granulomas (Delaby et al., 2012; Eldin et al., 2017). Cytokines and chemokines play a critical role in granuloma formation through their control of the recruitment and activation of immune cells (Turner et al., 2014). Indeed, type 1 cytokines such as interferon (IFN)-γ, tumor necrosis factor (TNF), and interleukin (IL)-12 are involved in the acquisition of the microbial competence of macrophages and contribute substantially to the ability of the host to eradicate pathogens. Conversely, IL-10, an anti-inflammatory cytokine, negatively regulates the protective immune response (Gallegos et al., 2011). M1 macrophages are induced by IFN-γ with or without pathogen-associated patterns, they are characterized by increased expression of Toll-like receptors, MHC class II, production of inflammatory cytokines and oxygen derivatives; they promote Th1 responses, microbicidal and tumoricidal activities. In contrast, M2 macrophages are induced by IL-4 or IL-13, express a large panel of C-type lectins, MHC class II and CD163; they express arginase and anti-inflammatory cytokines, promote Th2 responses, parasite clearance and inflammation termination (Murray et al., 2014). In intracellular bacterial infections, $CD4^+$ T cells differentiate into T helper type 1 (Th1) effector cells that secrete IFN-γ and TNF; these mediate protection by stimulating the anti-microbial activity of macrophages (Saunders and Britton, 2007). In a mouse model of mycobacterial infection, the absence of TNF and IFN-γ leads to impaired granuloma formation and increases bacterial infection (Beham et al., 2011; Gallegos et al., 2011). Furthermore, the use of anti-TNF antibodies in patients highlights the role of TNF in granuloma formation. Clinical observations have revealed that anti-TNF-α treatment is associated with a risk of tuberculosis reactivation. However, we recently reported that anti-TNF antibodies do not affect the formation of granulomas but that of MGCs (Mezouar et al., 2019). In humans, impaired IL12/IFN-γ predisposes patients to mycobacterial infections and interferes with granuloma formation depending on the severity of IFN-γ impairment (Naranbhai, 2016).

The study of tissue granulomas in patients requires biopsies, which cannot be performed routinely. Recently, an *in vitro* alternative was proposed. The method is based on the culture of peripheral blood mononuclear cells (PBMCs) with Sepharose beads coated with extracts from BCG, an attenuated strain of *Mycobacterium bovis* (Puissegur et al., 2004), and from *Coxiella burnetii* (CB) (Delaby et al., 2010). The *in vitro* formation of these cell culture systems provides an easy mean for studying the coordination of innate and adaptive immunity that is not possible in patients and may be difficult in animal models. This method is convenient to study the initial phases of granuloma formation and the transcriptional signature. More than 50% of genes are commonly modulated in response to CB and BCG. They include M1-related genes such as HESX1, TNFSF10, IDO1, and TNF, and genes related to chemotaxis (CCL2, CCL5). CB strongly upmodulates the expression of genes involved in microbicidal response, especially ISGs including IFIT1. Furthermore, the expression of genes such as FASLG and GNLY involved in cell death is increased in response to BCG (Faugaret et al., 2014). This approach enables the formation of granulomas to be investigated in clinical practice. Indeed, the *in vitro* formation of granulomas is defective in the majority of patients with chronic Q fever due to a lack of migration of monocytes toward CB-coated beads (Delaby et al., 2012). In brain injury patients, the defective *in vitro* formation of granulomas involving monocytes, natural killer cells, and γδ T cells, is associated with increased nosocomial pneumonia (Deknuydt et al., 2013). In patients with severe sepsis, the defective *in vitro* formation of granulomas is associated to monocytopenia and a reduced production of TNF (Alingrin et al., 2016).

Elderly individuals are at risk of contracting infectious diseases due to their declining immune system known as "immunosenescence." If the latter affects both innate and adaptive immunity, other factors likely contribute to the increased risk; these include undernutrition, comorbidities, altered mucosal barriers, decreased cough reflex, and changes in the urinary tract (Gavazzi and Krause, 2002; Hepper et al., 2013). The most common comorbidities associated to an increased risk of infection are congestive heart failure, chronic kidney failure, diabetes mellitus, cirrhosis, chronic obstructive lung disease, and malignancies (Esper et al., 2006). In infectious diseases, patient outcome is dependent by a complex interplay between pro- and anti-inflammatory host responses (Faix, 2013). In most patients, the pro-inflammatory response is self-limited. However, in patients in sepsis, the response is exaggerated and leads to a compensatory downregulation of the immune system during which the patient is susceptible to organ dysfunction and nosocomial infection. The mechanisms of resistance or susceptibility of individuals are not well-understood. A major risk factor seems to be a pre-existing immune dysfunction. For instance, elderly patients and immunosuppressed patients have a higher incidence of sepsis and a higher mortality rate (Faix, 2013). Martin et al. (2006) showed that the incidence of sepsis is higher in elderly adults and age is an independent predictor of mortality.

We hypothesized that the efficiency of mononuclear cells from infected patients to form granulomas *in vitro* was lower compared to elderly controls which can predispose to nosocomial infections. To test this hypothesis, we assessed the ability of PBMCs to generate granulomas *in vitro* in response to BCG and CB, in order to limit a possible bias linked to our prior immunization (a majority vs. a minority of immunized patients).

MATERIALS AND METHODS

Study Population

Patients recruitment was provided from an ancillary study to NCT02734017. Written informed consent was obtained from the patients or their relatives in accordance with the Declaration of

TABLE 1 | Characteristics of the study population.

	Patients with infection ($n = 23$)	Patients without infection ($n = 24$)	*p*
Age (years)			
mean (min-max)	81.7 (62–100)	84.6 (74–100)	0.78
Male, *n* (%)	9 (39.1)	11 (45.8)	0.25
Medical history, *n* (%)			
Diabetes Mellitus	10 (43.5)	4 (16.6)	0.06
Undernutrition (BMI<21)	4 (17.4)	1 (4.2)	0.16
Chronic lung disease	1 (4.3)	2 (8.3)	0.56
Cardiac insufficiency	6 (26.1)	7 (29.2)	0.75
Dementia	5 (21.7)	9 (37.5)	0.21
Number of circulating cells on admission			
Leukocytes (Giga/L)			
mean [min-max]	10.3 [4.4–20]	6.7 [4.4–11]	<0.001*
Lymphocytes (Giga/L)			
mean [min-max]	1.3 [0.44–3.6]	1.7 [0.62–3.6]	0.09
Neutrophils (Giga/L)			
mean [min-max]	8.1 [3–17]	4.4 [2.1–9.6]	<0.001*
Monocytes (Giga/L)			
mean [min-max]	0.7 [0.21–1.6]	0.7 [0.22–3.8]	0.75
CRP (mg/L)			
mean [min-max]	163.3 [10–449.8]	10.1 [0–48]	<0.001*
Albumin (g/L)			
mean [min-max]	28.7 [18–41.8]	36.1 [29–44.3]	<0.001*

p values for comparisons between patients with infection and healthy controls.
$^*p < 0.05$.

Helsinki. Patients from the geriatric unit at Timone Hospital in Marseille, France were enrolled from January 1st 2017 to April 30th 2017 according to the following criteria: aged over 65 years with at least three chronic illnesses or over 75 years and with presence or absence of sepsis without organ failure lasting for <48 h requiring empirical antimicrobial treatment. We included 23 infected patients with different pathogens and sources of infection and 24 patients without infection as controls. The latter were devoid of immunodeficiency, cancer in the previous 5 years, and immunosuppressive and immunomodulatory drugs. At the time of blood collection, we also collected demographic variables, the body mass index (BMI) to identify undernourished patients (BMI < 21, threshold set for the elderly by the French National Health Authority), comorbidities, biological data, and the source of infection for the infected patients. The main clinical characteristics of the 47 patients enrolled are summarized in **Table 1**.

Mononuclear Cell Isolation

EDTA-anticoagulated blood samples (5 mL) were collected (on day of initiation of empirical antibiotic treatment for infected patients) and immediately sent to the laboratory. Peripheral blood mononuclear cells (PBMCs) from infected patients and controls were isolated from whole blood using a Ficoll gradient (MSL, Eurobio) and suspended in RPMI 1640 containing 25 mM HEPES and 2 mM L-glutamine (Invitrogen) (Alingrin et al., 2016). After centrifugation at 500 × g, PBMCs were washed in sterile phosphate-buffered saline (PBS, Life Technologies) and suspended (about 5×10^6 cells/ml) in RPMI 1640 supplemented with 20% fetal calf serum (FCS, Invitrogen) and 10% dimethylsulfoxide, and preserved at −80°C.

Coupling of Beads With Bacterial Extracts

CB organisms (Nine Mile strain, RSA 495) and BCG (CIP 105050) were cultured as described previously (Delaby et al., 2010). The bacteria (10^9 per assay) were sonicated in a coupling buffer (0.1 M NaHCO3 pH 8.3 containing 0.5 M NaCl) and their protein content was determined using Bradford's method (BioRad protein assay) (Delaby et al., 2010). Cyanogen-bromide (CN-Br)-activated Sepharose 4B beads 40 to 100 µm in diameter (GE Healthcare, France) were suspended in 1 mM HCl for 15 min and then washed in a coupling buffer according to the manufacturer's instructions.

Bacterial extracts (0.5 mg of protein corresponding to about 2.5×10^8 bacteria) were added to 10 mg (4×10^4 beads) of beads and mixed overnight at 4°C in a coupling buffer. After centrifugation at 120 × g for 10 min, the coupling efficiency of the bacterial extracts was determined by measuring the protein content of the supernatants. The beads were then washed, and the remaining CN-Br active groups were blocked by incubating the beads with 0.1 M Tris–HCl buffer pH 8.0 for 2 h. After centrifugation at 120 × *g* for 10 min, the beads were washed again three times in acetate and Tris-HCl buffers. The beads were finally stored at 4 °C in PBS for 1 month.

Granuloma Formation

In vitro granuloma formation was assessed after incubation of 2.5×10^5 PBMCs with 50 Sepharose beads coated with either CB or BCG extracts in 96-well plates containing RPMI 1640 medium supplemented with 25 mM HEPES, 2 mM of L-glutamine, 10% FCS, and antibiotics at 37°C. The formation of granulomas was evaluated after 3, 6, and 9 days of culture using inverse microscopy (DIM3000 B, Leica). Only beads completely covered with cells were considered granulomas. The percentage of beads with granulomas was determined by optical microscope examination of 3 wells per experiment.

Cell Characterization

Granulomas were collected with manual pipette. They were then incubated with 0.05% Trypsine-0.53Mm EDTA for 15 min at 37°C to dissociate cells. Cells were collected, plated onto glass slides with a cytospin (5 min at 1,500 rpm) and then stained with May-Grünwald Giemsa (Sigma, France) to identify epithelioid cells and MGCs in dissociated granuloma cells (Puissegur et al., 2004; Delaby et al., 2010). MGCs were identified by the presence of more than three nuclei. The percentage of epithelioid cells and MGCs in the stained preparations was quantified by optical microscope examination after 3, 6, and 9 days of culture.

Dissociated granuloma cells (5×10^5) were also analyzed using flow cytometry (Puissegur et al., 2004; Delaby et al., 2010).

PBMCs were labeled with a mixture of the following fluorescent antibodies: CD3-PC5 (Beckman Coulter, France), CD4-APC (Dako, France), CD8-PE (Beckman Coulter, France), CD68-FTIC (Dako, France), and CD45-APC H7 (Becton Dickinson Biosciences, France) with isotype-matched fluorophore-conjugated immunoglobulin G (IgG) for the controls. Cell populations were identified using a CANTO II flow cytometer (Becton Dickinson Biosciences) and DIVA BD software (San Jose, CA) was used to analyze the data.

In patients unable to form granulomas, the cells were recovered without having to dissociate them from the beads and analyzed in the same way as the granuloma cells with May-Grünwald Giemsa staining and immunophenotyping.

Cytokine Measurement

PBMCs (2.5×10^5 cells/well) were incubated with coated beads (50 beads/well) and the supernatants were collected after 1 and 3 days, whether or not granulomas have formed. TNF and IL-10 production were measured in the supernatants from cell cultures forming or not granulomas, using enzyme immunoassays (R&D Systems, Quantinine® ELISA kit) according to the manufacturer's instructions. The results were expressed as pg/ml. The intra- and inter-specific coefficients of variation ranged from 5 to 10%.

Transcriptomic Analysis (RNA Extraction and qRT-PCR)

Granuloma cells were dissociated by incubation in PBS buffer containing 2 mM EDTA (Invitrogen) if necessary. Total RNA from granuloma cells or mononuclear cell was extracted and treated with DNase using the RNeasy® Mini Kit (Qiagen). Reverse transcription of 150 ng of total RNA was performed as described previously (Ben Amara et al., 2010). We assessed the expression of nine M1 (TNFSF10, IL15RA, IDO1, IL2RA, TNF, IL15, EDN1, HESX1, CXCL29), seven M2 (ALOX15, FN1, CCL23, CCL13, CLEC4, CSTE, HRH1), and four granulomatous genes (EPBH2, FASLG, GNLY, IFIT1) in response to CB and BCG, as previously studied (Faugaret et al., 2014). Gene expression was analyzed in cells from granulomas after dissociation in eight individuals (5 were infected) who formed granulomas and in mononuclear cells in three patients who did not form granulomas (2 were infected). PBMCS were cultured without coated beads (unstimulated cells) and were used as control for fold change calculation. All selected primers were designed using Primer3 (version 0.4.0; http://bioinfo.ut.ee/primer3/). Quantitative PCR was performed using LightCycler FastStart DNA Master^{PLUS} SYBR Green I (Roche). The results were normalized with the housekeeping gene β-actin. The fold change (FC) of the target genes relative to β-actin was computed using the formula $FC = 2^{-\Delta\Delta Ct}$, where $\Delta\Delta Ct = (Ct_{Target} - Ct_{Actin})_{stimulated} - (Ct_{Target} - Ct_{Actin})_{unstimulated}$ (Ben Amara et al., 2010).

Statistical Analysis

Quantitative data are presented as the mean with range or standard deviation. Qualitative results are presented as absolute counts and percentages. Results between groups were compared using Student's *t*-test or Mann-Whitney non-parametric test when the conditions for applying the *t*-test were not met. Differences were considered significant when $p < 0.05$. Data

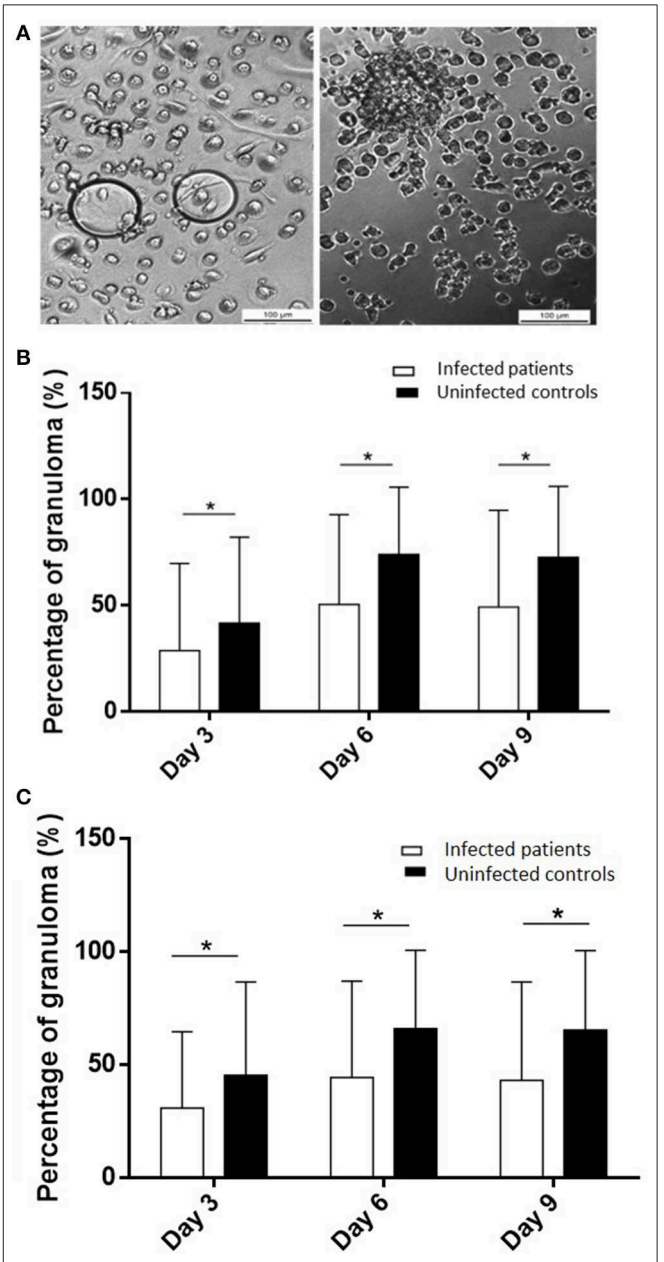

FIGURE 1 | Granuloma formation in infected patients and uninfected controls. PBMCs ($2.5 \times 10^{5)}$ from healthy and infected patients were incubated with 50 Sepharose beads coated with bacterial extracts for 9 days. The entire content of three wells per experiment was examined under an optical microscope to determine the number of granulomas. Only beads completely covered by cells were considered granulomas. **(A)** Representative micrographs of beads coated with BCG with PBMCs from an infected patient with no granuloma (left) and from a control with a representative granuloma (right). **(B,C)** The number of generated granulomas in response to BCG extracts **(B)** and CB extracts **(C)** was enumerated and the results are expressed in percentage of bead-associated granulomas and presented as the mean ± SD. *$p < 0.05$.

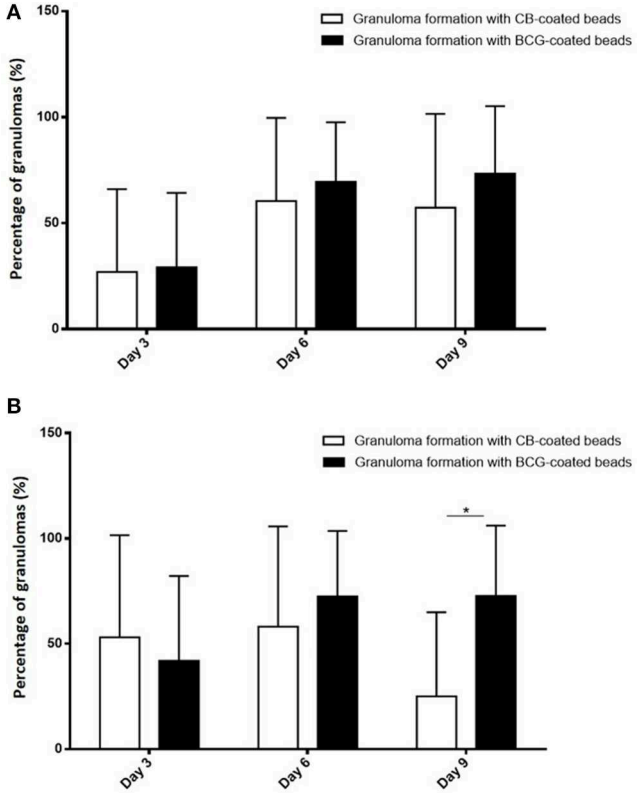

FIGURE 2 | Comparison of granuloma formation in response to BCG and CB extract. PBMCs (2.5×10^5) from healthy and infected patients were incubated with 50 Sepharose beads coated with bacterial extracts for 9 days. The entire content of three wells per experiment was examined under an optical microscope to determine the number of granulomas. Only beads completely covered by cells were considered granulomas. The results are expressed in percentage of bead-associated granulomas and presented as the mean ± SD. *$p < 0.05$. **(A)** There was no significant difference in granuloma formation in infected patients, regardless of the beads used. **(B)** In **controls**, the percentage of granulomas on day 9 was significantly lower with the CB-coated beads than the BCG-coated beads.

analysis was performed, and plots were generated using GraphPad Prism 5 (GraphPad Software Inc).

RESULTS

Patient Characteristics

The characteristics of the study population are shown in **Table 1.** Twenty-three infected patients (14 women and 9 men) with an average age of 81.7 years and 24 uninfected controls (13 women and 11 men) with an average age of 84.6 years were included. The leukocyte and neutrophil counts were significantly ($p < 0.001$) higher in infected patients than in controls, whereas the monocyte and lymphocyte counts were not significantly different. C-reactive protein and albumin levels were significantly ($p < 0.001$) higher and lower, respectively, in infected patients. The most frequent infections were urinary tract infections (7 patients) and pneumonia (7 patients). The microbial etiology was identified in <50% of infected patients and consisted mainly of gram-negative bacilli ($n = 8$). No patient had a medical history of tuberculosis or Q fever.

Defective Formation of Granulomas in Infected Patients

To test if the occurrence of infection in elderly subjects was associated with impaired granuloma formation, PBMCs from

TABLE 2 | Granuloma formation and characteristics of infected patients.

	Infected patients forming granulomas	Infected patients not forming granulomas	*p*
Number of patients	11/23 (48%)	12/23 (52%)	0.77
Patients (female/male)	9/2	4/7	1
Age (years)			
mean (min-max)	82.9 [65–100]	80.7 [65–93]	0.59
Medical history, n			
Diabetes Mellitus	3/11	7/12	0.14
Undernutrition (BMI<21)	0/11	4/12	0.02*
Chronic lung disease	0/11	0/12	1
Cardiac insufficiency	3/11	2/12	0.56
Dementia	2/11	4/12	0.43
Leukocytes (Giga/L)			
mean [min-max]	12 [5.9–20]	9.2 [4.4–12]	0.5
Neutrophils (Giga/L)			
mean [min-max]	9.8 [4.5–17]	7.0 [3–10]	0.7
Monocytes (Giga/L)			
mean [min-max]	0.9 [0.33–1.6]	0.6 [0.21–1.3]	0.1
Lymphocytes (Giga/L)			
mean [min-max]	1.3 [0.44–3.6]	1.4 [0.8–2.3]	0.8
C-reactive protein (mg/L)			
mean [min-max]	195.3 [36.2–449.8]	143.1 [10–337]	0.25
Albumin (g/L)			
mean [min-max]	29.5 [19–41.8]	27.9 [18–34.6]	0.57

p-values for comparisons between infected patients that formed granulomas and infected patients that did not form granulomas.
**p < 0.05.*

TABLE 3 | Sources of infection and pathogens involved in infected patients.

	Infected patients forming granulomas	Infected patients not forming granulomas
Sources of infection, *n*	Urinary infection (*n* = 2) Pneumonia (*n* = 3) Digestive infection (*n* = 2) Skin infection (*n* = 2) Spondylitis (*n* = 1) Sepsis (*n* = 1)	Urinary infection (*n* = 5) Pneumonia (*n* = 4) Digestive infection (*n* = 1) Sepsis (*n* = 2)
Pathogens involved, *n*	4/11 *E. coli* (*n* = 3) *S. aureus* (*n* = 1)	7/12 *E. coli* (*n* = 3) *S. aureus* (*n* = 1) *P. mirabilis* (*n* = 1) *K. pneumoniae* (*n* = 1) Metapneumovirus (*n* = 1)

TABLE 4 | Granuloma formation and characteristics of uninfected controls.

	Controls forming granulomas	Controls not forming granulomas	*p*
Number of patients	22/24 (92%)	2/24 (8%)	
Patients (female/male)	12/10	2/0	0.23
Age (years)			
mean (min-max)	83.1 [74–100]	84 [81–87]	0.82
Medical history, n			
Diabetes Mellitus	4/22	0/2	0.53
Undernutrition (BMI < 21)	1/22	2/2	0.02 *
Chronic lung disease	2/22	0/2	0.67
Cardiac insufficiency	2/22	0/2	0.67
Dementia	7/22	0/2	0.36
Leukocytes (Giga/L)			
mean [min-max]	6.8 [4.4–11]	5.55 [5.4–5.7]	0.002*
Neutrophils (Giga/L)			
mean [min-max]	4.4 [2.9–9.6]	2.9 [2.1–3.2]	0.02*
Monocytes (Giga/L)			
mean [min-max]	0.71 [0.29–3.8]	0.4 [0.22–0.61]	0.34
Lymphocytes (Giga/L)			
mean [min-max]	1.65 [0.62–3.6]	1.75 [1.2–2.3]	0.89
C-reactive protein (mg/L)			
mean [min-max]	8.7 [0–33]	25.0 [2–48]	0.61
Albumin (g/L)			
mean [min-max]	36.3 [29–44.3]	34.1 [32.3–36]	0.44

p-values for comparisons between controls forming granulomas and controls not forming granulomas.
$^*p < 0.05$.

controls and infected patients were incubated with beads coated with BCG and granuloma formation was measured for 9 days (**Figure 1A**). The great majority of uninfected controls (22 out of 24, 92%) were able to form granulomas, whereas only 48% of infected patients were. The impaired formation of granulomas in infected patients was not due to a delayed formation because the formation of granulomas was significantly lower in infected patients than in controls at days 3, 6, and 9 ($p < 0.05$) (**Figure 1B**). After cultivating PBMCs with BCG-coated beads for 3 days, the formation of granulomas was significantly lower in infected patients ($22 \pm 36\%$), whereas it reached $42 \pm 40\%$ in controls. It was not a delayed formation because it remained lower in infected patients than in controls after 6 days (50 ± 42 vs. $74 \pm 31\%$) and 9 days (49 ± 45 vs. $72 \pm 33\%$). Interestingly, when CB-coated beads were used instead of BCG-beads, the patients who did not form granulomas in response to BCG extracts were also unable to form granulomas in response to CB extracts. After 3 days of culture of PBMCs with CB-coated beads, the formation of granulomas was also significantly low in infected patients ($p = 0.03$). The formation of granulomas remained lower in infected patients than controls after 6 and 9 days ($p = 0.0049$ and 0.002, respectively) (**Figure 1C**). The comparison of granuloma formation in response to BCG and CB extracts did not show any significant difference, except at day 9 for controls for whom the granuloma percentage was significantly lower in response to CB extracts than in response to BCG (**Figure 2**). Taken together, these results show that the ability to develop an *in vitro* granulomatous response to BCG or CB extracts was altered in infected elderly patients. Given these results, the following experiments were performed with BCG-coated beads only.

Granuloma Formation and Patient Characteristics

As infected patients were partitioned into two populations able or unable to form granulomas, we investigated if impaired granuloma formation was associated with some clinical and/or biological features of patients (**Tables 2**–**4**). We found that infected female patients were more prone to forming granulomas than their male counterparts. This gender effect was not observed in controls. Among the clinical parameters, undernutrition defined by a BMI <21 was significantly associated with impaired granuloma formation in both controls and infected patients ($p = 0.02$). The inflammatory status as assessed by the CRP level was not significantly different in infected patients who did or did not form granulomas. Leukocyte and neutrophil counts were significantly higher in controls who formed granulomas than in patients who did not form granulomas. No difference was found in infected patients. So, except undernutrition, no significant difference was found between patients with and without granuloma formation. Hence, clinical and biological parameters were not sufficient to account for impaired granuloma formation.

Cell Composition of Granulomas

We measured the proportion of cell populations placed in culture from patients who would form granulomas and those who would not. The proportion of monocytes and $CD4^+$ and $CD8^+$ T lymphocytes determined using flow cytometry was similar between controls and infected patients regardless of their capacity to form granulomas or not (data not shown).

In the absence of granuloma formation, the proportion of monocytes and T cells did not change during the culture. In the presence of granuloma formation in response to BCG, $CD4^+$ T lymphocytes steadily increased during the culture with BCG-coated beads, whereas $CD8^+$ T cells moderately decreased during the same time. No difference was observed between infected and controls. Monocytes from each group decreased during the 9 days of culture; this is related to their macrophage maturation (data not shown).

As granulomas are known to be rich in epithelioid cells and MGCs (**Figures 3A,B**), their presence was assessed using May-Grünwald-Giemsa staining after 3, 6, and 9 days. When cultured mononuclear cells were unable to form granulomas, especially in infected patients, neither epithelioid cells nor MGCs were found. When granulomas were formed, epithelioid cells and MGCs were detected from day 3 and reached almost 25 and 4% of granulomatous cells, respectively, on day 9 in controls (**Figure 3C**). In infected patients, epithelioid cells represented on average 13% of the granuloma cells on day 6 then decreased to reach about 10% after 9 days. Concerning MGCs, they did not exceed 2% after 6 days of culture then decreased (**Figure 3D**). Thus, granulomas of controls contained significantly more

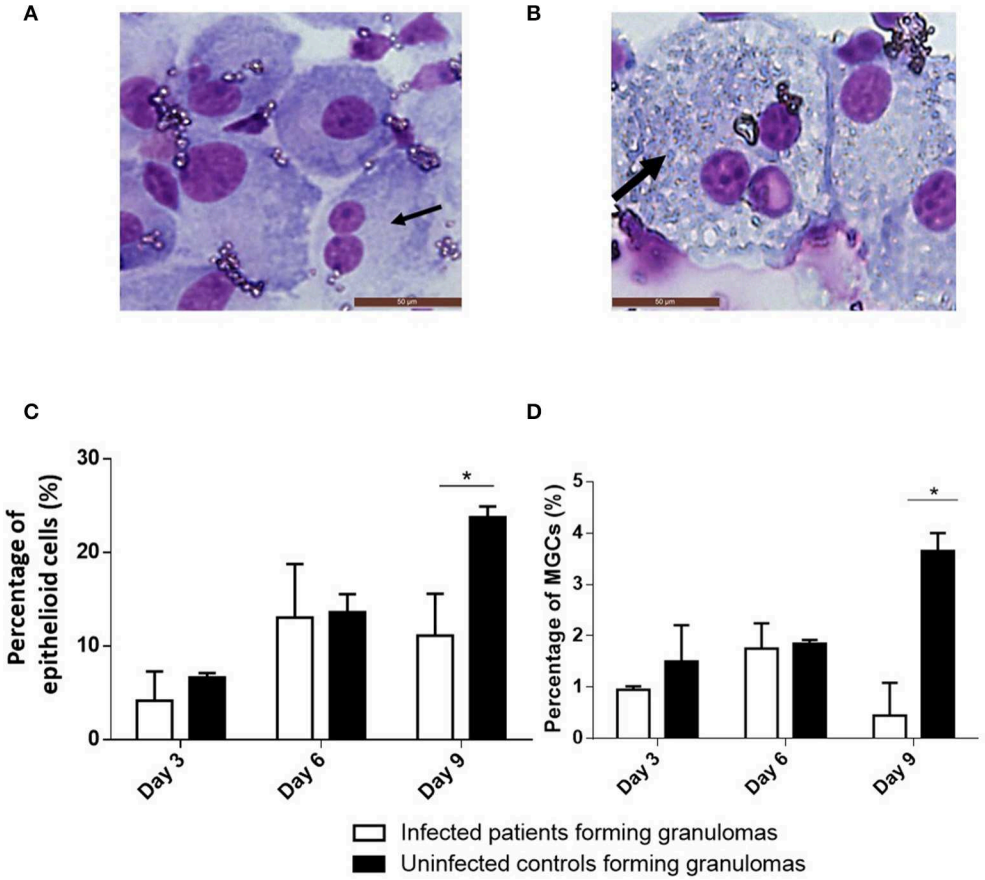

FIGURE 3 | Cell composition of granulomas. BCG-granulomas were recovered and the cells were dissociated from the beads by mechanical agitation. They were then stained using May-Grünwald Giemsa staining and observed under an optical microscope. The percentages of cells were compared between six infected patients and six controls. Each experiment was performed in duplicate. **(A)** The black arrow indicates a typical epithelioid cell. **(B)** The thick black arrow indicates a typical MGC. **(C,D)** The proportion of epithelioid cells and MGCs relative to the granuloma cells was determined after 3, 6, and 9 days. The results are presented as the mean ± SD. *$p < 0.05$.

epithelioid cells and MGCs than granulomas of infected patients ($p = 0.04$ and $p = 0.02$, respectively). These results highlighted that the defective formation of granulomas was associated with deficient epithelioid cell and MGC formation.

Cytokines and Deficient Granuloma Formation in Infected Patients

As the defective formation of granulomas in infected patients may be associated with a decrease in inflammatory cytokines, we measured the release of TNF and IL-10 by cells incubated with BCG-coated beads for 1 and 3 days. First, we noticed that the amounts of TNF in the supernatants were lower on day 3 compared with the results on day 1. The amounts were significantly lower in controls and infected patients who did not form granulomas than in controls and infected patients with granuloma formation on day 1 as well as on day 3 ($p < 0.05$ for controls and $p < 0.001$ for infected patients) (**Figure 4**). The decrease in production of TNF may be related to an increase of an immunosuppressive cytokine such as IL-10. Therefore, the amounts of IL-10 in the supernatants were measured. They were low and similar in infected and controls with or without granuloma formation (**Figure 4**). These results suggested that the defective formation of granulomas was associated with a decrease in TNF production without an increase in IL-10 production.

Gene Expression Programs and Deficient Granuloma Formation in Infected Patients

As the alteration in granuloma formation was related to TNF deficiency, we investigated the activation status of granulomatous cells in individuals who formed granulomas. We collected cells from granulomas after dissociation in eight patients who formed granulomas (5 infected patients and 3 controls) and assessed the expression of a panel of nine M1, seven M2, and four granulomatous genes, as reported previously (Naranbhai, 2016). In patients who formed granulomas, M1, M2, and granulomatous genes were upregulated, suggesting strong activation of granulomatous cells without M1 or M2 polarization (**Figure 5A**). It is noteworthy that in patients who did not form granulomas ($n = 3$), the expression of M1, M2, and granulomatous genes was markedly depressed, with

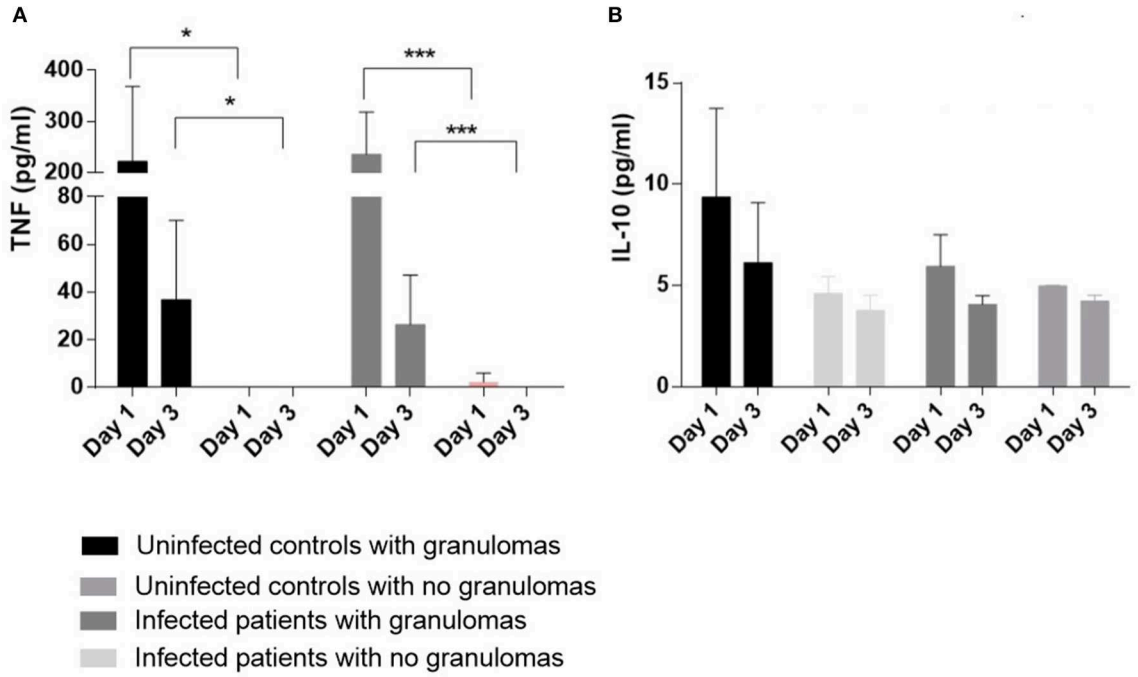

FIGURE 4 | Cytokine production PBMCs (2.5×10^5) from 13 controls (11 who formed granulomas and 2 who did not form granulomas) and 16 infected patients (7 who formed granulomas and 9 unable to form granulomas) were incubated with 50 Sepharose beads coated with BCG extracts for 1 and 3 days. The supernatants were collected after 1 and 3 days. TNF measurements **(A)** and IL-10 measurements **(B)** were performed with the supernatants from cell cultures forming or not granulomas, using enzyme immunoassays. The results are expressed as pg/mL and presented as the mean ± SD. $^*p < 0.05$, $^{***}p < 0.0001$.

the exception of TNFSF10 (**Figure 5B**). Hence, the granulomas formed in healthy individuals and infected patients exhibited normal activation profiles. Uninfected and infected patients with impaired formation of granulomas are associated with a profound alteration in the activation program of immune cells.

DISCUSSION

Elderly patients are susceptible to infection. Several factors affect the prognosis of infected elderly patients such as immunosenescence-associated immunosuppression, age-related organ changes, comorbidities, undernutrition or polypharmacy (Tannaou et al., 2019). A major risk factor seems also to be a pre-existing immune dysfunction. We hypothesized that the efficiency of mononuclear cells from infected patients to form granulomas *in vitro* was lower compared to elderly controls and we proposed answering this question by measuring the *in vitro* formation of granulomas using beads coated with BCG (Puissegur et al., 2004) and CB (Delaby et al., 2012) extracts. The choice of this model was only intended to explore the overall immune response to pathogens at a given time, which is difficult with other cell-mediated immune assays.

We showed that granuloma formation was impaired in infected patients compared to uninfected controls in response to both BCG and CB extracts. To exempt our data from the constraints of prior immunization, we compared granuloma formation in response to BCG to which a majority of individuals are immunized and CB to which a minority of individuals are immunized. Clearly, our results are not dependent on prior immunization as the modulation of BCG and CB granulomas was similar. This result is consistent with defective granuloma formation observed in patients with severe sepsis (Alingrin et al., 2016). Likewise, PBMCs from brain-injured patients with nosocomial pneumonia formed significantly fewer granulomas compared with brain-injured patients without nosocomial pneumonia and healthy donors (Deknuydt et al., 2013).

Deficient granuloma formation was observed in a large proportion (48%) of infected patients and a minority of uninfected controls (8%). No relationship was found between defective granuloma formation and age, sex or comorbidities. Clinically, only undernutrition was significantly associated with the impairment of granuloma formation. The causes of undernutrition in the elderly are varied and often multiple. They can be divided into three main types: medical, social, and psychological. Besides the causes of undernutrition unrelated to age (cancers, chronic inflammatory and psychiatric diseases for example), there are many risk situations that are more specific to the elderly. Aging is often associated with decreases in taste acuity and smell, deteriorating dental health, polypharmacy, cognitive disorders and less physical activity, which may all affect nutrient intake. Malnutrition can lead to a decrease in T cells. The number of $CD4^+$ T cells from spleens of fasted mice is 40 to 50% lower compared to fed control animals (Saucillo et al., 2014). Other studies have shown that mice fed a protein-deficient diet

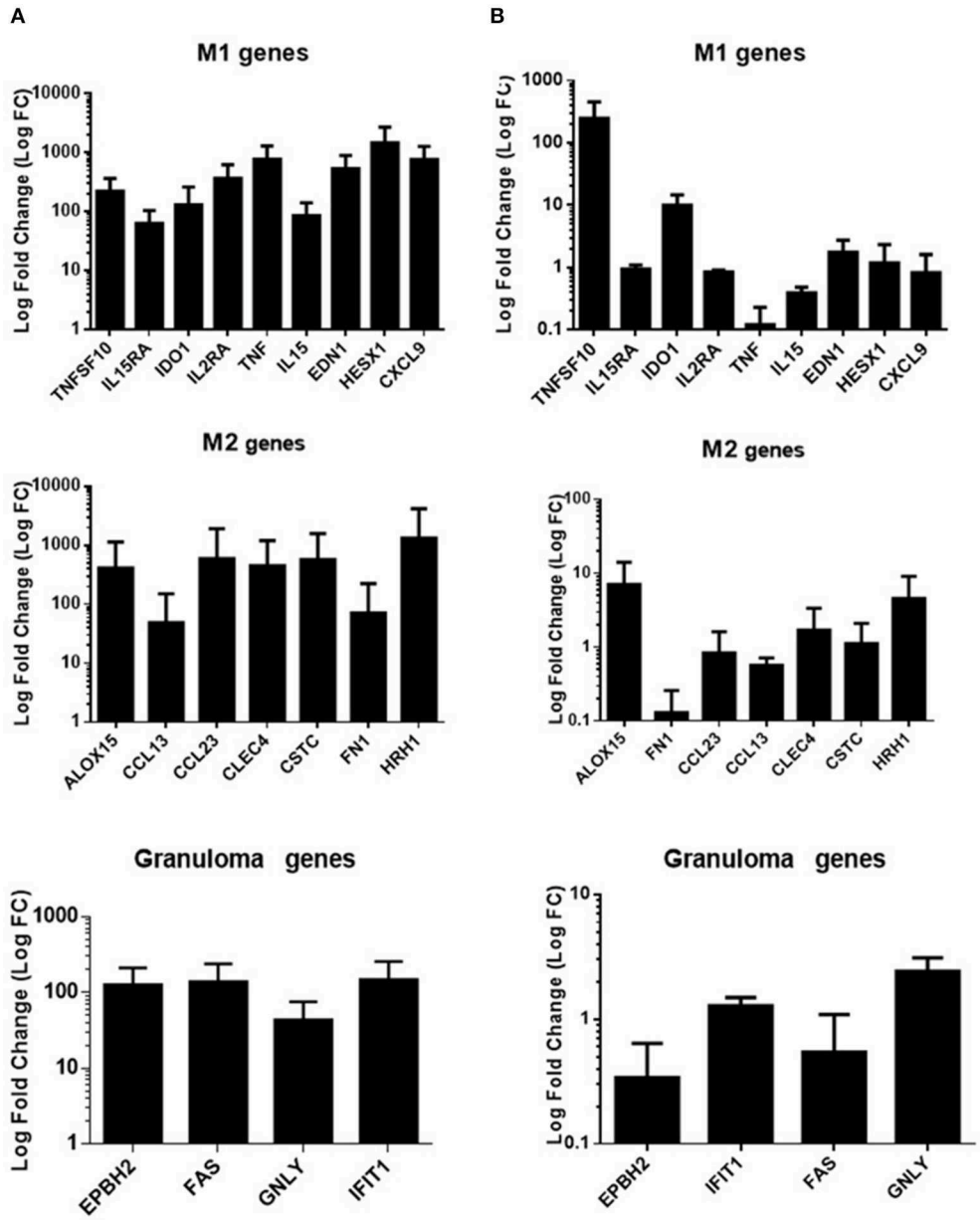

FIGURE 5 | Gene expression program in infected patients. qRT-PCR was performed on a panel of M1, M2, and granulomatous genes. Gene expression was analyzed in cells from granulomas after dissociation in eight individuals (5 were infected) who formed granulomas **(A)** and in mononuclear cells in three patients who did not form granulomas (2 were infected) **(B)**. PBMCS were cultured without coated beads (unstimulated cells) and were used as control for fold change calculation. The results were normalized with the housekeeping gene β-actin. The FC of the target genes relative to β-actin was computed using the formula FC $= 2^{\Delta\Delta Ct}$, where $\Delta\Delta Ct = (Ct_{Target} - Ct_{Actin})_{stimulated} - (Ct_{Target} - Ct_{Actin})_{unstimulated.}$ The results are expressed as the log fold change ± SD.

exhibit lower T cell numbers compared to chow-fed control mice (Pena-Cruz et al., 1989; Taylor et al., 2013). A similar observation was made in humans. Malnourished children have lower circulating $CD4^+$ and $CD8^+$ T cell numbers compared to well-nourished children (Najera et al., 2004). The decrease in immune cell numbers during malnutrition contributes to a reduced ability of the immune system to mount a successful immune response to infection. This accounts for increased susceptibility to microbial pathogens such as influenza, *Mycobacterium tuberculosis*, *Streptococcus pneumonia*, and gastrointestinal infection microbes in malnourished individuals (Cegielski and McMurray, 2004; Verhagen et al., 2013). A relationship between defective granuloma formation and monocyte and lymphocyte counts has been reported in the absence of undernutrition. In patients with severe sepsis, the defective granuloma formation was associated with monocytopenia, whereas brain-injured

patients experienced lymphopenia with a non-significant trend toward a lower lymphocyte count in patients with nosocomial pneumonia compared with patients without infection (Deknuydt et al., 2013; Alingrin et al., 2016).

We showed previously that monocytes migrate to the beads, mature into macrophages, then progress to epithelioid cells and MGCs under the influence of lymphocytes (Delaby et al., 2010). We found that when mononuclear cells did not form granulomas, neither epithelioid cells nor MGCs were found. When mononuclear cells formed granulomas, the number of epithelioid cells and MGCs in infected elderly patients was lower than in granulomas of controls. This alteration of granuloma organization is consistent with other reports. In brain-injured patients, the percentage of MGCs was lower in patients, especially with infection, compared with healthy donors (Deknuydt et al., 2013). These results suggest that the maturation process of macrophages is impaired in infected patients.

As many reports have established a relationship between cytokine production and granuloma formation, including the presence of epithelioid cells and MGCs, we investigated pro/anti-inflammatory cytokine imbalance. TNF is necessary for the formation of granulomas and Il-10 is involved in the inhibition of macrophage activation and high levels are associated with a disorganization of granulomas (Boomer et al., 2014; Pagán and Ramakrishnan, 2018). We found that TNF release decreased in PBMCs from patients unable to form granulomas with no increase in IL-10, suggesting that the modulation of TNF production was not related to the overproduction of IL-10. Similar results were obtained in patients with severe sepsis (Alingrin et al., 2016). Several studies have highlighted through the use of TNF deficient mice or anti-TNF-α drugs that TNF-α is essential for the formation and maintenance of granulomas (Kindler et al., 1989; Roach et al., 2000). Recently, we showed that etanercept (a fusion protein of IgG1 Fc domain and the extracellular ligand-binding portion of the human p75 TNF receptor) slightly delayed the formation of granulomas and reduced the generation of MGCs by inhibiting cell fusion in the same way as adalimumab treatment (a human monoclonal anti-TNF-α IgG1) (Mezouar et al., 2019). As the transformation and fusion of macrophages require autocrine stimulation by TNF production, the low production of TNF can explain the defective differentiation of granuloma macrophages we observed (Takashima et al., 1993).

We previously reported that BCG- and CB-induced granulomas were characterized by the expression of genes related to M1 macrophage polarization and chemotaxis (Faugaret et al., 2014). First, we found that polarization and granuloma formation-associated gene expression was dramatically decreased in mononuclear cells that did not form granulomas. M1, M2, and granulomatous gene expression was upregulated without polarization in patients who formed granulomas. The lack of polarization may be related to immunosenescence.

Altogether, we have shown that infection in elderly patients decreases granuloma formation and reduces the production of TNF-α and the formation of epithelioid cells and MGCs (**Supplementary Figure 1**). This study also suggests that the impact of infection on the granuloma formation is heterogeneous in elderly patients. Further studies are necessary to understand why some patients form granulomas and others do not when they are infected.

DATA AVAILABILITY STATEMENT

The raw data supporting the conclusions of this article will be made available by the authors, without undue reservation, to any qualified researcher.

ETHICS STATEMENT

This study was approved by regional ethic committee Sud Méditerranée I. All the methods described were in accordance with the Declaration of Helsinski and national and international standards. The patients provided their written informed consent to participate in this study.

AUTHOR CONTRIBUTIONS

AD and J-LM designed the study. AD, JA, CC, and AB carried out the experiments. AD, BC, PV, and J-LM carried out the statistical analysis and drafted the manuscript. All authors read and approved the final version of the manuscript.

ACKNOWLEDGMENTS

We thank Christian Capo for his attentive reading of our manuscript and Catherine Lepolard for his help in setting up experiments.

SUPPLEMENTARY MATERIAL

The Supplementary Material for this article can be found online at: https://www.frontiersin.org/articles/10.3389/fcimb.2020.00189/full#supplementary-material

Supplementary Figure 1 | Summarizes the main results of the study. Most healthy elderly patients (92%) were able to form granulomas compared to only 48% of infected elderly patients. Granulomas typically comprise epithelioid cells and multinucleated giant cells. The impairment of granuloma formation was associated with reduced production of TNF without overproduction of IL-10. All genes specifically modulated in granulomatous cells were down-modulated in patients with defective granuloma formation.

REFERENCES

Alingrin, J., Coiffard, B., Textoris, J., Belenotti, P., Daumas, A., Leone, M., et al. (2016). Impaired granuloma formation in sepsis: impact of monocytopenia. *PLoS ONE* 11:e0158528. doi: 10.1371/journal.pone.0158528

Beham, A. W., Puellmann, K., Laird, R., Fuchs, T., Streich, R., Breysach, C., et al. (2011). A TNF-regulated recombinatorial macrophage immune receptor implicated in granuloma formation in tuberculosis. *PLoS Pathog.* 7:e1002375. doi: 10.1371/journal.ppat.1002375

Ben Amara, A., Ghigo, E., Le Priol, Y., Lépolard, C., Salcedo, S. P., Lemichez, E., et al. (2010). Coxiella burnetii, the agent of Q fever, replicates within trophoblasts and induces a unique transcriptional response. *PLoS ONE* 5:e15315. doi: 10.1371/journal.pone.0015315

Boomer, J. S., Green, J. M., and Hotchkiss, R. S. (2014). The changing immune system in sepsis: is individualized immuno-modulatory therapy the answer? *Virulence* 5, 45–56. doi: 10.4161/viru.26516

Cegielski, J. P., and McMurray, D. N. (2004). The relationship between malnutrition and tuberculosis: evidence from studies in humans and experimental animals. *Int. J. Tuberc. Lung Dis*. 8, 286–298.

Deknuydt, F., Roquilly, A., Cinotti, R., Altare, F., and Asehnoune, K. (2013). An *in vitro* model of mycobacterial granuloma to investigate the immune response in brain-injured patients. *Crit. Care Med*. 41, 245–254. doi: 10.1097/CCM.0b013e3182676052

Delaby, A., Espinosa, L., Lépolard, C., Capo, C., and Mège, J. L. (2010). 3D reconstruction of granulomas from transmitted light images implemented for long-time microscope applications. *J. Immunol. Methods* 360, 10–19. doi: 10.1016/j.jim.2010.06.008

Delaby, A., Gorvel, L., Espinosa, L., Lépolard, C., Raoult, D., Ghigo, E., et al. (2012). Defective monocyte dynamics in Q fever granuloma deficiency. *J. Infect. Dis*. 205, 1086–1094. doi: 10.1093/infdis/jis013

Eldin, C., Mélenotte, C., Mediannikov, O., Ghigo, E., Million, M., Edouard, S., et al. (2017). From Q fever to coxiella burnetii infection: a paradigm change. *Clin. Microbiol. Rev*. 30, 115–190. doi: 10.1128/CMR.00045–16

Esper, A. M., Moss, M., Lewis, C. A., Nisbet, R., Mannino, D. M., and Martin, G. S. (2006). The role of infection and comorbidity; factors that influence disparities in sepsis. *Crit. Care Med*. 34, 2576–2582. doi: 10.1097/01.CCM.0000239114.50519.0E

Faix, J. D. (2013). Biomarkers of sepsis. *Crit. Rev. Clin. Lab Sci*. 50, 23–36. doi: 10.3109/10408363.2013.764490

Faugaret, D., Ben Amara, A., Alingrin, J., Daumas, A., Delaby, A., Lépolard, C., et al. (2014). Granulomatous response to *Coxiella burnetii*, the agent of Q fever: the lessons from gene expression analysis. *Front. Cell Infect. Microbiol*. 4:172. doi: 10.3389/fcimb.2014.00172

Gallegos, A. M., van Heijst, J. W., Samstein, M., Su, X., Pamer, E. G., and Glickman, M. S. (2011). A gamma interferon independent mechanism of CD4 T cell mediated control of M. *tuberculosis* infection *in vivo*. *PLoS Pathog*. 7:e1002052. doi: 10.1371/journal.ppat.1002052

Gavazzi, G., and Krause, K. H. (2002). Ageing and infection. *Lancet Infect Dis*. 2, 659–666. doi: 10.1016/S1473–3099(02)00437–1

Hepper, H. J., Sieber, C., Walger, P., Bahrmann, P., and Singler, K. (2013). Infections in the elderly. *Crit. Care Clin*. 29, 757–774. doi: 10.1016/j.ccc.2013.03.016

Herndon, G., and Rogers, H. J. (2013). Multiple "doughnut" granulomas in Coxiella burnetii infection, (Q fever). *Blood* 122:3099. doi: 10.1182/blood-2013–06-511063

Kindler, V., Sappino, A. P., Grau, G. E., Piguet, P. F., and Vassalli, P. (1989). The inducing role of tumor necrosis factor in the development of bactericidal granulomas during BCG infection. *Cell* 56, 731–740. doi: 10.1016/0092–8674(89)90676–4

Martin, G. S., Mannino, D. M., and Moss, M. (2006). The effect of age on the development and outcome of adult sepsis. *Crit. Care Med*. 34, 15–21. doi: 10.1097/01.CCM.0000194535.82812.BA

Mezouar, S., Diarra, I., Roudier, J., Desnues, B., and Mege, J. L. (2019). Tumor necrosis factor-alpha antagonist interferes with the formation of granulomatous multinucleated giant cells: new insights into *Mycobacterium tuberculosis* infection. *Front. Immunol*. 10:1947. doi: 10.3389/fimmu.2019.01947

Murray, P. J., Allen, J. E., Biswas, S. K., Fisher, E. A., Gilroy, D. W., Goerdt, S., et al. (2014). Macrophage activation and polarization: nomenclature and experimental guidelines. *Immunity* 41, 14–20. doi: 10.1016/j.immuni.2014.06.008

Najera, O., Gonzalez, C., Toledo, G., Lopez, L., and Ortiz, R. (2004). Flow cytometry study of lymphocyte subsets in malnourished and well-nourished children with bacterial infections. *Clin. Diagn. Lab Immunol*. 11, 577–580. doi: 10.1128/CDLI.11.3.577–580.2004

Naranbhai, V. (2016). The role of host genetics, (and genomics) in Tuberculosis. *Microbiol Spectr*. 4:5. doi: 10.1128/microbiolspec.TBTB2-0011-2016

Pagán, A. J., and Ramakrishnan, L. (2018). The formation and function of granulomas. *Annu. Rev. Immunol*. 36, 639–665. doi: 10.1146/annurev-immunol-032712–100022

Pena-Cruz, V., Reiss, C. S., and McIntosh, K. (1989). Sendai virus infection of mice with protein malnutrition. *J. Virol*. 63:354164. doi: 10.1128/JVI.63.8.3541–3544.1989

Puissegur, M. P., Botanch, C., Duteyrat, J. L., Delsol, G., Caratero, C., and Altare, F. (2004). An *in vitro* dual model of mycobacterial granulomas to investigate the molecular interactions between mycobacteria and human host cells. *Cell Microbiol*. 6, 423–433. doi: 10.1111/j.1462–5822.2004.00371.x

Ramakrishnan, L. (2012). Revisiting the role of the granuloma in tuberculosis. *Nat. Rev. Immunol*. 12, 352–366. doi: 10.1038/nri3211

Roach, D. R., Bean, A. G., Demangel, C., France, M. P., Briscoe, H., and Britton, W. J. (2000). TNF regulates chemokine induction essential for cell recruitment, granuloma formation, and clearance of mycobacterial infection. *J. Immunol*. 168, 4620–4627. doi: 10.4049/jimmunol.168.9.4620

Saucillo, D. C., Gerriets, V. A., Sheng, J., Rathmell, J. C., and Maciver, N. J. (2014). Leptin metabolically licenses T cells for activation to link nutrition and immunity. *J Immunol*. 192, 136–144. doi: 10.4049/jimmunol.1301158

Saunders, B. M., and Britton, W. J. (2007). Life and death in the granuloma: immunopathology of tuberculosis. *Immunol. Cell Biol*. 85, 103–111. doi: 10.1038/sj.icb.7100027

Silva Miranda, M., Breiman, A., Allain, S., Deknuydt, F., and Altare, F. (2012). The tuberculous granuloma: an unsuccessful host defence mechanism providing a safety shelter for the bacteria? *Clin. Dev. Immunol*. 2012:139127. doi: 10.1155/2012/139127

Takashima, T., Ohnishi, K., Tsuyuguchi, I., and Kishimoto, S. (1993). Differential regulation of formation of multinucleated giant cells from concanavalin A-stimulated human blood monocytes by IFN-gamma and IL-4. *J. Immunol*. 150, 3002–310.

Tannaou, T., Koeberle, S., Manckoundia, P., and Aubry, R. (2019). Multifactorial immunodeficiency in frail elderly patients: contributing factors and management. *Med. Mal. Infect*. 49, 167–172. doi: 10.1016/j.medmal.2019.01.012

Taylor, A. K., Cao, W., Vora, K. P., De La Cruz, J., Shieh, W. J., and Zaki, S. R., et al. (2013). Protein energy malnutrition decreases immunity and increases susceptibility to influenza infection in mice. *J. Infect. Dis*. 207, 501–510. doi: 10.1093/infdis/jis527

Turner, M. D., Nedjai, B., Hurst, T., and Pennington, D. J. (2014). Cytokines and chemokines: at the crossroads of cell signalling and inflammatory disease. *Biochim Biophys. Acta*. 1843, 2563–2582. doi: 10.1016/j.bbamcr.2014.05.014

Verhagen, L. M., Gomez-Castellano, K., Snelders, E., Rivera-Olivero, I., Pocaterra, L., Melchers, W. J., et al. (2013). Respiratory infections in Enepa Amerindians are related to malnutrition and *Streptococcus pneumoniae* carriage. *J. Infect*. 67, 273–281. doi: 10.1016/j.jinf.2013.06.010

Conflict of Interest: The authors declare that the research was conducted in the absence of any commercial or financial relationships that could be construed as a potential conflict of interest.

Copyright © 2020 Daumas, Coiffard, Chartier, Ben amara, Alingrin, Villani and Mege. This is an open-access article distributed under the terms of the Creative Commons Attribution License (CC BY). The use, distribution or reproduction in other forums is permitted, provided the original author(s) and the copyright owner(s) are credited and that the original publication in this journal is cited, in accordance with accepted academic practice. No use, distribution or reproduction is permitted which does not comply with these terms.

frontiers in Cellular and Infection Microbiology

ORIGINAL RESEARCH
published: 29 April 2020
doi: 10.3389/fcimb.2020.00180

Mesoporous Hydroxyapatite/Chitosan Loaded With Recombinant-Human Amelogenin Could Enhance Antibacterial Effect and Promote Periodontal Regeneration

Yue Liao[1,2†], *Huxiao Li*[1,2†], *Rong Shu*[1,2], *Huiwen Chen*[1,2], *Liping Zhao*[3], *Zhongchen Song*[1,2*] *and Wei Zhou*[2,4*]

[1] *Department of Periodontology, Shanghai Ninth People's Hospital, Shanghai Jiao Tong University School of Medicine, Shanghai, China,* [2] *Shanghai Key Laboratory of Stomatology, National Clinical Research Center for Oral Diseases, Shanghai Research Institute of Stomatology, Shanghai, China,* [3] *State Key Laboratory for Metallic Matrix Composite Materials, School of Materials Science and Engineering, Shanghai Jiao Tong University, Shanghai, China,* [4] *Laboratory of Oral Microbiota and Systemic Disease, Shanghai Research Institute of Stomatology, Ninth People's Hospital, Shanghai Jiao Tong University School of Medicine, Shanghai, China*

The recovery of impaired periodontium is still a challenge to the treatment of periodontitis. This study was the first to apply the mesoporous hydroxyapatites/chitosan (mHA/CS) composite scaffold to periodontal regeneration. The aim of our study is to evaluate the biological effects of mesoporous hydroxyapatite/chitosan (mHA/CS) loaded with recombinant human amelogenin (rhAm) on periodontal regeneration. The physicochemical properties of mHA/CS scaffolds were examined by Fourier transform infrared spectroscopy (FTIR), transmission electron microscopy (TEM), and Brunauer–Emmett–Teller (BET) analysis. Then, the biological effects of the mHA/CS loaded with rhAm were evaluated, including antibacterial effect, controlled-release capacity, osteogenic and cementogenic effects *in vitro* and *in vivo*. The antibacterial effect was tested on 1.5 mg/mL CS; 3 mg/mL mHA; 2.25 mg/mL mHA/CS; 4.5 mg/mL mHA/CS and 20 μg/mL rhAm. Tryptic Soy Broth culture medium was used as a baseline control. Osteogenic effect of rhAm (20 μg/mL rhAm), mHA/CS (4.5 mg/mL mHA/CS), and mHA/CS-rhAm (4.5 mg/mL mHA/CS and 20 μg/mL rhAm) on human periodontal ligament cells (hPDLCs) was evaluated in osteogenic media. The hPDLCs treated either with osteogenic media or Dulbecco's modified Eagle's medium (DMEM) alone were used as the baseline control. In the animal model, 4-week-old nude mice (BALB/c) ($n = 6$) implanted with root slices subcutaneously were used to observe the cementogenic effect *in vivo*. The root slices were treated with rhAm (20 μg/mL rhAm), mHA/CS (4.5 mg/mL mHA/CS), and mHA/CS-rhAm (4.5 mg/mL mHA/CS and 20 μg/mL rhAm). The root slices treated with osteogenic medium alone were used as the baseline control. The analyses showed that the mHA/CS particles were 2 μm in diameter and had a uniform pore size.

OPEN ACCESS

Edited by:
Sigrun Lange, University of Westminster, United Kingdom

Reviewed by:
Krishnamurithy Genasan, University of Malaya, Malaysia
Daniel Champlin Propheter, University of Texas Southwestern Medical Center, United States

***Correspondence:**
Zhongchen Song
szhongchen@sina.com
Wei Zhou
sweetzw@hotmail.com

[†] These authors have contributed equally to this work and co-first authors

Specialty section:
This article was submitted to Microbiome in Health and Disease, a section of the journal Frontiers in Cellular and Infection Microbiology

Received: *06 February 2020*
Accepted: *06 April 2020*
Published: *29 April 2020*

Citation:
Liao Y, Li H, Shu R, Chen H, Zhao L, Song Z and Zhou W (2020) Mesoporous Hydroxyapatite/Chitosan Loaded With Recombinant-Human Amelogenin Could Enhance Antibacterial Effect and Promote Periodontal Regeneration. Front. Cell. Infect. Microbiol. 10:180. doi: 10.3389/fcimb.2020.00180

The mesoporous structure was 7 nm in diameter and its surface area was 33.95 m^2/g. The scaffold exhibited antibacterial effects against *Fusobacterium nucleatum* and *Porphyromonas gingivalis*. The mHA/CS scaffold sustainably released rhAm. The mHA/CS loaded with 20 μg/mL rhAm upregulated ALP activity, the expression levels of osteogenesis-related genes and proteins *in vitro*. Additionally, it promoted the formation of cementum-like tissue *in vivo*. Our findings suggest that mHA/CS loaded with 20 μg/mL rhAm could inhibit the growth of periodontal pathogens and promote the formation of bone and cementum-like tissue.

Keywords: mesoporous hydroxyapatite, Chitosan, rhAm, periodontal regeneration, antibacterial effect

INTRODUCTION

Periodontitis, as one of the most prevalent oral diseases, which is characterized by the destruction of alveolar bone, which will result in the loosening of teeth and even the loss of teeth (Miranda et al., 2016). Periodontal treatment can eliminate chronic inflammation and infection and stop the progression of disease. However, periodontal defects could hardly be restored to their original form and function (Ivanovski et al., 2014). Therefore, many studies have focused on the use of tissue engineering techniques to achieve the periodontal regeneration, which include three major elements: seed cells, scaffolds, and growth factors (Ogawa et al., 2016).

Periodontal ligament cells have been convinced as the ideal seed cells for periodontal regeneration (Gauthier et al., 2017), which have the capacity of forming cementum-like and periodontal ligament-like tissues (Mrozik et al., 2017). Scaffolds play a vital role in supporting cell adherence and proliferation, maintaining space, and sustainably releasing of growth factors. In addition, the scaffold should be biocompatible and degradable, as it will eventually be replaced by the newly formed tissue (Han et al., 2014; Liu et al., 2016).

A mesoporous structure is a kind of nanostructure with pore sizes ranging from 2 to 50 nm that had attracted great attention in recent years owing to its well-ordered channel system, high porosity, and large surface area (Wu and Chang, 2012; Lee et al., 2016). With the aid of mesoporous structures, scaffolds can load more growth factors and improve bioactivity and cell attachment (Baino et al., 2016).

Hydroxyapatite (HA) is regarded as one of the ideal scaffolds in periodontal tissue engineering. As its similarity to the mineral composition of bones, it has good biocompatibility and bioactive properties (Xiong et al., 2015; Cholas et al., 2016). Thus, mesoporous hydroxyapatites (mHA) scaffold retain the benefits of both hydroxyapatites and mesoporous structures. Experimental studies have shown that nanostructured hydroxyapatites were beneficial to the proliferation and osteogenic differentiation of hPDLCs (Ou et al., 2019), bone marrow mesenchymal stem cells (BMSCs) (Krishnamurithy et al., 2019; Liu et al., 2019; Jose et al., 2020) and adipose-derived stem cells (ADSCs) (Huang et al., 2020). Moreover, nanostructured hydroxyapatites show higher levels of alkaline phosphatase activity than microhydroxyapatites (Domingos et al., 2017). However, compared with the traditional nanohydroxyapatites, few studies have focused on the mesoporous hydroxyapatite.

Despite their benefits, mesoporous hydroxyapatites still have limitations in terms of their mechanical properties, degradation rates and drug release properties (Xiao et al., 2016; Jang et al., 2017). In addition, natural high-polymer materials, such as chitosan (CS), possess high elasticity, and porosity (Rodríguez-Vázquez et al., 2015). Additionally, chitosan has broad-spectrum antimicrobial and anti-inflammatory properties. It has exhibited effective antibacterial activity against several oral pathogens and inhibited the growth of periodontal pathogens (Hu et al., 2019; Zupančič et al., 2019). However, chitosan has inevitable disadvantages, such as the high degradation rate and low mechanical strength (Rodríguez-Vázquez et al., 2015).

When hydroxyapatite and chitosan are combined together as a composite scaffold, it could retain the benefits of good biocompatibility and mechanical strength. The degradation rate is also adjusted. Organic-inorganic nanocomposites have been shown to be beneficial in many fields, such as tissue engineering and drug delivery (Ali and Ahmed, 2017), and a nano hydroxyapatite/chitosan composite scaffold has been used to achieve favorable outcomes for bone regeneration (Deepthi et al., 2016). A positive effect was observed when it was used for periodontal regeneration (Qasim et al., 2015). However, few studies have focused on the biological effects of mHA/CS when used in the field of periodontal regeneration.

Growth factors are also crucial elements in tissue engineering. Enamel matrix proteins (EMPs) have been widely used in periodontal regeneration and have demonstrated the capacity for promoting wound healing, restricting epithelial downgrowth, and supporting the regeneration of a complete periodontal attachment apparatus (Bosshardt et al., 2015; Talebi Ardakani et al., 2019). Amelogenin is the main composition of enamel matrix proteins (Wyganowska-Swiatkowska et al., 2015). The recombinant human amelogenin (rhAm) used in our study was purified from prokaryotic expression system. As periodontitis is a chronic inflammatory disease caused by bacteria plaque, the destructive periodontium is usually under an inflammatory and hypoxia microenvironment, which is unfavorable for the healing of periodontium. So, one of the challenges is to recover the periodontal tissue under the inflammatory microenvironment, and even reverse the inhibitory effect of the inflammatory and hypoxia (Song et al., 2017). The rhAm at a concentration of 20 μg/mL can promote the proliferation of hPDLCs and

enhance ALP activity in an inflammatory microenvironment, which indicates that rhAm could improve the osteogenic effect of hPDLCs and compensate for the bone resorption caused by *P. gingivalis* LPS (Dong et al., 2016). The mHA/CS could be an appropriate carrier for rhAm. Firstly, the large specific surface area of mHA could improve loading capacity of rhAm. Secondly, the positive charges from chitosan will be attracted to the negatively charged surface of mHA, which could form a coating layer (Zhang et al., 2016; Feiz and Meshkini, 2019). So, it is suggested that rhAm could be released sustainably accompanied by lower degradation rate of CS with the help of electrostatic interaction between mHA and CS.

It is the first time to apply the mesoporous hydroxyapatite/chitosan loaded with rhAm (mHA/CS-rhAm) to periodontal regeneration. This study was aimed to analyze the physicochemical properties, sustained-release effect and antibacterial effect of mHA/CS against periodontal pathogens. Then the osteogenesis effects of mHA/CS/rhAm was examined on hPDLCs *in vitro*, and cementogenic effects was observed on root slices *in vivo* (**Supplementary Figure 1**). So, our study is to provide an experimental basis for further investigations in the field of clinical periodontal regeneration.

MATERIALS AND METHODS

Fabrication of mHA and mHA/CS

Briefly, a Cetyltrimethyl Ammonium Bromide (CTAB) solution was mixed with a $(NH_4)_2HPO_4$ solution. After 3 h of vigorous stirring, $CaCl_2$ solution was dripped into the solution (10 drops/min) at room temperature and stirred for 1 h. The mixed solution was transferred to a reaction kettle to react for 24 h at 100°C. The precipitates were washed with ethyl alcohol for four times, and then dried up in a vacuum-drying oven for 8 h at 40°C. The precipitates were ground into powder. Finally, the mesoporous hydroxyapatites could be obtained after calcination in a muffle furnace for 5 h at 600°C. The Ca/P molar ratio is 5/3.

Mesoporous hydroxyapatite/chitosan scaffolds were synthesized by a hydrothermal method. Chitosan (1 g) was dissolved in acetic acid solution (2 wt%, 50 mL), followed by the addition of mesoporous hydroxyapatites (2 g). Chitosan was mixed with mesoporous hydroxyapatites at a mass ratio of 1:2. After 10 h of vigorous stirring, liquid paraffin (50 mL) and Span 80 (5 mL) were added dropwise into the solution at room temperature. Dilute the 25% glutaraldehyde solution (0.25 mL) with acetic acid solution (2 wt%, 50 mL) before incorporating it into the mixed solution. The precipitates were centrifuged and washed with a chloroform and ethyl alcohol solution for four times. Finally, the mesoporous hydroxyapatite/chitosan composites could be obtained after dehydration in a vacuum-drying oven at 40°C for 8 h.

Characterization of mHA and mHA/CS

The chemical compositions of the scaffolds were analyzed by Fourier transform infrared spectroscopy (Nicolet 6700, Thermo Fisher Scientific, USA). Then, the surface morphology was observed by objective TEM (JEM-2010F; JEOL Ltd, Japan). The specific surface area and pore size were automatically calculated by an automatic analysis instrument (Autosorb IQ, Quantachrome, USA) via the Brunauer–Emmett–Teller (BET) method.

Bacterial Culture

Fusobacterium nucleatum (*F. nucleatum*; ATCC 25586) and *Porphyromonas gingivalis* (*P. gingivalis*; ATCC 33277) were provided by the Shanghai Research Institute of Stomatology and the Shanghai Key Laboratory of Stomatology, Shanghai Ninth People's Hospital (Shanghai, China). *F. nucleatum* and *P. gingivalis* were maintained in Tryptic Soy Broth (TSB; Bacto™, BD, Sparks, MD, USA) and Tryptic Soy Agar (TSA; Bacto™, BD, Sparks, MD, USA), supplemented with 0.5% yeast extract and 0.5% L-cysteine hydrochloride. In addition, 10 μg/mL vitamin K and 5 μg/mL hemin were added to the culture medium of *P. gingivalis*.

Antibacterial Activity of mHA/CS

TSB-based culture medium was added into a flat-bottomed 24-well plate. *F. nucleatum* and *P. gingivalis* suspensions at final concentrations of 1×10^4 colony-forming units (CFU)/mL and 1×10^7 CFU/mL, respectively, were added to the culture medium in the presence of 1.5 mg/mL CS, 3 mg/mL mHA, 2.25 mg/mL mHA/CS, 4.5 mg/mL mHA/CS or 20 μg/mL rhAm. As CS and mHA were mixed at a mass ratio of 1:2, 4.5 mg/mL mHA/CS was consisted of 1.5 mg/mL CS and 3 mg/mL mHA. TSB-based culture medium was used as a blank control, and the culture medium containing bacterial suspension was used as a negative control. After 48 h of culture, the antibacterial activity was evaluated on the basis of the OD values at a wavelength of 600 nm.

F. nucleatum and *P. gingivalis* biofilms were prepared as the description of Zhou et al. (2016), and the samples were also divided into six groups in accordance with the treatment conditions described above. The bacterial cells were stained with the LIVE/DEAD® BacLightTM Bacterial Viability Kit (Molecular Probes Inc., Eugene, OR, USA). After 15 min, the samples were observed from a confocal laser scanning microscope (CLSM, Leica TCS SP2, Germany).

Isolation and Culture of Human PDLCs

The isolation and culture of hPDLCs were performed on the basis of the method of Song Z. C. et al. (2012). Informed consent was obtained from the patients prior to acquire samples. The Institute Review Board number for the use of human tissue samples is 2018-120-T98, which was proved by Shanghai Ninth People's Hospital. Human PDLCs were obtained from healthy premolars and impacted third molars. The extracted tooth were washed with sterilized PBS for three times. Then the periodontal ligament tissues were scraped off carefully from the root of extracted tooth with surgical blade, and cultured in Dulbecco's modified Eagle's medium (DMEM, Sigma, USA), which is supplemented with 20% fetal bovine serum (FBS). The DMEM was changed every 5–7 days until confluent cells appeared.

MTT Assay

The hPDLCs were added (1×10^5 cells/well) to 96-well plates. Then, 4.5 mg/mL mHA/CS was added to the culture media of the mHA/CS group. The samples were cultured for 1, 3, and 7 days. Twenty microliter MTT solution (5 mg/mL, Sigma, USA) was added into each well and incubated with hPDLCs for 4 h. Subsequently, solution in each well was replaced by 150 μl DMSO. After 5 min standing, the plate was shaken slightly for about 5 min before detection. The absorbance was measured at a wavelength of 490 nm.

Measurement of rhAm Release

The samples were divided into three groups. The mHA, CS and mHA/CS suspension liquids were mixed with 20 μg/mL rhAm. The controlled release effect of mHA/CS was measured according to the approach described by Xia et al. with some modifications (Xia et al., 2018). The mHA and mHA/CS composite particles were immersed in phosphate-buffered saline solution (PBS, Sigma, USA) for 24 h in the presence of 20 μg/mL rhAm. After centrifugation, the mHA and mHA/CS particles loaded with rhAm were added to 1 mL PBS. One hundred milliliters of supernatant were extracted at 1, 2, 4, 8 h, 1, 3, and 7 days. The amount of rhAm in the supernatant was evaluated by an ELISA kit.

Evaluation of the Osteogenic Effect of mHA/CS

The samples were divided into five groups: group D (Dulbecco's modified Eagle's medium); group C (osteogenic differentiation medium only); group rhAm (osteogenic differentiation medium with 20 μg/mL rhAm); group mHA/CS (4.5 mg/mL mHA/CS and osteogenic differentiation medium); group mHA/CS-rhAm (4.5 mg/mL mHA/CS and osteogenic differentiation medium with 20 μg/mL rhAm). Group C was the control group. The osteogenic induction medium (Cyagen, USA) consists of DMEM with 20% fetal bovine serum, β-glycerophosphate disodium salt (10 mmol/L), dexamethasone (0.1 μmol/L) and ascorbic acid (50 mg/L).

The hPDLCs were implanted (1×10^5 cells/well) into 24-well plates and incubated for 24 h. Then, the samples were divided into four groups as previously described and different culture media were added into each well according to their grouping. The samples were incubated for 7 days before the staining. The ALP activity was determined with BCIP-NBT Alkaline Phosphatase Color Development Kit (Beyotime Biotechnology, China) on the basis of the method described by Dumont et al. (2016). After 7 days' treatment, the hPDLCs were fixed with 4% paraformaldehyde for 30 min, then washed with PBS for three times. Subsequently, the solution of BCIP-NBT was prepared as the instructions. One hundred microliters of BCIP-NBT was added dropwise into each well and incubated for 2 h before the observation of the staining.

Cells from different groups were collected at days 3 and 7 after treatment. The osteogenic genes were evaluated by real-time PCR, including RUNX-2, OPN, and DLX-5. The mRNA level of glyceraldehyde-3-phosphate dehydrogenase (GAPDH) acted as an internal control. The ΔΔCt method was used to determine the expression of the target genes. The primers used in the determination are as follows (**Table 1**).

TABLE 1 | The primers sequence of genes used in RT-PCR.

Target gene	Primer sequence
RUNX2	Forward: 5′-GCGGTGCAAACTTTCTCCAG-3′
	Reverse: 5′-TCACTGCACTGAAGAGGCTG-3′
OPN	Forward: 5′-CCAGCCAAGGACCAACTACA-3′
	Reverse: 5′-AGTGTTTGCTGTAATGCGCC-3′
DLX5	Forward: 5′-GCTCAATCAATTCCCACCTGC-3′
	Reverse: 5′-AGCCCATCTAATAAAGCGTCCC-3′
GAPDH	Forward: 5′-CGGGAAACTGTGGCGTGAT-3′
	Reverse: 5′-GTCGCTGTTGAAGTCAGAGGAG-3′

RS, root slice; M, ePTFE membrane; MT, mouse tissue; NFT, new fibrous tissue; NFC, newly-formed cementum-like tissue.

Samples for Western Blotting were also obtained at days 3 and 7. The primary antibodies used are as follows: RUNX-2, OPN, DLX-5, and GAPDH. Subsequently, secondary antibodies were used for the incubation of PVDF membranes. The protein bands were detected by a chemiluminescence detection system (Gel Doc 200, Bio-Rad Laboratories, USA). The intensities of protein bands were analyzed by Image J software to obtain the gray values, which could be analyzed statistically.

In vivo Experiment

All experimental protocols were performed according to the guidelines in EU Directive (2010/63/EU), which was also approved by the ethical committee of the Animal Care and Experimental Committee of the Shanghai Jiao Tong University School of Medicine (Approval no. SH9H-2019-A499-1). Six 4-week-old nude mice (BALB/c) were used for the experiment. They were raised together for 1 week before the experiment to accustomed to the environment.

The preparation of the root slices was according to the method described by Song et al. (2007). The extracted teeth were subject to careful scaling and root planning. Then, the roots were cut into slices longitudinally. After conditioning with 24% EDTA for 2 min, the root slices were washed with PBS repeatedly and sterilized under ultraviolet light for 4 h.

The samples were also divided into four groups: group C; group rhAm; group mHA/CS, and group mHA/CS-rhAm. The root slices were transported in 6-well plates with one root slice per well. Then, hPDLCs were added (2×10^6 cells/well) into the 6-well plates and cocultured with root slices. The culture medium was added, respectively: group C (2 mL osteogenic differentiation medium/well); group rhAm (2 mL osteogenic differentiation medium + 40 μg rhAm/well); group mHA/CS (2 mL osteogenic differentiation medium + 9 mg mHA/CS/well) and group mHA/CS-rhAm (2 mL osteogenic differentiation medium + 9 mg mHA/CS + 40 μg rhAm/well).

After 7 days of coculture, the root slices were wrapped with polytetrafluoroethylene (ePTFE) membranes and implanted into nude mice subcutaneously under anesthesia. At the eighth week after surgery, the root slices were removed along with the surrounding skin and subcutaneous tissue. The specimens were

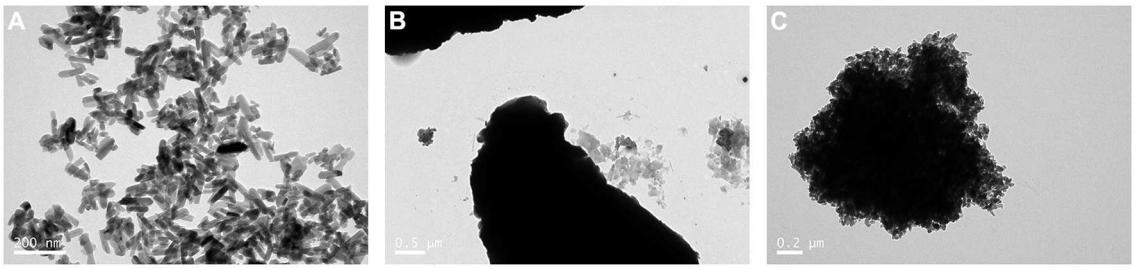

FIGURE 1 | TEM image of mHA, CS, and mHA/CS. **(A)** mHA, observed as short rod-like particles (scale bar 0.2 μm). **(B)** CS, observed as particles with no fixed shape and size (scale bar 0.5 μm). **(C)** mHA/CS, constructed with spherical agglomerates (scale bar 0.2 μm).

demineralized and dehydrated. The specimens were stained and observed from the microscope.

Statistical Analysis

The statistical analyses of the data were performed with SAS 9.3 (SAS Institute, Cary, NC, USA). Analysis of variance (ANOVA) and Student's *t*-test were used to evaluate the data in the different groups. The *in vitro* experiments were repeated for more than three times, and the sample size for animal model was based on the study of (Fawzy El-Sayed and Dörfer, 2017). The statistical differences were achieved at $p < 0.05$.

RESULTS

Characterization of mHA and mHA/CS

The results of the TEM analysis showed that mHA are short rod-like particles that are approximately 20–30 nm in width and 50–100 nm in length (**Figure 1A**). The particles of chitosan have no fixed shapes (**Figure 1B**). However, when the mHA particles were combined with chitosan, the composites formed spherical agglomerates with a diameter of 2 μm (**Figure 1C**).

The FTIR spectra of mHA, CS and the synthetic mHA/CS are presented in **Figure 2**. The spectrum of mHA was characterized by bands at 562 and 1029 cm^{-1}, which were assigned to the peak of PO_4^{3-}. The peaks at 634 and 3,659 cm^{-1} were the results of the peak of OH^-. In the spectrum of chitosan, peaks were observed at 2,920 and 2,877 cm^{-1}, which contributed to the C-H bond in chitosan. The bands for amide I and amide II were detected at 1,655 and 1,599 cm^{-1}. All the characteristic peaks of mHA and CS could be found in the spectrum of the synthesized sample, which means the sample was mHA/CS.

As shown in **Figure 3**, the synthesized sample was mesoporous with an average pore diameter of 7 nm, and a peak was detected along the horizontal axis. The specific surface was 33.95 m^2/g.

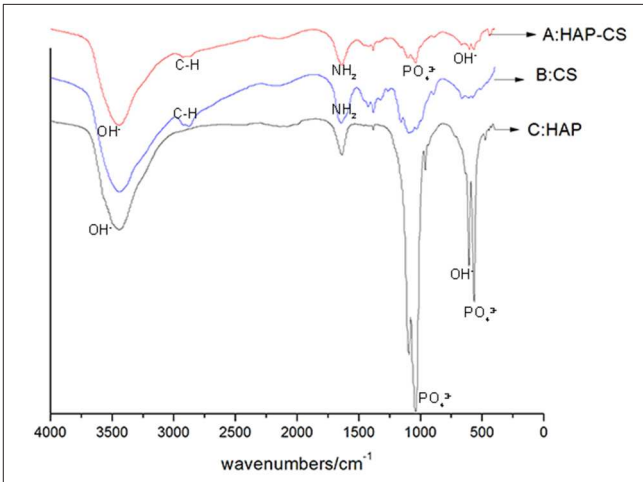

FIGURE 2 | FTIR spectra of mesoporous hydroxyapatite (HAP), chitosan (CS), and mesoporous hydroxyapatite/chitosan (HAP-CS). **(A)** FTIR spectra of HAP-CS, containing characteristic peaks of both HAP and CS. **(B)** FTIR spectra of CS, containing characteristic peaks of C-N and $-NH_2$. **(C)** FTIR spectra of HAP, containing characteristic peaks of PO_4^{3-} and OH^-.

Antibacterial Effects

The antibacterial effects of mHA, CS, mHA/CS and rhAm were evaluated on the basis of the OD values (**Figures 4**, **5**). The mHA/CS exhibited dose-dependent inhibition of the growth of *F. nucleatum* and *P. gingivalis*. When mHA/CS was at a concentration of 2.25 mg/mL, the OD values of *F. nucleatum* and *P. gingivalis* showed a declining trend. However, there was no statistically significant difference compared with the control group ($p > 0.01$). When the concentration of mHA/CS reached 4.5 mg/mL, the OD values of *F. nucleatum* and *P. gingivalis* were significantly lower than those of the control group ($p < 0.01$).

The presence of 3 mg/mL of mHA and 20 μg/mL rhAm did not result in antibacterial effects on *F. nucleatum* and *P. gingivalis* ($p > 0.01$). However, 1.5 mg/mL chitosan was shown to decrease the growth of both *F. nucleatum* and *P. gingivalis* in comparison with the control group ($p < 0.01$).

The bacterial live/dead fluorescence staining was observed with CLSM to identify the antibacterial effects on *F. nucleatum* and *P. gingivalis* biofilms (**Figures 6**, **7**). The bacteria stained green have intact cell membranes, while the bacteria stained red have impaired cell membranes. It meant that live cells were green and dead cells were red. According to the results, most of the cells were alive in the control group, the 3 mg/mL mHA group and the 20 μg/mL rhAm group. There were several small clusters of dead cells in the 2.25 mg/mL mHA/CS group. While, large amount of

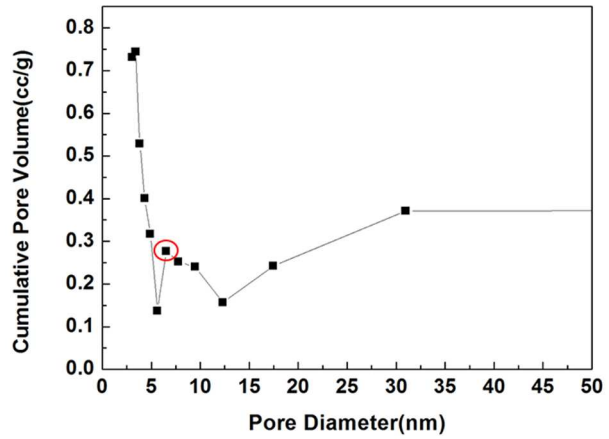

FIGURE 3 | BET image of mHA/CS. Circle, A peak was detected at 7 nm along the horizontal axis, which is the pore size.

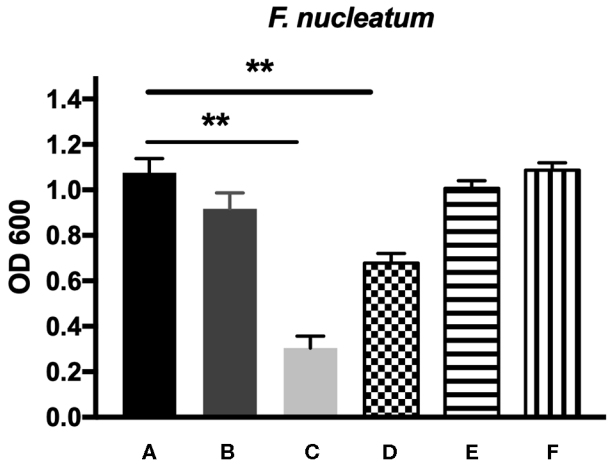

FIGURE 4 | The antibacterial effects of mHA, CS, mHA/CS, and rhAm on 10^4 CFU/mL *F. nucleatum*. **(A)** Tryptic Soy Broth culture (baseline control), **(B)** 2.25 mg/mL mHA/CS, **(C)** 4.5 mg/mL mHA/CS, **(D)** 1.5 mg/mL CS, **(E)** 3 mg/mL mHA, and **(F)** 20μg/mL rhAm (statistically significant against baseline control, $^{**}p < 0.01$).

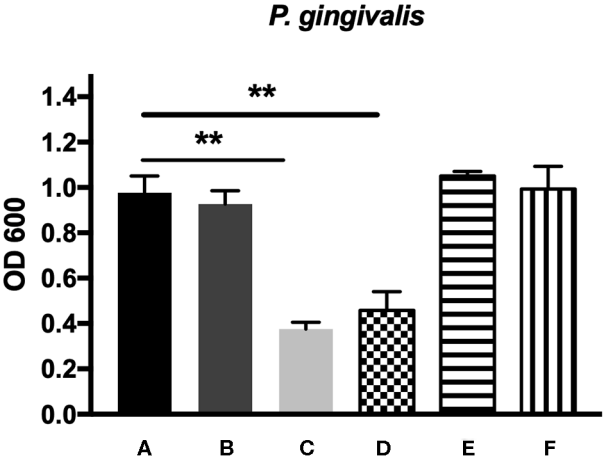

FIGURE 5 | The antibacterial effects of mHA, CS, mHA/CS, and rhAm on 10^7 CFU/mL *P. gingivalis*. **(A)** Tryptic Soy Broth culture (baseline control), **(B)** 2.25 mg/mL mHA/CS, **(C)** 4.5 mg/mL mHA/CS, **(D)** 1.5 mg/mL CS, **(E)** 3 mg/mL mHA, and **(F)** 20μg/mL rhAm (statistically significant against baseline control, $^{**}p < 0.01$).

dead cells were observed in the 4.5 mg/mL mHA/CS group and the 1.5 mg/mL CS group, which was far more than the live cells in number.

Examination of Cytotoxicity

The cytotoxic effect of mHA/CS on hPDLCs was examined by an MTT assay. On the basis of the results of the assays of antibacterial effects, mHA/CS at a concentration of 4.5 mg/mL was used for the following study. There was no significant difference observed between the mHA/CS and baseline control at days 1, 3, or 7 (**Figure 8**).

Controlled-Release Profile

The amount of rhAm released from mHA, CS and mHA/CS at selected time points is shown in **Figure 9**. As the sustained release of rhAm lasted for 7 days, the cumulative release amount of rhAm was calculated according to the results of Elisa test and compared with the release amount at the other time point.

The mHA group exhibited a "release burst" within the initial hour and had a cumulative release percentage of 89%. Subsequently, rhAm was released at a relatively low rate until day 7. However, the early release rate of rhAm in the mHA/CS group was relatively slow. The cumulative amount of rhAm released within the initial hour was 67%, and then the release rate decreased over time until day 7. As chitosan degraded rapidly, 75% of the rhAm was released within the first hour. And then the rhAm was released sustainably as the chitosan was degraded. At day 7, the total amount released by mHA and mHA/CS group was statistically higher than that released by the CS group ($p < 0.05$).

Alkaline Phosphatase (ALP) Activity

The ALP activity assay was performed to observe the osteogenic differentiation of hPDLCs (**Figure 10**). The results showed that ALP staining in the group rhAm and group mHA/CS-rhAm was stronger in color than that in the group mHA/CS, C and D. Furthermore, the staining in group mHA/CS was stronger than that in group C and D, and the staining in group mHA/CS-rhAm was stronger than that in group rhAm. The staining in group D was the palest among all the groups. The staining results indicated that hPDLCs in the rhAm and mHA/CS-rhAm groups exhibited stronger osteogenic differentiation capability, which indicated that 4.5 mg/mL mHA/CS loaded with 20 μg/mL rhAm was beneficial to the osteogenic differentiation of hPDLCs *in vitro*.

Expression Levels of Osteogenesis-Related Genes

The expression levels of RUNX-2 and DLX-5 mRNA were significantly upregulated in the mHA/CS-rhAm group when cells

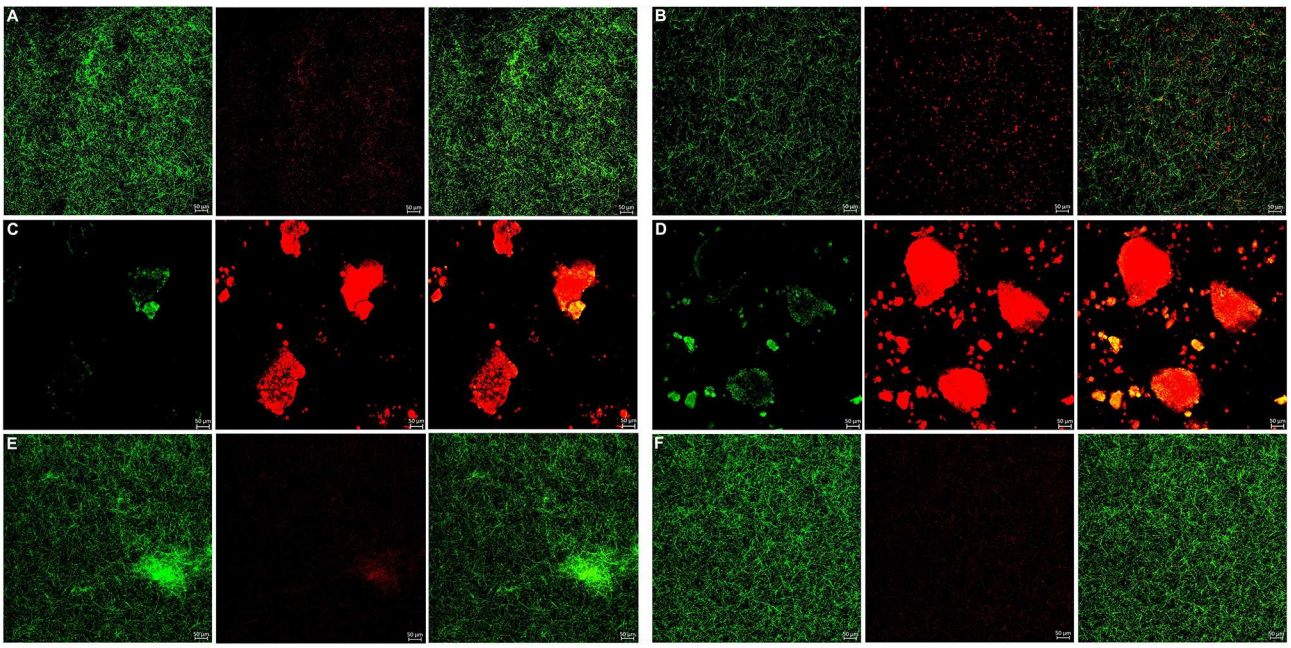

FIGURE 6 | Live/dead fluorescent staining images of *F. nucleatum biofilms*. **(A)** Tryptic Soy Broth culture (baseline control), **(B)** 2.25 mg/mL mHA/CS, **(C)** 4.5 mg/mL mHA/CS, **(D)** 1.5 mg/mL CS, **(E)** 3 mg/mL mHA, and **(F)** 20μg/mL rhAm. Dead cells were stained red, whereas live bacteria were stained green (scale bar 50μm).

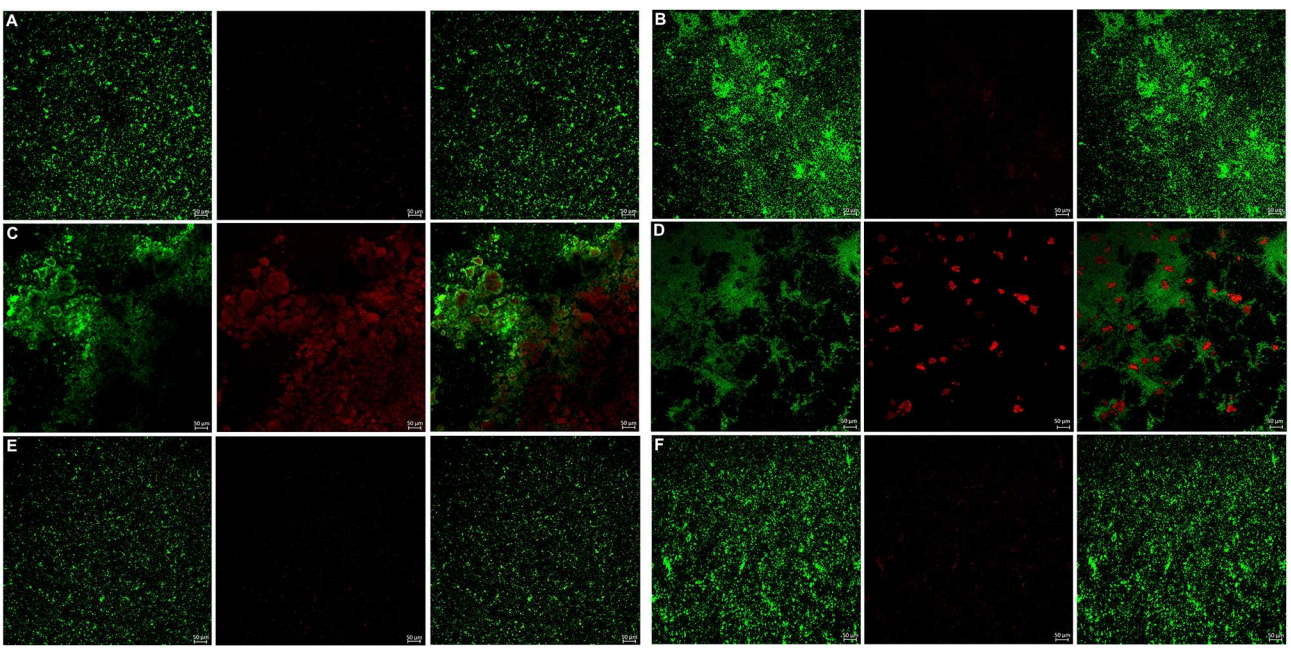

FIGURE 7 | Live/dead fluorescent staining images of *P. gingivalis biofilms*. **(A)** Tryptic Soy Broth culture (baseline control), **(B)** 2.25 mg/mL mHA/CS, **(C)** 4.5 mg/mL mHA/CS, **(D)** 1.5 mg/mL CS, **(E)** 3 mg/mL mHA, and **(F)** 20μg/mL rhAm. Dead cells were stained red, whereas live bacteria were stained green (scale bar 50μm).

were cultured for 3 and 7 days (**Figure 11**) ($p < 0.05$). In terms of OPN mRNA expression, the mHA/CS-rhAm group exhibited an upward trend at day 3, and the statistically significant differences were observed between the mHA/CS-rhAm group and the C group when cells were cultured for 7 days (**Figure 11**) ($p < 0.05$). The expression levels of RUNX-2, OPN, and DLX-5 mRNA in group D were significantly lower than those in group C at both days 3 and 7 ($p < 0.05$). Although all osteogenesis-related

genes were upregulated in group rhAm, the expressions levels in group mHA/CS-rhAm were the highest among the five groups, demonstrating the osteogenic effects of 4.5 mg/mL mHA/CS loaded with 20 μg/mL rhAm in hPDLCs.

Expression Levels of Osteogenesis-Related Proteins

According the gene expression levels, hPDLCs in group D barely showed osteogenic differentiation potential. So, samples from group D were excluded from Western Blotting. The expressions levels of all osteogenesis-related proteins were significantly upregulated in groups rhAm and mHA/CS-rhAm on both days 3 and 7 (**Figure 12**) ($p < 0.05$).

Additionally, the protein expression level in group mHA/CS-rhAm was higher than that in the other groups (**Figure 12**). This result indicated that mHA/CS loaded with 20 μg/mL rhAm could effectively upregulate the expression levels of osteogenesis-related proteins, which was consistent with the gene expression results.

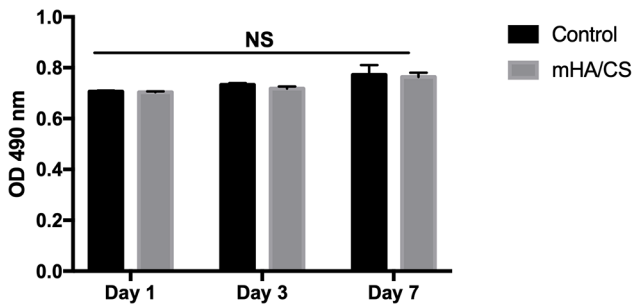

FIGURE 8 | hPDLCs were stimulated by 4.5 mg/mL mHA/CS for 1, 3, and 7 days, and the proliferation was measured by MTT assay. The results showed that 4.5 mg/mL mHA/CS had no cytotoxicity on hPDLCs. NS, no statistical difference.

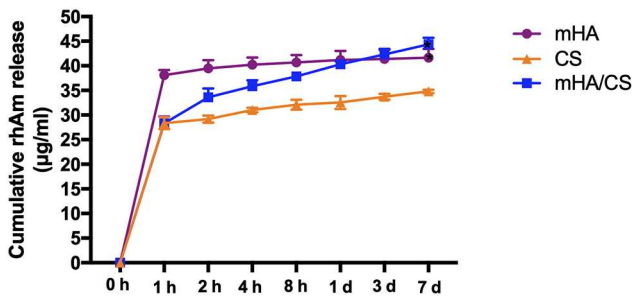

FIGURE 9 | The cumulative release amount of rhAm in group mHA, group CS and group mHA/CS. (Statistically significant against group CS, (*$p < 0.05$).

Histological Observation of Root Slices

In the specimens obtained from group C, there was no soft or hard tissue formation on the root slices. The original cementum had been removed, and the dentine remained. Subcutaneous tissue from mice was observed on the outside of the ePTFE membrane (**Figure 13A**). In group mHA/CS, new fibrous tissue had formed along the root surfaces and there were large spaces between the newly formed tissue and the root surface. Hard tissue formation could hardly be observed on the specimens. However, no subcutaneous tissue from mice was observed along the inner side of the membrane (**Figure 13B**). The results suggested that the ePTFE membrane was able to prevent the fibroblasts from entering the membrane and to maintain the space for tissue regeneration. In group rhAm, there was newly formed fibrous tissue containing cells along the root slices. Soft tissue was attached to the root surface with no splits in the space in some areas (**Figure 13C**). In group mHA/CS-rhAm, there was a thin layer of newly formed cementum-like tissue (NFC) attached to the dentin in most areas. However, there was a split between the fibrous tissue and NFC (**Figure 13D**).

DISCUSSION

In recent years, different combinations of scaffolds and growth factors have been applied to the field of periodontal regeneration to repair the periodontium and recover its function (Gümüşderelioglu et al., 2019; Liang et al., 2020). Despite of the achievements in past decades, further studies are

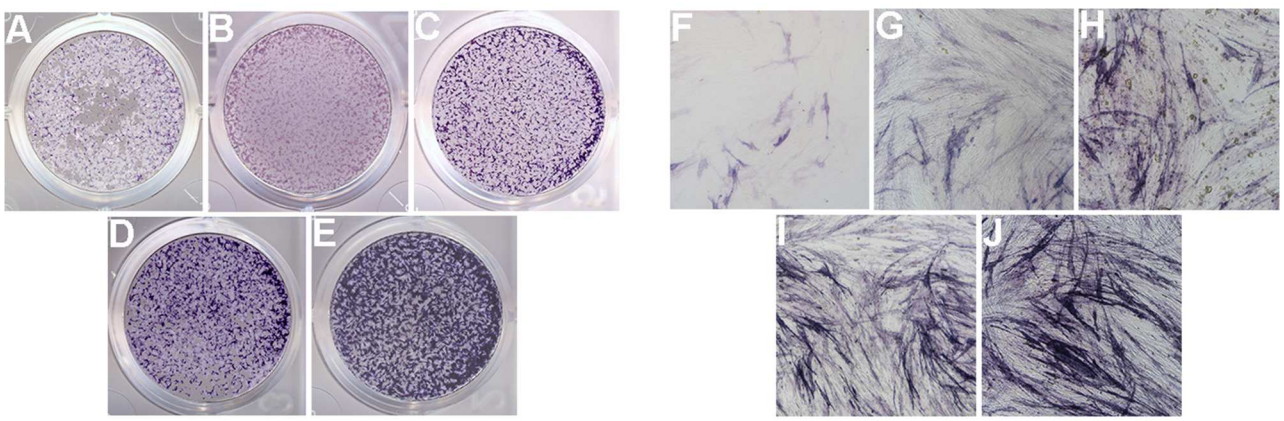

FIGURE 10 | ALP activity of hPDLCs (× 100). ALP activity of hPDLCs with the stimulation of DMEM (group D; **A,F**), osteogenic differentiation medium (group C; **B,G**), 4.5 mg/mL mHA/CS (group mHA/CS; **C,H**), 20μg/mL rhAm (group rhAm; **D,I**), and 4.5 mg/mL mHA/CS+20μg/mL rhAm (group mHA/CS-rhAm; **E,J**).

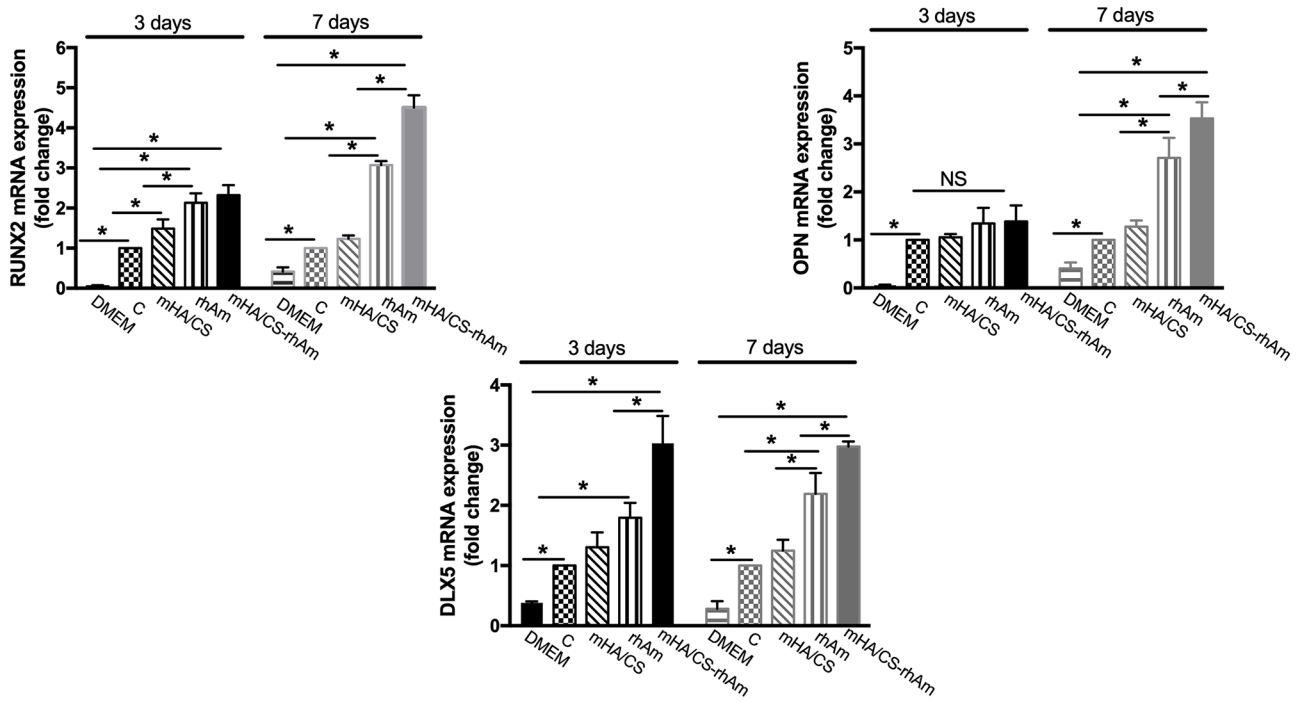

FIGURE 11 | The osteogenesis-related genes RUNX-2, OPN, and DLX-5 were measured by real-time PCR. The RUNX-2 mRNA and DLX-5 mRNA expression level were up-regulated in group mHA/CS-rhAm at both days 3 and 7. The OPN mRNA expression level in mHA/CS-rhAm were up-regulated significantly at day 7 (*$p < 0.05$).

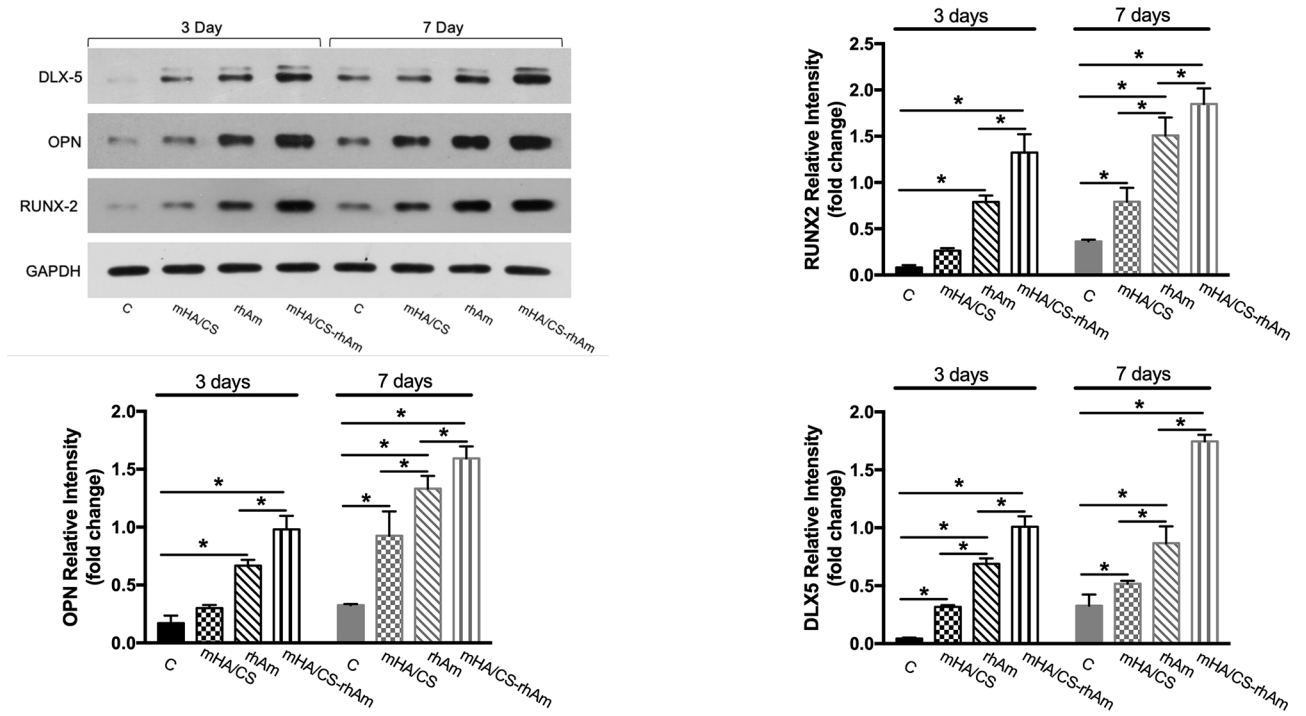

FIGURE 12 | The osteogenesis-related proteins RUNX-2, OPN, and DLX-5 were measured by Western blot at days 3 and 7. The protein expression levels of RUNX-2, OPN, and DLX-5 of hPDLCs in group rhAm and mHA/CS-rhAm were higher than those in the other groups (*$p < 0.05$).

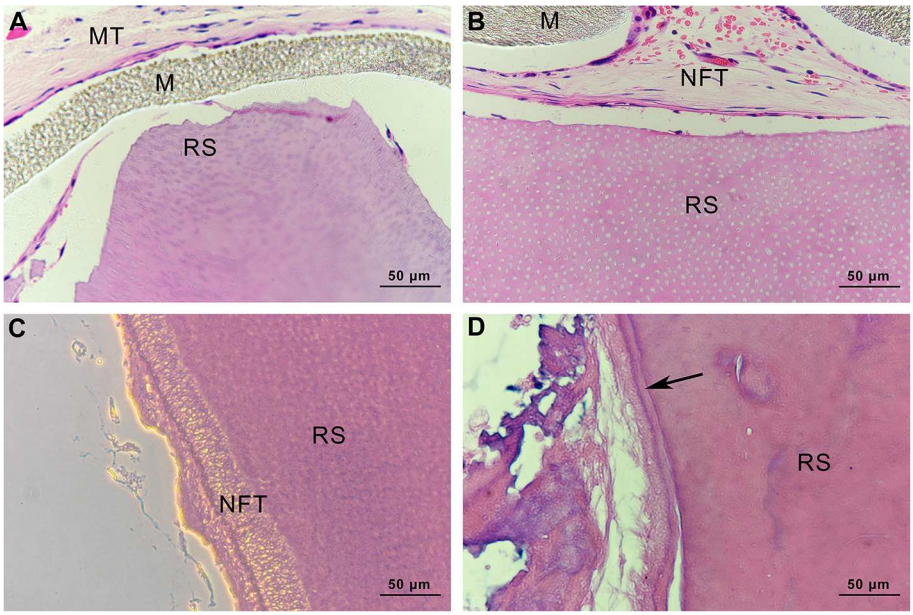

FIGURE 13 | Histological observation of root slices (HE stain, × 400). **(A)** group C. There was no newly-formed soft or hard tissue on the slices; **(B)** group mHA/CS. There was newly-formed fibrous tissue along the inner side of membrane, which had no contact with slices; **(C)** group rhAm. There was newly-formed fibrous tissue along the root surfaces; **(D)** group mHA/CS-rhAm. Newly-formed cementum-like tissue was observed along the root surfaces (arrow) .

still needed to provide a foundation for clinical treatments. The challenges of periodontal regeneration result from the complicated structure of the periodontium and the chronic inflammatory microenvironment. So, our study was aimed to analyze the physicochemical properties, sustained release and antibacterial effects against periodontal pathogens of mHA/CS. Then the osteogenesis effects of mHA/CS/rhAm was examined on hPDLCs *in vitro*, and cementogenic effects was observed on root slices *in vivo*. It is the first time to apply the mesoporous hydroxyapatite/chitosan loaded with rhAm (mHA/CS-rhAm) to periodontal regeneration.

Hydroxyapatite (HA) has been widely used in preclinical and clinical studies of tissue engineering and has components similar to those of natural bone (Gross et al., 2014; Inzana et al., 2014). Compared with the traditional HA, nanohydroxyapatite (nHA) has a larger surface area and better bioactivity and loading capacity. There were sufficient preclinical and clinical findings to support the osteogenic effect of nHA in tissue engineering (Shirmohammadi et al., 2014; Kamboj et al., 2016; Dayashankar et al., 2017; Sadeghi et al., 2017). Chitosan has been used for periodontal treatments in many studies. A 15% Chitosan gel was effective in reducing intrabony defects and improving attachment level (Babrawala et al., 2016). Previous studies have evaluated the osteogenic effects of nHA/CS composite scaffolds (Tu et al., 2017). However, few studies have focused on mHA/CS, especially in the field of periodontal regeneration (Feiz and Meshkini, 2019; Song et al., 2019). On the basis of images of FITR spectra and BET, we synthesized the mHA/CS successfully by the hydrothermal method.

F. nucleatum and *P. gingivalis* are the major pathogens that cause periodontitis (Hajishengallis et al., 2012; Yang et al., 2014; Han, 2015; How et al., 2016). Furthermore, coinfection of *F. nucleatum* and *P. gingivalis* could enhance their adherence and invasive capacity in human gingival epithelial cells and inhibit the host innate immune response (Li et al., 2015; Jung et al., 2017). Therefore, we tested the antibacterial activity against both planktonic cultures and biofilms.

From the previous studies, chitosan exhibited antimicrobial activity against not only gram-positive and gram-negative bacteria, but also fungi (Verlee et al., 2017), aim several oral pathogens (Husain et al., 2017; Qasim et al., 2017b). Although Arancibia et al. suggested that chitosan could inhibit the growth of *P. gingivalis* at the concentration of 5 mg/mL, the antibacterial effect of the mHA/CS composite scaffold on periodontal pathogens has not yet been reported. In our study, the OD values indicated that 3 mg/mL mHA and 20 μg/mL rhAm neither inhibited the growth of *F. nucleatum* and *P. gingivalis* planktonic cultures, nor the growth of *F. nucleatum* and *P. gingivalis* biofilms. There were more viable bacteria in these groups which formed dense biofilms. They were stained green from the CLSM images. However, 1.5 mg/mL CS and 4.5 mg/mL mHA/CS had significant antibacterial effects on both planktonic pathogens and biofilms. In the 2.25 mg/mL mHA/CS group, more red staining was observed compared with the control group. The dead bacteria were integrated together and formed into crumb structures instead of dense biofilms. So, the dead bacteria were easily washed away before the staining, which may explain the sparse distributions of staining in 4.5 mg/mL mHA/CS group and 1.5 mg/mL CS group. These results suggested that the mHA/CS scaffold could inhibit the growth of *F. nucleatum* and *P. gingivalis* in both planktonic cultures and biofilms and that the antibacterial effects should be attributed

to chitosan. In addition, the MTT assay demonstrated that 4.5 mg/mL mHA/CS has good compatibility with hPDLCs, which could be useful in future studies.

Additionally, chitosan nanocomposites have been developed as prominent materials used for the loading and controlled release of growth factors over time, but few studies have been conducted on mHA/CS (Qasim et al., 2017a; Park et al., 2018). The mHA/CS could be an appropriate carrier for rhAm, which has been proved in our study. As mentioned before, the large specific surface area of mHA could improve the loading capacity of protein. Also, the positive charges from chitosan will be attracted to the negatively charged surface of mHA by electrostatic interaction, which could form a coating layer and slow down the degradation rate of CS. So, it is suggested that rhAm could be released sustainably accompanied by lower degradation rate of CS. In the **Figure 9**, the cumulative amount of rhAm released by mHA and mHA/CS was constantly higher than CS within 7 days, which confirm that mHA had larger loading capacity of rhAm than CS. Based on the release profile of group CS, 75% of the rhAm was released within the first hour, which was higher than the percentage of group mHA/CS. So, the lowest release amount of group CS implied that CS released less protein than group mHA and group mHA/CS, rather than CS released more slowly.

In our study, the osteogenic effects of mHA/CS loaded with rhAm on hPDLCs were observed *in vitro*. First, ALP activity was observed because of its pivotal role in the regulation of phosphate metabolism and the formation of mineral (Cao et al., 2016). Then, the expression of osteogenesis-related genes and proteins, which represent the different stages of osteogenesis, was detected. RUNX-2 is essential for chondrocyte maturation, matrix production, and mineralization (Liu et al., 2001; Liu and Lee, 2013). As RUNX-2 is the dominant transcription factor in early osteoblast differentiation stage, the statistical differences have already been observed at day 3. The expression levels of RUNX-2 were increased in group H-R at both days 3 and 7. OPN is associated with bone metabolism and remodeling and is an important protein in the middle and late stages of bone formation (Ram et al., 2015; De Fusco et al., 2017). So, there was no statistical significance among four groups at the early stage until day 7. Dlx-5 is regarded as a key regulator of bone formation, and the inhibition of DLX-5 can decrease the expression level of both RUNX-2 and OPN (Samee et al., 2008; Heo et al., 2017). Although, there were no statistical significance between group H and group R at day 3, the expression level of group H-R was upregulated significantly. All the results have proved that mHA/CS loaded with 20 μg/mL rhAm could promote the osteogenic effects *in vitro*.

In the animal model study, only the group containing both mHA/CS and 20 μg/mL rhAm demonstrated the formation of cementum-like tissue that was attached to the dentin with fibrous tissue along the other side. This tissue seems to be similar to that observed in normal periodontium. In the group containing 20 μg/mL rhAm only, there were some newly formed fibrous tissue-containing cells along the root slice. Many factors could influence the outcome of experiment, such as the seed cells, growth factor, root surface condition, and so on. In the research of Song et al., the seed cells were porcine bone marrow-derived stromal cells (BMSCs) and root slices were also derived from pig (Song et al., 2007). While in our study, the seed cells, root slices, and protein were derived from human, so the outcomes of our study would be much closer to the process of clinical periodontal regeneration. According to the HE staining, the old cementum of root slices was removed in our experiment while Song et al. preserved part of the old cementum. Root surface conditioning was essential for the removal smear layer and endotoxin contamination (Karam et al., 2016). However, Song et al. suggested that preservation of healthy root cementum may promote the formation of cementum-like tissue (Song A. et al., 2012). More examinations on the expression levels of genes and proteins related to cementogenic differentiation and animal model studies with extended time span are necessary for the further study.

CONCLUSION

In summary, this study demonstrated that the mHA/CS scaffold could inhibit the growth of periodontal pathogens. The cumulative amount of rhAm released by mHA and mHA/CS was statistically higher than CS at day 7 ($p < 0.05$), which confirm that mHA and mHA/CS had larger loading capacity of rhAm than CS. The composite scaffold loaded with rhAm significantly upregulated ALP activity, and the gene and protein expression levels of RUNX-2, OPN, and DLX-5 *in vitro* ($p < 0.05$). Additionally, it successfully induced the cementum-like tissue formation *in vivo*. This study provided a new substitute scaffold for periodontal regeneration that exhibited antibacterial activity and promoted both osteogenic and cementogenic effects.

DATA AVAILABILITY STATEMENT

The raw data supporting the conclusions of this article will be made available by the authors, without undue reservation, to any qualified researcher.

ETHICS STATEMENT

The studies involving human participants were reviewed and approved by Shanghai Ninth People's Hospital. The Institute Review Board number is 2018-120-T98. The patients/participants provided their written informed consent to participate in this study. The animal study was reviewed and approved by the ethical committee of the Animal Care and Experimental Committee of the Shanghai Jiao Tong University School of Medicine (Approval no. SH9H-2019-A499-1).

AUTHOR CONTRIBUTIONS

All authors contributed to the writing of this article. YL, HC, ZS, and WZ conceptualized the study. YL and HL curated the data, conducted a formal analysis, and reviewed and edited the article. ZS and WZ acquired funding. YL worked on the methodology. YL, HL, and LZ administered the project. YL and LZ provided resources. RS, ZS, and WZ supervised the study.

FUNDING

This research was supported by the National Nature Science Foundation of China (No. 81670992 and 81271156) and the Interdisciplinary Program of Shanghai Jiao Tong University (project number: YG2015MS04).

SUPPLEMENTARY MATERIAL

The Supplementary Material for this article can be found online at: https://www.frontiersin.org/articles/10.3389/fcimb.2020.00180/full#supplementary-material

Supplementary Figure 1 | The graphical abstract.

REFERENCES

Ali, A., and Ahmed, S. (2017). A review on chitosan and its nanocomposites in drug delivery. *Int. J. Biol. Macromol.* 109, 273–286. doi: 10.1016/j.ijbiomac.2017.12.078

Babrawala, I., Munivenkatappa Lakshmaiah Venkatesh, P., and Bangalore Varadhan, K. (2016). A novel approach using 15% natural chitosan gel in the management of intrabony defects: a pilot study. *Chin. J. Dent. Res.* 19, 231–237. doi: 10.3290/j.cjdr.a37148

Baino, F., Fiorilli, S., and Vitale-Brovarone, C. (2016). Bioactive glass-based materials with hierarchical porosity for medical applications: review of recent advances. *Acta Biomater.* 42, 30310–30315. doi: 10.1016/j.actbio.2016.06.033

Bosshardt, D. D., Stadlinger, B., and Terheyden, H. (2015). Cell-to-cell communication-periodontal regeneration. *Clin. Oral. Implants Res.* 26, 229–239. doi: 10.1111/clr.12543

Cao, F. Y., Fan, J. X., Long, Y., Zeng, X., and Zhang, X. Z. (2016). A smart fluorescence nanoprobe for the detection of cellular alkaline phosphatase activity and early osteogenic differentiation. *Nanomedicine* 12, 1313–1322. doi: 10.1016/j.nano.2016.01.010

Cholas, R., Kunjalukkal Padmanabhan, S., Gervaso, F., Udayan, G., Monaco, G., Sannino, A., et al. (2016). Scaffolds for bone regeneration made of hydroxyapatite microspheres in a collagen matrix. *Mater. Sci. Eng. C Mater. Biol. Appl.* 63, 499–505. doi: 10.1016/j.msec.2016.03.022

Dayashankar, C. P., Deepika, P. C., and Siddaramaiah, B. (2017). Clinical and radiographic evaluation of citric acid-based nano hydroxyapatite composite graft in the regeneration of intrabony defects - a randomized controlled trial. *Contemp. Clin. Dent.* 8, 380–386. doi: 10.4103/ccd.ccd_213_17

De Fusco, C., Messina, A., Monda, V., Viggiano, E., Moscatelli, F., Valenzano, A., et al. (2017). Osteopontin: relation between adipose tissue and bone homeostasis. *Stem Cells Int.* 2017:4045238. doi: 10.1155/2017/4045238

Deepthi, S., Venkatesan, J., Kim, S. K., Bumgardner, J. D., and Jayakumar, R. (2016). An overview of chitin or chitosan/nano ceramic composite scaffolds for bone tissue engineering. *Int. J. Biol. Macromol.* 93(Pt B), 1338–1353. doi: 10.1016/j.ijbiomac.2016.03.041

Domingos, M., Gloria, A., Coelho, J., Bartolo, P., and Ciurana, J. (2017). Three-dimensional printed bone scaffolds: the role of nano/micro-hydroxyapatite particles on the adhesion and differentiation of human mesenchymal stem cells. *Proc. Inst. Mech. Eng. H.* 231, 555–564. doi: 10.1177/0954411916680236

Dong, J. C., Song, Z. C., Shu, R., Li, S., Sun, M. J., and Lin, Z. K. (2016). Recombinant human amelogenin reverses osteogenesis suppression induced by an inflammatory microenvironment in human periodontal ligament cells. *Int. J. Clin. Exp. Med.* 9, 23276–23284.

Dumont, V. C., Mansur, H. S., Mansur, A. A., Carvalho, S. M., Capanema, N. S., and Barrioni, B. R. (2016). Glycol chitosan/nanohydroxyapatite biocomposites for potential bone tissue engineering and regenerative medicine. *Int. J. Biol. Macromol.* 93(Pt B), 1465–1478. doi: 10.1016/j.ijbiomac.2016.04.030

Fawzy El-Sayed, K. M. and Dörfer, C. E. (2017). Animal Models for Periodontal Tissue Engineering: A Knowledge-Generating Process. *Tissue Eng Part C Methods.* 23, 900–925. doi: 10.1089/ten.TEC.2017.0130

Feiz, M. S., and Meshkini, A. (2019). Targeted delivery of adenosine 5'-triphosphate using chitosan-coated mesoporous hydroxyapatite: a theranostic pH-sensitive nanoplatform with enhanced anti-cancer effect. *Int. J. Biol. Macromol.* 129, 1090–1102. doi: 10.1016/j.ijbiomac.2018.08.158

Gauthier, P., Yu, Z., Tran, Q. T., Bhatti, F. U., Zhu, X., and Huang, G. T. (2017). Cementogenic genes in human periodontal ligament stem cells are downregulated in response to osteogenic stimulation while upregulated by vitamin C treatment. *Cell Tissue Res.* 368, 79–92. doi: 10.1007/s00441-016-2513-8

Gross, B. C., Erkal, J. L., Lockwood, S. Y., Chen, C., and Spence, D. M. (2014). Evaluation of 3D printing and its potential impact on biotechnology and the chemical sciences. *Anal. Chem.* 86, 3240–3253. doi: 10.1021/ac403397r

Gümüşderelioglu, M., Sunal, E., Tolga Demirtaş, T., and Kiremitçi, A. S. (2019). Chitosan-based double-faced barrier membrane coated with functional nanostructures and loaded with BMP-6. *J Mater. Sci. Mater. Med.* 31:4. doi: 10.1007/s10856-019-6331-x

Hajishengallis, G., Darveau, R. P., and Curtis, M. A. (2012). The keystone-pathogen hypothesis. *Nat. Rev. Microbiol.* 10, 717–725. doi: 10.1038/nrmicro2873

Han, J., Menicanin, D., Gronthos, S., and Bartold, P. M. (2014). Stem cells, tissue engineering and periodontal regeneration. *Aust. Dent. J. Suppl.* 1, 117–130. doi: 10.1111/adj.12100

Han, Y. W. (2015). *Fusobacterium nucleatum*: a commensal-turned pathogen. *Curr. Opin. Microbiol.* 23, 141–147. doi: 10.1016/j.mib.2014.11.013

Heo, J. S., Lee, S. G., and Kim, H. O. (2017). Distal-less homeobox 5 is a master regulator of the osteogenesis of human mesenchymal stem cells. *Int. J. Mol. Med.* 40, 1486–1494. doi: 10.3892/ijmm.2017.3142

How, K. Y., Song, K. P., and Chan, K. G. (2016). *Porphyromonas gingivalis*: an overview of periodontopathic pathogen below the gum line. *Front. Microbiol.* 7:53. doi: 10.3389/fmicb.2016.00053

Hu, F., Zhou, Z., Xu, Q., Fan, C., Wang, L., Ren, H., et al. (2019). A novel pH-responsive quaternary ammonium chitosan-liposome nanoparticles for periodontal treatment. *Int. J. Biol. Macromol.* 129, 1113–1119. doi: 10.1016/j.ijbiomac.2018.09.057

Huang, B., Vyas, C., Byun, J. J., El-Newehy, M., Huang, Z., and Bártolo, P. (2020). Aligned multi-walled carbon nanotubes with nanohydroxyapatite in a 3D printed polycaprolactone scaffold stimulates osteogenic differentiation. *Mater. Sci. Eng. C Mater. Biol. Appl.* 108:110374. doi: 10.1016/j.msec.2019.110374

Husain, S., Al-Samadani, K. H., Najeeb, S., Zafar, M. S., Khurshid, Z., Zohaib, S., et al. (2017). Chitosan biomaterials for current and potential dental applications. *Materials* 10, 602–621. doi: 10.3390/ma10060602

Inzana, J. A., Olvera, D., Fuller, S. M., Kelly, J. P., Graeve, O. A., Schwarz, E. M., et al. (2014). 3D printing of composite calcium phosphate and collagen scaffolds for bone regeneration. *Biomaterials* 35, 4026–4034. doi: 10.1016/j.biomaterials.2014.01.064

Ivanovski, S., Vaquette, C., Gronthos, S., Hutmacher, D. W., and Bartold, P. M. (2014). Multiphasic scaffolds for periodontal tissue engineering. *J. Dent. Res.* 93, 1212–1221. doi: 10.1177/0022034514544301

Jang, S. J., Kim, S. E., Han, T. S., Son, J. S., Kang, S. S., and Choi, S. H. (2017). Bone regeneration of hydroxyapatite with granular form or porous scaffold in canine alveolar sockets. *In Vivo* 31, 335–341. doi: 10.21873/invivo.11064

Jose, G., Shalumon, K. T., Liao, H. T., Kuo, C. Y., and Chen, J. P. (2020). Preparation and characterization of surface heat sintered nanohydroxyapatite and nanowhitlockite embedded poly (lactic-co-glycolic acid) microsphere bone graft scaffolds: *in vitro* and *in vivo* studies. *Int. J. Mol. Sci.* doi: 10.3390/ijms21020528. [Epub ahead of print].

Jung, Y. J., Jun, H. K., and Choi, B. K. (2017). *Porphyromonas gingivalis* suppresses invasion of *Fusobacterium nucleatum* into gingival epithelial cells. *J. Oral. Microbiol.* 9:1320193. doi: 10.1080/20002297.2017.1320193

Kamboj, M., Arora, R., and Gupta, H. (2016). Comparative evaluation of the efficacy of synthetic nanocrystalline hydroxyapatite bone graft (Ostim®) and synthetic microcrystalline hydroxyapatite bone graft (Osteogen®) in the treatment of human periodontal intrabony defects: A clinical and denta scan study. *J. Indian Soc. Periodontol.* 20, 423–428. doi: 10.4103/0972-124X.184036

Karam, P. S., Sant'Ana, A. C., de Rezende, M. L., Greghi, S. L., Damante, C. A., and Zangrando, M. S. (2016). Root surface modifiers and subepithelial connective tissue graft for treatment of gingival recessions: a systematic review. *J. Periodontal. Res*. 51, 175–185. doi: 10.1111/jre.12296

Krishnamurithy, G., Mohan, S., Yahya, N. A., Mansor, A., Murali, M. R., Raghavendran, H. R. B., et al. (2019). The physicochemical and biomechanical profile of forsterite and its osteogenic potential of mesenchymal stromal cells. *PLoS ONE* 14:e0214212. doi: 10.1371/journal.pone.0214212

Lee, J. H., Kang, M. S., Mahapatra, C., and Kim, H. W. (2016). Effect of aminated mesoporous bioactive glass nanoparticles on the differentiation of dental pulp stem cells. *PLoS ONE* 11:e0150727. doi: 10.1371/journal.pone.0150727

Li, Y., Guo, H., Wang, X., Lu, Y., Yang, C., and Yang, P. (2015). Coinfection with *Fusobacterium nucleatum* can enhance the attachment and invasion of *Porphyromonas gingivalis* or *Aggregatibacter* actinomycetemcomitans to human gingival epithelial cells. *Arch. Oral. Biol*. 60, 1387–1393. doi: 10.1016/j.archoralbio.2015.06.017

Liang, Y., Luan, X., and Liu, X. (2020). Recent advances in periodontal regeneration: a biomaterial perspective. *Bioact. Mater*. 5, 297–308. doi: 10.1016/j.bioactmat.2020.02.012

Liu, C., Wu, J., Gan, D., Li, Z., Shen, J., Tang, P., et al. (2019). The characteristics of mussel-inspired nHA/OSA injectable hydrogel and repaired bone defect in rabbit. *J. Biomed. Mater. Res. B Appl. Biomater*. doi: 10.1002/jbm.b.34524. [Epub ahead of print].

Liu, T. M., and Lee, E. H. (2013). Transcriptional regulatory cascades in Runx2-dependent bone development. *Tissue Eng. B Rev*. 19, 254–263. doi: 10.1089/ten.teb.2012.0527

Liu, W., Toyosawa, S., Furuichi, T., Kanatani, N., Yoshida, C., Liu, Y., et al. (2001). Overexpression of Cbfa1 in osteoblasts inhibits osteoblast maturation and causes osteopenia with multiple fractures. *J. Cell Biol*. 155, 157–166. doi: 10.1083/jcb.200105052

Liu, Z., Yin, X., Ye, Q., He, W., Ge, M., Zhou, X., et al. (2016). Periodontal regeneration with stem cells-seeded collagen-hydroxyapatite scaffold. *J. Biomater. Appl*. 31, 121–131. doi: 10.1177/0885328216637978

Miranda, D. G., Malmonge, S. M., Campos, D. M., Attik, N. G., Grosgogeat, B., and Gritsch, K. (2016). A chitosan-hyaluronic acid hydrogel scaffold for periodontal tissue engineering. *J. Biomed. Mater. Res. B Appl. Biomater*. 104, 1691–1702. doi: 10.1002/jbm.b.33516

Mrozik, K., Gronthos, S., Shi, S., and Bartold, P. M. (2017). A method to isolate, purify, and characterize human periodontal ligament stem cells. *Methods Mol. Biol*. 1537, 413–427. doi: 10.1007/978-1-4939-6685-1_24

Ogawa, K., Miyaji, H., Kato, A., Kosen, Y., Momose, T., Yoshida, T., et al. (2016). Periodontal tissue engineering by nano beta- tricalcium phosphate scaffold and fibroblast growth factor-2 in one-wall infrabony defects of dogs. *J. Periodontal. Res*. 51, 758–767. doi: 10.1111/jre.12352

Ou, Q., Miao, Y., Yang, F., Lin, X., Zhang, L. M., and Wang, Y. (2019). Zein/gelatin/nanohydroxyapatite nanofibrous scaffolds are biocompatible and promote osteogenic differentiation of human periodontal ligament stem cells. *Biomater. Sci*. 7, 1973–1983. doi: 10.1039/C8BM01653D

Park, K. H., Kim, S. J., Jeong, Y. H., Moon, H. J., Song, H. J., and Park, Y. J. (2018). Fabrication and biological properties of calcium phosphate/chitosan composite coating on titanium in modified SBF. *Mater. Sci. Eng. C Mater. Biol. Appl*. 90, 113–118. doi: 10.1016/j.msec.2018.04.060

Qasim, S. B., Delaine-Smith, R. M., Fey, T., Rawlinson, A., and Rehman, I. U. (2015). Freeze gelated porous membranes for periodontal tissue regeneration. *Acta Biomater*. 23, 317–328. doi: 10.1016/j.actbio.2015.05.001

Qasim, S. B., Husain, S., Huang, Y., Pogorielov, M., Deineka, V., Lyndin, M., et al. (2017a). *In-vitro* and *in-vivo* degradation studies of freeze gelated porous chitosan composite scaffolds for tissue engineering applications. *Polym. Degrad. Stab*. 136, 31–38. doi: 10.1016/j.polymdegradstab.2016.11.018

Qasim, S. B., Najeeb, S., Delaine-Smith, R. M., Rawlinson, A., and Ur Rehman, I. (2017b). Potential of electrospun chitosan fibers as a surface layer in functionally graded GTR membrane for periodontal regeneration. *Dent. Mater*. 33, 71–83. doi: 10.1016/j.dental.2016.10.003

Ram, V. S., Parthiban, S. U., Mithradas, N., and Prabhakar, R. (2015). Bonebiomarkers in periodontal disease: a review article. *J. Clin. Diagn. Res*. 9, ZE07–10. doi: 10.7860/JCDR/2015/11268.5438

Rodríguez-Vázquez, M., Vega-Ruiz, B., Ramos-Zúñiga, R., Saldaña-Koppel, D. A., and Quiñones-Olvera, L. F. (2015). Chitosan and its potential use as a scaffold for tissue engineering in regenerative medicine. *Biomed. Res. Int*. 2015:821279. doi: 10.1155/2015/821279

Sadeghi, R., Najafi, M., Semyari, H., and Mashhadiabbas, F. (2017). Histologic and histomorphometric evaluation of bone regeneration using nanocrystalline hydroxyapatite and human freeze-dried bone graft: an experimental study in rabbit. *J. Orofac. Orthop*. 78, 144–152. doi: 10.1007/s00056-016-0067-8

Samee, N., Geoffroy, V., Marty, C., Schiltz, C., Vieux-Rochas, M., Levi, G., et al. (2008). Dlx5, a positive regulator of osteoblastogenesis, is essential for osteoblast-osteoclast coupling. *Am. J. Pathol*. 173, 773–780. doi: 10.2353/ajpath.2008.080243

Shirmohammadi, A., Roshangar, L., Chitsazi, M. T., Pourabbas, R., Faramarzi, M., and Rahmanpour, N. (2014). Comparative study on the efficacy of anorganic bovine bone (bio-oss) and nanocrystalline hydroxyapatite (ostim) in maxillary sinus floor augmentation. *Int. Sch. Res. Notices* 2014:967091. doi: 10.1155/2014/967091

Song, A., Cai, J., Pan, K., and Yang, P. (2012). Pre-existing root cementum may promote cementoblast differentiation of human periodontal ligament cells. *Cell Prolif*. 45, 249–258. doi: 10.1111/j.1365-2184.2012.00815.x

Song, A. M., Shu, R., Xie, Y. F., Song, Z. C., Li, H. Y., Liu, X. F., et al. (2007). A study of enamel matrix proteins on differentiation of porcine bone marrow stromal cells into cementoblasts. *Cell Prolif*. 40, 381–396. doi: 10.1111/j.1365-2184.2007.00441.x

Song, Q., Jia, J., Niu, X., Zheng, C., Zhao, H., Sun, L., et al. (2019). An oral drug delivery system with programmed drug release and imaging properties for orthotopic colon cancer therapy. *Nanoscale* 11, 15958–15970. doi: 10.1039/C9NR03802G

Song, Z. C., Li, S., Dong, J. C., Sun, M. J., Zhang, X. L., and Shu, R. (2017). Enamel matrix proteins regulate hypoxia-induced cellular biobehavior and osteogenic differentiation in human periodontal ligament cells. *Biotech. Histochem*. 92, 606–618. doi: 10.1080/10520295.2017.1370131

Song, Z. C., Zhou, W., Shu, R., and Ni, J. (2012). Hypoxia induces apoptosis and autophagic cell death in human periodontal ligament cells through HIF-1alpha pathway. *Cell Prolif*. 45, 239–248. doi: 10.1111/j.1365-2184.2012.00810.x

Talebi Ardakani, M. R., Meimandi, M., Shaker, R., and Golmohammadi, S. (2019). The effect of platelet-rich fibrin (PRF), plasma rich in growth factors (PRGF), and enamel matrix proteins (Emdogain) on migration of human gingival fibroblasts. *J. Dent*. 20, 232–239.

Tu, Y., Chen, C., Li, Y., Hou, Y., Huang, M., and Zhang, L. (2017). Fabrication of nano-hydroxyapatite/chitosan membrane with asymmetric structure and its applications in guided bone regeneration. *Biomed. Mater. Eng*. 28, 223–233. doi: 10.3233/BME-171669

Verlee, A., Mincke, S., and Stevens, C. V. (2017). Recent developments in antibacterial and antifungal chitosan and its derivatives. *Carbohydr. Polym*. 164, 268–283. doi: 10.1016/j.carbpol.2017.02.001

Wu, C., and Chang, J. (2012). Mesoporous bioactive glasses: structure characteristics, drug/growth factor delivery and bone regeneration application. *Interface Focus*. 2, 292–306. doi: 10.1098/rsfs.2011.0121

Wyganowska-Swiatkowska, M., Urbaniak, P., Nohawica, M. M., Kotwicka, M., and Jankun, J. (2015). Enamel matrix proteins exhibit growth factor activity: a review of evidence at the cellular and molecular levels. *Exp. Ther. Med*. 9, 2025–2033. doi: 10.3892/etm.2015.2414

Xia, Y. J., Xia, H., Chen, L., Ying, Q. S., Yu, X., Li, L. H., et al. (2018). Efficient delivery of recombinant human bone morphogenetic protein (rhBMP-2) with dextran sulfate-chitosan microspheres. *Exp. Ther. Med*. 15, 3265–3272. doi: 10.3892/etm.2018.5849

Xiao, W., Sonny, B. B., and Rahaman, M. N. (2016). Preparation of resorbable carbonate-substituted hollow hydroxyapatite microspheres and their evaluation in osseous defects *in vivo*. *Mater. Sci. Eng. C Mater. Biol. Appl*. 60, 324–332. doi: 10.1016/j.msec.2015.11.039

Xiong, L., Zeng, J., Yao, A., Tu, Q., Li, J., Yan, L., et al. (2015). BMP2-loaded hollow hydroxyapatite microspheres exhibit enhanced osteoinduction and osteogenicity in large bone defects. *Int. J. Nanomed*. 10, 517–526. doi: 10.2147/IJN.S74677

Yang, N. Y., Zhang, Q., Li, J. L., Yang, S. H., and Shi, Q. (2014). Progression of periodontal inflammation in adolescents is associated with increased number of *Porphyromonas gingivalis*, *Prevotella* intermedia, *Tannerella*

forsythensis, and *Fusobacterium nucleatum*. *Int. J. Paediatr. Dent*. 24, 226–233. doi: 10.1111/ipd.12065

Zhang, Y., Dong, R., Park, Y., Bohner, M., Zhang, X., Ting, K., et al. (2016). Controlled release of NELL-1 protein from chitosan/hydroxyapatite-modified TCP particles. *Int. J. Pharm*. 511, 79–89. doi: 10.1016/j.ijpharm.2016.06.050

Zhou, W., Zhang, X., Zhu, C. L., He, Z. Y., Liang, J. P., and Song, Z. C. (2016). Melatonin receptor agonists as the "Perioceutics" agents for periodontal disease through modulation of *Porphyromonas gingivalis* virulence and inflammatory response. *PLoS ONE* 11:e0166442. doi: 10.1371/journal.pone.0166442

Zupančič, Š., Casula, L., Rijavec, T., Lapanje, A., Luštrik, M., Fadda, A. M., et al. (2019). Sustained release of antimicrobials from double-layer nanofiber mats for local treatment of periodontal disease, evaluated using a new micro flow-through apparatus. *J. Control Release* 316, 223–235. doi: 10.1016/j.jconrel.2019.10.008

Conflict of Interest: The authors declare that the research was conducted in the absence of any commercial or financial relationships that could be construed as a potential conflict of interest.

Copyright © 2020 Liao, Li, Shu, Chen, Zhao, Song and Zhou. This is an open-access article distributed under the terms of the Creative Commons Attribution License (CC BY). The use, distribution or reproduction in other forums is permitted, provided the original author(s) and the copyright owner(s) are credited and that the original publication in this journal is cited, in accordance with accepted academic practice. No use, distribution or reproduction is permitted which does not comply with these terms.

frontiers in Cellular and Infection Microbiology

ORIGINAL RESEARCH
published: 18 November 2020
doi: 10.3389/fcimb.2020.577819

Serum Proteomics Reveals Alterations in Protease Activity, Axon Guidance, and Visual Phototransduction Pathways in Infants With *In Utero* Exposure to Zika Virus Without Congenital Zika Syndrome

Janaina Macedo-da-Silva[1,2†], *Lívia Rosa-Fernandes*[1*†], *Raquel Hora Barbosa*[3], *Claudia B. Angeli*[1], *Fabiana Rabe Carvalho*[3,4], *Renata Artimos de Oliveira Vianna*[3,4], *Paulo C. Carvalho*[2], *Martin R. Larsen*[5], *Claudete Araújo Cardoso*[3,4] *and Giuseppe Palmisano*[1*]

[1] GlycoProteomics Laboratory, Department of Parasitology, Institute of Biomedical Sciences, University of Sao Paulo, Sao Paulo, Brazil, [2] Laboratory for Structural and Computational Proteomics, Carlos Chagas Institute, Fiocruz, Curitiba, Brazil, [3] Maternal and Child Department, School of Medicine, Universidade Federal Fluminense, Niteroi, Brazil, [4] Multiuser Laboratory for Research in Nephrology and Medical Sciences (LAMAP), School of Medicine, Universidade Federal Fluminense, Niteroi, Brazil, [5] Department of Biochemistry and Molecular Biology, University of Southern Denmark, Odense, Denmark

In 2015, ZIKV infection attracted international attention during an epidemic in the Americas, when neurological disorders were reported in infants who had their mothers exposed to ZIKV during pregnancy. World Health Organization (WHO) epidemiological data show that 5 to 15% of neonates exposed to ZIKV in the uterus have complications included in abnormalities related to Congenital Zika Syndrome (CZS). The risk of complications after birth is not well documented, however, clinical evidence shows that 6% of infants exposed to ZIKV during pregnancy have complications present at birth, and this rate rises to 14% when medical monitoring is performed in all exposed infants, regardless of birth condition. Thus, the evaluation and monitoring of all exposed infants are of foremost importance as the development of late complications has been increasingly supported by clinical evidence. The identification of changes in protein profile of infants exposed to ZIKV without CZS could provide valuable findings to better understand molecular changes in this cohort. Here, we use a shotgun-proteomics approach to investigate alterations in the serum of infants without CZS symptoms but exposed to intrauterine ZIKV (ZIKV) compared to unexposed controls (CTRL). A complex pattern of differentially expressed proteins was identified, highlighting the dysregulation of proteins involved in axon orientation, visual phototransduction, and global protease activity in children exposed to ZIKV without CZS. These data support the importance of monitoring children exposed to ZIKV during gestation and without early CZS symptoms. Our study is

OPEN ACCESS

Edited by:
Sigrun Lange, University of Westminster, United Kingdom

Reviewed by:
Emma Mohr, University of Wisconsin-Madison, United States
Michael F. Criscitiello, Texas A&M University, United States

***Correspondence:**
Giuseppe Palmisano
palmisano.gp@gmail.com
Lívia Rosa-Fernandes
liviarosa.f@gmail.com

[†]*These authors have contributed equally to this work*

Specialty section:
This article was submitted to Virus and Host, a section of the journal Frontiers in Cellular and Infection Microbiology

Received: *30 June 2020*
Accepted: *20 October 2020*
Published: *18 November 2020*

Citation:
Macedo-da-Silva J, Rosa-Fernandes L, Barbosa RH, Angeli CB, Carvalho FR, de Oliveira Vianna RA, Carvalho PC, Larsen MR, Cardoso CA and Palmisano G (2020) Serum Proteomics Reveals Alterations in Protease Activity, Axon Guidance, and Visual Phototransduction Pathways in Infants With In Utero Exposure to Zika Virus Without Congenital Zika Syndrome. Front. Cell. Infect. Microbiol. 10:577819. doi: 10.3389/fcimb.2020.577819

the first to assess molecular evidence of possible late disorders in children victims of the ZIKV outbreak in the Americas. We emphasize the importance of medical monitoring of symptomatic and asymptomatic children, as apparently unexplained late neurological and eye disorders may be due to intrauterine ZIKV exposure.

Keywords: Zika virus, late abnormalities, serum proteomics, mass spectrometry, biomarker, Congenital Zika Syndrome

INTRODUCTION

Zika is a single-stranded RNA virus belonging to the *Flaviviridae* family that was first isolated in 1947 from a rhesus monkey in Kampala, Uganda (Dick et al., 1952). The vectors of these viruses are infected mosquitoes, also responsible for the spread of important diseases such as dengue fever, West Nile fever, and yellow fever (Noorbakhsh et al., 2019). Between 1960 and 1980, Zika virus (ZIKV) was associated with mild diseases in Asian and African populations, however, in 2013-2014, during an outbreak in French Polynesia, the possibility of transplacental transmission from mother to fetus has been described (Kindhauser et al., 2016; Noorbakhsh et al., 2019). In 2015, Zika virus infection attracted international attention during an epidemic in the Americas (Venancio et al., 2019), due to its association with increasing cases of microcephaly, congenital malformation and other neurological disorders in newborns who had their mothers infected during pregnancy (Kindhauser et al., 2016; Mlakar et al., 2016). In 2016, WHO declared the infection a public health emergency of international interest (PHEIC) (Lowe et al., 2018), including 11,546 exposed pregnant women between 2016 and 2017 only in Brazil (Heukelbach et al., 2016). In addition, data published by the Brazilian Ministry of Health indicate 14,558 suspected cases of congenital microcephaly and others central nervous system (CNS) malformations between 2015 and 2017 (Pan American Health Organization/World Health Organization, 2017).

The set of abnormalities resulting from ZIKV intrauterine infection is called congenital Zika syndrome (CZS) and is characterized by severe neurological damage and loss of intracranial volume (Wheeler, 2018). Clinical evidences of CZS are divided into structural components, such as changes in cranial morphology, and functional components that include neurological impairment (Moore et al., 2017; Mohr et al., 2018). The latest published epidemiological bulletin by the Brazilian Ministry of Health reported 19,000 suspected cases of CZS from November 2015 to May 2020, being 3,534 (18.6%) confirmed and 2,784 cases under investigation (Pan American Health Organization/World Health Organization, 2017). CZS has symptoms that are common to other congenital infections, however, has characteristics not previously seen, including severe microcephaly, macular scarring, congenital contractures, and hypertonia (Moore et al., 2017). In 2016, the suggested Zika virus seroprevalence peak in Brazil was 63% (Netto et al., 2017), and following reports indicate that ZIKV continues to circulate in the cycle of human transmission in Brazil and the Americas (Lowe et al., 2018).

The risk of complications after birth is not well established, however, clinical evidence show that 6% of infants exposed to Zika virus during pregnancy have complications at birth, and this rate rises to 14% when medical monitoring is performed on all exposed infants, regardless of birth condition (Rice et al., 2018; Musso et al., 2019; Souza et al., 2019). In addition, subcortical calcifications and an enlarged ventricle have been demonstrated in exposed children, but who were born without clinical evidence of CZS. Another interesting clinical data shows that 60% of these children have seizures during development (Rice et al., 2018; Souza et al., 2019). Reports of other congenital infections, such as cytomegalovirus and toxoplasmosis, indicate that hearing loss and eye damage can occur from 33 to 44 months after birth for symptomatic and asymptomatic infants, respectively (Dahle et al., 2000). Thus, stressing the importance of evaluating and monitoring not only symptomatic infants, but all exposed ones as the development of late complications has been increasingly supported by reports of clinical evidence (Pomar et al., 2018; Rice et al., 2018; Soares et al., 2019; Valdes et al., 2019).

Upon *in utero* zika virus exposure, 12.5% neonates who tested negative for the infection still presented severe, moderate, or mild complications, such as jaundice, hypotonia, hypertonia, hepatomegaly, and elevated liver enzymes (Pomar et al., 2018). Moreover, zika virus exposure without evidence of microcephaly has also been connected to events of asphyxia, hypersalivation, and reflux. In addition, exposed children had lower weight, length, and fat-free masses in the first three months of life compared to unexposed children (Soares et al., 2019). Zika virus-exposed infants without CZS also showed lower receptive language scores in the first year of life (Valdes et al., 2019), besides multiple cerebral and visual abnormalities, which would not have been identified without prolonged medical monitoring (Rice et al., 2018).

In view of the previously reported clinical data, the identification of molecular changes in infants exposed to ZIKV, but who did not have CZS, is important to understand molecular alterations underlying the occurrence of late abnormalities. Here, we use a shotgun-proteomic approach to investigate molecular markers in the serum of infants exposed to intrauterine ZIKV (ZIKV), but without symptoms of CZS, compared to those not exposed to ZIKV (CTRL). A complex pattern of differentially abundant proteins has been identified, highlighting the deregulation of proteins involved in axon guidance, visual phototransduction and global protease activity in children exposed to ZIKV without CZS. These data support

the importance of monitoring children exposed to ZIKV during pregnancy and without early symptoms of CZS.

MATERIALS AND METHODS

Patient Cohort

This study includes 20 infants aged between 3 and 23 months referred to the Pediatrics Service of the Antonio Pedro University Hospital, Universidade Federal Fluminense, Brazil. The cohort was divided in CTRL group (non-exposed to ZIKV and negative maternal qPCR, n = 10) and ZIKV group (positive maternal qPCR, n = 10), which consisted of patients with maternal ZIKV exposure during pregnancy and no clinical evidence of CZS. In both CTRL and ZIKV conditions, the mothers tested negative to other infectious agents (syphilis, toxoplasmosis, rubella, cytomegalovirus, and HIV). This study was approved by the institutional review board and the ethics committee of the Universidade Federal Fluminense (protocol CAAE number 79890517.6.0000.5243) and followed the guidelines of the Declaration of Helsinki. All samples were collected upon informed and written consent from the parents/legal guardians of each participant. All participants were clinically evaluated by a multidisciplinary team and are included in a currently ongoing clinical follow-up program (Vianna et al., 2019). The clinical diagnosis was performed based on the guidelines of the Ministry of Health (Brazil, Ministry of Health, 2017).

Sample Collection

Venous blood samples were collected in Vacutainer blood collection tubes with clot activator (Becton Dickson, USA) and centrifuged (1,210*g* for 15 min) to obtain the serum. Subsequently, the samples were aliquoted in sterile tubes and frozen at -80°C until further analysis. Clinical data were obtained during the outpatient clinic visit and from the patients' medical records. Epidemiological and demographic data were retrieved from the questionnaire for investigating suspected cases of microcephaly related to ZIKV infection, made available by the Brazilian Ministry of Health, and applied to all patients.

Sample Preparation for Mass-Spectrometry Based-Proteomics

Serum samples were depleted using the Multiple Affinity Removal System Spin Depletion Cartridge (Agilent Technologies) as per the manufacturer's instructions. This approach reduces the levels of the 14 most abundant serum proteins (albumin, IgG, antitrypsin, IgA, transferrin, haptoglobin, fibrinogen, alpha2-macroglobulin, alpha1-acid glycoprotein, IgM, apolipoprotein AI, apolipoprotein AII, complement C3, and transthyretin) by approximately 94%. In parallel, non-depleted serum samples were diluted 10× without any pretreatment. Depleted and non-depleted samples were quantified using the Qubit Protein Assay Kit platform (Invitrogen) according to the manufacturer's instructions. A total of 20 µg proteins were reduced with 10 mM Dithiothreitol (DTT) at 30°C for 45 min and alkylated with 40 mM of iodoacetamide (IAA) for 30 min at room temperature in the dark. The samples were digested with 10% (m/m) trypsin (Promega) during 16 h at 30°C. Following digestion, all reactions were acidified with 1% (v/v) trifluoroacetic acid and tryptic peptides were desalted using C18 in-house stage-tips (3M Empore), dried and suspended in 0.1% formic acid (FA) prior to LC-MS/MS analysis.

Mass Spectrometry Analysis

For analysis of the depleted samples, an UltiMate 3000 Nanoflow LC system (Thermo Scientific) coupled online to a hybrid Quadrupole-Orbitrap mass spectrometer HF-X (Thermo Fisher Scientific) was used. The peptide mixture was loaded on an in-house packed reversed-phase pre-column (4 cm × 100 µm inner diameter, ReproSil-Pur C18-AQ 5 µm particles) and subsequently eluted onto a 20-cm 75-µm inner diameter analytical column containing ReproSil-Pur C18-AQ 3-µm particles. We applied a 66-min gradient using 0 to 35% solvent B in 40 min, 35 to 45% in 15 min, 45 to 99% B in 3 min and 5% B for 2 min (A = 0.1% FA; B = 90% ACN, 0.1% FA). After each run, the trap column and column were equilibrated with mobile phase A. The Quadrupole-Orbitrap HF-X instrument was set to data-dependent acquisition (DDA) and was operated in a positive mode. Survey scans (350–1,600 m/z) were acquired in the Orbitrap system with a resolution of 120,000 at m/z 200. The 20 most intense ions were sequentially isolated and HCD (Higher Energy Collision Dissociation) fragmented using normalized collision energy. The general mass spectrometric conditions were as follows: 2 kV spray voltage, no sheath and auxiliary gas flow, heated capillary temperature of 275°C, predictive automatic gain control (AGC) enabled, and an S-lens RF level of 40%.

The non-depleted samples were analyzed on an LTQ-Orbitrap Velos ETD (Thermo Fisher Scientific) coupled with Easy NanoLC II (Thermo Scientific). The peptide mixture was loaded on a ReproSil-Pur C18-AQ C18 reversed phase column (4 cm × 100 µm inner diameter, 5 µm particles) and subsequently eluted onto a 20 cm 75 inner diameter analytical column containing ReproSil-Pur C18-AQ 3 µm particles. We applied a 130-min gradient using the from 3 to 28% solvent B in 100 min, 28 to 45% in 20 min, 45 - 95% B in 2 min and 8 min at 95% B (A = 0.1% FA; B = 90% ACN, 0.1% FA). After each run, the trap column and column were equilibrated with mobile phase A. The LTQ-Orbitrap Velos instrument was set to data-dependent acquisition (DDA) and was operated in a positive mode. Survey scans (350–1,500 m/z) were acquired in the Orbitrap system with a resolution of 60,000 at *m/z* 110. The 20 most intense ions, excluding unassigned and 1+ charge state, were sequentially isolated and CID (Collision-induced dissociation) fragmented using normalized collision energy of 35. The general mass spectrometric conditions were as follows: 1.9 kV spray voltage, no sheath and auxiliary gas flow, heated capillary temperature of 280°C, predictive automatic gain control (AGC) enabled, and an S-lens RF level of 65.88%.

Database Search and Statistical Analysis

The raw files corresponding to the depleted and non-depleted serum were searched using Proteome Discoverer v2.3.0.523 and

PatternLab for proteomics v4.1.1.17 (Carvalho et al., 2016) (http://patternlabforproteomics.org/), using the SEQUEST search engine. The *H. sapiens* Swiss-Prot database was downloaded on January 24, 2020; a reversed version of each sequence plus those from 127 common mass spectrometry contaminants was included. Trypsin was used as a cleavage enzyme (fully tryptic and semi-tryptic), allowing a maximum of 2 missed cleavage sites. Cysteine carbamidomethylation and methionine oxidation were considered as a static and dynamic modifications, respectively. In the Proteome Discoverer and PatternLab for Proteomics tools, false Discovery Rate (FDR) was 1% for peptide and protein identification. Label free quantification (LFQ) was performed by applying the extracted ion chromatogram (XIC) area. In PatternLab, the quantitation was performed according to Normalized Ion Abundance Factors (NIAF) as a relative quantitation strategy. NIAF is the equivalent to NSAF (Zybailov et al., 2006), but applied to XIC (Neilson et al., 2011). Statistical analyzes were performed using the Perseus 1.5.3.2 software (Cox and Mann, 2008), Proteome Discoverer, and PatternLab for Proteomics (Carvalho et al., 2016). Differentially regulated proteins and semi-tryptic peptides were determined by applying a t-test with an adjusted p-value <0.1 (Benjamini-Hochberg method).

Bioinformatics Analysis

For gene ontology (GO) analysis, the tool g: Profiler (Raudvere et al., 2019) was employed. The analyses were performed separately for proteins identified upregulated and downregulated between the groups evaluated. A q-value threshold of 0.05 was used, corrected by the Benjamini-Hochberg method. The Gene Enrichment Analysis (GSEA) (Subramanian et al., 2007) was applied to evaluate enriched pathways using the Reactome platform as reference data. Other parameters were used with configurations: permutation method: genes, minimum number of members: 3, maximum number of members: 84, metric for ranking genes: T-test. The Database for Annotation, Visualization and Integrated Discovery (DAVID) v6.8 (Huang et al., 2009) was used to complement bioinformatics analysis. IceLogo tool (Colaert et al., 2009), BRENDA enzyme database (Placzek et al., 2017), Proteasix (http://www.proteasix.org/) and MEROPS - the Peptidase Database (Rawlings et al., 2018) were used to access and analyze peptidases activity.

Analysis of Enzyme Activity

To analyze the enzymatic activity of the samples, a gelatin zymography was performed as previously described (Toth and Fridman, 2001). Proteins were resolved electrophoretically in 12% SDS-PAGE containing 0.1% gelatin. To remove the SDS, the gel was incubated two times of 30 min with wash buffer (2.5% Triton X-100, 50 mM Tris HCl, 5 mM CaCl2, 1 μM ZnCl2, and H2O); followed by a wash in water and incubation for 12 h in incubation buffer (Triton x 100 at 1%, Tris HCl 50 mM pH 7.5, 5 mM CaCl2, 1 μM ZnCl2) at 37°C in a water bath. The gels were stained with 0.5% Coomassie blue and MMPs activity was determined by the intensity of the band using the ImageLab 3.0 software. Statistical significance was assessed by Student t-test using Graphpad Prism 5 software.

RESULTS

The Serum Proteomic Profile of ZIKV Exposed Children Without CZS Is Altered Compared to Controls

The serum of infants without symptoms of CZS, but with intrauterine exposure to ZIKV and unexposed controls was evaluated by a proteomic approach based on mass spectrometry, with and without depletion of the 14 most abundant serum proteins (**Figure 1A**). The gestational and maternal age was similar between ZIKV and CTRL infants (**Supplementary Figures 1A–C** and **Supplementary File 1**). The age of infants varied from 3 to 23 months (CTRL = 14.4 and ZIKV = 13.2) without statistical significance (p-value = 0.3379) (**Supplementary Figure 1B** and **Supplementary File 1**). The average head circumference was smaller in the ZIKV group, however, this difference was not statistically significant (p-value = 0.2792) (**Supplementary Figure 1D** and **Supplementary File 1**).

All mothers presented rash during the second or third trimester of pregnancy. Boys and girls distribution between CTRL and ZIKV groups are six boys and four girls each, and 75% of 20 families were favela residents. One child of the ZIKV exposed group presented developmental delays and was diagnosed with apraxia of speech and attention deficit hyperactivity disorder. This child had abnormal magnetic resonance findings, with the high signal at the periventricular area in T2 and FLAIR, prominence of perivascular spaces with unspecific aspect, and corpus callosum thinning (**Supplementary File 1**).

Proteomics identified a total of 383 and 449 proteins in the depleted serum using the Proteome Discoverer and PatternLab software, respectively (**Supplementary 2**). The 383 common proteins between the two software were selected for further statistical analysis. The identifications in the non-depleted serum were 278 and 438 proteins by Proteome Discoverer and PatternLab for Proteomics, respectively. The 278 proteins identified by both search engines were considered for further analysis. A total of 190 proteins were identified in common between the depleted and non-depleted serum: and 193 and 88 exclusive proteins in the non-depleted and depleted treatment, respectively (**Figure 1B**). The Principal Component Analysis (PCA) of depleted (**Supplementary Figure 1E**) and non-depleted (**Supplementary Figure 1F**) serum are different, with separation between two distinct groups only in the depleted serum (**Supplementary File 1**). GO analysis of each dataset was performed to evaluate the effect of serum depletion on the cellular components (CC) of identified proteins. As expected, the variety of CC identified in the depleted (**Figure 1C**) and non-depleted (**Figure 1D**) serum revealed minor variation; however, proteins of the immunoglobulin complex were enriched only in the non-depleted serum. We also evaluated tissues that express the identified proteins (**Figures 1E, F**). The depleted serum shows greater diversity in the tissue distribution of identified proteins (**Figure 1E**), with several proteins being expressed in the placenta (**Supplementary File 2**). In the depleted serum, 84 proteins were regulated, with 36 upregulated and 48

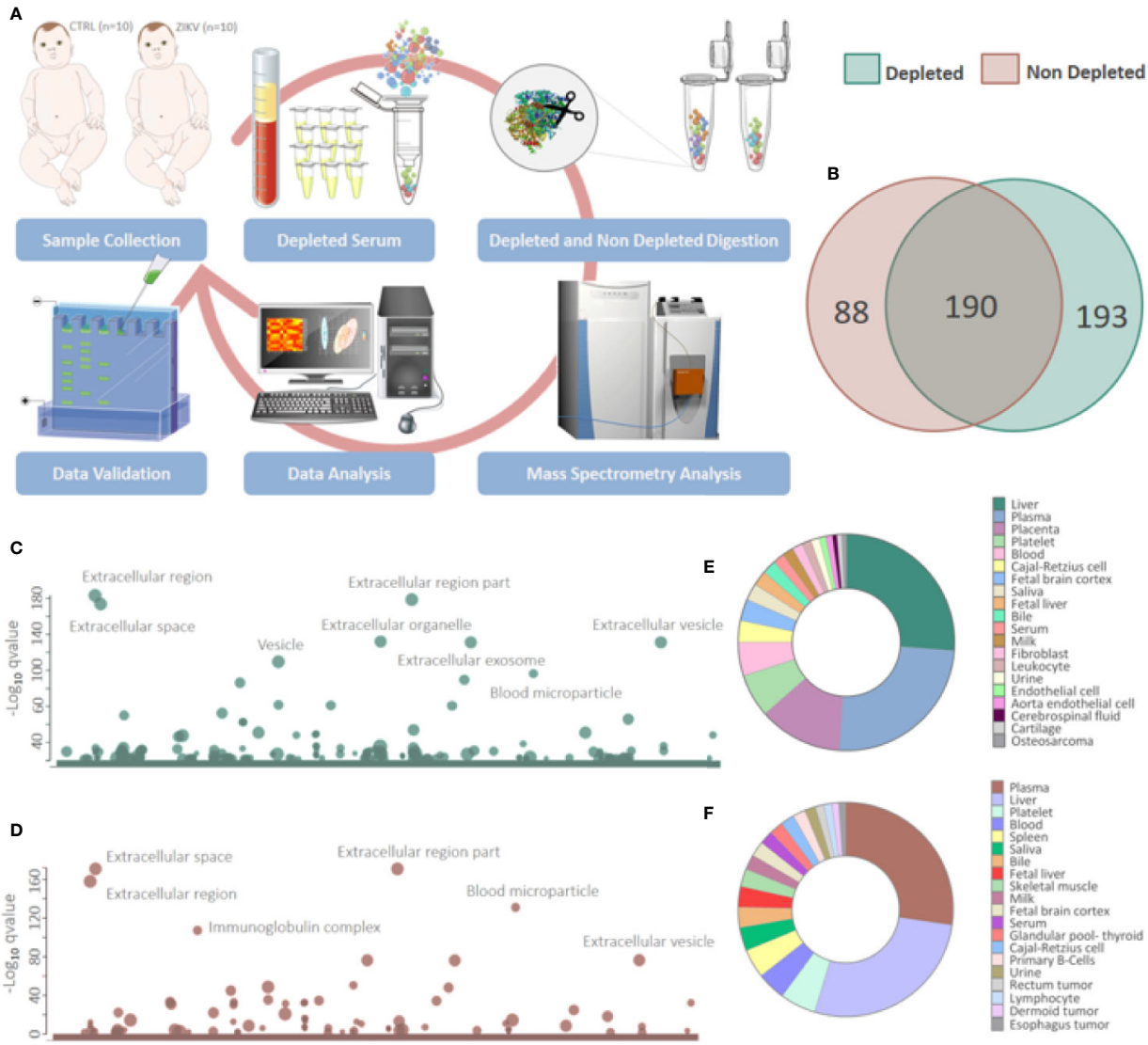

FIGURE 1 | Proteins identified in depleted and non-depleted serum. **(A)** Workflow adopted for sample preparation and data analysis. **(B)** Venn diagram of proteins identified in the depleted and non-depleted serum. Only proteins identified by the Proteome Discoverer and PatternLab for Proteomics software were considered for posterior analysis. **(C, D)** Cellular components attributed to the total proteins identified in depleted and non-depleted treatment were determined using the tool g: Profiler. (q-value < 0.05). **(E, F)** Tissues that express identified proteins were evaluated by the Database for Annotation, Visualization and Integrated Discovery (DAVID) v6.8 platform. Only identifications with a p-value equal to or less than 0.05 and that present at least five proteins were considered.

downregulated in the serum of infants with ZIKV intrauterine exposure compared to controls (**Figure 2A**). A total of 37 proteins showed fold change greater than 1 time (**Figure 2B** and **Table 1**) while the non-depleted serum indicated only two regulated proteins, one upregulated and one downregulated (**Figure 2C**, **Supplementary File 3**).

Disease-Related and Enriched Pathways Analysis

The results of disease-related and enriched protein analysis are broad, due to proteins that are shared between multiple pathological processes (**Supplementary File 4**). Indeed, evaluation of diseases related to all differentially regulated proteins showed different classes of disorders, which include metabolic, renal, brain, cardiovascular abnormalities, among others (**Figure 3A**). When evaluation was performed for upregulated proteins, data indicate that proteins associated to macular degeneration, thrombosis, retinopathy of prematurity, and cerebrovascular disease (**Figure 3B**). These data provide insight of important molecular changes that might be related to exposure to ZIKV *in utero*.

The GSEA Reactome analysis showed 27 differently regulated pathways (**Figure 4A**). The colors red and blue represent

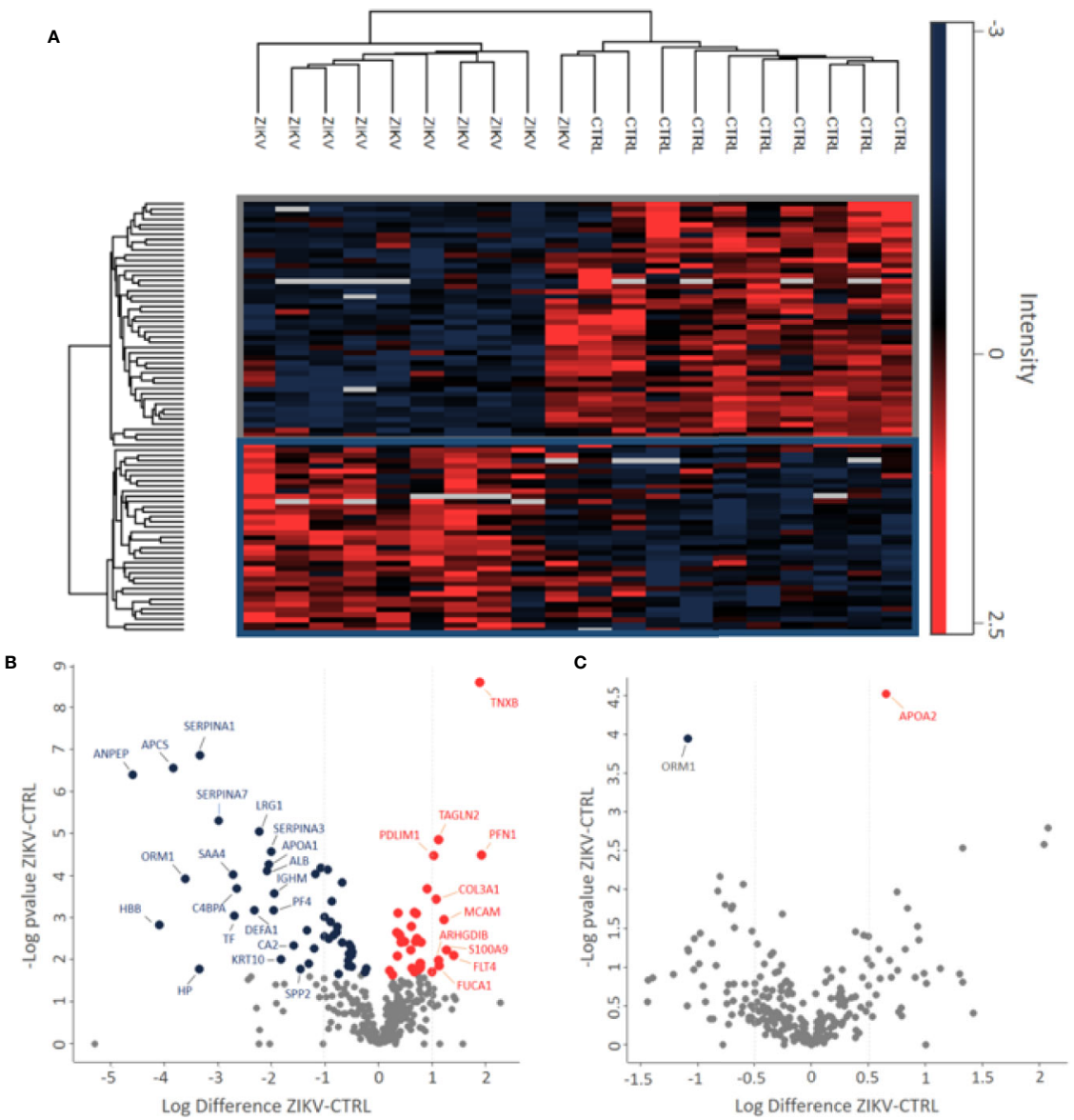

FIGURE 2 | Differently abundant proteins identified in the groups of patients CTRL and ZIKV. **(A)** Heatmap of the proteins regulated in the depleted serum between the evaluated groups. The intensities were normalized using the z-score function. The red and blue colors show upregulated and downregulated proteins, respectively. The blank color indicates that the protein did not show any intensity in the sample. **(B, C)** Volcano plot of depleted and non-depleted serum proteins, respectively. The fold change is represented by the ratio between ZIKV and CTRL protein intensities; negative values indicate greater abundance in the CTRL group compared to the ZIKV group. In **(B)** proteins with fold change > 1 were marked, in **(C)** both regulated proteins were marked.

upregulated and downregulated pathways, respectively; heatmaps indicate proteins and their related pathways. Axon guidance and RHO GTPase signaling were identified upregulated in the ZIKV group, while visual phototransduction and retinoid metabolism are downregulated (**Figure 4A**). The pathways were represented in relation to p-value; in positive regulation **(Figure 4B)** and negative regulation **(Figure 4C)**. Complete information on the GSEA analysis is available in **Supplementary file 5**.

GO analysis for upregulated and downregulated proteins was performed for molecular function (MF), biological process (BP), and cellular component (CC). Events related to coagulation, leukocyte aggregation, synapse maturation, fibrinolysis, and platelet degranulation are increased in the ZIKV group **(Figure 5A)**. On the other hand, downregulated proteins are involved with immune responses, tissue homeostasis, and remodeling of the lipid-protein complex. The CC of differently regulated proteins is similar, with emphasis on lipoprotein complexes for downregulated proteins **(Figure 5B)**. Both upregulated and downregulated proteins showed MFs related to the activities of endopeptidases, indicating higher protease activity in the ZIKV

TABLE 1 | Differently abundant proteins identified in CTRL and ZIKV patient groups.

Gene name	ZIKV/CTRL Log2 Ratio	Description
PFN1	1.91954	Profilin-1
TNBX	1.88759	Tenascin-X
FLT4	1.40468	Vascular endothelial growth factor receptor 3
S100A9	1.2597	Protein S100-A9
MCAM	1.21672	Cell surface glycoprotein MUC18
FUCA1	1.12497	Tissue alpha-L-fucosidase
TAGLN2	1.11761	Transgelin-2
ARHGDIB	1.11735	Rho GDP-dissociation inhibitor 2
COL3A1	1.07535	Collagen alpha-1(III) chain
PDLIM1	1.03179	PDZ and LIM domain protein 1
B4GALT1	−1.00354	Beta-1,4-galactosyltransferase 1
LAMP1	−1.00966	Lysosome-associated membrane glycoprotein 1
APOM	−1.07515	Apolipoprotein M
FCGR3A	−1.18018	Low affinity immunoglobulin gamma Fc region receptor III-A
GGH	−1.20471	Gamma-glutamyl hydrolase
A2M	−1.3034	Alpha-2-macroglobulin
PEPD	−1.3376	Xaa-Pro dipeptidase
SPP2	−1.46451	Secreted phosphoprotein 24
CA2	−1.58602	Carbonic anhydrase 2
KRT10	−1.82313	Keratin, type I cytoskeletal 10
IGHM	−1.94719	Immunoglobulin heavy constant mu
PF4	−1.95174	Platelet factor 4
SERPINA3	−2.00752	Alpha-1-antichymotrypsin
APOA1	−2.05201	Apolipoprotein A-I
ALB	−2.08527	Serum albumin
LRG1	−2.23184	Leucine-rich alpha-2-glycoprotein
DEFA1	−2.31688	Neutrophil defensin 1
C4BPA	−2.64302	C4b-binding protein alpha chain
TF	−2.69371	Serotransferrin
SAA4	−2.71299	Serum amyloid A-4 protein
SERPINA7	−2.98174	Thyroxine-binding globulin
SERPINA1	−3.34126	Alpha-1-antitrypsin
HP	−3.34659	Haptoglobin
ORM1	−3.60256	Alpha-1-acid glycoprotein 1
APCS	−3.83006	Serum amyloid P-component
HBB	−4.09269	Hemoglobin subunit beta
ANPEP	−4.59327	Aminopeptidase N

Protein ID: Swiss-Prot protein identifier.
Fold change: ratio between ZIKV and CTRL protein intensities; negative values indicate greater abundance in the CTRL group compared to the ZIKV group. Protein description: according to the Swiss-Prot database. All proteins satisfy a q-value < 0.1.

exposed serum. The interaction between proteins upregulated (red dots) and downregulated (blue dots) and the respective ontologies are shown in **Figure 5C**, including TGF-beta signaling and complement activation (**Supplementary File 6**).

Aberrant Pattern of Protease Activity in the Serum of Infants With ZIKV Intrauterine Exposure Compared to Control

Semi-tryptic peptides are those cleaved at the C-terminus by trypsin (arginine and lysine residues) and at the other terminal (N-terminus) by another endogenous enzyme. The analysis of semi-tryptic peptides can indicate the action of proteases. In depleted serum, we identified a total of 3,258 peptides and among these, 976 were semi-tryptic (**Figure 6A**). To determine the semi-tryptic peptides differentially regulated between the groups evaluated, the same approach described above for proteins was applied. Our results show 547 semi-tryptic peptides upregulated and 47 downregulated in the ZIKV group (**Figure 6B** and **Supplementary File 7**); suggesting a higher proteolytic activity in the serum of ZIKV exposed infants. In total, 87 proteases and protease inhibitors were identified in our dataset (**Table 2**).

Motif analysis of most frequent cleavage sites for semi-tryptic peptides upregulated in the ZIKV group showed alanine and leucine at the cleaved sites (**Figure 6C**). On the other hand, the downregulated semi-tryptic peptides showed tyrosine and phenylalanine as the most frequent cleavage sites (**Figure 6D**). The prediction of proteases involved in the cleavage of the all semi-tryptic peptides identified showed that metalloproteinase family is responsible for the cleavage of 24% and plasminogen of 4%. The individual analysis of upregulated and downregulated semi-tryptic peptides showed that metalloproteinases are responsible for the cleavage of 22.8% and 12.6%, respectively (**Table 2** and **Supplementary 7**).

Evaluation of serum protease activity (**Figure 7A**) showed an increase in the metalloproteinase 2 (MMP2) (**Figure 7B**) and metalloproteinase 9 (MMP9) (**Figure 7C**) in serum from ZIKV group compared to CTRL, which are shown by the intensity of the molecular weight bands of 72 KDa and 92 KDa, respectively (**Supplementary File 8**). In addition, the formation of MMPs complexes is indicated by the presence of high molecular weight bands (~ 250 KDa) (Roy et al., 2008) (**Figure 7D**). The intensity of all quantified bands was summed, and the result is shown in (**Figure 7E**), with p-value <0.0001 (**Supplementary File 8**).

DISCUSSION

Exposure to ZIKV Is Related to Coagulation, Thrombotic Events, and Late Cerebrovascular Disorders

Quantitative proteomics approaches have been applied to investigate the molecular mechanisms involved in intrauterine ZIKV infection. Infection of primary human neural stem cells (McGrath et al., 2017), neural progenitor cells (Scaturro et al., 2018), and neurospheres derived from induced pluripotent stem cells are used in modeling the effects of first-trimester infections *in vitro* (Garcez et al., 2017; Rosa-Fernandes et al., 2019). In this study, we performed large-scale serum quantitative proteomics to identify molecular changes in infants exposed to ZIKV without early clinical symptoms compared to paired controls, in order to explore and predict molecular evidence of possible late abnormalities during the ongoing follow-up of this cohort.

Proteins related to venous thrombosis and blood coagulation, such as Coagulation factor VII (F7) and Fibrinogen alpha chain (FGA), were upregulated in the ZIKV group. The relationship between viral infections and changes in coagulation processes has already been described for ZIKV (Ramacciotti et al., 2019) and other viruses (Kimmel, 1967; Bibas et al., 2011; da Costa et al., 2012; Goeijenbier et al., 2012; Roy et al., 2013; Wang et al., 2015; Wijarnpreecha et al., 2017; Marques et al., 2017;

FIGURE 3 | Disease-related proteins. **(A)**. The "Diseases" module in the Database for Annotation, Visualization and Integrated Discovery (DAVID) tool was used to determine the disease classes related to all regulated proteins. **(B)** The analysis for proteins related to diseases was performed separately for upregulated and downregulated proteins. Only tissues and diseases that presented p-value <0.05 were represented in the graph.

Neppelenbroek et al., 2018; Ngu et al., 2018; Ramacciotti et al., 2019).

After the occurrence of isolated cases of venous thrombosis in patients who had a positive diagnosis for ZIKV, Ramacciotti et al. (2019) assessed blood D-dimer levels, which are usually monitored for the diagnosis of deep venous thrombosis, of 172 patients who had ZIKV or chikungunya, without cross-infection. The results showed an increase of 19.4% and 63.8% in the D-dimer levels of patients with ZIKV and chikungunya, respectively. Moreover, pro-thrombosis effects related to viral infection of the CNS can result in cerebrovascular complications (Tang et al., 2019). Landais et al. (2017) reported a case of stroke in a 10-month-old child who was positive for ZIKV. A second case of fetal cerebral infarction has been reported, in which a child has been exposed to ZIKV and had no brain changes on MRI. However, at 16 days of age, an area of chronic encephalomalacia was found (Mulkey et al., 2018). A third study confirmed the presence of ZIKV RNA in the placenta, umbilical cord and amniotic membrane on the maternal side of the placenta of a pregnant woman who delivered a child without clinical evidence of microcephaly and CZS. The medical follow-up showed that the child had a stroke on the eighth day of life, even without apparent abnormalities in complete blood count, cranial ultrasound and ammonia values (Raymond and Jakus, 2018). In addition, a report of cerebral vasculitis in an adult patient with ZIKV positive PCR was published (Acevedo et al., 2017). Cerebral vasculitis in neonates is characteristic of congenital diseases (Koeppen et al., 1981; Baskin and Hedlund, 2007; Hauer et al., 2019). Although case reports related to ZIKV exposure are punctual, our study agrees with these findings as we identified proteins related to upregulated cerebrovascular disease in children exposed to ZIKV compared to CTRL group. In our cohort, a patient in the ZIKV group showed changes in MRI and developmental delay. This finding corroborates previous studies applied to the larger cohorts, such as Pomar et al. (2018) and Rice et al. (2018), in which 12.5% and 1.6% of the population exposed to ZIKV who were born without microcephaly and CZS developed complications, respectively. Due do that, we emphasize the importance of medical monitoring of symptomatic and asymptomatic children, as apparently unexplained late neurological complications might be due to exposure to ZIKV in the uterus.

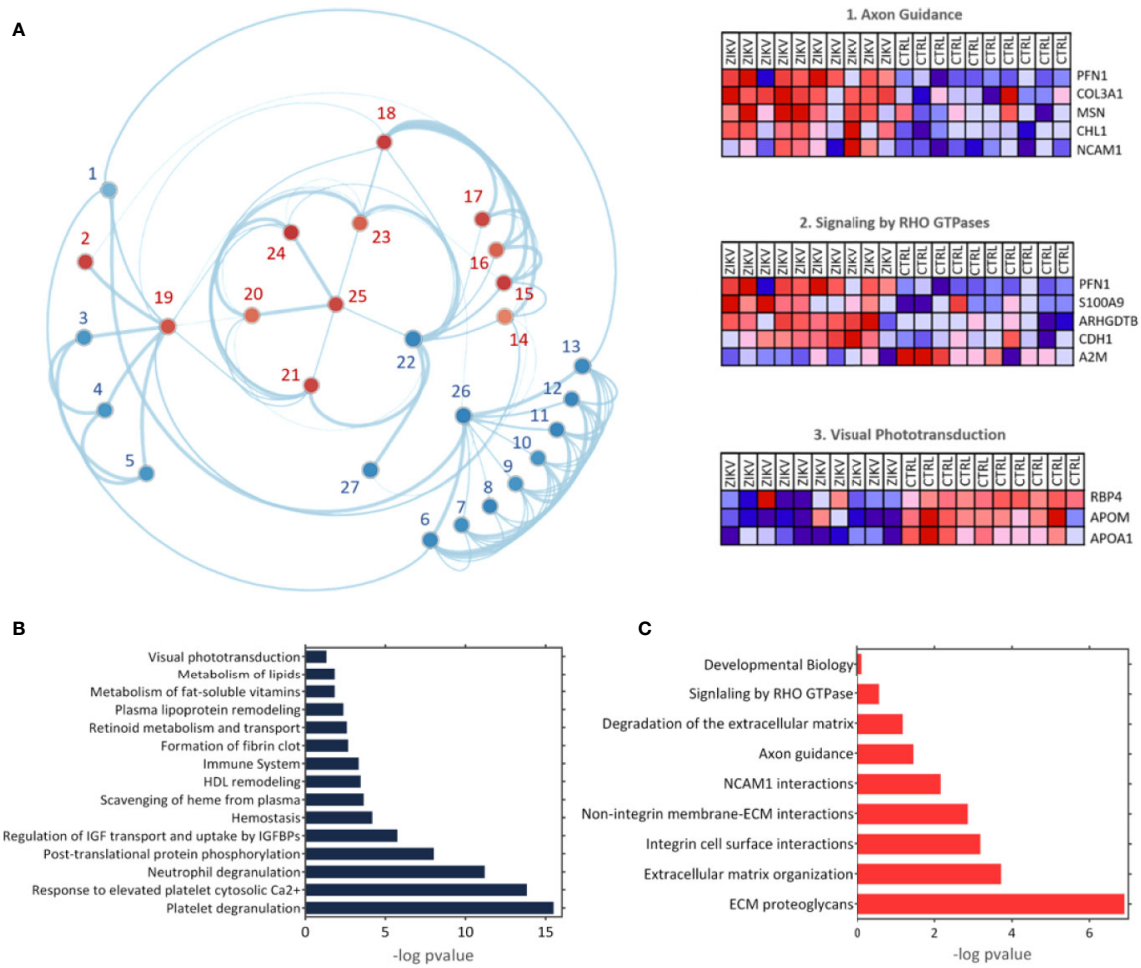

FIGURE 4 | The Gene Enrichment Analysis (GSEA). **(A)** Results obtained with the GSEA analysis; the reference data used were the Reactome platform pathways. The red and blue dots indicate upregulated and downregulated pathways, respectively. The numbered pathways correspond to: 1: Formation of fibrin clot, 2: Signaling by RHO GTPase, 3: Metabolism of fat-soluble vitamins, 4: Retinoid metabolism and transport, 5: Visual phototransduction, 6: Response to elevated platelet cytosolic Ca^{2+}, 7: Metabolism of lipids, 8: Scavenging of heme from plasma, 9: Plasma lipoprotein remodeling, 10: HDL remodeling, 11: Post-translational protein phosphorylation,12: Regulation of Insulin-like Growth Factor (IGF) transport and uptake by Insulin-like Growth Factor Binding Proteins (IGFBPs), 13: Platelet degranulation, 14: Degradation of the extracellular matrix, 15: Integrin cell surface interactions, 16: Non-integrin membrane-ECM interactions, 17: ECM proteoglycans, 18: Extracellular matrix organization, 19: Signal Transduction, 20: Developmental Biology, 21: Signaling by Interleukins, 22: Immune System, 23: Cytokine signaling in immune system,24: Axon guidance, 25: NCAM1 interactions, 26: Hemostasis, 27: Neutrophil degranulation. Heatmaps represent proteins related to three chosen pathways: Axon guidance, RHO GTPase signaling, and visual phototransduction. **(B, C)** Upregulated and downregulated pathways, respectively.

Cerebrovascular Disorders Related to Increased Activity of Metalloproteinases

MMPs are proteolytic enzymes that degrade the extracellular matrix and basement membranes and participate in biological homeostatic and pathological processes (Birkedal-Hansen et al., 1993). Among the neuronal pathologies linked to MMPs, neuronal apoptosis and oxidative damage to DNA are apparent (Xie et al., 2017). MMPs are expressed in different tissues, including the CNS, where they perform pathological functions linked to the opening of the blood-brain barrier after cerebral ischemia (Cunningham et al., 2005). Reports show that MMPs play a key role in chronic inflammatory diseases of the CNS and participate in the degradation of myelin components (Walker and Rosenberg, 2010). Our study identified an increased activity of MMPs 2 and 9 in the serum of children exposed to ZIKV, as well as an increase in the levels of the Profilin-1 (PFN-1) protein, which is fundamental for myelination (Montani et al., 2014). Neuronal death after cerebrovascular disorders has been reported, and studies show a possible role for MMPs in this phenomenon. Lee (2004) showed increased activity of MMP2 and 9 located mainly in neurons of rats after transient global ischemia. Yang et al. (2010) demonstrated that MMP2 and 9 cleave the proteins Poly(ADP-Ribose) Polymerase 1 (PARP-1) and DNA repair protein XRCC1 (XRCC1), which facilitates oxidative damage in neurons during early ischemia. These proteins are involved in events of cell survival and apoptosis.

FIGURE 5 | Gene ontology analysis. **(A, B)** From top to bottom are indicated the molecular function (MF), Biological Process (BP), and Cellular Component (CC) related to upregulated and downregulated proteins, respectively. q-value < 0.05. **(C)** Interaction between upregulated (red dots) and downregulated (blue dots) proteins, with their respective related ontologies. The gray color show the ontology related to proteins identified upregulated and downregulated. The analysis was performed in the ClueGo app. Only interactions with a p-value less than or equal to 0.05 were considered, with correction by the Benjamini-Hochberg method. The size of the node shows the significance of the interactions, based on the adjusted p-value.

Macular Degeneration and Eye Abnormalities Related Proteins

Ocular complications have already been described in infants diagnosed with CZS (Ventura and Ventura, 2018). Moreover, a recently developed label-free proteomics methodology has also been applied to evaluate the alteration of the ocular protein of children exposed to ZIKV during pregnancy, comparing groups with and without CZS (Rosa-Fernandes et al., 2020). The study showed that the biomolecules involved in neutrophil degranulation, neurodevelopment, cell infiltration, and ocular

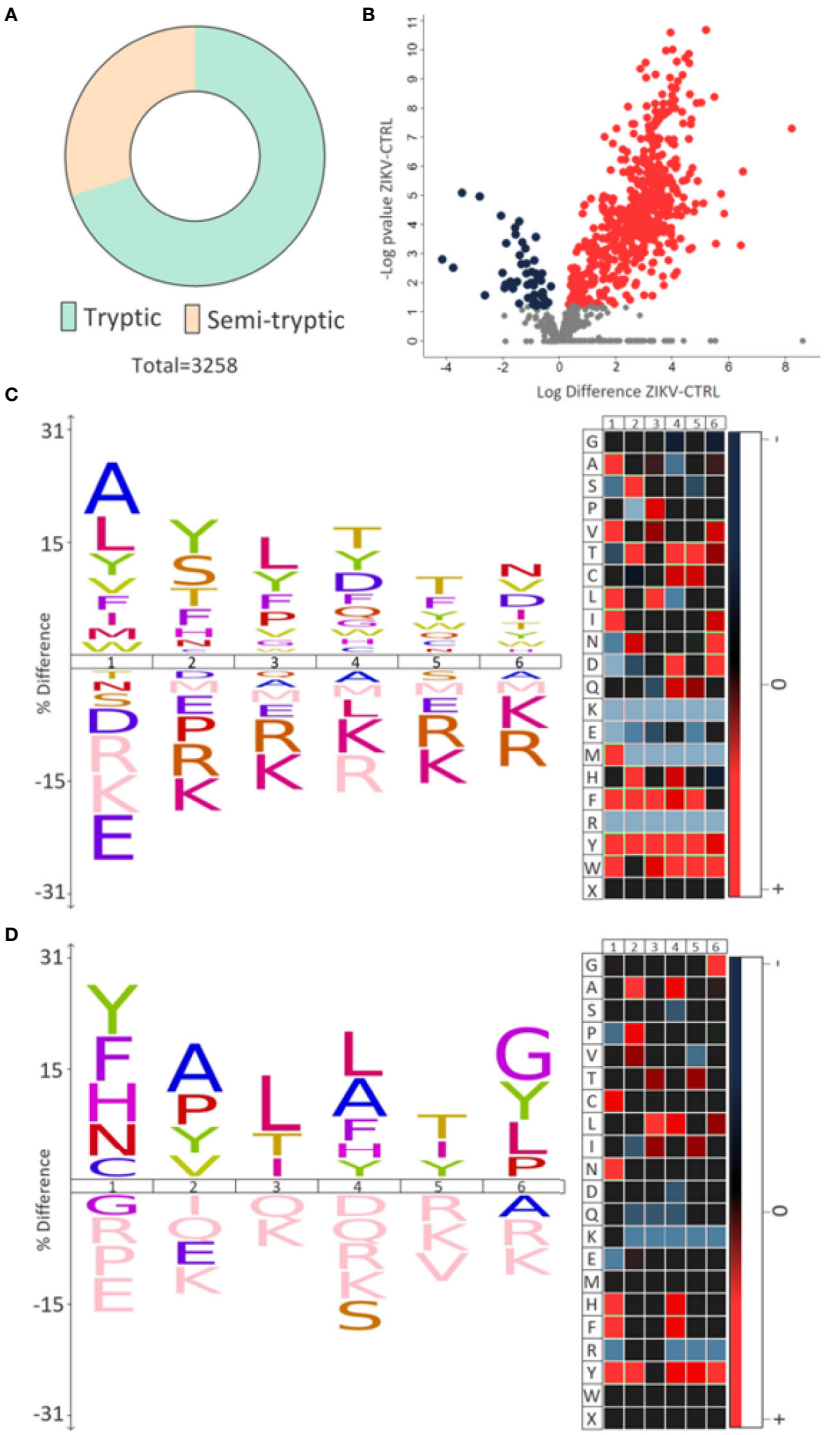

FIGURE 6 | Semi-tryptic peptides. **(A)** The number of tryptic and semi-tryptic peptides identified in samples of depleted serum. q-value < 0.1. **(B)** Volcano plot of differently regulated semi-tryptic peptides. A total of 547 upregulated (red dots) and 47 downregulated (blue dots) were identified. **(C, D)** The most frequent cleavage sites (%) identified by the upregulated and downregulated semi-tryptic peptides, respectively. The numbers 1-6 indicate the position of the amino acids in the peptide sequence and the endopeptidase cleavage site is between positions 1 and 2. In heatmaps, red is the most represented amino acid, while blue is the least represented amino acid.

TABLE 2 | Proteases and protease inhibitors identified in our dataset.

Gene name	Description
A2M	Alpha-2-macroglobulin
A2ML1	Alpha-2-macroglobulin-like protein 1
ACAA1	3-ketoacyl-CoA thiolase, peroxisomal
ADAMTS13	A disintegrin and metalloproteinase with thrombospondin motifs 13
ALDOA	Fructose-bisphosphate aldolase A
AMBP	Protein AMBP
ANPEP	Aminopeptidase N
AOC2	Retina-specific copper amine oxidase
AOC3	Membrane primary amine oxidase
BCHE	Cholinesterase
BLVRB	Flavin reductase (NADPH)
BTD	Biotinidase
CA1	Carbonic anhydrase 1
CAT	Catalase
CD109	CD109 antigen
CFB	C3/C5 convertase
CFD	C3 convertase activator
CNDP1	Beta-Ala-His dipeptidase
CPB2	Carboxypeptidase B2
CPN1	Carboxypeptidase N catalytic chain
CPN2	Carboxypeptidase N subunit 2
CST3	Cystatin-C
CTBS	Di-N-acetylchitobiase
DBH	Dopamine beta-hydroxylase
DCP1	Dipeptidyl carboxypeptidase I
DNMT3A	DNA (cytosine-5)-methyltransferase 3A
DPEP2	Dipeptidase 2
DPP4	Dipeptidyl peptidase 4
ENPP2	Ectonucleotide pyrophosphatase/phosphodiesterase family member 2
FAP	Prolyl endopeptidase
FKBP1A	Peptidyl-prolyl cis-trans isomerase FKBP1A
FSAP	Factor VII-activating protease
FUCA2	Plasma alpha-L-fucosidase
GGH	Gamma-glutamyl hydrolase
GPLD1	Phosphatidylinositol-glycan-specific phospholipase D
GPX3	Glutathione peroxidase 3
HSPG2	Basement membrane-specific heparan sulfate proteoglycan core protein
ITIH1	Inter-alpha-trypsin inhibitor heavy chain H1
ITIH2	Inter-alpha-trypsin inhibitor heavy chain H2
ITIH3	Inter-alpha-trypsin inhibitor heavy chain H3
ITIH4	Inter-alpha-trypsin inhibitor heavy chain H4
KNG1	Alpha-2-thiol proteinase inhibitor
LCAT	Phosphatidylcholine-sterol acyltransferase
LDHA	L-lactate dehydrogenase A chain
LDHAL6A	L-lactate dehydrogenase A-like 6A
LDHB	L-lactate dehydrogenase B chain
LDHC	L-lactate dehydrogenase C chain
MAN1A1	Mannosyl-oligosaccharide 1,2-alpha-mannosidase IA
MAN2A1	Alpha-mannosidase 2
MASP1	Mannan-binding lectin serine protease 1
MASP2	Mannan-binding lectin serine protease 2
METTL18	Histidine protein methyltransferase 1 homolog
MINPP1	Multiple inositol polyphosphate phosphatase 1
MMP2	72 kDa type IV collagenase
MMP9	Matrix metalloproteinase-9
NAGLU	Alpha-N-acetylglucosaminidase
PCOLCE	Procollagen C-endopeptidase enhancer 1
PCY	Prenylcysteine oxidase 1
PEPD	Xaa-Pro dipeptidase
PGLYRP2	N-acetylmuramoyl-L-alanine amidase
PI16	Peptidase inhibitor 16
PLG	Plasminogen
PON1	Serum paraoxonase/arylesterase 1
PPA2	Inorganic pyrophosphatase 2, mitochondrial
PPIA	Peptidyl-prolyl cis-trans isomerase A
PPIAL4A	Peptidyl-prolyl cis-trans isomerase A-like 4A
PPIAL4C	Peptidyl-prolyl cis-trans isomerase A-like 4C
PPIAL4D	Peptidyl-prolyl cis-trans isomerase A-like 4D
PPIAL4E	Peptidyl-prolyl cis-trans isomerase A-like 4E
PPIAL4F	Peptidyl-prolyl cis-trans isomerase A-like 4F
PPIAL4H	Peptidyl-prolyl cis-trans isomerase A-like 4H
PTGDS	Prostaglandin-H2 D-isomerase
PTPRG	Receptor-type tyrosine-protein phosphatase gamma
PZP	Pregnancy zone protein
QSOX2	Sulfhydryl oxidase 1
RNASE4	Ribonuclease 4
SERPINA1	Alpha-1 protease inhibitor
SERPINA10	Protein Z-dependent protease inhibitor
SERPINA4	Peptidase inhibitor 4
SERPINA5	Plasma serine protease inhibitor
SERPINC1	Antithrombin-III
SERPINF2	Alpha-2-antiplasmin
SERPING1	Plasma protease C1 inhibitor
SOD1	Superoxide dismutase [Cu-Zn]
SOD3	Extracellular superoxide dismutase [Cu-Zn]
TIMP1	Metalloproteinase inhibitor 1
TIMP2	Metalloproteinase inhibitor 2
VNN1	Pantetheinase

Protein description: according to the Swiss-Prot database.

dysfunction were identified in different abundances between the groups evaluated, being able to discriminate infants exposed to ZIKV during gestation and without early clinical symptoms (Rosa-Fernandes et al., 2020).

In addition, other flaviviruses, such as West Nile fever, transmitted from the mother to the fetus have also been shown to cause eye abnormalities (Alpert et al., 2003). In our analysis, we identified proteins related to premature retinopathy and macular degeneration, such as pigment epithelium-derived factor (SERPINF1), transforming growth factor beta-1 proprotein (TGFB1), fibrinogen alpha chain (FGA), mannan-binding lectin serine protease 1 (MASP1), moesin (MSN), and vitronectin (VTN), upregulated in the ZIKV group, suggesting the possibility of developing these complications. Our analysis of enriched pathways showed that visual phototransduction events are downregulated in this group compared to CTRL. Visual phototransduction is a photochemical and biochemical process that consists of photon absorption by photoreceptor cells, which convert this signal into an electrical cellular response. This electrical response is sent to the brain through action potentials and electrochemical changes. Therefore, the normal activity of this pathway, which is highly conserved in many species, is essential for the proper functioning of vision neurobiology (Mannu, 2014).

Our data together with other reports in the literature, reinforce the possibility of the occurrence of abnormalities related to ZIKV infection, not only including neurological, but also ophthalmological disorders.

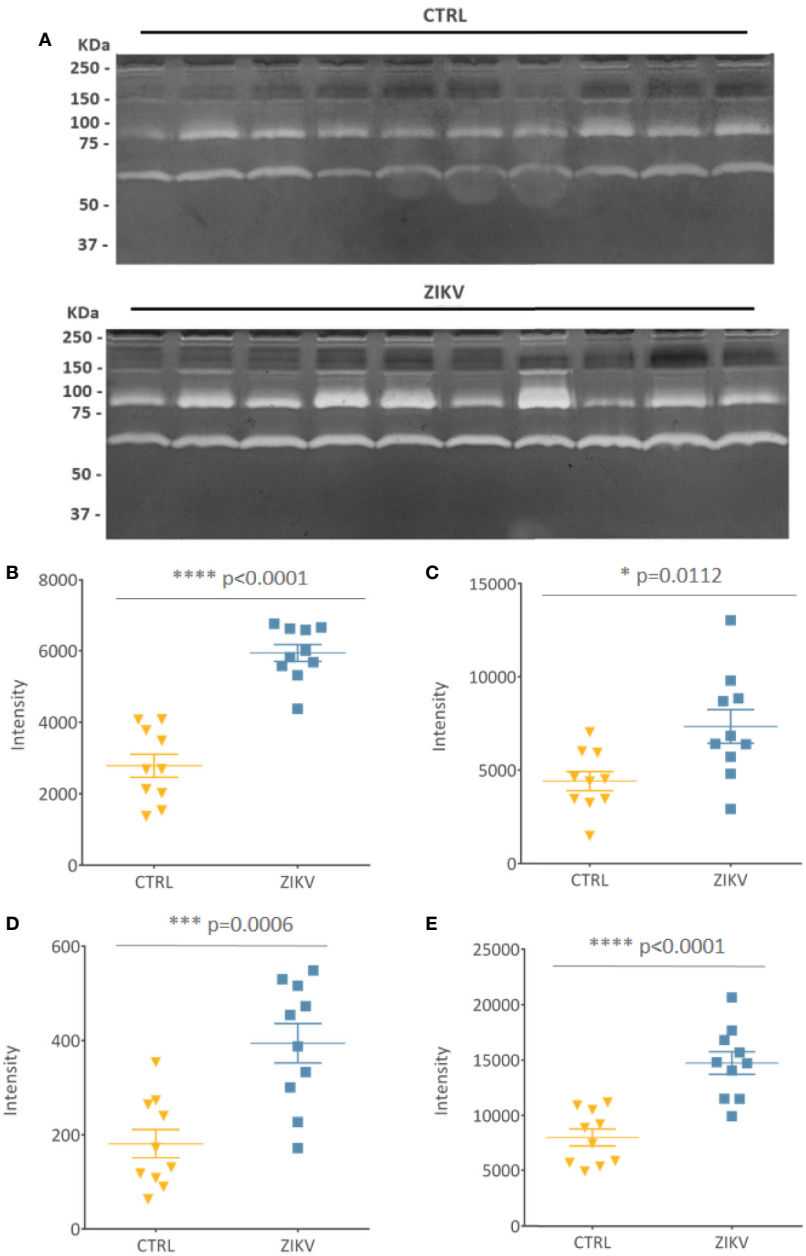

FIGURE 7 | Gelatin zymography. **(A)** Gelatinolytic activity of the samples from the CTRL and ZIKV group, with emphasis on the activities of MMP 9 (92 kDa) and MMP 2 (72 KDa). **(B–D)** The intensities of the molecular weight bands of 72, 92, and 250 kDa, with their respective p-value. **(E)** Shows the sum of all quantified intensities, with their respective p-value.

The children included in this study are currently monitored by a multidisciplinary clinical team to assess the outcome of exposure to ZIKV. Here, we demonstrate molecular differences between the groups evaluated and we emphasize the activity of MMP2 and MMP9 can emerge as potential biomarkers of exposure to the virus. We have demonstrated the increased activity of MMPs in the cohort exposed to ZIKV, making it possible to apply this finding to monitor MMPs activity in children exposed to ZIKV and who may develop late abnormalities.

CONCLUSIONS

Serum provides information on the entire content of circulating proteins and, as the main fluid available for routine clinical evaluations, has great potential in diagnostic and prognostic analyses. We have shown that children exposed to ZIKV during pregnancy, but who were born without any complications, can present molecular evidence for late abnormalities related to CZS. Our study has shown alterations in proteins that participate in

processes related to neuronal death and cerebrovascular abnormalities in the ZIKV group, even if these children do not present clinical evidences of CZS at birth. In addition, vision-related proteins have been identified as downregulated, which may indicate ocular and visual impairments, a frequent characteristic in infants that develop CZS. Another key finding was the increased activity of MMP-2 and MMP-9 in all serum samples in the ZIKV group, which could be associated to neuronal death. The children included in this study are currently monitored by multidisciplinary clinical teams to assess the outcome of long-term exposure to the virus. Our study is the first to assess molecular alterations for late disorders in child victims of the ZIKV epidemic in the Americas, demonstrating that medical follow-up should be carried out on all children exposed to the virus, as late complications can occur.

DATA AVAILABILITY STATEMENT

The original contributions presented in the study are publicly available. The mass spectrometry proteomics data have been deposited to the ProteomeXchange Consortium via the PRIDE partner repository with the dataset identifier PXD020294.

ETHICS STATEMENT

The studies involving human participants were reviewed and approved by Institutional review board and the ethics committee of the Universidade Federal Fluminense (protocol CAAE number 79890517.6.0000.5243). Written informed consent to participate in this study was provided by the participants' legal guardian/next of kin.

AUTHOR CONTRIBUTIONS

Conceptualization, methodology and project administration : LR-F and GP. Formal analysis: JM-d-S LR-F and GP. Investigation: JM-d-S, LR-F, RB, CA. Resources: RB, FC, RV, PC, ML and CC. Validation: JM-d-S. Visualization: JM-d-S and LR-F. Writing – original draft preparation: JM-d-S, LR-F and GP. Writing – review and editing: all authors. All authors contributed to the article and approved the submitted version.

FUNDING

RB was supported by FAPERJ (201.779/2017); GP was supported by FAPESP (2014/06863-3, 2018/18257-1, 2018/15549-1) and CNPq ("Bolsa de Produtividade"). This work was also supported by the VILLUM Center for Bioanalytical Sciences at the University of Southern Denmark.

ACKNOWLEDGMENTS

The authors would like to thank the medical team at the Hospital Universitário Antonio Pedro at Universidade Federal Fluminense for assisting with the sample's collections, and all mothers and children included in this project. We would like to thank Professor Luigi Palmieri, University of Bari, Italy, for useful commentaries and for reviewing this paper.

SUPPLEMENTARY MATERIAL

The Supplementary Material for this article can be found online at: https://www.frontiersin.org/articles/10.3389/fcimb.2020.577819/full#supplementary-material

SUPPLEMENTARY FIGURE 1 | Details of the participants. **(A)** Gestational age (GA) of birth of the study participants. The ZIKV group has nine points, as one participant GA was not noted. **(B)** The age of blood collection for the study. A t-test was applied, and no statistical significance was observed between the groups (p-value = 0.3379). **(C)** Age of the mothers included in the study. **(D)** Circumference of the infants heads in centimeters. The measurements were taken in the first week of the participants life. The ZIKV group has nine points, as one participant head circumference was not noted. **(E, F)** Principal Component Analysis (PCA) for depleted and non-depleted serum, respectively. The yellow and blue dots represent the CTRL and ZIKV groups, respectively. The "Principal Component Analysis" module, available in the Perseus tool, was used to build the graph. Previously, a filter was applied to select only proteins present in all samples.

SUPPLEMENTARY FILE 1 | Demographic, clinical, and radiological characteristics of the study population. Data relating to children included in this study, indicating results of maternal PCR, maternal age, child's age when collecting serum samples, gestational age of maternal rash, head circumference in the first week of life, gestational age of birth, TORCH analysis, gender, place of residence and clinical follow-up data.

SUPPLEMENTARY FILE 2 | Proteins identified by Proteome Discoverer v2.3.0.523 and PatternLab for proteomics v4.1.1.17 in depleted and non-depleted serum; cellular component analysis, and tissue-related protein. Total signal (NSAF): sum of PatternLab's normalized label-free quantitation derived from the extracted ion chromatograms (XIC). Adjusted p-value refers to the application of the correction by the Benjamini-Hochberg method. Description: protein description from the Swiss-Prot database. Name: identifier from SwissProt/UniProt database.

SUPPLEMENTARY FILE 3 | Complete information for protein differently regulated between the CTRL and ZIKV groups. Protein ID: Swiss-Prot protein identifier. Fold change: ratio between ZIKV and CTRL protein intensities; negative values indicate greater abundance in the CTRL group compared to the ZIKV group. Protein description: according to the Swiss-Prot database. All proteins satisfy a q-value < 0.1, corrected by Benjamini-Hochberg method. In the analysis of the heat map, the intensities were normalized using the z-score function. Positive values indicate that the data is above average and, when negative, it means that the data is below average.

SUPPLEMENTARY FILE 4 | Disease-related proteins. Complete information from DAVID analysis for all differently regulated, upregulated, and downregulated proteins. GAD_Disease: Gene-Disease Associations.

SUPPLEMENTARY FILE 5 | Full list of pathways disclosed by the GSEA analysis. The results include the pathways identifier, statistical results, and name from Reactome.

SUPPLEMENTARY FILE 6 | Complete information of the DAVID and ClueGO Gene Ontology analysis. CTRL and ZIKV GO information. BP: biological process; CC: cellular component; MF: molecular function.

SUPPLEMENTARY FILE 7 | Analysis of semi-tryptic peptides. Result of the search performed by Proteome Discoverer software. Trypsin was used as a cleavage enzyme (semi-tryptic), allowing a maximum of 2 missed cleavage sites. Description: protein description from the Swiss-Prot database. Name: identifier from SwissProt/UniProt database.

SUPPLEMENTARY FILE 8 | Gelatin zymography. The intensity of the bands corresponds to the results of the ImageLab 3.0 software.

REFERENCES

Acevedo, N., Waggoner, J., Rodriguez, M., Rivera, L., Landivar, J., Pinsky, B., et al. (2017). Zika Virus, Chikungunya Virus, and Dengue Virus in Cerebrospinal Fluid from Adults with Neurological Manifestations, Guayaquil, Ecuador. *Front. Microbiol.* 8, 42. doi: 10.3389/fmicb.2017.00042

Alpert, S. G., Fergerson, J., and Noël, L.-P. (2003). Intrauterine West Nile virus: ocular and systemic findings. *Am. J. Ophthalmol.* 136, 733–735. doi: 10.1016/S0002-9394(03)00452-5

Baskin, H. J., and Hedlund, G. (2007). Neuroimaging of herpesvirus infections in children. *Pediatr. Radiol.* 37, 949–963. doi: 10.1007/s00247-007-0506-1

Bibas, M., Biava, G., and Antinori, A. (2011). HIV-ASSOCIATED VENOUS THROMBOEMBOLISM. *Mediterr. J. Hematol. Infect. Dis.* 3, e2011030. doi: 10.4084/mjhid.2011.030

Birkedal-Hansen, H., Moore, W. G., Bodden, M. K., Windsor, L. J., Birkedal-Hansen, B., DeCarlo, A., et al. (1993). Matrix metalloproteinases: a review. *Crit. Rev. Oral. Biol. Med.* 4, 197–250. doi: 10.1177/10454411930040020401

Carvalho, P. C., Lima, D. B., Leprevost, F. V., Santos, M. D. M., Fischer, J. S. G., Aquino, P. F., et al. (2016). Integrated analysis of shotgun proteomic data with PatternLab for proteomics 4.0. *Nat. Protoc.* 11, 102–117. doi: 10.1038/nprot.2015.133

Colaert, N., Helsens, K., Martens, L., Vandekerckhove, J., and Gevaert, K. (2009). Improved visualization of protein consensus sequences by iceLogo. *Nat. Methods* 6, 786–787. doi: 10.1038/nmeth1109-786

Cox, J., and Mann, M. (2008). MaxQuant enables high peptide identification rates, individualized p.p.b.-range mass accuracies and proteome-wide protein quantification. *Nat. Biotechnol.* 26, 1367–1372. doi: 10.1038/nbt.1511

Cunningham, L. A., Wetzel, M., and Rosenberg, G. A. (2005). Multiple roles for MMPs and TIMPs in cerebral ischemia. *Glia* 50, 329–339. doi: 10.1002/glia.20169

da Costa, P. S. G., Ribeiro, G. M., Junior, C. S., and da Costa Campos, L. (2012). Severe thrombotic events associated with dengue fever, Brazil. *Am. J. Trop. Med. Hyg.* 87, 741–742. doi: 10.4269/ajtmh.2012.11-0692

Dahle, A. J., Fowler, K. B., Wright, J. D., Boppana, S. B., Britt, W. J., and Pass, R. F. (2000). Longitudinal investigation of hearing disorders in children with congenital cytomegalovirus. *J. Am. Acad. Audiol.* 11 (5), 283–290.

Dick, G. W. A., Kitchen, S. F., and Haddow, A. J. (1952). Zika virusand serological specificity. *Trans. R. Soc Trop. Med. Hyg.* 46, 509–520. doi: 10.1016/0035-9203(52)90042-4

Garcez, P. P., Nascimento, J. M., de Vasconcelos, J. M., Madeiro da Costa, R., Delvecchio, R., Trindade, P., et al. (2017). Zika virus disrupts molecular fingerprinting of human neurospheres. *Sci. Rep.* 7:40780. doi: 10.1038/srep40780

Goeijenbier, M., van Wissen, M., van de Weg, C., Jong, E., Gerdes, V. E. A., Meijers, J. C. M., et al. (2012). Review: Viral infections and mechanisms of thrombosis and bleeding. *J. Med. Virol.* 84, 1680–1696. doi: 10.1002/jmv.23354

Hauer, L., Pikija, S., Schulte, E. C., Sztriha, L. K., Nardone, R., and Sellner, J. (2019). Cerebrovascular manifestations of herpes simplex virus infection of the central nervous system: a systematic review. *J. Neuroinflamm.* 16, 19. doi: 10.1186/s12974-019-1409-4

Heukelbach, J., Alencar, C. H., Kelvin, A. A., de Oliveira, W. K., and Pamplona de Góes Cavalcanti, L. (2016). Zika virus outbreak in Brazil. *J. Infect. Dev. Ctries* 10, 116–120. doi: 10.3855/jidc.8217

Huang, D. W., Sherman, B. T., and Lempicki, R. A. (2009). Systematic and integrative analysis of large gene lists using DAVID bioinformatics resources. *Nat. Protoc.* 4, 44–57. doi: 10.1038/nprot.2008.211

Kimmel, C. B. (1967). Lysosomes in the spleen of the chick embryo. II. Changes during the graft-versus-host reaction. *J. Exp. Zool.* 166, 447–458. doi: 10.1002/jez.1401660316

Kindhauser, M. K., Allen, T., Frank, V., Santhana, R. S., and Dye, C. (2016). Zika: the origin and spread of a mosquito-borne virus. *Bull. World Health Organ.* 94, 675–686C. doi: 10.2471/BLT.16.171082

Koeppen, A. H., Lansing, L. S., Peng, S. K., and Smith, R. S. (1981). Central nervous system vasculitis in cytomegalovirus infection. *J. Neurol. Sci.* 51, 395–410. doi: 10.1016/0022-510x(81)90117-9

Landais, A., Césaire, A., Fernandez, M., Breurec, S., Herrmann, C., Delion, F., et al. (2017). ZIKA vasculitis: A new cause of stroke in children? *J. Neurol. Sci.* 383, 211–213. doi: 10.1016/j.jns.2017.10.045

Lee, S.-R. (2004). Role of Matrix Metalloproteinases in Delayed Neuronal Damage after Transient Global Cerebral Ischemia. *J. Neurosci.* 24, 671–678. doi: 10.1523/JNEUROSCI.4243-03.2004

Lowe, R., Barcellos, C., Brasil, P., Cruz, O. G., Honório, N. A., Kuper, H., et al. (2018). The Zika Virus Epidemic in Brazil: From Discovery to Future Implications. *Int. J. Environ. Res. Public Health* 15, 96. doi: 10.3390/ijerph15010096

Mannu, G. S. (2014). Retinal phototransduction. *Neurosci. (Riyadh)* 19 (4), 275–280.

Marques, M. A., Adami de Sá, F. P., Lupi, O., Brasil, P., and von Ristow, A. (2017). Trombose venosa profunda e vírus chicungunha. *J. Vasc. Bras.* 16, 60–62. doi: 10.1590/1677-5449.009616

McGrath, E. L., Rossi, S. L., Gao, J., Widen, S. G., Grant, A. C., Dunn, T. J., et al. (2017). Differential Responses of Human Fetal Brain Neural Stem Cells to Zika Virus Infection. *Stem Cell Rep.* 8, 715–727. doi: 10.1016/j.stemcr.2017.01.008

Mlakar, J., Korva, M., Tul, N., Popović, M., Poljšak-Prijatelj, M., Mraz, J., et al. (2016). Zika Virus Associated with Microcephaly. *N. Engl. J. Med.* 374, 951–958. doi: 10.1056/NEJMoa1600651

Mohr, E. L., Block, L. N., Newman, C. M., Stewart, L. M., Koenig, M., Semler, M., et al. (2018). Ocular and uteroplacental pathology in a macaque pregnancy with congenital Zika virus infection. *PloS One* 13, e0190617. doi: 10.1371/journal.pone.0190617

Montani, L., Buerki-Thurnherr, T., de Faria, J. P., Pereira, J. A., Dias, N. G., Fernandes, R., et al. (2014). Profilin 1 is required for peripheral nervous system myelination. *Development* 141, 1553–1561. doi: 10.1242/dev.101840

Moore, C. A., Staples, J. E., Dobyns, W. B., Pessoa, A., Ventura, C. V., Fonseca, E. B., et al. (2017). Characterizing the Pattern of Anomalies in Congenital Zika Syndrome for Pediatric Clinicians. *JAMA Pediatr.* 171, 288–295. doi: 10.1001/jamapediatrics.2016.3982

Mulkey, S. B., DeBiasi, R. L., and du Plessis, A. J. (2018). Cerebral infarction due to Zika virus. *J. Neurol. Sci.* 387, 109–110. doi: 10.1016/j.jns.2018.01.032

Musso, D., Ko, A.II, and Baud, D. (2019). Zika Virus Infection — After the Pandemic. *N. Engl. J. Med.* 381, 1444–1457. doi: 10.1056/NEJMra1808246

Neilson, K. A., Ali, N. A., Muralidharan, S., Mirzaei, M., Mariani, M., Assadourian, G., et al. (2011). Less label, more free: Approaches in label-free quantitative mass spectrometry. *PROTEOMICS* 11, 535–553. doi: 10.1002/pmic.201000553

Neppelenbroek, S.II, Rootjes, P. A., Boxhoorn, L., Wagenaar, J. F. P., Simsek, S., and Stam, F. (2018). Cytomegalovirus-associated thrombosis. *Neth J. Med.* 76 (5), 251–254.

Netto, E. M., Moreira-Soto, A., Pedroso, C., Höser, C., Funk, S., Kucharski, A. J., et al. (2017). High Zika Virus Seroprevalence in Salvador, Northeastern Brazil Limits the Potential for Further Outbreaks. *mBio* 8, e01390-17. doi: 10.1128/mBio.01390-17

Ngu, S., Narula, N., Jilani, T. N., and Bershadskiy, A. (2018). Venous Thrombosis Secondary to Acute Cytomegalovirus Infection in an Immunocompetent Host: Consideration for New Screening Guidelines. *Cureus* 10 (6), e2742. doi: 10.7759/cureus.2742

Noorbakhsh, F., Abdolmohammadi, K., Fatahi, Y., Dalili, H., Rasoolinejad, M., Rezaei, F., et al. (2019). Zika Virus Infection, Basic and Clinical Aspects: A Review Article. *Iran. J. Public Health* 48, 20–31. doi: 10.18502/ijph.v48i1.779

Pan American Health Organization / World Health Organization. (2017). *Zika - Epidemiological Report Brazil*. (Washington, D.C.: PAHO/WHO). Available at: https://www.paho.org/hq/dmdocuments/2017/2017-phe-zika-situation-report-bra.pdf. Accessed on 08 November 2020.

Placzek, S., Schomburg, I., Chang, A., Jeske, L., Ulbrich, M., Tillack, J., et al. (2017). BRENDA in 2017: new perspectives and new tools in BRENDA. *Nucleic Acids Res.* 45, D380–D388. doi: 10.1093/nar/gkw952

Pomar, L., Vouga, M., Lambert, V., Pomar, C., Hcini, N., Jolivet, A., et al. (2018). Maternal-fetal transmission and adverse perinatal outcomes in pregnant women infected with Zika virus: prospective cohort study in French Guiana. *BMJ* 363, k4431. doi: 10.1136/bmj.k4431

Ramacciotti, E., Agati, L. B., Aguiar, V. C. R., Wolosker, N., Guerra, J. C., de Almeida, R. P., et al. (2019). Zika and Chikungunya Virus and Risk for Venous Thromboembolism. *Clin. Appl. Thromb. Hemost.* 25, 1076029618821184. doi: 10.1177/1076029618821184

Raudvere, U., Kolberg, L., Kuzmin, I., Arak, T., Adler, P., Peterson, H., et al. (2019). g:Profiler: a web server for functional enrichment analysis and conversions of gene listupdate). *Nucleic Acids Res.* 47, W191–W198. doi: 10.1093/nar/gkz369

Rawlings, N. D., Barrett, A. J., Thomas, P. D., Huang, X., Bateman, A., and Finn, R. D. (2018). The MEROPS database of proteolytic enzymes, their substrates and inhibitors in 2017 and a comparison with peptidases in the PANTHER database. *Nucleic Acids Res.* 46, D624–D632. doi: 10.1093/nar/gkx1134

Raymond, A., and Jakus, J. (2018). Cerebral Infarction and Refractory Seizures in a Neonate with Suspected Zika Virus Infection. *Pediatr. Infect. Dis. J.* 37, e112–e114. doi: 10.1097/INF.0000000000001832

Rice, M. E., Galang, R. R., Roth, N. M., Ellington, S. R., Moore, C. A., Valencia-Prado, M., et al. (2018). Vital Signs: Zika-Associated Birth Defects and Neurodevelopmental Abnormalities Possibly Associated with Congenital Zika Virus Infection - U.S. Territories and Freely Associated State. *MMWR Morb. Mortal. Wkly. Rep.* 67, 858–867. doi: 10.15585/mmwr.mm6731e1

Rosa-Fernandes, L., Barbosa, R. H., dos Santos, M. L. B., Angeli, C. B., Silva, T. P., Melo, R. C. N., et al. (2020). Cellular Imprinting Proteomics Assay: A Novel Method for Detection of Neural and Ocular Disorders Applied to Congenital Zika Virus Syndrome. *J. Proteome Res.* 19 (11), 4496–4515. doi: 10.1021/acs.jproteome.0c00320

Rosa-Fernandes, L., Cugola, F. R., Russo, F. B., Kawahara, R., de Melo Freire, C. C., Leite, P. E. C., et al. (2019). Zika Virus Impairs Neurogenesis and Synaptogenesis Pathways in Human Neural Stem Cells and Neurons. *Front. Cell Neurosci.* 13, 64. doi: 10.3389/fncel.2019.00064

Roy, R., Louis, G., Loughlin, K. R., Wiederschain, D., Kilroy, S. M., Lamb, C. C., et al. (2008). Tumor-specific urinary matrix metalloproteinase fingerprinting: identification of high molecular weight urinary matrix metalloproteinase species. *Clin. Cancer Res.* 14, 6610–6617. doi: 10.1158/1078-0432.CCR-08-1136

Roy, A., Chaudhuri, J., Chakraborty, S., Jasani, B., Nanavati, R., Jain, V., et al. (2013). Case reports. *Indian Pediatr.* 50, 1053–1057. doi: 10.1007/s13312-013-0269-8

Scaturro, P., Stukalov, A., Haas, D. A., Cortese, M., Draganova, K., Płaszczyca, A., et al. (2018). An orthogonal proteomic survey uncovers novel Zika virus host factors. *Nature* 561, 253–257. doi: 10.1038/s41586-018-0484-5

Soares, F., Abranches, A. D., Villela, L., Lara, S., Araújo, D., Nehab, S., et al. (2019). Zika virus infection in pregnancy and infant growth, body composition in the first three months of life: a cohort study. *Sci. Rep.* 9, 19198. doi: 10.1038/s41598-019-55598-6

Souza, I. N. O., Barros-Aragão, F. G. Q., Frost, P. S., Figueiredo, C. P., and Clarke, J. R. (2019). Late Neurological Consequences of Zika Virus Infection: Risk Factors and Pharmaceutical Approaches. *Pharmaceut. (Basel)* 12, 60. doi: 10.3390/ph12020060

Subramanian, A., Kuehn, H., Gould, J., Tamayo, P., and Mesirov, J. P. (2007). GSEA-P: a desktop application for Gene Set Enrichment Analysis. *Bioinformatics* 23, 3251–3253. doi: 10.1093/bioinformatics/btm369

Tang, C., Patel, N. K., Miller, R., Beale, T., and Hyare, H. (2019). Spectrum of neurovascular complications from central nervous system infections (viral, bacterial and fungal). *BJR|Open* 1:bjro.20180024. doi: 10.1259/bjro.20180024

Toth, M., and Fridman, R. (2001). Assessment of Gelatinases (MMP-2 and MMP-9 by Gelatin Zymography. *Methods Mol. Med.* 57, 163–174. doi: 10.1385/1-59259-136-1:163

Valdes, V., Zorrilla, C. D., Gabard-Durnam, L., Muler-Mendez, N., Rahman, Z.II, Rivera, D., et al. (2019). Cognitive Development of Infants Exposed to the Zika Virus in Puerto Rico. *JAMA Netw. Open* 2, e1914061. doi: 10.1001/jamanetworkopen.2019.14061

Venancio, F. A., Bernal, M. E. Q., Ramos, M., da C. de, B. V., Chaves, N. R., Hendges, M. V., et al. (2019). Congenital Zika Syndrome in a Brazil-Paraguay-Bolivia border region: Clinical features of cases diagnosed between 2015 and 2018. *PloS One* 14, e0223408. doi: 10.1371/journal.pone.0223408

Ventura, C. V., and Ventura, L. O. (2018). Ophthalmologic Manifestations Associated With Zika Virus Infection. *Pediatrics* 141, S161–S166. doi: 10.1542/peds.2017-2038E

Vianna, R. A., de, O., Lovero, K. L., Oliveira, S. A., Fernandes, A. R., Santos, T. C. S. D., et al. (2019). Children Born to Mothers with Rash During Zika Virus Epidemic in Brazil: First 18 Months of Life. *J. Trop. Pediatr.* 65, 592–602. doi: 10.1093/tropej/fmz019

Walker, E. J., and Rosenberg, G. A. (2010). Divergent role for MMP-2 in myelin breakdown and oligodendrocyte death following transient global ischemia. *J. Neurosci. Res.* 88, 764–773. doi: 10.1002/jnr.22257

Wang, C.-C., Chang, C.-T., Lin, C.-L., Lin, I.-C., and Kao, C.-H. (2015). Hepatitis C Virus Infection Associated With an Increased Risk of Deep Vein Thrombosis: A Population-Based Cohort Study. *Med. (Baltimore)* 94, e1585. doi: 10.1097/MD.0000000000001585

Wheeler, A. C. (2018). Development of Infants With Congenital Zika Syndrome: What Do We Know and What Can We Expect? *Pediatrics* 141, S154–S160. doi: 10.1542/peds.2017-2038D

Wijarnpreecha, K., Thongprayoon, C., Panjawatanan, P., and Ungprasert, P. (2017). Hepatitis C Virus Infection and Risk of Venous Thromboembolism: A Systematic Review and Meta-Analysis. *Ann. Hepatol.* 16, 514–520. doi: 10.5604/01.3001.0010.0279

Xie, Y., Mustafa, A., Yerzhan, A., Merzhakupova, D., Yerlan, P., N Orakov, A., et al. (2017). Nuclear matrix metalloproteinases: functions resemble the evolution from the intracellular to the extracellular compartment. *Cell Death Discovery* 3, 17036. doi: 10.1038/cddiscovery.2017.36

Yang, Y., Candelario-Jalil, E., Thompson, J. F., Cuadrado, E., Estrada, E. Y., Rosell, A., et al. (2010). Increased intranuclear matrix metalloproteinase activity in neurons interferes with oxidative DNA repair in focal cerebral ischemia. *J. Neurochem.* 112, 134–149. doi: 10.1111/j.1471-4159.2009.06433.x

Zybailov, B., Mosley, A. L., Sardiu, M. E., Coleman, M. K., Florens, L., and Washburn, M. P. (2006). Statistical analysis of membrane proteome expression changes in Saccharomyces cerevisiae. *J. Proteome Res.* 5, 2339–2347. doi: 10.1021/pr060161n

Conflict of Interest: The authors declare that the research was conducted in the absence of any commercial or financial relationships that could be construed as a potential conflict of interest.

Copyright © 2020 Macedo-da-Silva, Rosa-Fernandes, Barbosa, Angeli, Carvalho, de Oliveira Vianna, Carvalho, Larsen, Cardoso and Palmisano. This is an open-access article distributed under the terms of the Creative Commons Attribution License (CC BY). The use, distribution or reproduction in other forums is permitted, provided the original author(s) and the copyright owner(s) are credited and that the original publication in this journal is cited, in accordance with accepted academic practice. No use, distribution or reproduction is permitted which does not comply with these terms.

Advantages of publishing in Frontiers

OPEN ACCESS
Articles are free to read for greatest visibility and readership

FAST PUBLICATION
Around 90 days from submission to decision

HIGH QUALITY PEER-REVIEW
Rigorous, collaborative, and constructive peer-review

TRANSPARENT PEER-REVIEW
Editors and reviewers acknowledged by name on published articles

Frontiers
Avenue du Tribunal-Fédéral 34
1005 Lausanne | Switzerland

Visit us: www.frontiersin.org
Contact us: frontiersin.org/about/contact

REPRODUCIBILITY OF RESEARCH
Support open data and methods to enhance research reproducibility

DIGITAL PUBLISHING
Articles designed for optimal readership across devices

FOLLOW US
@frontiersin

IMPACT METRICS
Advanced article metrics track visibility across digital media

EXTENSIVE PROMOTION
Marketing and promotion of impactful research

LOOP RESEARCH NETWORK
Our network increases your article's readership